

## University of Southampton Research Repository ePrints Soton

Copyright © and Moral Rights for this thesis are retained by the author and/or other copyright owners. A copy can be downloaded for personal non-commercial research or study, without prior permission or charge. This thesis cannot be reproduced or quoted extensively from without first obtaining permission in writing from the copyright holder/s. The content must not be changed in any way or sold commercially in any format or medium without the formal permission of the copyright holders.

When referring to this work, full bibliographic details including the author, title, awarding institution and date of the thesis must be given e.g.

AUTHOR (year of submission) "Full thesis title", University of Southampton, name of the University School or Department, PhD Thesis, pagination

---

**University of Southampton**  
Faculty of Science  
School of Ocean and Earth Science

The Effects of Variation in Wave Period and  
Flow Asymmetry in Sediment Dynamics.

by  
David Owen Lambkin

Thesis for the degree of Doctor of Philosophy.  
July, 2004.

---

UNIVERSITY OF SOUTHAMPTON

## **Abstract**

FACULTY OF SCIENCE

SCHOOL OF OCEAN AND EARTH SCIENCE

Doctor of Philosophy

The Effects of Variation in Wave Period and Flow Asymmetry in Sediment Dynamics.

The results of laboratory experiments are described, relating to aspects of hydrodynamics and sediment dynamics under second-order Stokes type waves (or flows), of varying degrees of asymmetry. The majority of the measurements related to laminar and/or transitional flow conditions and were made using an oscillating trolley apparatus.

The transition to turbulence over smooth beds has been reported previously in terms of a (single) critical flow amplitude Reynolds number,  $Re_{crit} = U_{\infty} a / \nu$ . On the basis of observations undertaken using sinusoidal flows (Li, 1954) and during the present study, this is found to be the case for wave periods of  $T > 3.5s$ , where mean  $Re_{crit} = 1.66 \times 10^5$ . However, for  $T < 3.5s$ , it is shown that  $Re_{crit}$  decreases in proportion to  $T$ . On the basis of the observations made by Li (1954), Manohar (1955) and during the present study, transition over rough (granular) beds is described by  $Re_{crit} = c(a/D)$ , where  $c$  is a coefficient that, for relatively fine sediment ( $D < 275 \mu m$ ), is a linear function of  $T$ ; for relatively coarse sediment ( $D > 421 \mu m$ ), it is a linear function of  $D$ . At large values of  $Re_{crit}$ , corresponding to longer wave periods together with relatively small bed roughness length-scales, the observed values deviate from the rough-bed relationship and tend towards the smooth-bed limiting value. Flow asymmetry acts to stabilise the boundary layer, increasing either the critical boundary Reynolds number  $RE_{crit} = U_c \sqrt{2\nu/\omega} / \nu$  (in the case of smooth beds), or  $Re_{crit}$  (in the case of rough beds), following a non-linear relationship. Regulating mechanisms are proposed by which the transition to turbulence is governed over (relatively) smooth and/or rough beds. Of principle importance is the balance between the stabilising effect of fluid acceleration and the destabilising effects of vertical gradients in the horizontal velocity (thought to be important in regulating transition over a smooth-bed) and localised eddy formation around individual grains on the bed (similarly over rough beds).

The threshold of motion for non-cohesive, sand-sized sediment is expressed typically as a critical bed shear stress amplitude,  $\tau_o$ , relative to the resistant properties of individual grains

---

(due to gravity). On this basis, numerous critical shear stress (e.g. the well known approach of Shields, 1936) and velocity amplitude relationships have been presented elsewhere. Previously, Voulgaris *et al.* (1995) have identified that a higher  $\tau_0$  is required to cause threshold at smaller wave periods. On the basis of a large number of observations undertaken (elsewhere, and as part of the present study) using similar equipment, a negative linear relationship has been established between  $T$  and  $\tau_0$ ; this becomes progressively more significant, for threshold occurring under larger values of  $Re$  (into the transitional regime). Flow asymmetry has the effect of increasing  $\tau_{0\text{ crit}}$ ; however, the critical orbital diameter for given conditions remains approximately constant, irrespective of the asymmetry. Using these data, in combination with detailed observations of the phase of the onset and the subsequent duration of sediment motion, it is suggested that (especially under (near) laminar flows) the threshold of motion is in response to a 'time-' or 'phase-mean' shear stress, corresponding to some form of cumulative force. In addition, under turbulent or partially turbulent flow conditions, the stochastic distribution of the instantaneous shear stress is broader under waves of larger  $T$  and/or smaller  $R$ ; this permits similarity in the occurrence of high-shear events, over a range of conditions. However, the mean  $\tau_{0\text{ crit}}$  decreases. Hence, an artefact or anomalous decrease is included, at longer wave periods, in the (time-mean) peak value of  $\tau_{0\text{ crit}}$  used to represent such flows.

---

---

*Of waves we really can't fathom,  
why we get them as big as we 'ave 'em.  
To gargantuan size, they occasionally rise,  
and our very best matics' can't math em!*

*Anon.*

---

# Contents

<b>Acknowledgments</b> .....	<b>i</b>
<b>List of Figures</b> .....	<b>iii</b>
<b>List of Plates</b> .....	<b>ix</b>
<b>List of Tables</b> .....	<b>x</b>
<b>Notation and Symbols</b> .....	<b>xii</b>
<b>Chapter 1. Introduction</b> .....	<b>1</b>
1.1. Background.....	1
1.2. Objectives of the thesis .....	5
1.3. Structure of the thesis .....	6
<b>Chapter 2. Literature Review</b> .....	<b>8</b>
2.1. Introduction .....	8
<i>Waves and Oscillatory Flows</i> .....	8
2.2. General wave theory .....	8
2.2.1. <i>Basic definitions and nomenclature</i> .....	8
2.2.2. <i>The spectrum of wave theories</i> .....	10
2.2.3. <i>Validity of wave theories</i> .....	10
2.3. Linear and second-order Stokes theory .....	12
2.3.1. <i>The water surface</i> .....	12
2.3.2. <i>The water column and near bed flow</i> .....	13
<i>The Laminar Oscillatory Boundary Layer</i> .....	17
2.4. Linear theory.....	17
2.5. Second-order theory.....	18
2.6. Cnoidal theory .....	19
<i>Transition to Turbulence</i> .....	20
2.7. Introduction .....	20
2.8. Hydrodynamically smooth beds .....	22
2.8.1. <i>Sinusoidal flow</i> .....	22
2.8.2. <i>Asymmetric flow</i> .....	24
2.9. Hydrodynamically rough beds.....	25
2.9.1. <i>Sinusoidal flow</i> .....	25
2.9.2. <i>Asymmetric flow</i> .....	27
<i>Threshold of Sediment Motion</i> .....	27
2.10. Introduction .....	27
2.11. Basic definitions and nomenclature.....	28
2.12. Methods of observation .....	28
2.12.1. <i>Visual observation – descriptive methods</i> .....	29
2.12.2. <i>Visual observation – the Yalin Criterion</i> .....	30
2.13. The critical velocity approach .....	30
2.14. The Shields (1936) approach .....	35
2.15. The Moveability Number approach.....	38
2.16. The stochastic approach.....	39
<b>Chapter 3. Equipment Description</b> .....	<b>41</b>
3.1. The recirculating flume.....	41
3.2. The oscillating trolley .....	42
3.2.1. <i>General description</i> .....	42
3.2.2. <i>Control software</i> .....	44

---

3.2.3. <i>Plate positioner</i> .....	44
3.2.4. <i>Calibration of the plate positioner</i> .....	45
3.2.5. <i>Calibration/validation of the oscillating trolley</i> .....	45
3.2.6. <i>Sediments used in the present study</i> .....	46
3.2.7. <i>Smooth and fixed granular beds</i> .....	51
3.3. Flow velocity measurement.....	51
3.3.1. <i>The LDV system</i> .....	51
3.3.2. <i>Resolution and accuracy of the LDV</i> .....	52
<b>Chapter 4. Experimental Methodology</b> .....	<b>54</b>
4.1. Velocity profiling .....	54
4.1.1. <i>Introduction</i> .....	54
4.1.2. <i>General methodology</i> .....	55
4.1.3. <i>Data analysis</i> .....	56
4.2. Transition to turbulence .....	56
4.2.1. <i>Introduction</i> .....	56
4.2.2. <i>General methodology</i> .....	57
4.2.3. <i>Visual observation method</i> .....	57
4.2.4. <i>Velocity time-series method</i> .....	58
4.2.5. <i>Turbulent intensity method</i> .....	59
4.3. Threshold of motion .....	60
4.3.1. <i>Introduction</i> .....	60
4.3.2. <i>General methodology</i> .....	61
4.3.3. <i>Definition of threshold</i> .....	62
4.4. Quantities of interest.....	64
4.4.1. <i>Angle of repose</i> .....	64
4.4.2. <i>Velocity and stroke amplitude</i> .....	65
4.4.3. <i>Fluid shear stress</i> .....	65
4.4.4. <i>Acceleration of the bed and of mobile grains</i> .....	70
4.4.5. <i>Resistive forces</i> .....	72
4.4.6. <i>Ballistic momentum flux</i> .....	72
4.5. Phase and duration of sediment motion .....	72
<b>Chapter 5. Velocity Profiling</b> .....	<b>74</b>
5.1. Introduction .....	74
5.2. Results: The outer layer .....	74
5.2.1. <i>The form of outer layer oscillations</i> .....	74
5.2.2. <i>Comparison with the model</i> .....	77
5.3. Discussion: The outer layer .....	77
5.4. Results: The inner layer .....	78
5.4.1. <i>Comparison with the model</i> .....	78
5.5. Discussion: The inner layer .....	81
5.5.1. <i>Summary of the sources of error</i> .....	81
5.5.2. <i>Use of the model for description of the boundary layer</i> .....	82
5.6. Results: Comparison between wave theories.....	83
5.6.1. <i>First order vs second order theory</i> .....	83
5.6.2. <i>Second order vs Cnoidal theory</i> .....	86
5.7. Discussion: Comparison between wave theories .....	89
<b>Chapter 6. Transition to Turbulence</b> .....	<b>91</b>
6.1. Introduction .....	91
6.2. Results: Critical flow parameters.....	91
6.2.1. <i>Sinusoidal flow</i> .....	91
6.2.2. <i>Asymmetric flow</i> .....	93
6.2.3. <i>Comparison of methods and estimation of error</i> .....	97

---

6.3. Results: Smooth beds.....	98
6.3.1. <i>Sinusoidal flows</i> .....	98
6.3.2. <i>Asymmetric flows</i> .....	100
6.4. Results: Rough beds .....	103
6.4.1. <i>Sinusoidal flows</i> .....	103
6.4.1.a. Critical length-scale method.....	103
6.4.1.b. Critical time-scale method .....	106
6.4.2. <i>Asymmetric flows</i> .....	110
6.5. Discussion: Processes regulating the transition to turbulence over smooth and rough beds.....	112
6.6. Discussion: Implications for the interpretation of previous studies concerning the transition to turbulence. ....	114
6.7. Discussion: Implications for future studies concerning the transition to turbulence.....	115
<b>Chapter 7. Threshold of Motion .....</b>	<b>117</b>
7.1. Introduction .....	117
7.2. Results: Critical flow parameters.....	117
7.2.1. <i>Sinusoidal flows</i> .....	117
7.2.2. <i>Asymmetric flows</i> .....	119
7.2.3. <i>Estimation of error</i> .....	121
7.3. Results: The effect of wave period on $\tau_{0\text{ crit}}$ .....	122
7.3.1. <i>Introduction</i> .....	122
7.3.2. <i>Observational errors</i> .....	126
7.3.3. <i>Experimental errors</i> .....	126
7.3.4. <i>Numerical errors</i> .....	127
7.3.5. <i>Physical mechanisms</i> .....	132
7.3.5.a. Apparent shear stress offset .....	133
7.3.5.b. Cumulative force effects .....	136
7.4. Results: The effect of flow asymmetry on $\tau_{c\text{ crit}}$ .....	137
7.4.1. <i>Introduction</i> .....	137
7.4.2. <i>Numerical error</i> .....	140
7.4.3. <i>Physical Mechanisms</i> .....	144
7.4.3.a. Apparent shear stress offset .....	144
7.4.3.b. Cumulative force effects .....	145
7.5. Results: The phase and duration of sediment motion at threshold. ....	150
7.5.1. <i>The presence of turbulence</i> .....	150
7.5.2. <i>Sinusoidal flows</i> .....	151
7.5.3. <i>Asymmetric flows</i> .....	154
7.6. Discussion: The effect of wave period and asymmetry on $\tau_{c\text{ crit}}$ under laminar and transitional flow conditions. ....	158
7.6.1. <i>Laminar flow conditions</i> .....	158
7.6.2. <i>Transitional/turbulent flow conditions</i> .....	159
7.7. Discussion: The suitability of various methods to predict the threshold of motion for sand under waves.....	161
7.7.1. <i>The critical velocity approach</i> .....	161
7.7.2. <i>The approach of Shields (1936)</i> .....	164
7.7.3. <i>The Moveability Number approach</i> .....	167
7.7.4. <i>Stochastic approaches</i> .....	169
<b>Chapter 8. Conclusions.....</b>	<b>171</b>
8.1. Velocity profiling .....	171
8.2. Transition to turbulence .....	171
8.3. Threshold of motion .....	172
8.4. Other findings .....	174

---

8.5. Recommendations for future research .....	175
<b>References .....</b>	<b>177</b>
<b>Appendix A. Laminar boundary layer theory.....</b>	<b>187</b>
<b>Appendix B. Velocity profiling results .....</b>	<b>191</b>
<b>Appendix C. Transition to turbulence results .....</b>	<b>195</b>
<b>Appendix D. Threshold of motion results.....</b>	<b>197</b>
<b>Appendix E. Lambkin, Collins and Paphitis (In Press).....</b>	<b>211</b>

---

## Acknowledgments

I would like to extend my warm thanks to my supervisor Professor Mike Collins for his encouragement and support with the thesis and with the paper. I appreciate the efforts that he has made, to make available the resources and equipment, without which this thesis would not have been possible.

Thanks also to the other members of my supervision panel – Prof. Martin Palmer (Chair) and Prof. Carl Amos. Also to Dr. Doros Paphitis for his valued and considerate help over a number of years. Thank you to Morten Kramer of the University of Ålborg, Denmark, for his help and friendship these last years.

Friends are always an essential ingredient for life and I will never forget the SOC crowd: Susanne Ufermann, Hans Fangohr, Babette Hoogakker, Uli Riemenschneider, Sinhue Torres, Anna Hilario, Cesar Ribero, James Harle, Agostino Merico, Charlie Thompson, Judith Homewood. And to the most fantastic group of friends: Karen Dock, Howard Osborne, Sarah Fletcher, Vicky Scott.

Thank you to the support and technical staff without whom, this project would not have been possible. Many thanks to John Davis, Ray Collins and John Hewitt for their support and efforts in the construction of some parts of the equipment used. Thank you to Kate Davis for her assistance in creating the schematic diagrams of the flume and trolley, also in finalising a number of the Figures used in publications resulting from this work.

I dedicate this thesis to my dear Mum and Dad, Carol and Geoff, who have supported me always with incredible love and motivation. I also dedicate this work to the spirit and enthusiasm of my Grandparents, who have encouraged me throughout my life. I also would like to recognise Sir David Attenborough for starting-, my many teachers throughout the years for developing-, and Dirk Pitt for romanticising my passion for the natural sciences.

Graduate School of the  
Southampton Oceanography Centre

This PhD dissertation by  
David Owen Lambkin  
has been produced under the supervision of the following persons

Supervisor: Prof. M.B. Collins.

Chair of Advisory Panel: Prof. M. Palmer

Members of Advisory Panel: Prof. C.L. Amos  
Dr. D. Paphitis

## List of Figures

Figure 2.1. Schematic illustration of the basic wave parameters. ....	9
Figure 2.2. Validity limits for various wave theories, in terms of wave height ( $H$ ), period ( $T$ ), wavelength ( $\lambda$ ) and water depth ( $d$ ), (from Sleath, 1984). Note: the coloured areas highlight the conditions represented in the present study. ....	11
Figure 2.3. Surface displacement about the mean water level, as predicted by second-order Stokes theory, for waves of: (a) low, (b) medium and (c) high wave asymmetry. Subplot (a) corresponds also to the surface displacement predicted by linear (Airy) wave theory. ....	13
Figure 2.4. Normalised velocity cycles for: (a) $R=0.5$ ; (b) $R=0.6$ ; and (c) $R=0.7$ . ....	16
Figure 2.5. Normalised velocity distribution within the laminar boundary layer (Eq. 2.11); linear theory ( $R=0.5$ ). ....	18
Figure 2.6. Normalised velocity distribution within the laminar boundary layer (Eq. 2.14); second-order Stokes theory ( $R=0.6$ ). ....	19
Figure 2.7. Normalised friction coefficient verses $Re$ (shown as ‘RE’ in this particular diagram) at different phase values over a smooth bed (from Jensen <i>et al.</i> , 1989). ....	23
Figure 2.8. Boundary layer stability, over a smooth bed, under cnoidal flows. From Tanaka <i>et al.</i> (2000). Key: $R_\delta=RE$ and $A_s=R$ . ....	24
Figure 2.9. Boundary layer stability, over a rough bed. ....	27
Figure 2.10. Predicted $U_{\infty \text{ crit}}$ from various threshold of motion relationships from Sleath (1984), for quartz grains: (a) $D=275\mu\text{m}$ and (a) $D=800\mu\text{m}$ . Highlighted are the curves of: (i) Bagnold (1946); (ii) Manohar (1955); (iii) Komar and Miller (1973, 1974) and additionally; (iv) Shields (1936); (v) You (2000) and (vi) Le Roux (2001). ....	31
Figure 2.11. Shields steady flow curve, with selected threshold observation data superimposed, collected under sinusoidal oscillatory flows. ....	37
Figure 3.1. The recirculating flume and oscillating trolley, located at SOC. Key: (a) hydraulic ram; (b) linear carriage; (c) oscillating plate; (d) raised upstream bed; (e) flow-straightening tiles. ....	41
Figure 3.2. The oscillating trolley equipment mounted within the recirculating flume (not to scale): (a) side and (b) cut-away along flume views. Note: see text for a description of the various components. ....	42
Figure 4.1. Theoretical combinations of wave height and water depth relating to the simulated conditions listed in Table 4.1 ( $R=0.5$ ). The values were derived on the basis of linear wave theory. Note: the text labelling indicates the stroke length (m). ....	55
Figure 4.2. Recorded velocity time-series, corresponding to: (a) & (b) laminar (stroke length = 66cm, and $RE = 573$ ); and, (c) & (d) transitional/turbulent, (stroke length = 82cm, and $RE = 712$ ) flows, over a smooth bed ( $T = 6\text{s}$ , $R=0.6$ , $z=3\text{mm}$ ). ....	59
Figure 4.3. Turbulent intensity, $E$ , at $z=3\text{mm}$ , with increasing stroke length, demonstrating the transition to turbulence. ( $D=275\mu\text{m}$ , $T=6\text{s}$ and $R=0.55$ ). ....	60

Figure 4.4. Wave friction factor diagrams: (a) Jonnson (1966); (b) Kamphuis (1975); and (c) Myrhaug (1989). .....	68
Figure 4.5. Acceleration limits of Hammond and Collins (1979) (a) and Davies and Wilkinson (1977) (b), in comparison to the threshold of motion data used in the present study.....	71
Figure 5.1. Representative time-series of velocity outside the boundary layer ( $z=20\text{mm}$ ), illustrating the presence of the ‘parasitic’ oscillatory flow for: (a) $[T=9\text{s}, S=0.5\text{m}, R=0.5]$ ; (b) $[T=9\text{s}, S=0.75\text{m}, R=0.5]$ ; (c) $[T=9\text{s}, S=0.5\text{m}, R=0.6]$ ; (d) $[T=9\text{s}, S=0.5\text{m}, R=0.7]$ ; (e) $[T=6\text{s}, S=0.5\text{m}, R=0.6]$ ; and (f) $[T=12\text{s}, S=0.5\text{m}, R=0.6]$ .....	75
Figure 5.2. Outer layer (parasitic) oscillatory flows: velocity amplitude (a) & (b); and phase lag (c) & (d), of the principle and second harmonics, respectively. ....	76
Figure 5.3. Flow structure of the outer flow and the boundary layer, for oscillation of $[T=9\text{s}, S=50\text{cm}, R=0.5]$ (left side) and $[T=12\text{s}, S=50\text{cm}, R=0.6]$ (right side) over a smooth bed. Vertical profiles of: (a) instantaneous velocity from $\omega t=0-\pi$ with axes of measurement fixed in the moving plate; (b) phase lag; and (c) velocity amplitude with the axes of measurement fixed in the still water. <b>Key:</b> grey lines – theoretical distribution (Du Toit and Sleath, 1981; see also Eq. A.8 and A.12); black lines and points – observed distribution; and red line – boundary layer extent ( $\delta_{0.99}=4.6052/\beta=7.8\text{mm}$ ). ....	79
Figure 5.4. Deviations and fluctuations observed in the velocity profiles. Data for $[T=9\text{s}, S=75\text{cm}, R=0.5]$ Key as Figure 5.3. ....	80
Figure 5.5. Wave boundary layers calculated using second-order Stokes theory. Subplots illustrate the vertical and temporal distribution of: (i) absolute velocity; (ii) fluid acceleration; fluid shear (iii) in the boundary layer; and, (iv) at the bed. These are in relation to the velocity cycle at the edge of the boundary layer (v). Values are shown as a percentage of the maximum value in the sinusoidal case for: (a) $R=0.5$ ; (b) $R=0.6$ ; and (c) $R=0.7$ . Key: blue lines – sinusoidal case (for comparison); red lines – asymmetric case.....	86
Figure 5.6. Comparison of second-order Stokes and cnoidal wave boundary layers: (i) absolute velocity; (ii) fluid acceleration; and (iii) fluid shear at the bed, relative to the outer layer velocity (iv). Percentage deviation from the second-order Stokes solution: (a) $R=0.6$ ; (b) $R=0.65$ ; and (c) $R=0.7$ . Key: blue lines – second-order Stokes theory; red lines – cnoidal theory. ....	88
Figure 6.1. $S_{\text{crit}}$ (a) and $U_{\infty \text{crit}}$ (b) causing transition to turbulence over uniform, fixed granular beds under sinusoidal flows. See text for more details. ....	92
Figure 6.2. Trends in the values of $\tau_{0 \text{crit}}$ causing transition to turbulence over uniform, fixed granular beds under sinusoidal flows.....	93
Figure 6.3. (a) Velocity distribution in the sinusoidal boundary layer and the location of the maximum velocity gradient (black points) through the phase range of the onset of transition (red lines); and (b) maximum observed values in sinusoidal flows causing transition to turbulence over uniform, fixed granular beds.....	93
Figure 6.4. Trends in the values of $S_{\text{crit}}$ ((a) and (b)) and $U_{c \text{crit}}$ ((c) and (d)), in relation to asymmetry and wave period, respectively, causing transition to turbulence over smooth beds under asymmetric flows.....	94
Figure 6.5. Trends in the values of $S_{\text{crit}}$ ((a) and (b)) and $U_{c \text{crit}}$ ((c) and (d)), in relation to asymmetry and wave period, respectively, causing transition to turbulence over uniform, fixed granular beds ( $D=275\mu\text{m}$ ) under asymmetric flows. ....	95

Figure 6.6. Trends in the values of $S_{crit}$ ((a) and (b)) and $U_{c\ crit}$ ((c) and (d)), in relation to asymmetry and wave period, respectively, causing transition to turbulence over uniform, fixed granular beds ( $D=550\mu\text{m}$ ).....	95
Figure 6.7. Trends in the value of $\tau_{0\ crit}$ in relation to asymmetry (a) and wave period (b), causing transition to turbulence. Observations made over smooth beds (i) and uniform, fixed granular beds, $D=275\mu\text{m}$ (ii) and $D=550\mu\text{m}$ (iii). Key for (a): $T=3\text{s}$ (o); $T=6\text{s}$ (+); $T=9\text{s}$ (x); $T=12\text{s}$ ( $\Delta$ ). Key for (b): $R=0.5$ (blue); $R=0.55$ (turquoise); $R=0.6$ (green); $R=0.65$ (orange); $R=0.7$ (red).....	96
Figure 6.8. Trends in the value of the velocity gradient parameter, $\delta u/\delta z$ (a measure of a destabilising fluid force), in relation to asymmetry (a) and wave period (b), at the transition to turbulence. Observations made over smooth beds (i) and uniform, fixed granular beds, $D=275\mu\text{m}$ (ii) and $D=550\mu\text{m}$ (iii). Key: (a) $T=3\text{s}$ (o); $T=6\text{s}$ (+); $T=9\text{s}$ (x); $T=12\text{s}$ ( $\Delta$ ); and (b) $R=0.5$ (blue); $R=0.55$ (turquoise); $R=0.6$ (green); $R=0.65$ (orange); $R=0.7$ (red). .....	97
Figure 6.9. Relative error between methods used in the present study for observation of the transition to turbulence. ....	98
Figure 6.10. The observed transition to turbulence over smooth beds, under sinusoidal oscillatory flows. The suggested fit to the data (Eq. 6.1) is superimposed.....	99
Figure 6.11. Stability of the oscillatory boundary layer over a flat, smooth bed. <b>Key:</b> Laminar (O) and transitional/turbulent ( $\bullet$ ) conditions and flows at initial transition under the crest (+) and trough (x) half cycles, as observed in the present study; solid line and envelope – least squares fit to crest data (and corresponding curve for the trough) and 99% confidence interval; dotted line – relationship for cnoidal flows, as proposed by Tanaka <i>et al.</i> (2000). See text for more details.....	101
Figure 6.12. The observed transition to turbulence over rough beds, under sinusoidal oscillatory flows, $D\geq 421\mu\text{m}$ . Colours have been used to differentiate between groups of data, corresponding to values of $D$ (as indicated); horizontal lines correspond to the mean value of each of the data subsets. ....	104
Figure 6.13. The observed transition to turbulence over rough beds, under sinusoidal oscillatory flows for $D\geq 421\mu\text{m}$ : trend analysis of the mean value of $c$ with $D$ . ....	105
Figure 6.14. The observed transition to turbulence over rough beds, under sinusoidal oscillatory flows for $D\leq 275\mu\text{m}$ . The linear dependence of $c$ on $T$ , together with the suggested fit to the data are shown. ....	105
Figure 6.15. Comparison of observed values of $Re_{crit}$ over flat, rough (granular) beds and those predicted using Eq. 6.5. ....	106
Figure 6.16. The observed transition to turbulence over rough beds, under sinusoidal oscillatory flows, for all values of $D$ : linear dependency of $Re$ with $T$ and the limiting ‘smooth bed’ condition are demonstrated. Colours have been used to differentiate between groups of data, corresponding to different values of $D$ (as indicated).....	107
Figure 6.17. The observed transition to turbulence over rough beds, under sinusoidal oscillatory flows, for all $D$ : variation of the gradient ( $\delta Re/\delta T$ ) with $D$ is illustrated... ..	108
Figure 6.18. Comparison of the observed values of $Re_{crit}$ over flat, rough (granular) beds and those predicted using Eq. 6.7, incorporating the sinusoidal data of Li (1954), Manohar (1955) and the present study. ....	109
Figure 6.19. The predicted transition to turbulence under sinusoidal oscillatory flows (Eq. 6.3 and Eq. 6.7). ....	109

---

Figure 6.20. Stability of the oscillatory boundary layer over a flat, rough (granular) bed: (a) $D=275\mu\text{m}$ ; (b) $D=550\mu\text{m}$ . <b>Key:</b> Transition to turbulence observed under the crest (+) and trough ( $\times$ ) half cycles, in the present study; solid line – least squares fit to crest data (Eq. 6.3 and Table 6.2, incorporating Eq. 6.5) and corresponding curve for the trough (Eq. 6.4 – not based on data). Colours are used to identify data subsets of different $T$ . .....	110
Figure 6.21. Normalised increase in $\text{Re}_{\text{crit}}$ caused by flow asymmetry for observations made under the crest (+) and trough ( $\times$ ) half-cycles. Best fit curves for data from the smooth bed (red lines and data), $D=275\mu\text{m}$ (green lines and data), and $D=550\mu\text{m}$ (blue lines and data) experiments (Eq. 6.8 and Table 6.3). .....	112
Figure 7.1. $S_{\text{crit}}$ (a) and $U_{\infty \text{crit}}$ (b) causing threshold of motion in sands, representative of the range of $D$ and $\rho_s$ in the main dataset. Data are sourced from Li (1954) and Manohar (1955), different grain types are identified in no order using a variety of colours and marker shapes.....	118
Figure 7.2. Variation of $\delta S_{\text{crit}}/\delta T$ (a) and $\delta U_{\text{crit}}/\delta T$ (b) with grain size for uniform sediments of density: $2450 < \rho_s < 2700$ (black points and lines); and $1260 < \rho_s < 1460$ (red points and lines). Also shown are the predictive curves of You (2000) (Eq. 2.36).....	119
Figure 7.3. Trends in $S_{\text{crit}}$ ((a) and (b)) and $U_{\text{c crit}}$ ((c) and (d)) causing threshold of motion in quartz sand, $D=390\mu\text{m}$ , in the presence of flow asymmetry. ....	120
Figure 7.4. Observed $\delta U_{\text{crit}}/\delta R$ with respect to wave period (a) and grain size (b).....	121
Figure 7.5. $\tau_{\text{c crit}}$ causing threshold of motion for: (a) all of the sinusoidal flow observations (sources listed in Section 7.1) showing values normalised to the mean of all data $T=6\text{s}$ , also line of best fit; and (b) for selected sinusoidal and all the asymmetric flow experiments undertaken using quartz sand during the present study (actual values)...	123
Figure 7.6. The magnitude of $\delta \tau_{0 \text{crit}}/\delta T$ under sinusoidal flows (including all data used in the present study). Data points represent particular grain sizes, of density: $\rho_s < 2650 \text{ kgm}^{-3}$ (blue); $\rho_s = 2650 \text{ kgm}^{-3}$ (green); $\rho_s > 2650 \text{ kgm}^{-3}$ (red).....	124
Figure 7.7. Variation of $\text{Re}$ with $D$ in the wave friction factor model ( $T=6\text{s}$ ): (a) [ $f_w=0.01$ ( $a/D=545.7$ ), $R=0.5$ ]; (b) [ $f_w=0.02$ ( $a/D=118.8$ ), $R=0.5$ ]. Key: blue line – flow $\text{Re}$ (stage 3); red line –the transition to turbulence. ....	129
Figure 7.8. The effect of wave period on the wave friction factor coefficient. Coloured arrows indicate the effect of increasing $T$ . See text for more details. ....	130
Figure 7.9. Percentage difference in $f_w$ between the fully turbulent (Eq. 4.11) and laminar (Eq. 4.9) solutions at the threshold of motion: (a) $D < 1\text{mm}$ ; and (b) $D < 1\text{cm}$ . Dotted arrows indicate the effect of increasing wave period.....	131
Figure 7.10. Comparison of $\tau_{0 \text{crit}}$ for threshold of motion under sinusoidal flows, calculated using the laminar solution (O) and the transitional model ( $\Delta$ ) for (a) [ $D=1800\mu\text{m}$ , $\rho_s=2600 \text{ kgm}^{-3}$ ]; and (b) [ $D=800\mu\text{m}$ , $\rho_s=2630 \text{ kgm}^{-3}$ ]. ....	132
Figure 7.11. Theoretical shear stress distribution causing threshold of motion.....	134
Figure 7.12. Modelled observations of instantaneous shear stress, for flow conditions at the threshold of motion for sand [ $\rho_s=2540 \text{ kgm}^{-3}$ and $D=600\mu\text{m}$ ] under sinusoidal flows. The effect of variation in the parameter $y$ is illustrated. ....	135
Figure 7.13. Definition of the mean force calculation variables for sinusoidal flows. ....	136
Figure 7.14. Mean shear stress causing threshold of motion in sands: (a) $\rho_s=2630 \text{ kgm}^{-3}$ , $D=800\mu\text{m}$ ; and (b) $\rho_s=1280 \text{ kgm}^{-3}$ , $D=3200\mu\text{m}$ . ....	137

---

Figure 7.15. Bed shear stress causing threshold of motion in sediments investigated during the present study, consisting of: (a) quartz (b) aragonite and (c) Bakelite. The result of increasing flow asymmetry is demonstrated.....	138
Figure 7.16. Variation in $\delta\tau_{c\text{ crit}}/\delta R$ calculated using laminar theory: (a) over the transitional range; and (b) in relation to wave period. Colours highlight differences in grain size, whilst symbols differentiate between the granular materials.....	139
Figure 7.17. The laminar wave friction factor, under asymmetric oscillatory flows.....	140
Figure 7.18. Variation of Re with D in the wave friction factor model ( $T=6s$ ): (a) [ $f_w=0.01$ ( $a/D=545.7$ ), $R=0.6$ ]; (b) [ $f_w=0.02$ ( $a/D=118.8$ ), $R=0.7$ ]. Key: blue line – flow Re; red line – the transition to turbulence.....	141
Figure 7.19. The wave friction factor, under asymmetric laminar flows. Arrows indicate the effect of increasing $R$ on the point of departure from the laminar solution. Values are based on a fixed value of $T=6s$ . ....	141
Figure 7.20. Variation in $\delta\tau_{c\text{ crit}}/\delta R$ calculated using the transitional model: (a) over the transitional range; and (b) with wave period. Colours highlight differences in grain size whilst symbols differentiate between the granular materials, also see text for more details.....	143
Figure 7.21. Comparison of $\tau_{c\text{ crit}}$ for threshold of motion under asymmetric flows, calculated using the laminar solution (O) and the transitional model ( $\Delta$ ), for quartz sediment ( $\rho_s=2650\text{ kgm}^{-3}$ ). Variation with asymmetry (for $T=6s$ ) and with wave period (for $R=0.7$ ) for (a) & (c), $D=550\mu\text{m}$ ; and (b) & (d), $D=327.5\mu\text{m}$ .....	144
Figure 7.22. Theoretical shear stress distribution causing threshold of motion; the observation frequency of $\tau'$ during the positive shear stress half-cycle for a range of $R$ . ....	145
Figure 7.23. Shear stress cycles calculated using laminar theory, causing threshold of motion in quartz sand ( $D=327.5\mu\text{m}$ ): (a) $4s < T < 10s$ ; and (b) $T=6s$ . Key: blue lines ( $R=0.5$ ); green lines ( $R=0.6$ ); red lines ( $R=0.7$ ).....	146
Figure 7.24. Peak shear stress causing threshold of motion in quartz sands ( $275\mu\text{m} < D < 550\mu\text{m}$ ) plotted in relation to the modified period (Eq. 7.4). The shaded area on the Figure represents the spread of the data, when plotted directly against $T$ . ....	147
Figure 7.25. Definition of the cumulative force calculation variables for asymmetric flows. ....	148
Figure 7.26. Mean shear stress causing threshold of motion in quartz sand ( $D=327.5\mu\text{m}$ ), for $T=5s$ and $9s$ . Data are truncated at the width of the positive shear stress peak, for each value of $R$ , accordingly. ....	149
Figure 7.27. Flow conditions for visual observation data of the onset and duration of sediment motion, at threshold. Key: data points – observed conditions; shaded area – the transitional range.....	150
Figure 7.28. Quartz sediment motion under sinusoidal flows: (a) the phase of onset relative to the phase of $\tau_0$ ; and (b), the duration of motion. Key: dotted lines show the mean trend. ....	152
Figure 7.29. Observations of the phase of onset and duration of quartz sand motion at the threshold of motion condition, under sinusoidal flows. Key: blue lines – outer flow velocity ( $\text{ms}^{-1}$ ); red lines – laminar shear stress ( $\text{Nm}^{-2}$ ); green lines – plate (grain) acceleration forces ( $\text{ms}^{-2}$ ); shaded area – period of observed grain motion.....	153

Figure 7.30. Sediment motion under asymmetric flows: (a) & (b) the phase of onset relative to the phase of  $\tau_c$ ; and (c) & (d), the duration of motion for quartz sands  $D=550\mu\text{m}$  and  $D=275\mu\text{m}$ , respectively. Key: Dashed lines – mean trend..... 154

Figure 7.31. Observations of the phase and duration of quartz sand motion, at the threshold of motion condition under asymmetric flows. Key: blue lines – outer flow velocity; red lines – laminar shear stress; green lines – grain inertial forces; shaded area – period of observed grain motion (lighter shade – mean duration; darker shade – individual observations)..... 157

Figure 7.32. Critical outer flow velocity amplitude observed in the present study, for threshold of motion in: (a) quartz sediment,  $D=550\mu\text{m}$ ; (b) quartz sediment,  $D=275\mu\text{m}$ ; (c) aragonite sediment,  $D=550\mu\text{m}$ ; and (d) Bakelite sediment,  $D=1500\mu\text{m}$ . Key: blue, green and red lines and data points – Eq. 7.6 using coefficients for all data, and observed data for  $R=0.5, 0.6$  and  $0.7$ , respectively; black lines – predictive equations of Shields (1936) [solid line], Manohar (1955) [dashed line], Komar and Miller (1973, 1974) [dotted line], You (2000) [dot-dashed line] and Le Roux (2001) [solid line with crosses]..... 163

Figure 7.33. The Shields curve for threshold of motion (Eq. 2.46) and threshold data for sinusoidal and asymmetric oscillatory flows. .... 165

Figure 7.34. The Moveability Number parameter for all sinusoidal and asymmetric threshold of motion observations used in the present study. .... 168

## List of Plates

Plate 3.1. The configuration of the central porous mats and solid plates used as flow baffles to maintain still water above the plate. ....	43
Plate 3.2. An example of the user interface screen for controlling the oscillating trolley, during the present study. ....	44
Plate 3.3. The plate positioner system, located (beneath the hydraulic ram) within the flume. ....	45
Plate 3.4. Quartz sediments used in the present study, of median diameter: (a) and (f) 550 $\mu$ m; (b) 472.5 $\mu$ m; (c) 390 $\mu$ m; (d) 327.5 $\mu$ m; and, (e) 275 $\mu$ m. Note: scale bar = 2mm. ....	48
Plate 3.5. Aragonite sediments used in the present study, of median diameter: (a) and (f) 550 $\mu$ m; (b) 472.5 $\mu$ m; (c) 390 $\mu$ m; (d) 327.5 $\mu$ m; and, (e) 275 $\mu$ m. Note: scale bar = 2mm. ....	49
Plate 3.6. Bakelite sediments used in the present study, of median diameter: (a) 1850 $\mu$ m; (b) 1550 $\mu$ m; (c) 1200 $\mu$ m; (d) and (e) 925 $\mu$ m. Note: scale bar = 2mm. ....	50
Plate 3.7. The LDV system: (i) placement within the laboratory; and (ii), in use during a velocity profiling experiment. Key: (a) optic bench, laser source and beam splitter; (b) 'ColorLink' module; (c) 3D traverse; (d) optic head. ....	52

## List of Tables

Table 2.1. Critical combinations of wave parameters delimiting the validity of linear (Lin) and second-order Stokes (Stokes) theory: (1) for waves in deep water, beginning to ‘feel’ the bed ( $d/gT^2=0.0795$ ); and (2) for shallower water depths ( $d/gT^2=0.0075$ ). Values calculated from Figure 2.2. ....	12
Table 2.2. Fitting coefficients for the threshold relationship of Le Roux (2001). (Eq. 2.41). 35	
Table 3.1. Characteristics of the sediments used in the present study. ....	47
Table 4.1. Summary of the velocity profiles measured (wave period and stroke length). Key: (1), high-resolution data set; (2), low-resolution data set; (3), medium-resolution data set. (see also, Section 4.1.2 and Appendix B). ....	55
Table 6.1. Fitting coefficients for Eq. 6.3, describing the transition to turbulence over smooth beds, for second-order Stokes (present study) and cnoidal flows (Tanaka <i>et al.</i> , 2000) .....	101
Table 6.2. Fitting coefficients for Eq. 6.3, describing the transition to turbulence over a rough bed ( $D=550\mu\text{m}$ ), for second-order Stokes flows as observed in the present study. ....	110
Table 6.3. Fitting coefficients for Eq. 6.8, describing the transition to turbulence for second-order Stokes flows, as observed in the present study. ....	111
Table 7.1. Summary of potential causes of the observed dependency on wave period and flow asymmetry. ....	125
Table 7.2. Fitting coefficients for Eq. 7.6, predicting $U_{c \text{ crit}}$ for the threshold of motion. (1) all the data used in the present study; (2) all the sinusoidal data from the present and previous studies (excluding the parameter $R$ ); (3) and all the sinusoidal and asymmetric data collected during the present study. ....	162
Table B.1. Summary of phase referenced velocity profiling cases and results. ....	193
Table B.2. Summary of non-phase referenced velocity profiling cases and results. ....	194
Table B.3. Profile resolutions used during the velocity profiling experiments. Values indicate heights above the bed, $z$ (mm) at which time series were collected. ....	195
Table C.1. Transition to turbulence results for experiments using a smooth bed. ....	196
Table C.2. Transition to turbulence results for experiments using a fixed granular bed roughness, $D=275\mu\text{m}$ . ....	196
Table C.3. Transition to turbulence results for experiments using a fixed granular bed roughness, $D=550\mu\text{m}$ . ....	197
Table D.1. Threshold of motion results for aragonite sediment [ $\rho_s=2700\text{kgm}^{-3}$ , $D=275\mu\text{m}$ ]. ....	199
Table D.2. Threshold of motion results for aragonite sediment [ $\rho_s=2700\text{kgm}^{-3}$ , $D=327.5\mu\text{m}$ ]. ....	200
Table D.3. Threshold of motion results for aragonite sediment [ $\rho_s=2700\text{kgm}^{-3}$ , $D=390\mu\text{m}$ ]. ....	201

Table D.4. Threshold of motion results for aragonite sediment [ $\rho_s=2700\text{kgm}^{-3}$ , $D=462.5\mu\text{m}$ ]	202
Table D.5. Threshold of motion results for aragonite sediment [ $\rho_s=2700\text{kgm}^{-3}$ , $D=550\mu\text{m}$ ]	203
Table D.6. Threshold of motion results for Bakelite sediment [ $\rho_s=1400\text{kgm}^{-3}$ , $D=925\mu\text{m}$ ]	204
Table D.7. Threshold of motion results for Bakelite sediment [ $\rho_s=1400\text{kgm}^{-3}$ , $D=1200\mu\text{m}$ ]	204-5
Table D.8. Threshold of motion results for Bakelite sediment [ $\rho_s=1400\text{kgm}^{-3}$ , $D=1550\mu\text{m}$ ]	205-6
Table D.9. Threshold of motion results for quartz sediment [ $\rho_s=2650\text{kgm}^{-3}$ , $D=275\mu\text{m}$ ]	207
Table D.10. Threshold of motion results for quartz sediment [ $\rho_s=2650\text{kgm}^{-3}$ , $D=327.5\mu\text{m}$ ]	208
Table D.11. Threshold of motion results for quartz sediment [ $\rho_s=2650\text{kgm}^{-3}$ , $D=390\mu\text{m}$ ]	209
Table D.12. Threshold of motion results for quartz sediment [ $\rho_s=2650\text{kgm}^{-3}$ , $D=462.5\mu\text{m}$ ]	210
Table D.13. Threshold of motion results for quartz sediment [ $\rho_s=2650\text{kgm}^{-3}$ , $D=550\mu\text{m}$ ]	211

## Notation and Symbols

$\beta$	Stokes parameter = $1/\delta = \sqrt{\omega/2\nu}$ .
$\delta$	Stokes length (m) = $\sqrt{2\nu/\omega}$ .
$\delta_{0.99}$	Boundary layer thickness (m) = $4.6052/\beta$
$\lambda$	Wavelength (m).
$\mu$	Molecular viscosity ( $\text{m}^2\text{s}^{-1}$ ).
$\nu$	Kinematic viscosity ( $\text{m}^2\text{s}^{-1}$ ) = $\mu/\rho$ .
$\theta$	Shields parameter = $\tau_{\text{crit}}/((\rho_s-\rho)gD)$ .
$\rho$	Density ( $\text{kgm}^{-3}$ ).
$\tau$	Bed shear stress ( $\text{Nm}^{-2}$ )
$\omega$	Radian frequency = $2\pi/T$ .
$\varphi$	Phase lag ( <i>deg</i> or <i>rad</i> ).
$\Delta t$	time interval or bandwidth (s).
$\Delta\omega t$	Phase interval or bandwidth ( <i>rad</i> ).
$a$	Amplitude of near-bed wave orbital motion (m).
$a$	Wave surface elevation amplitude (m).
$d$	Water depth (m).
$D$	Grain diameter (m).
$g$	Acceleration due to gravity = $9.81\text{ms}^{-2}$ .
$H$	Wave height (m).
$L$	Wave length (m).
$R$	Asymmetry parameter = $U_c/(U_c + U_t)$ .
$S$	Orbital excursion (m).
$t$	Time (s).
$T$	Wave period (s).
$U_\infty$	Orbital velocity amplitude ( $\text{ms}^{-1}$ ).
$U_{1+2}$	First and second harmonic amplitudes of asymmetric velocity, respectively ( $\text{ms}^{-1}$ ).
$U_{c+t}$	Velocity amplitude under the crest and trough of a wave, respectively ( $\text{ms}^{-1}$ ).
$u$	Component of velocity in the x direction ( $\text{ms}^{-1}$ ).

---

$u_*$	Friction velocity ( $\text{ms}^{-1}$ ) = $\sqrt{\tau/\rho}$
$v$	Component of velocity in the y direction ( $\text{ms}^{-1}$ ).
$w$	Component of velocity in the z direction ( $\text{ms}^{-1}$ ).
$x$	Along flume coordinate, positive in direction of unidirectional flow.
$y$	Cross flume coordinate, positive $90^\circ$ from unidirectional flow.
$z$	Vertical coordinate, positive upwards.

*Subscripts*

c	peak value associated with the wave crest
t	peak value associated with the wave trough
s	sediment
w	wave
crit	critical value
max	maximum value
z	At given height, $z$ .
t	At given time, $t$ .
0	At the bed ( $z=0$ )
$\infty$	At the edge of the boundary layer ( $z = \delta_{0.99}$ ); or ( $z \geq \delta_{0.99}$ ) when describing flows over the oscillating trolley with axes fixed in the moving plate.

*Dimensionless Numbers*

$$\text{Re}_c = U_c a / \nu$$

$$\text{Re}_t = U_t a / \nu$$

$$\text{Re}_{\text{crit}} = U_{\text{crit}} a_{\text{crit}} / \nu$$

$$\text{RE}_c = U_c \sqrt{2\nu/\omega} / \nu$$

$$\text{RE}_t = U_t \sqrt{2\nu/\omega} / \nu$$

$$\text{RE}_{\text{crit}} = U_{\text{crit}} \sqrt{2\nu/\omega} / \nu$$

$$\text{Re}_* = \frac{u_* D}{\nu}$$

$$D_* = \left( \frac{\rho_s - \rho}{\rho} \frac{g}{\nu^2} \right)^{1/3} D$$

# Chapter 1. Introduction

## 1.1. Background

Understanding the hydrodynamic behaviour of oscillatory flows at the seabed is of great importance to oceanographers, sedimentologists and coastal engineers within the context of fluid- and sediment-dynamics processes. Such information may be used to model and investigate a wide range of processes, including: sediment mobility; seabed or coastal geomorphological changes; and flow interaction with structures and the seabed. In the context of these sediment-dynamics processes, the threshold of motion alone may not be important, but it is a common factor that may be used as a reference for subsequent calculations.

On the basis of investigations undertaken by Komar and Miller (1973, 1974), a grain size of 500 $\mu\text{m}$  for quartz sand was suggested as the critical break point between sediment erosion under laminar or turbulent flows. This grain size relates directly with the Shields diagram minima where it was assumed to correlate with significant shedding of eddies from individual roughness elements, causing turbulence. In general, sediments are more readily eroded by the presence of turbulence; however, the full transition to turbulence is a gradual process, over a range of flow conditions (Jensen *et al.*, 1989; Lodahl *et al.*, 1998). For quartz sands, this range of flows corresponds to the threshold of motion for grains  $\sim 100\text{-}2000\mu\text{m}$  in diameter. Therefore, the prediction of the transition to turbulence, together with an understanding of the intermediate stages of turbulence development, are of fundamental importance for the accurate prediction of the initiation of motion of these sediments.

The hydrodynamic stability of the boundary layer and, in particular, the transition to turbulence under sinusoidal oscillatory flows, has been investigated previously in both laboratory and numerical studies. These data, together with the numerical techniques used previously are reviewed elsewhere (e.g. Hino *et al.*, 1976; Jensen *et al.*, 1989; Sleath, 1984, 1990; Tanaka and Sana, 1994; Lodahl *et al.*, 1998; and Tanaka *et al.*, 2000). The term 'transition' in relation to turbulence is considered generally as the beginning of 'transitional' flow or initial deviation from laminar flow. Previous laboratory investigations into boundary layer stability (transition to turbulence and turbulence structure) have typically utilised oscillating water tunnels or types of pipe flow equipment. Such equipment has been used to simulate sinusoidal (e.g. Sleath 1987; Jensen *et al.* 1989) and asymmetric oscillatory flows (e.g. Tanaka *et al.*, 1998; Tanaka *et al.*, 2000). In these investigations, air and water have been used successfully as the fluid medium. Likewise, other researchers have observed the

---

transition to turbulence under sinusoidal flow conditions in wave flumes (Vincent, 1957; Lhermitte, 1958) and over oscillating trolleys (Li, 1954; Manohar, 1955). In such studies, it was noted that oscillating trolleys do not reproduce the horizontal pressure gradients associated with free surface gravity waves or oscillating water tunnels. The vector of this pressure gradient is periodic and is considered to interact with and enhance to some extent, the stabilising/destabilising effects of fluid acceleration and vertical gradients in horizontal velocity.

The transition to turbulence over smooth beds has traditionally been defined as occurring at a particular Reynolds number; in these, the velocity is represented by the peak positive orbital value and the length scale is either that of the orbital amplitude or a measure of the boundary layer thickness. However, as first described by Hino *et al.* (1976), the full transition from laminar to fully turbulent flow over smooth beds occurs over a range of Reynolds numbers. More recently, similar observations relating to pipe flow and oscillating tunnel experiments have been discussed quantitatively by Jensen *et al.* (1989) and Lodahl *et al.* (1998). These results have shown that the early stages of turbulence are evident as small amplitude fluctuations in velocity about the laminar signal. This condition is followed by the sudden development of turbulent ‘spikes’ in the observed velocity or shear stress, limited initially to periods of flow deceleration. Described as ‘conditional turbulence’ by Hino *et al.*, this early transition is characterised by re-laminarisation of the signal during flow acceleration. Lodahl *et al.* suggest that the adverse pressure gradient during the deceleration phase combined with small near-wall velocities provides a favourable environment for the initiation of turbulence. Lodahl *et al.* suggest also that turbulence during these phases may be caused by shear instability of the velocity profile in the region of flow inflection. As the Reynolds number is increased, turbulence spreads progressively throughout the oscillatory cycle. Limited data have been presented for transition over a smooth bed under asymmetric (cnoidal) oscillatory flows (Tanaka *et al.*, 2000); here, the critical Reynolds number was expressed as a non-linear function of the degree of asymmetry.

Over a hydrodynamically rough bed, limits have been proposed to describe the initial transition (Manohar, 1955) and the limit for fully developed turbulence (Kajiura, 1968). These limits expressed the critical Reynolds number as  $[c \times (a/D)]$  where  $c$  is a scalar coefficient (104 and 1000 for initial and fully developed turbulence, respectively),  $a$  is the orbital amplitude and  $D$  is the grain size. The relationship of Manohar was an empirical fit to a large dataset, collected using an oscillating trolley; this included a similar data set collected using the same equipment as Li (1954). The relationship represented the earliest transition to

---

turbulence observed in the data, on the chosen axes for graphical representation. However, for the majority of the data, the transition was significantly under-estimated by the relationship proposed. Similar relationships have been proposed by Jonsson (1966) and Kamphuis (1975), both of whom predicted earlier transition values than those of Manohar.

The threshold of motion for non-cohesive, uniform, sand-sized particles resting on a flat (featureless) and horizontal bed is an important reference or baseline quantity for sediment dynamic processes that occur in conditions exceeding threshold (i.e. various aspects of sediment transport). A wide range of relationships have been proposed that relate the rate of such transport to the amount of shear stress in excess of that required for threshold. This approach has been applied to transport under sinusoidal (e.g. Madsen and Grant, 1976; Sleath, 1978, 1982; Vincent *et al.*, 1981; Soulsby, 1997; Li and Davies, 1996, 2001; Nielsen and Callaghan, 2003) and asymmetric flows (e.g. Sato and Horikawa, 1986; Tanaka, 1988; Davies and Li, 1997; Li and Davies, 2001; and Nielsen and Callaghan, 2003). In all cases, the resultant transport was compared typically to the peak velocity value, irrespective of the degree of asymmetry. Parameters representing the threshold of motion (e.g. that of Shields, 1936) are used also to scale sediment in mobile bed scaled models (Hughes, 1993). The effect of flow asymmetry on bedload transport and ripple initiation has been investigated using a wave channel by Kaczmarek and Ostrowski (1996) and Sekiguchi and Sunamura (2004), respectively.

Threshold studies have been undertaken using a variety of approaches, including: analysis of observations from the laboratory, or from the field; or numerical modelling, on the basis of individual grains, or by stochastic representation of the bed as a whole. The majority of large laboratory data sets concerning oscillatory flow alone were collected using oscillating trolley apparatus (Bagnold, 1946; Manohar, 1955; Sleath, 1978; Hammond and Collins, 1979; Rigler and Collins, 1984; Tomlinson, 1993; and Voulgaris *et al.* 1995), combined flow experiments were similarly undertaken by Lee Young and Sleath (1988) and Wallbridge *et al.* (1999). A great many empirical and semi-empirical relationships have been developed to express the threshold of motion under unidirectional, oscillatory or combined flows; these yield, typically, a critical value of near-bed velocity or bed shear stress. In most cases, for any type of flow, it is assumed that a single critical value of peak shear stress is sufficient to describe threshold of a given sediment; this value is assumed not to vary with wave period, or other wave parameters, e.g. shallow water depth causing flow asymmetry.

The well-known relationship of Shields (1936), for threshold under unidirectional flows, has been applied directly to the oscillatory flow case (e.g. Sleath, 1984; Soulsby, 1997). The

---

Shields curve provides a reasonable estimate of data observed at longer wave periods (which are similar to the unidirectional case), but otherwise tends to underestimate the critical shear stress. For similar reasons, the majority of critical velocity approaches do not represent well the trend of the data, in relation to wave period; further, the full range of such relationships predict widely differing solutions depending on the sediment in question. Wave period dependencies have largely been ignored, however, it was noted by Voulgaris *et al.* (1995) that a greater shear stress was apparently needed to cause the threshold of motion under shorter wave periods.

The use of oscillating trolleys for the simulation of wave-induced flows at the seabed is well established within the field of fluid dynamics. The principle of the apparatus is that when a plate is oscillated within a still fluid medium, the dynamic response of the fluid (in terms of boundary layer development and flow stability relative to axes fixed in the moving plate) will be the same as for the reciprocal case. Simple oscillations of the plate are characterised by an oscillatory period and a stroke length (equivalent to the orbital excursion of fluid at the bed). Mobile sediment resting upon such an apparatus will experience an additional inertial force, due to acceleration; however, it has been argued that this does not affect the results obtained if the magnitude of the inertial force remains small in comparison to the fluid shear force (Davies and Wilkinson, 1977; Hammond and Collins, 1979). Inertial force considerations are not necessary in fluid experiments over fixed beds, as with the velocity profiling or transition to turbulence experiments undertaken during the present study.

Several experimental studies have utilised an oscillating trolley to investigate: the threshold of motion for sand (Bagnold, 1946; Manohar, 1955; Hammond and Collins, 1979; Rigler and Collins, 1984; Voulgaris *et al.*, 1995; Pangiopotoulos *et al.*, 1997; and Paphitis *et al.* 2001); the velocity distribution above the bed (Kalkanis, 1964; Du Toit and Sleath, 1981); lift/drag forces at the bed (Bagnold, 1946; Rosenthal and Sleath, 1986); the transition to turbulence (Li, 1954; Manohar, 1955); and turbulence structure (Sleath, 1987). In these investigations, various experimental trolley designs, methodologies and fluids have been used, to great effect. Such arrangements have allowed process studies to be undertaken, over a variety of time and length scales not possible in traditional wave tanks. Due to equipment design, studies have often represented oscillatory flows as sinusoidal variations in fluid displacement or velocity (*sinusoidal flow*). Consequently, flows exhibiting non-linear shallow-water effects, including wave and flow asymmetry (*asymmetric flow*) have not yet been considered in studies utilising oscillating trolleys. Oscillating tunnels have also been used in a small number of studies for the investigation of sediment transport, velocity structure, boundary layer stability and turbulence under asymmetric flows (e.g. Ribberink and Al-Salem, 1995;

---

Tanaka *et al.*, 1998a,b,c; and Tanaka *et al.*, 2000). Such studies have indicated the potential importance of flow asymmetry in sediment dynamics.

## **1.2. Objectives of the thesis**

The research described in this thesis is structured in order to investigate the potential mechanisms by which wave period and flow asymmetry are important in regulating both the transition to turbulence over (flat) smooth or granular beds and the threshold of motion for sediment (on similarly flat beds).

Relationships reported previously, describing the transition to turbulence over rough beds are not fully representative of large grain sizes; likewise, for both smooth and rough beds, they do not account for variations associated with wave period or flow asymmetry. This investigation presents new data describing the transition to turbulence, under sinusoidal and asymmetric oscillatory flows, over flat featureless beds of immobile uniform sediments (ranging from fine to coarse sands). These data were collected using an oscillating trolley system in a fluid medium (fresh water), using a variety of visual and numerical interpretative methods. New empirical relationships for sinusoidal and asymmetric flows are derived from these data in conjunction with the large (sinusoidal) data sets of Li (1954) and Manohar (1955). These latter data sets provide observations made using similar equipment and methodology, over relatively large ranges of grain size and wave period. By using laboratory observations, no numerical assumptions are necessary regarding the mechanisms by which turbulence is initiated, under such a variety of conditions. Accepting the relatively small degree of scatter caused potentially by experimental noise and differences in methodology, the absolute and relative effect of the flow and bed parameters are studied. The relationships between several aspects of the boundary layer, considered to be important in regulating the transition to turbulence, are then discussed.

Likewise, a detailed study is undertaken in order to investigate the effect of wave period and flow asymmetry, on the threshold of motion for sand sized sediments. Observations of threshold, undertaken as part of the present study, are presented covering a wide range of sediments and flow types, specifically incorporating a range of wave periods and flow asymmetry (not previously reported elsewhere). In addition, the data sets of Bagnold (1946), Manohar (1955), Hammond and Collins (1979) and Tomlinson (1993) are utilised, in order to provide a greater number and range of observations; likewise, new observations are made over a wide range of sediment types and wave periods, using oscillating trolleys to simulate sinusoidal flows. Patterns in the data are identified initially in terms of basic flow parameters

---

and subsequently in terms of the critical bed shear stress (used typically to represent the flow in such investigations). Mechanisms are then proposed in order to explain the observed patterns; they are also applied to relationships used previously to describe the threshold of motion.

### **1.3. Structure of the thesis**

In Chapter 2, a review of work previously undertaken and the present state of knowledge regarding transition to turbulence and the threshold of motion for non-cohesive sand-sized sediment under oscillatory flows is presented. Selected details of various wave theories and associated laminar boundary layer models are also presented; the practical use of such models in the context of the present study is addressed in more detail in Chapter 4.

Firstly, the instruments and equipment used in the context of the present study are described in detail in Chapter 3, for the benefit of the reader and/or of future investigators planning to replicate or continue any aspect of the present study. Secondly, the experimental methodology applied during these investigations are presented in Chapter 4. Utilising the boundary layer models discussed in Chapter 2, important secondary parameters (e.g. velocity gradients, bed shear stress, fluid acceleration, etc.) are identified and quantified, in order to provide a basis for analysis and comparison between hydrodynamic conditions.

The results of the detailed boundary layer velocity profiling experiments are described in Chapter 5. These data are used to confirm the proper simulation, by the equipment, of the intended flow and also the validity of the laminar boundary layer model, used latterly, to describe such flows. A comparison study is undertaken between the laminar sinusoidal and asymmetric boundary layers, including both second-order Stokes and cnoidal theories.

Chapters 6 and 7 are concerned with investigation of the transition to turbulence and of the threshold of motion for sand, respectively, under oscillatory flows; specifically, these investigations address previously unrecognised dependencies on wave period and flow asymmetry. Latterly, the threshold of motion investigations draws on the relationships and processes presented and discussed previously, regarding the transition to turbulence. Both Chapters utilise the flow model discussed in Chapter 5. Chapter 6 is based upon a paper (written by the author of this thesis, in collaboration with M.B. Collins and D. Paphitis – see Appendix E) accepted by the *Journal of Geophysical Research* (May, 2004); however, Chapter 6 provides significantly more detail and discussion of the data than the paper alone.

Finally, the principle conclusions of the present study are summarised then in Chapter 8, together with recommendations for future research.

Appendix A provides a more detailed description of the laminar boundary layer model used in the present study. Appendix B is a tabulated summary of the velocity profiling experiments undertaken and presented in Chapter 5; other important information regarding the observed flow conditions and resolution of the measuring profiles are also included.

Appendices C and D are tabulated summaries of the observations made in the present study, concerning the transition to turbulence (Chapter 6) and the threshold of motion (Chapter 7), respectively. Appendix E is an unformatted copy of the text and figures from a paper accepted by the *Journal of Geophysical Research* (May 2004), concerning the transition to turbulence results and discussion, presented in Chapter 6.

## Chapter 2. Literature Review

### 2.1. Introduction

The background to the simulated hydro- and sediment-dynamics is presented in three parts: firstly, in terms of the fluid environment, describing the flow of water (velocity distribution) in the overlying water column, but most importantly, immediately adjacent to the seabed in the form of the oscillatory boundary layer; also, secondly, the onset of turbulence in the boundary layer; thirdly, in terms of fluid-sediment interaction, specifically, the initial stages of sediment motion under oscillatory flow.

The fluid environment outside the boundary layer is described using wave theory. From the wide range of wave theories available, three such theories are highlighted, namely: (i) linear or ‘Airy’ theory; (ii) second-order Stokes theory; and to a lesser extent (iii) cnoidal theory. The equations describing flow within the boundary layer under such waves are presented for laminar conditions. The validity of this simple (laminar) case is delimited by relationships for the transition to turbulence.

Such wave and boundary layer models may be used to derive useful quantities, such as the velocity amplitude and fluid shear stress, resulting from given wave conditions. A range of previously proposed relationships are presented that estimate the transition to turbulence and the threshold of motion for sediment under oscillatory flow, utilising such parameters.

It is seen that the majority of such investigations, especially those simulating oscillatory flow in the laboratory, consider only a harmonic or sinusoidal variation in fluid velocity. As such, the various empirically derived predictive relationships, and the assumptions upon which they are based, have not yet been comprehensively tested under non-linear (asymmetric) oscillatory flow conditions.

## *Waves and Oscillatory Flows*

### 2.2. General wave theory

#### *2.2.1. Basic definitions and nomenclature*

In the context of the present study, the term ‘wave’ is used to refer to free surface, progressive, gravity waves propagating at the air-fluid interface. In particular, this study

---

refers to such waves on open bodies of water such as the ocean or lakes, but equally includes such wave features induced under controlled laboratory conditions.

Important basic variables in the description of a wave are: the wave period,  $T$ , the wave height,  $H$ , or wave amplitude,  $a$  ( $=H/2$ ), and the wavelength,  $\lambda$ . The wave propagates in water of depth,  $d$ . These parameters are illustrated using an idealised wave in Figure 2.1. The positive  $x$  direction is identified typically as the direction of wave propagation;  $y$  is the corresponding normal component in the horizontal plane. In wave theory construction, the vertical component,  $z$ , is measured typically from the mean water surface as a negative value; it should be noted that sections of the present study concerned with sediment- and fluid-dynamics processes at the seabed use  $z$  measured instead from the sediment/water interface.

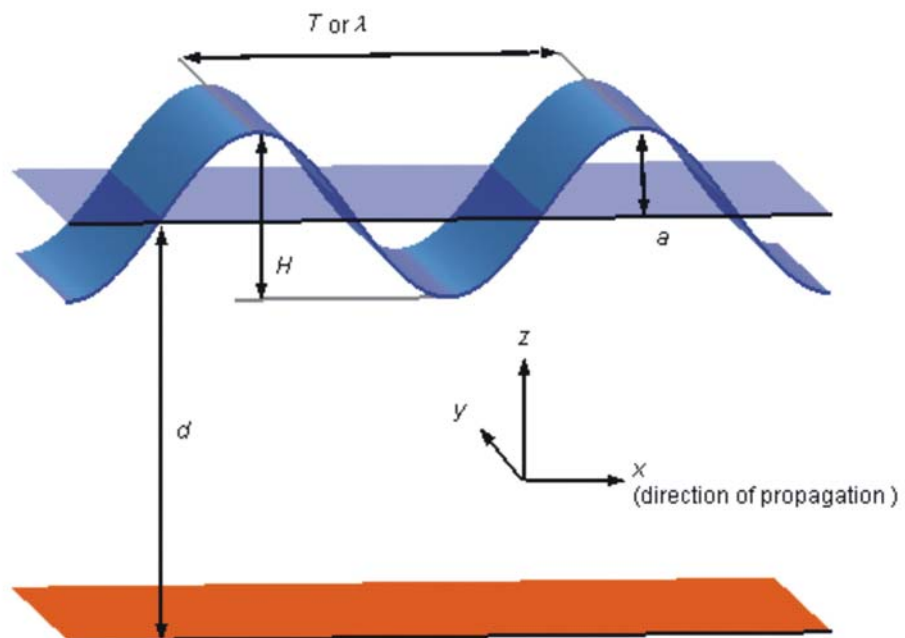


Figure 2.1. Schematic illustration of the basic wave parameters.

Waves induce motion beneath the fluid surface; the spatial and temporal displacement of the fluid is a function of the surface displacement and the depth of observation (see Section 2.3.2). Such periodic flows, specifically when observed at the seabed, are referred to herein as ‘oscillatory flows’, howsoever created, e.g. by wave action, or, by mechanical means in a controlled environment.

### 2.2.2. *The spectrum of wave theories*

A broad range of wave theories has been developed to describe numerically the motion of water associated with gravity waves. These theories cover the wide spectrum of hydrodynamic conditions found in nature. Following Sleath (1984), wave theories may be grouped as follows:

- (i) Small-amplitude theory. First approximations are commonly called ‘linear’ or ‘Airy’ waves, higher approximations are referred to as ‘Stokes’ waves.
- (ii) Shallow-water theory, including ‘cnoidal’ waves and ‘solitary’ waves.
- (iii) Rotational wave theory, referred to as ‘trochoidal’ theory.
- (iv) Numerical solutions, referred to as the ‘Cokelet’ exact solution or the less computationally intensive but nonexact ‘stream function’ and ‘vocaloid’ theories.

Reviews of practical wave theory in relation to sediment dynamics are presented elsewhere (e.g. Sleath, 1984; Soulsby, 1997; and Dean and Dalrymple, 2002). Further detailed information on the mathematical construction of selected theories may be found in Le Mehaute (1976), Dean and Dalrymple (1990), or Tucker (1991). Aspects of the Airy and second-order Stokes approximations (small-amplitude theory) were chosen for use in the present study.

### 2.2.3. *Validity of wave theories*

As summarised by Sleath (1984), the spectrum of wave theories provides approximations of varied complexity and therefore, of varied accuracy. The accuracy of the model is primarily dependant on the particular combination of hydrodynamic parameters being simulated. Although exact numerical solutions for velocity and pressure distributions are available, such solutions may be mathematically complex, making them impractical and/or computationally expensive. Hence, for use in numerical studies, an appropriate wave theory is chosen according to: the hydrodynamic environment being simulated (for mathematical validity); the degree of accuracy required; and the acceptable degree of computational complexity.

After Dean (1970) and Le Mehaute (1976), Sleath (1984) presented a graphical summary, outlining the numerical validity for various wave theories (Figure 2.2). In addition, these and other wave theories are described in more detail by Kirkgoz (1986), Barltrop (1990), Tucker (1991), Soulsby *et al.* (1993) and Soulsby (1997).

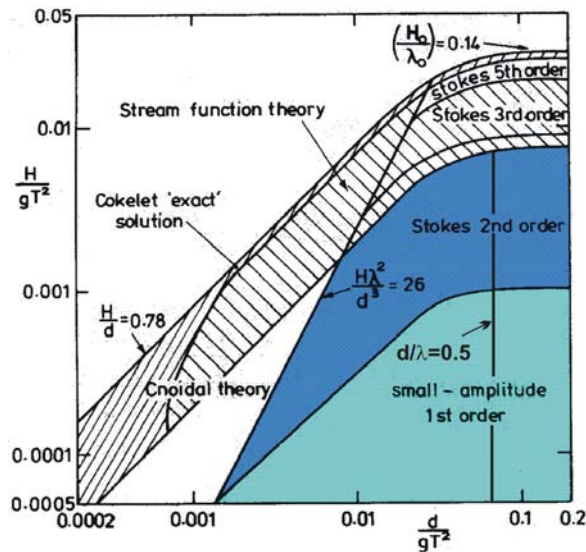


Figure 2.2. Validity limits for various wave theories, in terms of wave height ( $H$ ), period ( $T$ ), wavelength ( $\lambda$ ) and water depth ( $d$ ), (from Sleath, 1984). Note: the coloured areas highlight the conditions represented in the present study.

In studies relating to sediment-dynamics, the most relevant region of the validity diagram shown in Figure 2.2, is located to the left of the ‘transitional wave’ to ‘deep-water wave’ limit ( $d/\lambda=0.5$ ), i.e. in water sufficiently shallow for oscillatory flow to be ‘felt’ at the seabed, and consequently, to interact with any potentially mobile particles that may be present.

Table 2.1 gives examples of the range of conditions (combinations of  $d$ ,  $T$  and  $H$ ), best represented by linear or by second-order Stokes theory. These values were calculated directly from Figure 2.2, for the marginal deep water/transitional condition  $d/gT^2=0.0795$  ( $d/\lambda=0.5$ ) and for a shallow water example at  $d/gT^2=0.0075$ . A linear interpolation may be used to approximate the limiting values of  $H$ , for intermediate values of  $d$ .

From Figure 2.2, waves steeper (of greater  $H$ ) than those given in Table 2.1 for the second-order Stokes solution in deep water, are better described by either: a higher-order Stokes approximation; stream function theory; or, the Cokelet ‘exact’ solution. In water shallower than that given in the shallow water example, cnoidal theory may also become more appropriate, at smaller wave heights.

$T$	Transitional/Deep water limit <sup>1</sup>			Shallower water example <sup>2</sup>		
	$d$ (m)	$H$ Lin (m)	$H$ Stokes (m)	$d$ (m)	$H$ Lin (m)	$H$ Stokes (m)
2	> 3.12	< 0.04	0.04 - 0.27	0.39	< 0.01	0.01 - 0.08
3	> 7.02	< 0.09	0.09 - 0.62	0.88	< 0.03	0.03 - 0.18
4	> 12.48	< 0.16	0.16 - 1.10	1.57	< 0.05	0.05 - 0.31
5	> 19.50	< 0.25	0.25 - 1.72	2.45	< 0.08	0.08 - 0.49
6	> 28.08	< 0.35	0.35 - 2.47	3.53	< 0.11	0.11 - 0.71
7	> 38.21	< 0.48	0.48 - 3.36	4.81	< 0.15	0.15 - 0.96
8	> 49.91	< 0.63	0.63 - 4.39	6.28	< 0.20	0.20 - 1.26
9	> 63.17	< 0.79	0.79 - 5.56	7.95	< 0.25	0.25 - 1.59
10	> 77.99	< 0.98	0.98 - 6.87	9.81	< 0.31	0.31 - 1.96
11	> 94.37	< 1.19	1.19 - 8.31	11.87	< 0.38	0.38 - 2.37
12	> 112.30	< 1.41	1.41 - 9.89	14.13	< 0.45	0.45 - 2.83
13	> 131.80	< 1.66	1.66 - 11.61	16.58	< 0.53	0.53 - 3.32
14	> 152.86	< 1.92	1.92 - 13.46	19.23	< 0.62	0.62 - 3.85
15	> 175.48	< 2.21	2.21 - 15.45	22.07	< 0.71	0.71 - 4.41

Table 2.1. Critical combinations of wave parameters delimiting the validity of linear (Lin) and second-order Stokes (Stokes) theory: (1) for waves in deep water, beginning to ‘feel’ the bed ( $d/gT^2=0.0795$ ); and (2) for shallower water depths ( $d/gT^2=0.0075$ ). Values calculated from Figure 2.2.

## 2.3. Linear and second-order Stokes theory

### 2.3.1. The water surface

Linear theory corresponds to a sinusoidal displacement of the water surface (see Figure 2.3). In close relation, second-order Stokes theory (Stokes, 1851) is constructed as the sum of a primary and secondary harmonic with periods  $T$  and  $T/2$  respectively (Le Mehaute, 1976); of these, the second harmonic is typically of smaller amplitude than the primary. Using a cosine function to represent the harmonics (Eq. 2.4), there is no phase lag between the two components. As illustrated in Figure 2.3, the resulting wave is characterised by a narrower peaked crest and a longer, shallower trough; in more extreme cases, a secondary ‘crest’ or hump may be observed in the wave trough. The degree of wave deformation is described herein as wave ‘asymmetry’; the concept and definition of asymmetry is defined, in terms of the near bed velocity cycle, in Section 2.3.2. At low asymmetry, the amplitude of the second harmonic approaches zero and the second-order Stokes and linear theories converge at this point.

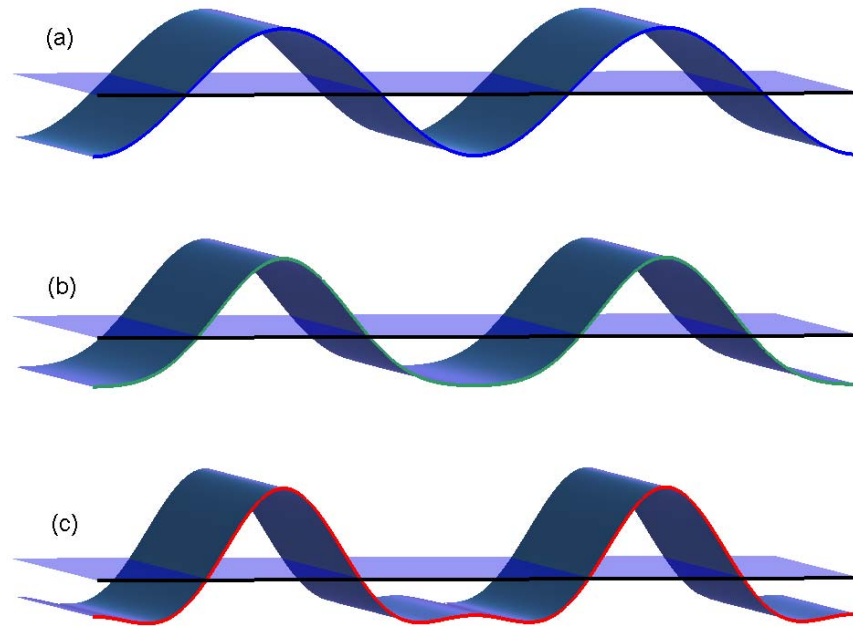


Figure 2.3. Surface displacement about the mean water level, as predicted by second-order Stokes theory, for waves of: (a) low, (b) medium and (c) high wave asymmetry. Subplot (a) corresponds also to the surface displacement predicted by linear (Airy) wave theory.

Details of the mathematical construction of second-order Stokes theory, over uniform or variable bathymetry may be found in Belibassakis and Athanassoulis (2002) and the references contained therein.

### 2.3.2. *The water column and near bed flow*

Beneath linear waves, water moves in closed elliptical orbits. In shallow water, the orbits are initially circular at the surface but become progressively flattened towards the bed, at which point the flow describes a to-and-fro oscillation parallel to the bed surface. Beneath second-order Stokes waves, the elliptic orbits of water motion, as observed under linear waves, are deformed. Orbits become peaked under the crest and flattened under the trough (Le Mehaute, 1976) and are no longer closed, resulting in a mean drift in the direction of wave propagation associated with such waves (in the absence of return currents in the near-shore zone). The contribution to near-bed flow caused by mass transport drift has been excluded in the context of the present study for two reasons: (i) drift is not reproduced naturally over oscillating trolleys (the equipment used for flow simulation) and (ii), the magnitude of the drift velocity

---

is typically small or insignificant compared with the orbital velocity amplitude of flows simulated during studies of transition to turbulence or threshold of motion (Sleath, 1984).

For given combinations of wave parameters, the orbital velocity is often represented as a velocity potential,  $\phi$ . The full equations for  $\phi$  and drift velocity, using Airy and second-order Stokes theories, in deep and intermediate water depths, may be found elsewhere (Belibassakis and Athanassoulis, 2002; Sleath, 1984; Le Mehaute, 1976). Temporal and spatial detail of the three velocity components is achieved by solving:

$$u = -\frac{\partial \phi}{\partial x} \quad v = -\frac{\partial \phi}{\partial y} \quad w = -\frac{\partial \phi}{\partial z} \quad \text{Eq. 2.1}$$

These equations may be used: to calculate the velocity cycle near to the bed (outside of the boundary layer) for observed surface wave parameters and subsequently to apply the results of the present study to such observations; conversely, to convert the results of the present study into representative surface wave parameters.

Throughout the investigations presented herein, velocity parameters were not predetermined as the result of chosen surface wave parameters; instead, near bed flow parameters were selected independently, to form a focused and systematic investigative program. This is a common approach for investigations utilising laboratory equipment, where only the near bed oscillatory flow is simulated.

To a first order of approximation (linear theory), the horizontal component of velocity at the edge of the boundary layer is described by:

$$u = U_{\infty} \cos \omega t \quad \text{Eq. 2.2}$$

where

$$U_{\infty} = \frac{\omega H}{2 \sinh(2\pi d / \lambda)} \quad \text{Eq. 2.3}$$

Where  $\omega = 2\pi/T$  is the radian frequency. In the absence of drift, the horizontal component of velocity at the bed is described to a second order of approximation by:

$$u_{z=\delta_{0.99}} = U_1 \cos \omega t + U_2 \cos 2\omega t \quad \text{Eq. 2.4}$$

where  $U_1$  and  $U_2$  are the velocity amplitude of the primary and second harmonics respectively. Kemp (1975) gives the following solution for the horizontal component of the two harmonics,

$$U_1 = \frac{\pi H}{T} \cdot \frac{\cosh(z+d)/\lambda}{\sinh 2\pi d/\lambda}, \quad U_2 = \frac{3\pi^2 H^2}{4\lambda T} \cdot \frac{\cosh 4\pi(z+d)/\lambda}{\sinh^4 2\pi d/\lambda} \quad \text{Eq. 2.5}$$

Where  $z$  is the depth as measured from the mean water surface. The resulting velocity cycle will have velocity  $U_c$  under the wave crest,  $U_t$  under the wave trough and a degree of asymmetry,  $R$ , where,

$$U_c = U_1 + U_2, \quad U_t = U_1 - U_2 \quad \text{Eq. 2.6}$$

and

$$R = \frac{U_c}{U_c + U_t} \quad \text{Eq. 2.7}$$

Soulsby (1997) provides an alternative construction of this relationship,

$$U_c = U_\infty \left[ 1 + \frac{3kd}{8 \sinh^3(kd)} \frac{H}{d} \right], \quad U_t = U_\infty \left[ 1 - \frac{3kd}{8 \sinh^3(kd)} \frac{H}{d} \right] \quad \text{Eq. 2.8}$$

where  $U_\infty$  is given by Eq. 2.3. Eq. 2.8 will tend to overestimate  $U_c$ ; Soulsby suggests to consider then the method of Isobe and Horikawa (1982)

$$U_c = U_\infty, \quad U_t = U_\infty [1 - r_2 \exp(-r_3 d / L_0)] \quad \text{Eq. 2.9}$$

with  $r_2 = 3.2(H_0/L_0)^{0.65}$  and  $r_3 = -27 \log_{10}(H_0/L_0) - 17$ , where  $H_0$  and  $L_0$  are the deep-water wave height and wavelength. By combining Eq. 2.6 and Eq. 2.7, the harmonic components are related by

$$U_2 = (2RU_1) - U_1 \quad \text{Eq. 2.10}$$

Therefore,  $R$  represents the relative increase in the peak (crest) velocity, in proportion to the peak-trough range; hence a value of  $R=0.5$  implies a sinusoidal flow and in this case  $U_{\infty}=U_c=U_t$ . Examples illustrating selected degrees of asymmetry are given in Figure 2.4.

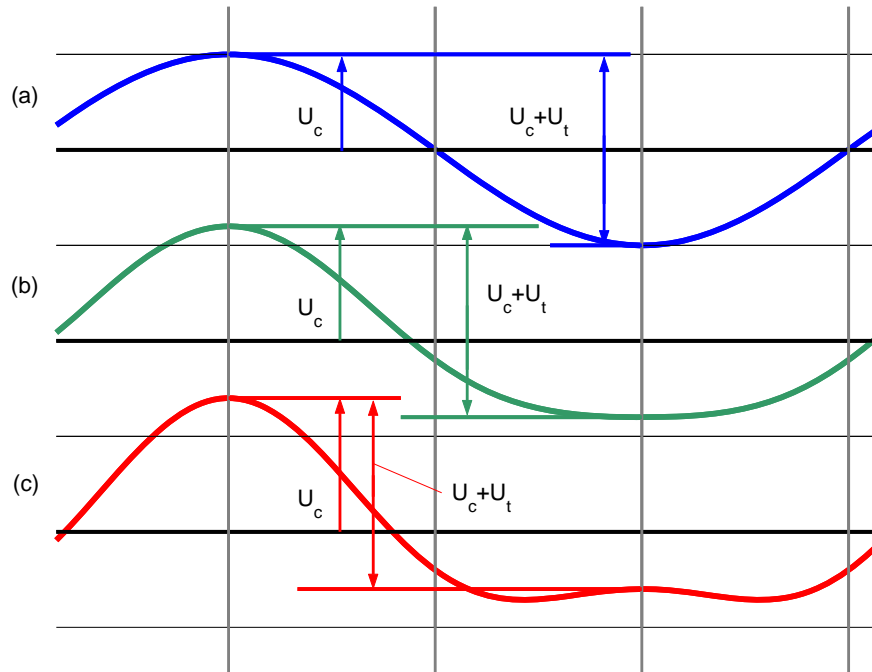


Figure 2.4. Normalised velocity cycles for: (a)  $R=0.5$ ; (b)  $R=0.6$ ; and (c)  $R=0.7$ .

Previously, principle contributors of laboratory data sets (described below) have simulated flows of  $R=0.63$ - $0.67$  using oscillating trolley or water tunnel apparatus in conjunction with second-order Stokes theory. Typically, these investigations related either to turbulence structure (e.g. Sato and Horikawa, 1986) or sediment transport (e.g. Ribberink and Al Salem, 1994) and the upper limit of  $R$  corresponded approximately to the initial development of the secondary hump in the trough half-cycle. Larger values of  $R$  (up to 0.8) have been simulated also, using cnoidal theory (e.g. Tanaka *et al.*, 2000).

Typical values of  $R$  from the field have not yet been reported in investigations relating to sediment dynamics or other similar areas of research; instead, the description of individual waves are often excluded in favour of description of the wave spectrum. However, using second-order Stokes theory, a representative storm wave ( $T=5$ s,  $H=1$ m) will produce significant asymmetry ( $R=0.55$ ) at a water depth of  $d\approx 7$ m, this increases quickly and smoothly to  $R=0.65$  at  $d\approx 5$ m; likewise, a representative swell wave ( $T=10$ s,  $H=3$ m) is similarly affected at  $d\approx 25$ m and  $d\approx 18$ m, respectively.

## *The Laminar Oscillatory Boundary Layer*

### **2.4. Linear theory**

Under laminar flow conditions, the ‘boundary layer’ is the region of flow adjacent to the bed, directly affected by viscous friction with the boundary. In this region, momentum is transmitted by fluid shear between adjacent flow lamina, which remain parallel to the bed surface. The boundary layer is relatively thin, e.g. in fresh water at 20°C, for wave periods of  $T=2\text{s}$  and  $15\text{s}$ , this region is approximately 3.5mm and 10.1mm in thickness, respectively.

The form of the velocity profile in the laminar boundary layer, under free surface gravity waves following linear theory (herein referred to as ‘sinusoidal flow’), is given by:

$$u_{(z,t)} = U_{\infty} (\cos(\omega t + \varphi) - e^{-\beta z} \cos(\omega t + \varphi - \beta z)) \quad \text{Eq. 2.11}$$

Where  $u_{(z,t)}$  is the instantaneous flow at height  $z$  and time  $t$ ;  $U_{\infty}$  is the velocity amplitude;  $\varphi$  is the phase lag; and  $\beta$  is the Stokes parameter,

$$\beta = \frac{1}{\delta} = \sqrt{\frac{\omega}{2\nu}} \quad \text{Eq. 2.12}$$

Where  $\delta$  is the Stokes length (a measure of the boundary layer thickness); and  $\nu$  is the kinematic viscosity. The normalised solution of Eq. 2.11 is shown in Figure 2.5. The development of this model and the intermediate solutions pertaining to the present study are given in more detail in Appendix A.

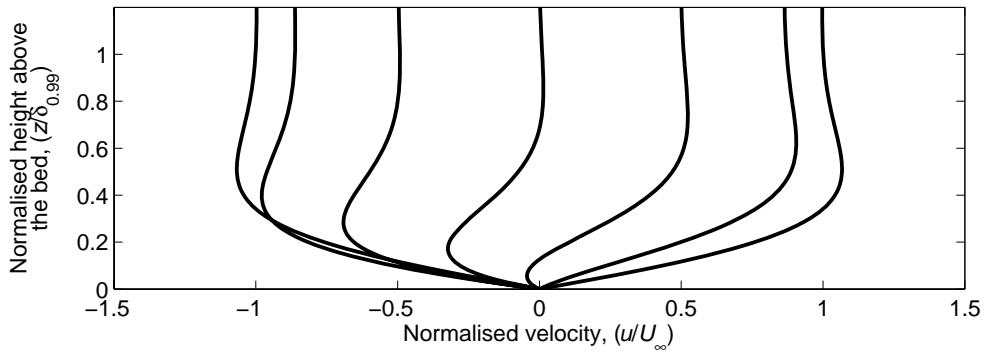


Figure 2.5. Normalised velocity distribution within the laminar boundary layer (Eq. 2.11); linear theory ( $R=0.5$ ).

Additional measures may be taken directly from these formulae. From Eq. 2.11, fluid layers above the bed oscillate with a damped harmonic motion of amplitude  $U_\infty e^{-\beta z}$  and with a phase lead  $-\beta z$  in relation to the motion of the fluid outside of the boundary layer. The height at which  $|U_{(z)}|_{\max} = 0.99U_\infty$  (i.e. the extent of the boundary layer), is given by:

$$\delta_{0.99} = 4.6052 / \beta \quad \text{Eq. 2.13}$$

## 2.5. Second-order theory

The laminar boundary layer solution for near-bed flows determined by higher-order theories has not often been presented in the literature; this is mostly due to the lack of studies incorporating such flows. Indeed, only a small number of examples have been forthcoming: Sleath (1984) and Tanaka, Sumer and Lodahl, (1998) provide generic analytical solutions for irrotational,  $n$ 'th order waves, encompassing potentially all of the Stokes higher-order and cnoidal theories (Eq. 2.18). Mouazé (2001) presented measurements of velocity within the boundary layer, made under free surface gravity waves in a laboratory wave channel, where the data exhibited a significant degree of asymmetry and were more closely described by a second-order Stokes model.

A first approximation to higher-order solutions may be found by the summation of the flow induced by each of the component harmonics; summation in this manner is only possible with laminar flows. The form of the velocity profile in the laminar boundary layer, under free surface gravity waves following second-order Stokes theory (herein referred to as 'asymmetric flow'), is given by:

$$u_{(z,t)} = U_1 \cos(\omega t + \varphi_1) + U_2 \cos(2\omega t + \varphi_2) - \dots \quad \text{Eq. 2.14}$$

$$[U_1 (e^{-\beta_1 z} \cos(\omega t + \varphi_1 - \beta_1 z)) + U_2 (e^{-\beta_2 z} \cos(2\omega t + \varphi_2 - \beta_2 z))]$$

Where:  $\varphi_1$  and  $\varphi_2$  are the phase lags and  $\beta_1$  and  $\beta_2$  are the Stokes parameters for the principle and second harmonics respectively:

$$\beta_1 = \sqrt{\frac{\omega}{2\nu}} \quad \beta_2 = \sqrt{\frac{2\omega}{2\nu}} \quad \text{Eq. 2.15}$$

The full solution for asymmetric flows, as developed for use in the present study, is described in more detail, in Appendix A. The normalised solution of Eq. 2.14 is shown in Figure 2.6. Eq. 2.13 applies also to second-order flows, if  $\beta$  is replaced by  $\beta_1$ .

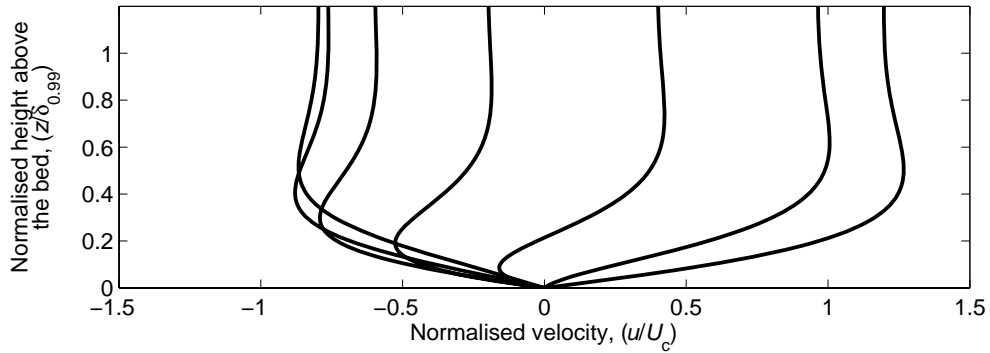


Figure 2.6. Normalised velocity distribution within the laminar boundary layer (Eq. 2.14); second-order Stokes theory ( $R=0.6$ ).

## 2.6. Cnoidal theory

A mechanical method by which to generate cnoidal flows in an oscillating tunnel was developed by Tanaka *et al.* (1998a,b,c). Also described therein is the solution for the outer boundary layer flow under cnoidal waves, where the degree of asymmetry in the wave and hence the near-bed flow is related to the Ursell parameter ( $Ur = HL^2/d^2$ ). For the purposes of the present study, the normalised outer layer velocity may be calculated as:

$$\frac{u_{\infty,t}}{U_c} = \frac{(b_* - 1)(b_* \cos \omega t - 1)}{(b_* \cos \omega t - 1)^2} \quad \text{Eq. 2.16}$$

where the coefficient  $b_*$  relates to a length ratio in the mechanism. By calculating time series of velocity over a range of  $b_*$  and then determining the resulting value of  $R$ , cnoidal flows of given asymmetry could be reproduced using the following empirical relationship, in conjunction with Eq. 2.16,

$$\begin{aligned} b_* = & (172036.06982 * R^6) - (755407.88888 * R^5) + \dots & \text{Eq. 2.17} \\ & (1378145.43453 * R^4) - (1337411.78925 * R^3) + \dots \\ & (728358.11192 * R^2) - (211152.87765 * R) + 25475.07552 \end{aligned}$$

Fourier analysis was used then to find the first 10 harmonics of the outer layer velocity signal (as recommended by Tanaka *et al.* 1998d); this was applied then to the general laminar boundary layer solution:

$$u_{t,z} = u_{\infty,t} - \sum_{n=1}^N U_n e^{-\beta_n z} \cos n\omega t - \beta_n z \quad \text{Eq. 2.18}$$

using (N=10) and where

$$\beta_n = \sqrt{\frac{n\omega}{2\nu}} \quad \text{Eq. 2.19}$$

Eq. 2.13 applies also to cnoidal flows, if  $\beta$  is replaced by  $\beta_{n=1}$ .

## *Transition to Turbulence*

### **2.7. Introduction**

The largest data sets describing the transition to turbulence are sourced from Li (1954) and Manohar (1955). Using the same oscillating trolley apparatus, both investigators presented observations of transition made over flat beds of varying granular roughness and also over simplified rippled beds, represented by half rods of different diameter. Li (1954) also provides a number of observations over a smooth bed. Observations for each bed type were made over a wide range of oscillatory periods, using a sinusoidal trolley motion. Smaller data sets covering only a limited range of wave periods and sediment types were collected in wave channels by Vincent (1957) and Lhermitte (1958). In the studies of Li, Manohar and Lhermitte, transition was observed by the sudden dispersion of dye at the bed by large scale eddies (ignoring molecular diffusion), whereas Vincent reports the first appearance of jets of fluid being ejected from the boundary layer. It has been proposed that the latter condition is

most closely representative of transition because although the scale of the turbulence is not the same as that at larger Reynolds numbers, such jets and eddies modify the velocity profile from the laminar solution (Sleath, 1974a,b, 1982, 1984).

Prior to the mid-1980's, the majority of research in this field had been condensed into empirical relationships, based upon laboratory data from equipment simulating sinusoidal oscillatory flows (i.e.  $R=0.5$ ). Transition was expressed typically in terms of the wave Reynolds number,

$$\text{Re} = \frac{U_0 a}{\nu} \quad \text{Eq. 2.20}$$

where  $a$  is the orbital amplitude of fluid motion ( $S/2$ ), outside the boundary layer, at the seabed. Latterly, the transition to turbulence under oscillatory (and, to a lesser extent, unidirectional) flows has not been addressed commonly in the general (theoretical) hydrodynamics texts (e.g. Hinze, 1975) and it does not seem that any major new laboratory studies have been undertaken to expand on the existing data sets or empirical relationships. This is due in part to the chaotic and stochastic nature of turbulence, making it less suitable for direct mathematical interpretation (typically the preferred method for such research since the early 1980's). A summary of work prior to the 1980's is given by Sleath (1984) and another, more recent, summary of numerical and practical studies, including an extensive reference list, is provided by Godreche *et al.* (1998). The majority of information detailing the results of experimental and numerical approaches may be found in the context of sediment-dynamics studies (e.g. Jonnson 1966, 1980; Sleath, 1984; Jensen *et al.*, 1989; Lodahl *et al.*, 1998)

Related investigations have been undertaken relatively recently by Francisco and Santos (2001) to simulate numerically the transition to turbulence observed in the original experiments by Reynolds (1883) for unidirectional flow. Numerical experiments have been undertaken by Cosgrove *et al.* (2003) and Juárez and Ramos (2003) to simulate the transition to turbulence in oscillatory pipe flow; Blennerhassett and Bassom (2002) provide a similar investigation for stokes layer flow over a flat oscillating plate. The effect of suspended particulate solids on transition in unidirectional pipe flow has been investigated also in the laboratory (Matas *et al.*, 2003).

---

## 2.8. Hydrodynamically smooth beds

In the context of laminar oscillatory flow over a flat bed, a hydraulically smooth bed has been defined as the condition where the Nikuradse roughness length,  $k_s$ , is small in comparison to the boundary layer thickness ( $k_s \ll \delta$ ), (Tomlinson, 1993) where,  $k_s = 2.5D_{50}$  (Soulsby, 1997). Jonsson (1966) proposed a more definitive value of ( $k_s/\delta < 0.25$ ).

### 2.8.1. Sinusoidal flow

A number of proposed critical values of the Reynolds number,  $Re_{crit}$ , based upon a variety of experimental and observational methodologies are summarised by Sleath (1984). Here, the orbital amplitude is utilised as the length scale. Although significant scatter was reported, over half of the proposed critical values were in the range  $Re_{crit} = 1.3\text{--}1.6 \times 10^5$ . Furthermore, Sleath suggests that there is no reason to discount the value of  $Re_{crit}$  suggested originally by Li (1954),

$$Re_{crit} = \frac{U_{\infty} a}{\nu} = 1.6 \times 10^5 \quad \text{Eq. 2.21}$$

as this value is in good general agreement with the majority of the data reported and also with the value of  $Re_{crit} = 1 \times 10^5$  suggested by Jonsson (1980) for design purposes.

First described by Hino *et al.* (1976) - Jensen *et al.* (1989) and Lodahl *et al.* (1998) have presented observations of the measured friction factor, at selected phases of the wave cycle, for values of  $Re$  spanning the laminar-transitional region (Figure 2.7). Here, the phase  $\omega t$  refers to a sinusoidal variation in velocity (i.e.  $u_{80.99} = U_{\infty} \times \sin \omega t$ ) and the wave friction factor has been normalised to that predicted by the laminar solution, allowing application to all wave periods. The Figure shows that as  $Re$  is increased, turbulence occurs initially during the phase of fluid deceleration, reverting to laminar flow during the reversal and subsequent acceleration of the flow. Following this, the initiation of turbulence occurs progressively earlier in the cycle and the phase duration of turbulence increases, until eventually, fully developed turbulence is observed.

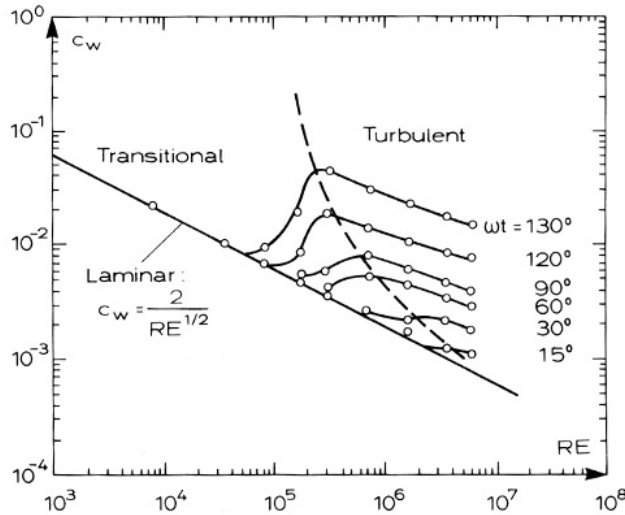


Figure 2.7. Normalised friction coefficient verses Re (shown as ‘RE’ in this particular diagram) at different phase values over a smooth bed (from Jensen *et al.*, 1989).

Figure 2.7 suggests that the early stages of transition occur as early as  $Re = 6 \times 10^4$ ; turbulence is observed throughout the entire wave cycle (fully developed turbulence) at approximately  $Re = 6-7 \times 10^6$ . In comparison, the value of Li (1954) (Eq. 2.21) corresponds to a (transitional) turbulent phase duration of approximately  $40^\circ$  (between  $\omega t = 90^\circ - 130^\circ$ ).

The principles of the progression of transition, presented by Jensen *et al.* (1989), are important in the context of the present study. Here, although laminar flow conditions are assumed to dominate when calculating boundary layer flow for transitional conditions, if the phase of an observed event is known, then the potential presence of (transitional) turbulence at the phase of interest may be more accurately estimated.

The observations described above have been reproduced successfully, using a variety of numerical models, (e.g. Vittori and Verzicco, 1998; Blennerhassett and Bassom, 2002; Cosgrove *et al.*, 2003; Juarez and Ramos, 2003). All of these investigations reported generally the same transitional patterns described in Figure 2.7. The studies suggested that transition occurred at  $RE \approx 500$ ,  $500 < RE < 550$  and  $RE \approx 550$ , respectively, where RE is the boundary Reynolds number, utilising the Stokes length (a measure of boundary layer thickness),

$$RE = \frac{U_c \delta}{\nu} = \frac{U_c \sqrt{2\nu/\omega}}{\nu} \quad \text{Eq. 2.22}$$

For sinusoidal flows ( $R=0.5$ ), RE and Re are related by  $RE = \sqrt{2Re}$ ; therefore, the range  $RE=500-550$  corresponds to  $Re=1.25-1.51 \times 10^5$ . The typically smaller critical value is likely

to be due to differences in the criteria used to define the transition to turbulence, between such numerical and other physical experiments. In addition, Waywell and Sajjadi (1997) compare directly the results from three numerical models with the observed data of Jensen *et al.* (1989); in this report, the observed patterns were successfully reproduced with varying degrees of accuracy.

### 2.8.2. Asymmetric flow

Investigations concerning the transition to turbulence under asymmetric flows are very rarely found in the literature. In the only such study found, by Tanaka *et al.* (2000), the results of numerical and laboratory experiments simulating flow under cnoidal waves are presented. Transition was determined as the point at which the friction factor, as determined by a  $k-\epsilon$  boundary layer model, ‘first deviated from the laminar flow solution’. Flows representing a broad range of RE and  $R$  were simulated and individually identified as being in the laminar or transitional/turbulent regimes. A relationship representing the boundary between the two conditions was drawn (see Figure 2.8). These data were compared subsequently, with a limited number of observations made in an oscillating tunnel apparatus simulating cnoidal oscillatory flows (in order of the key: Nadaoka *et al.*, 1994; Nadaoka *et al.*, 1996; Tanaka *et al.*, 1998a; and Tanaka *et al.*, 1998b); each observation was individually classified as ‘laminar’ or ‘turbulent’ but was not directly indicative of the point of transition.

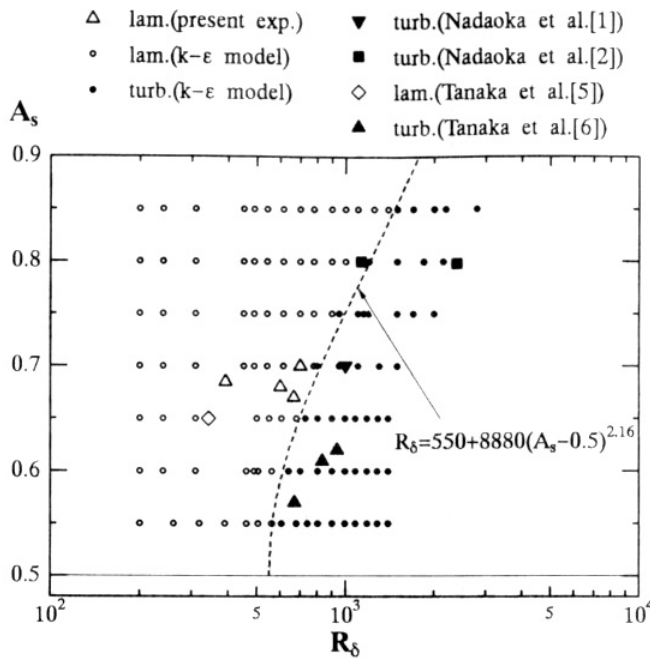


Figure 2.8. Boundary layer stability, over a smooth bed, under cnoidal flows. From Tanaka *et al.* (2000). Key:  $R_\delta=RE$  and  $A_s=R$ .

No laboratory data sets showing the experimentally determined transition to turbulence under asymmetric flows over smooth beds have been found in the course of the present study.

## 2.9. Hydrodynamically rough beds

### 2.9.1. Sinusoidal flow

The transition to turbulence over flat, rough (granular) beds occurs when the orbital amplitude and/or the bed roughness are sufficiently large (Jensen *et al.*, 1989). In addition to the general texts highlighted in Sections 1.1, 2.7 and 2.8, a number of authors have compiled summaries of the theoretical, numerical and laboratory studies conducted, using such beds, within the context of sediment dynamics, (e.g. Jensen *et al.*, 1989; Sleath, 1984; Jonnson, 1980, 1966).

Based on the visual observations made using an oscillating trolley apparatus by Li (1954) and Manohar (1955), Manohar proposed that the transition to turbulence for fine sands, occurs at,

$$\text{Re} = 104(a / D) \quad \text{Eq. 2.23}$$

Kalkanis (1964) conducted further investigations using the same equipment and based on the results, suggested that this relationship may be used also for coarse sands and gravels.

Kajiura (1968) found a similar relationship for the onset of turbulence but proposed that turbulence is not fully developed until

$$\text{Re} = 1000(a / D) \quad \text{Eq. 2.24}$$

Based on a large data set of observations of the wave friction factor over smooth and rough beds, collected using an oscillating water tunnel, Kamphuis (1975) suggested that transition occurs at

$$\frac{a}{D} \approx \frac{2.5 \text{Re} \sqrt{\frac{(2/\sqrt{\text{Re}})}{2}}}{15} \quad \text{Eq. 2.25}$$

This limit was derived by extrapolation of data to the point where the solution for the wave friction factor first deviated from the laminar solution. In addition, Kamphuis suggested also that the full transition to rough turbulent flow did not occur until

$$\frac{a}{D} \approx \frac{2.5 \operatorname{Re} \sqrt{\frac{f_w}{2}}}{200} \quad \text{Eq. 2.26}$$

Where  $f_w$  is the wave friction factor which is described in more detail in Section 4.4.3. Also often quoted is the ‘*LR*’ curve of Jonsson (1966) representing the initial deviation from the laminar solution (the start of transition) in the rough turbulent regime

$$\frac{a}{D} = \frac{10\sqrt{2}}{\pi} \sqrt{\operatorname{Re}} \quad \text{Eq. 2.27}$$

Jonsson also gives the ‘*RL*’ curve for fully developed rough turbulent flow,

$$\operatorname{Re} = 500 \frac{a}{2.5D} \frac{1}{\left(\sqrt{\pi/4} \cdot \sqrt{\nu T}\right) / 2.5D} \quad \text{Eq. 2.28}$$

Selected threshold limits and the fully developed turbulence limit of Kajiura (1968) are shown in comparison to the transition to turbulence data used in the present study, in Figure 2.9.

In Figure 2.9, in addition to the observations of Li (1954) and Manohar (1955), the wave channel observations of Lhermitte (1958) and Vincent (1957), are shown also. Lhermitte suggests that the earlier transition observed in these data, was due to differences in the experimental apparatus used. However, Sleath (1984) argues that the near bed flow induced by the two types of apparatus will theoretically be identical and that a more likely explanation would come from differences in the criteria and observational methodology used to define transition.

---

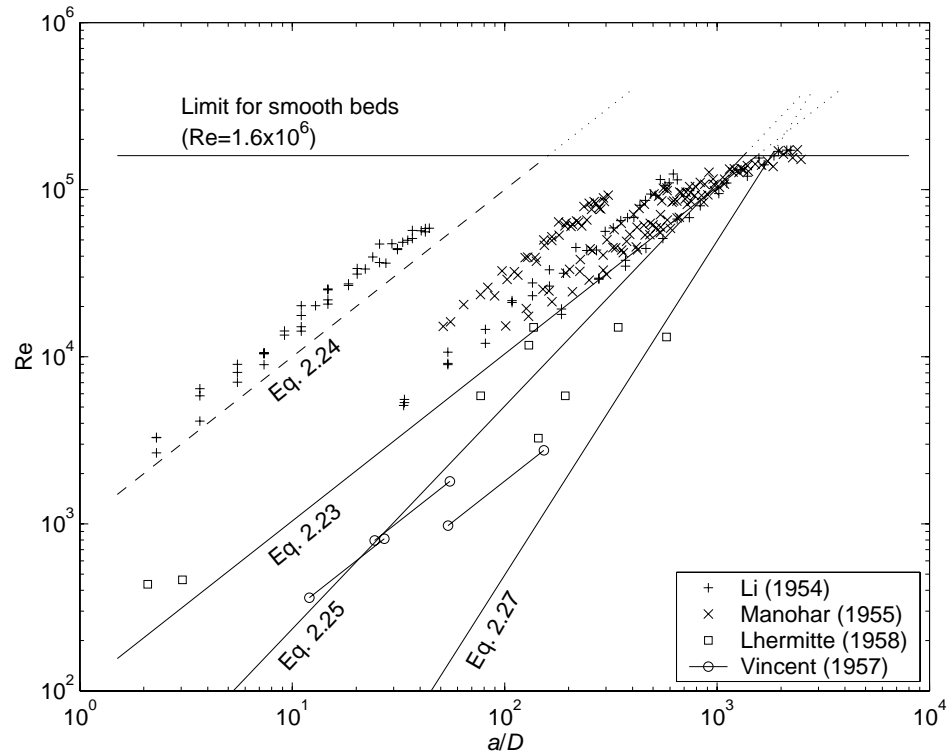


Figure 2.9. Boundary layer stability, over a rough bed.

### 2.9.2. Asymmetric flow

At present, there are no data sets apparently available in the literature that describe the transition to turbulence, under asymmetric oscillatory flow, over rough beds.

## *Threshold of Sediment Motion*

### 2.10. Introduction

Christensen (1981) reports that the first investigations relating (unidirectional) fluid flow to (non-cohesive) sediment movement appear in the 17<sup>th</sup> century. Latterly, the broader field of sediment transport studies has been divided into component areas, including the ‘threshold of motion’ for sand-sized, non-cohesive sediment. Studies have been varied in their approaches, investigating the threshold of sediment motion in terms of a broad spectrum of hydraulic and sediment parameters; as such, by parameterising progressively more of the natural variability found in the environment, increasingly accurate predictions and simulations of sediment mobility have become possible. During this time, it has been suggested also, that threshold relationships by the very nature of the processes they describe, should not attempt to provide an explicit solution (i.e. in terms of a single critical velocity or shear stress amplitude);

rather, that the solution should represent stochastic parameters (the probability or risk) of grain or bed motion (Lavelle and Mofjeld, 1987). Lavelle and Mofjeld (1987), Buffington (1999) and Paphitis (2001) have published detailed, critical reviews of this subject area, including extensive reference lists of investigations previously undertaken.

In relation to threshold under unidirectional flows, investigations have been undertaken, in addition to those summarised in Section 1.1, to determine the effect of grain sorting and pivoting angles (Li and Komar, 1986, 1992; Komar, 1987) and infiltration or seepage of water at the sediment water interface (Watters and Rao, 1971; Oldenziel and Brink, 1974; Willetts and Drossos, 1975; and Ramakrishna Rao and Sitram, 1999). However, these studies represent only a fraction of the natural variability in the field. The present study will concern itself with the simple case of (sinusoidal or asymmetric) oscillatory flows, above a flat (featureless) bed of uniform sediment, unaffected by additional biological, physical or chemical forcing.

### **2.11. Basic definitions and nomenclature**

In the context of the present study, phrases such as: the ‘point of inception’; ‘onset’; the ‘threshold of motion’; or simply ‘threshold’, may be used interchangeably, as all imply the beginning of, but none of them quantifies, the state of initial sediment transport. In the literature, numerous other terms or phrases have been used to classify or quantify the concept of threshold (e.g. Lavelle and Mofjeld, 1987; Buffington, 1999; and Garcia *et al.*, 2000 ). These terms can be individually descriptive, but still rely on the subjective opinion of the individual observing the phenomenon. These phrases tend to include adjectives such as ‘first’, ‘weak’ or ‘initial’ in describing the threshold condition of sediment motion.

### **2.12. Methods of observation**

Flume based laboratory experiments have been used to collect a large quantity and wide variety of data pertaining to the threshold of motion for sand under unidirectional, oscillatory and combined flows. These data were used to derive coefficients for predictive equations, but comparison between researchers shows a substantial amount of variability and scatter. It is suggested that differences in observational methodology (and hence the definition of threshold) are a primary cause of such variability (Lavelle and Mofjeld, 1987, Buffington, 1999). Differences in instrumentation (i.e. wave channels vs. oscillating trolleys) may contribute also to scatter in the data; however, Sleath (1984) argues that, theoretically, there

is minimal difference between the near-bed flow generated in wave channels and corresponding flows over oscillating trolleys.

There are presently a variety of methods used to define incipient motion, resulting in a certain degree of complication and ambiguity when comparing data sets that have been collected using subtly different definitions of threshold. After Lavelle and Mofjeld (1987), the methods for definition fall into four broad categories, namely: (i) visual observation methods, (ii) flux regression methods, (iii) erosion rate methods (for cohesive sediments) and (iv) practical field methods. Visual observation methods include descriptive (qualitative) and stochastic (quantitative) methods; aspects of these methods were utilised in the present study and are discussed below in more detail. Flux regression and erosion rate methods do not rely upon the observation of a single condition, instead, a number of observations of sediment transport as bedload or in suspension, respectively, are made at a range of flow rates in excess of that required for threshold; these data are plotted then against some parameter representing the flow (velocity or shear stress, etc) and regression analysis is performed to find the threshold flow corresponding to zero transport. Practical field methods (e.g. Sternberg, 1971, 1975; Davies, 1980, 1984, 1985) are necessarily varied because of certain aspects or limitations of the equipment used or the site chosen for study; typically, some combination of the visual and regression methods are used.

### *2.12.1. Visual observation – descriptive methods*

Threshold may be considered as a characteristic state of transport, visually interpreted by the observer. Visual observation of a condition described in qualitative terms may be used to define a threshold state. Kramer (1935) identified four transport states, commonly referred to for visual classification.

- |       |                  |  |
|-------|------------------|--|
| (i)   | No movement      | $\tau_0$ below which no particles are moving                           |
| (ii)  | Weak movement    | $\tau_0$ moving a few particles at isolated points                     |
| (iii) | Medium movement  | $\tau_0$ moving many grains but discharge is small                     |
| (iv)  | General movement | $\tau_0$ moving many grains of all sizes in all places all of the time |

Visual definition of inception using the ‘weak movement’ definition or similar, has been adopted by many researchers in the last 70 years. However, it is generally accepted that visual classification in this way is subjective to the opinion of the observer, almost by definition; as such, Kramer acknowledges, that it is difficult in practice to differentiate and

---

distinguish clearly between the mobility states that he describes. The classifications of Kramer, as used in latter day studies, have remained largely unchanged; however, a number of similar descriptive terms (e.g. ‘first movement’ by White (1970) and ‘incipient transport’ by Mantz (1980)) have been used also.

### 2.12.2. Visual observation – the Yalin Criterion

A stochastic similarity approach for unidirectional flows is presented by Neill and Yalin (1969) and refined by Yalin (1972). Although not widely used, this method does draw a closer parallel with the latterly used stochastic approaches to sediment threshold relationships (see Section 2.16). In this approach, threshold is defined by the dimensionless ‘Yalin Criterion’,

$$\varepsilon = \frac{n}{At} \left( \frac{\rho D^5}{(\rho_s - \rho)g} \right)^{1/2} \quad \text{Eq. 2.29}$$

In practice, the criterion defines the number of grain detachments ( $n$ ) that must be observed over area ( $A$ ) within time ( $t$ ). Hence, the criterion is scaled: (i) by the grain size; (ii) by the density of the sediment and the fluid; and (iii) by the Yalin parameter,  $\varepsilon$ , which should be a suitably small but non-zero value and should be kept constant between experiments.

A number of threshold studies including unidirectional, oscillatory and combined flows have been undertaken using the Yalin Criterion (Paphitis *et al.*, 2002; Paphitis *et al.*, 2001; Paphitis, 2001; Voulgaris *et al.*, 1995; Hammond and Collins, 1979). In all of these experiments, the recommended lower limit of  $\varepsilon = 10^{-6}$  was used and in some cases was used to make observations under oscillatory and combined flows also. According to Lavelle and Mofjeld (1987), based on statistical arguments, this corresponds to a rate of grain movement 10 times less than that expected at threshold as defined by the method of Shields (1936) for unidirectional flows; however, it is not clear from the original works of Shields whether the visual criteria of Kramer (1935) or a regression method were used (Buffington, 1999).

## 2.13. The critical velocity approach

In order to represent the critical conditions for threshold of motion for sediment under oscillatory flow, the peak orbital velocity outside of the boundary layer,  $U_\infty$ , may be used as a critical parameter. Sleath (1984) presents a number of such relationships and two examples of the range of  $U_{\infty \text{ crit}}$  predicted by these many formulae are shown in Figure 2.10; also

---

shown in the Figure are the relationships of Shields (1936), You (2000) and Le Roux (2001), described later in this Section. Under oscillatory flow, the majority of these formulae are typically period dependant; such relationships selectively include also, parameters of grain size, grain density and fluid density.

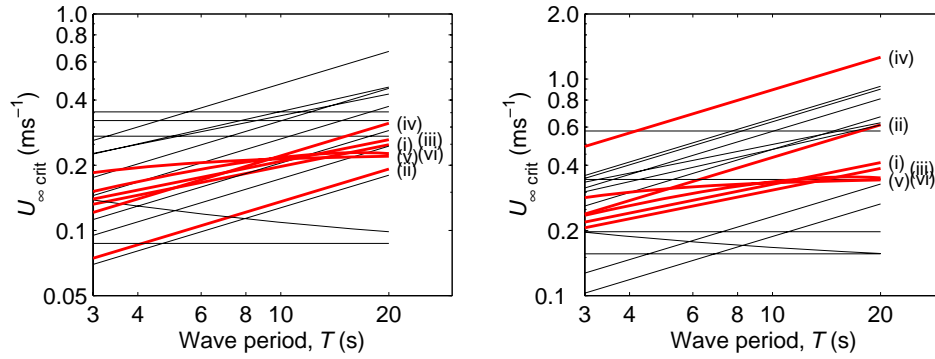


Figure 2.10. Predicted  $U_{\infty \text{ crit}}$  from various threshold of motion relationships from Sleath (1984), for quartz grains: (a)  $D=275\mu\text{m}$  and (a)  $D=800\mu\text{m}$ . Highlighted are the curves of: (i) Bagnold (1946); (ii) Manohar (1955); (iii) Komar and Miller (1973, 1974) and additionally; (iv) Shields (1936); (v) You (2000) and (vi) Le Roux (2001).

Three of the most commonly used relationships are those of Bagnold (1946), Manohar (1955) and Komar and Miller (1973, 1974). The relationship of Bagnold,

$$\frac{U_{\infty}}{\left(\frac{\rho_s - \rho}{\rho}\right)^{2/3} D^{0.433} T^{1/3}} = 2.38 \quad \text{Eq. 2.30}$$

was often used previously as a standard equation from which to compare other such formulae (Tomlinson, 1993) and tends to lie in the middle of the range of such relationships (see Figure 2.10). Manohar (1955) presented two relationships to describe threshold of motion. For threshold under laminar flow conditions,

$$\frac{U_{\infty} \nu^{1/2}}{\left(\frac{\rho_s - \rho}{\rho}\right) g D T^{1/2} \tan \phi} = 0.025 \quad \text{Eq. 2.31}$$

and for threshold under turbulent flow conditions, utilising the angle of repose,  $\phi$  (Section 4.4.1),

$$\frac{U_{\infty}}{\left(\frac{\rho_s - \rho}{\rho}\right)^{0.4} g^{0.4} \nu^{0.2} D^{0.2}} = 7.45 \quad \text{Eq. 2.32}$$

These formulae were more in line with the patterns observed in the work of Shields (1936) and recognised that differences were apparent in the erosive processes occurring under laminar and turbulent flows. Based on threshold observations of quartz grains, Komar and Miller (1973, 1974) provide a similarly separated and also commonly used set of relationships. For threshold of (quartz or similar) grains  $D < 0.05\text{cm}$  (deemed to represent threshold occurring under laminar flow),

$$\frac{U_{\infty}}{\left(\frac{\rho_s - \rho}{\rho}\right)^{2/3} g^{2/3} D^{1/3} T^{1/3}} = 0.24 \quad \text{Eq. 2.33}$$

and for threshold of grains  $D > 0.05\text{cm}$  (representative of turbulent flows),

$$\frac{U_{\infty}}{\left(\frac{\rho_s - \rho}{\rho}\right)^{4/7} g^{4/7} D^{3/7} T^{1/7}} = 1.05 \quad \text{Eq. 2.34}$$

Although separating the two conditions by grain size may be appropriate for a single sediment material, Sleath (1984) offers an alternative boundary for the relationships of Komar and Miller (1973, 1974) where, for threshold under laminar flow conditions,

$$\left(\frac{\rho_s - \rho}{\rho} \frac{g}{\nu^2}\right)^{1/3} D \leq 12.5 \quad \text{Eq. 2.35}$$

This allows application of Eq. 2.33 and Eq. 2.34 to sediment of  $\rho_s$  significantly different to that of quartz. The critical velocity approach is, to some extent, interchangeable with the approach of Shields (1936) (see Section 2.14), where the velocity amplitude may be used to calculate the bed shear stress amplitude. Sleath (1984) recommends the use of the graphical method of Kamphuis (1975) for the calculation of bed shear stress from other flow parameters in threshold of motion studies. This method was preferable to the earlier

relationship of Jonsson (1966) because of the uncertain connection between the laminar and turbulent solutions therein, whilst the transitional region in the diagram of Kamphuis is based on (limited) actual data. More detail regarding the calculation of bed shear stress may be found in Section 4.4.3.

More recently, two distinct models have been provided by You (1998) and You (2000). The latter investigation is described as superior to the first as it relies less heavily on empirical fitting; a wider range of data had also been incorporated. You (2000) reanalyses the threshold of motion data from several of the main datasets, mainly collected using oscillating trolley equipment. You (2000) notes that when the critical stroke length,  $S_{crit}$  is plotted against  $T$ , the linear regression for data at larger values of  $T$  has an intercept such that at  $S_{crit} \Rightarrow 0, T > 0$ . The critical value of  $T$ , above which this condition applies, is typically very small for most sediment (0.5-1s) and only very limited data exists from which to draw similar relationships, hence, these are not included here. At smaller  $T$ , the data gradually deviate from the linear regression towards the origin. You suggested the following formula, to predict the critical orbital amplitude at relatively large  $T$ :

$$a_{crit} = \frac{U_{crit}T}{2\pi} = \frac{2.53s_*^{0.92}\nu}{D} \left( T - \frac{53.0s_*^{-1.3}D^2}{\nu} \right) \quad \text{Eq. 2.36}$$

Where  $s_*$  is the scaled dimensionless immersed weight,

$$s_* = \frac{D\sqrt{\left(\frac{\rho_s}{\rho} - 1\right)gD}}{4\nu} \quad \text{Eq. 2.37}$$

Quantities such as  $U_{crit}$  ( $=S_{crit}\pi/T$ ) and other derivative parameters may be calculated directly using the equations described later in Sections 4.4.2 and 4.4.3. When these equations were applied to the data sets used in the present study, the value  $S_{crit}$  was typically underestimated by around 11% of the actual recorded value although this value ranged from 0-50%. This may be attributed potentially to differences in the methodology or equipment used to collect the data sets used by You in the construction of the empirical relationships.

The majority of the formulae depicted in Figure 2.10 are empirical relationships derived from laboratory data; as such, these results typically represent laminar or near-laminar flows.

---

In addition, relationships representing analytical solutions tended to assume that laminar flow conditions prevailed. From the analytical relationships between  $T$ ,  $U_\infty$  and the bed shear stress,  $\tau_0$  (described in more detail in Section 4.4.3), under laminar flow conditions, the critical velocity is typically assumed to take the form

$$U_{\infty crit} \propto \sqrt{T} \quad \text{Eq. 2.38}$$

Sleath (1984) suggests that differences in the magnitude of  $U_{\infty crit}$  are most likely representative of the scatter in the experimental data (the result of experimental noise and differences in observational methodology and equipment design), upon which the various empirical relationships are based.

Le Roux (2001) relates the threshold orbital velocity to the dimensionless settling velocity as

$$U_{\infty crit} = -0.01 \left[ \frac{(\theta_{wl} gD(\rho_s - \rho))^2}{(\rho\mu/T)} \right] + 1.3416 \left[ \frac{\theta_{wl} gD(\rho_s - \rho)}{\sqrt{\rho\mu/T}} \right] - 0.6485 \quad \text{Eq. 2.39}$$

Where the units of Eq. 2.39 to Eq. 2.42 inclusive, are in grams, centimetres and seconds. Eq. 2.39 uses the dimensionless quantity

$$\theta_{wl} = \frac{U_\infty (\rho\mu/T)^{0.5}}{gD(\rho_s - \rho)} = 0.0246W_d^{-0.55} \quad \text{Eq. 2.40}$$

where  $W_d$  is the dimensionless settling velocity

$$W_d = (aD_* + b)^c \quad \text{Eq. 2.41}$$

where  $a$ ,  $b$  and  $c$  are fitting coefficients given in Table 2.2 and  $D_*$  is the dimensionless grain size,

$$D_* = \left( \frac{\rho_s - \rho}{\rho} \frac{g}{v^2} \right)^{1/3} D \quad \text{Eq. 2.42}$$

D*		Coefficients		
From	To	<i>a</i>	<i>b</i>	<i>c</i>
0	1.254	0.2354	0	2
1.254	2.907	0.208	-0.0652	3/2
2.907	22.987	0.2636	-0.37	0
22.987	134.922	0.8255	-5.4	2/3
134.922	1750	2.531	160	1/2

Table 2.2. Fitting coefficients for the threshold relationship of Le Roux (2001). (Eq. 2.41).

A number of the comments and assumptions made by Le Roux (2001) were questioned by You and Yin (2004) and clarified subsequently by Le Roux (2004) with no significant change to the proposed relationships.

### 2.14. The Shields (1936) approach

The work of Shields (1936) provided a relationship between critical grain and flow parameters at the point of threshold under unidirectional flow. The work of Shields has since been developed and extended and it is now commonly used by consumers of threshold information as an accessible, graphical form of the available data for threshold of motion under unidirectional, oscillatory and combined flows. A review of the many Shields type relationships, previously proposed for unidirectional flows, may be found in Paphitis (2001). Buffington (1998) presented a detailed and critical review of the original methods of Shields and of subsequent work undertaken that incorporate these data or similar analytical techniques. Buffington argues that the Shields diagram and some of the original data sets are misrepresented in latter day studies due to erroneous interpretation of the original works and that these errors have been propagated and amplified over time. Grass (1970) also points out that the Shields curve is unique only for fully developed open channel flow and observations deviate from this solution under other unidirectional situations (e.g. convergent/divergent flows, flow around ripples, etc).

The Shields diagram is a dimensionless representation of the balance of forces between the bed shear stress,  $\tau_0$ , acting upon grains of diameter,  $D$  and density,  $\rho_s$  in water of density,  $\rho$ , in the form,

$$\theta = \frac{\tau_0}{(\rho_s - \rho)gD} \quad \text{Eq. 2.43}$$

Where  $\theta$  is referred to typically as the Shields parameter. For unidirectional flows,  $\theta$  is plotted typically against the grain Reynolds number,  $Re_*$ , which is a combined measure of bed shear stress and the roughness of the hydrodynamic interface,

$$Re_* = \frac{u_* D}{\nu} \quad \text{Eq. 2.44}$$

where  $u_*$  is the friction velocity and is related to  $\tau_0$  by,

$$u_* = \sqrt{\frac{\tau_0}{\rho}} \quad \text{Eq. 2.45}$$

The Shields diagram may be used also to describe threshold under oscillatory flows, where  $\tau_0$  in Eq. 2.43 and Eq. 2.45 represents specifically the peak orbital bed shear stress.

A number of alternative parameters to  $Re_*$  (reviewed in Paphitis, 2001) have been proposed by Vanoni (1964), Yalin (1972), and Madsen and Grant (1976). Another parameter commonly used in threshold curves (Van Rijn, 1993) is the dimensionless grain size,  $D_*$  (Eq. 2.42) and the scaled dimensionless immersed weight,  $s_*$  (Eq. 2.37), has also been used to represent oscillatory flows. Using these alternative parameters removes  $\tau_0$  and its derivatives from the abscissa, simplifying the calculation of the critical value of  $\tau_0$  for threshold of motion (Soulsby, 1997; Paphitis, 2001)

Soulsby and Whitehouse (1997) propose that the original form of the Shields curve, is described closely by,

$$\theta_{crit} = \frac{0.24}{D_*} + 0.055[1 - \exp(-0.020D_*)] \quad \text{Eq. 2.46}$$

This relationship provided a reasonable fit to a large data set of threshold observations made under unidirectional, oscillatory and combined flows and is shown in relation to the oscillatory flow threshold data in Figure 2.11. Soulsby and Whitehouse (1997) also propose a modified curve, where  $\theta$  is reduced and becomes almost constant in the laminar region, in order to incorporate a number of unidirectional results of small grain sizes that were over-predicted by the Shields curve. However, only limited oscillatory flow data is available in

---

this region to accept the alternative curve in the context of the present study; the difference between the two curves was negligible within the range of  $D_*$  investigated.

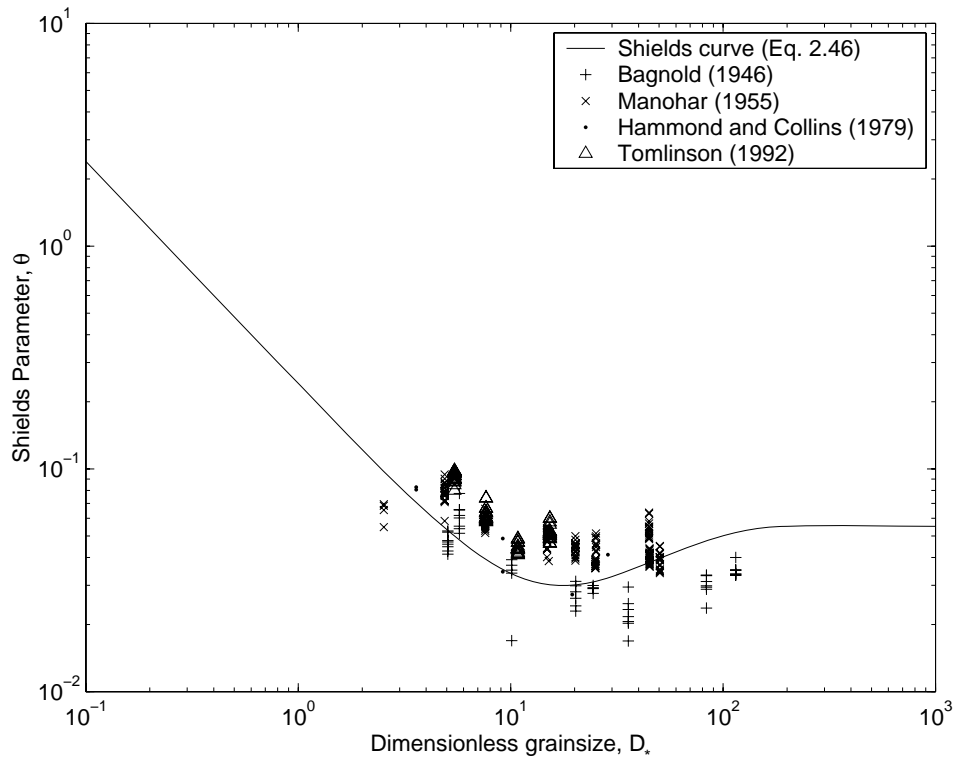


Figure 2.11. Shields steady flow curve, with selected threshold observation data superimposed, collected under sinusoidal oscillatory flows.

Since its conception, the unidirectional Shields diagram has been extended into the higher and lower grain Reynolds numbers, referring to low flow, fine grain regimes (Mantz, 1977) and energetic gravel transport (Miller *et al.*, 1977), respectively. Using combinations of laboratory and analytical numerical studies, the effects of sediment packing and bioturbation (Nowell *et al.*, 1981; Grant *et al.*, 1982; and Middleton, 1992), water temperature (Miller *et al.*, 1977; Taylor and Vanoni 1972), sediment density (Collins and Rigler, 1982), sediment sorting, protrusion and armouring (Kapdasli and Dyer, 1986), grain shape influence (Childs 2000; Komar and Li, 1986), bed slope (Dey and Debnath, 2000; Soulsby, 1997) and bedforms (Bagnold, 1963) have been considered also in relation to the unidirectional Shields curve. In addition, Buffington and Montgomery (1997) have provided a review of such processes influencing particle motion; Paphitis (2001) and Paphitis *et al.* (2001a) also suggests a number of additional references relating to sediment or bed parameters important in unidirectional threshold studies. The unidirectional Shields curve has also been

reinterpreted in terms of stochastic parameters (Lopez and Garcia, 2001; Lavelle and Mofjeld, 1987).

Such parallel or complementary studies have not yet been undertaken to such an extent for purely oscillatory flows; however, there is a tendency for researchers to translate assumptions based upon one type of flow, to others. Most importantly, it is assumed from all such Shields curves, that a single value of the critical shear stress magnitude may be used to predict the threshold of motion for given sediment under unidirectional, oscillatory and combined flows.

### 2.15. The Moveability Number approach

Named by Collins and Rigler (1982), the ‘Moveability Number’ provides a measure of grain mobility that may be used as an alternative to the Shields parameter. The Moveability Number is the dimensionless parameter,

$$\frac{u_*}{W_s} \tag{Eq. 2.47}$$

Where  $u_*$  is the friction velocity (Eq. 2.45) and  $W_s$  is the settling or fall velocity of the particle in the fluid environment being considered. From Van Rijn (1993), for non-spherical particles  $100\mu\text{m} < D < 1000\mu\text{m}$ ,

$$W_s = \frac{10\nu}{D} \left[ \left( 1 + \frac{0.01(\rho_s - \rho / \rho) g D^3}{\nu^2} \right)^{1/2} - 1 \right] \tag{Eq. 2.48}$$

It was first noticed by Rubey (1933), during an analysis of grain settling velocities, that the magnitude of the (unidirectional) current required to entrain a particle is approximately similar to the fall velocity of the same particle (Komar and Clemens, 1986). The moveability number incorporates all of the variables used in the Shields relationship, ( $\tau_0$ ,  $\rho$ ,  $\rho_s$ ,  $D$ ); in addition, if  $W_s$  for the sediment in question is measured directly, rather than indirectly via predictive equations, then grain shape effects are included implicitly also.

The development of the Moveability Number is summarised, and subsequently quantitatively compared to the Shields entrainment function, by Komar and Clemens (1986). The Moveability Number has been used since by a number of authors (Collins and Rigler, 1982;

---

Komar and Clemens, 1986; Paphitis, 2001; Paphitis *et al.*, 2001a; and Paphitis *et al.* 2002) for the expression of threshold under unidirectional flows. Le Roux (2001) has applied a Moveability Number-type approach to predicting threshold under oscillatory flows, yielding a critical velocity value (see Section 2.13).

## **2.16. The stochastic approach**

The stochastic approach rejects the concept of a single value of a critical (threshold) velocity or shear stress. Results are expressed instead as a range of flow conditions, corresponding to the range of probability, for the erosion of individual grains from a given bed of sediment. This argument is summarised by Lavelle and Mofjeld (1985) for unidirectional flows and an extensive reference list is provided therein. The stochastic approach was first presented by Einstein (1950) and used subsequently by Grass (1970) to describe the initial motion of fine sand under unidirectional flows incorporating coincidental observations of individual grain motion and instantaneous shear stress. The subsequent development of stochastic numerical models in this format, and the relationships used within them, seem to have been largely undertaken for unidirectional flows only.

Mingmin and Qiwei (1982) describe how early users of the stochastic approach assumed that either the fluid shear force or the susceptibility of individual grains to erosion were stochastic rather than deterministic variables; the other was maintained as a constant. The instantaneous fluid shear force and susceptibility to erosion were assumed to vary due to turbulence and to non-uniform exposure of particles to the flow or variations in grain properties, respectively; these stochastic relationships were assumed to follow a roughly normal distribution. These models were later combined but were limited typically by the lack of research into the quantitative relationships between the stochastic variables and other flow or sediment parameters.

Recent papers (e.g. Lopez and Garcia, 2001; Kleinhans and van Rijn, 2002; Dancey *et al.*, 2002; and, Papanicolaou *et al.*, 2002) summarise the latter development of stochastic relationships. These developments have been made by a combination of experimental and numerical investigations, typically using uniform spherical grains and all under unidirectional flows. The list of important stochastic variables remains largely the same, but exposure of particles is referred to instead in terms of the bed surface packing conditions (Papanicolaou *et al.*, 2002) and the distribution of shear stress is recognised as being positively skewed from a normal distribution due to the organisation of streaks and other coherent structures in the viscous sublayer of turbulent (unidirectional) flow (Lopez and

---

Garcia, 2001). Lopez and Garcia have presented stochastic results in comparison to part of the laminar/transitional region of the Shields curve; they suggested that in this region, the Shields curve corresponded approximately to a 40% probability of grain erosion.

Vittori (2003) presents the results of a quasi-stochastic numerical transport model for oscillatory flows. Rather than using a 1- or 2-dimensional stochastic representation of the fluid, the complete 4-dimensional flow field (including time) was modelled to reproduce coherent boundary layer structures (i.e. turbulence of a statistically representative distribution). A sheet of mobile grains are ‘released’ periodically into the flow at the bed, representing uniform erosion caused by each oscillatory flow half-cycle; the subsequent suspension of individual grains into the flow by eddies was observed then in the numerical domain. These data was used to investigate concentration profiles and the mechanisms of sediment suspension over a small range of wave periods; in this study, wave period was not provided explicitly but was represented by the ratio of the boundary layer thickness (a function of the wave period) and grain diameter. Although the model was designed to investigate suspension events and therefore did not resolve the threshold of motion, this provides an alternative method by which the stochastic approach may potentially be applied to sediment dynamics.

## Chapter 3. Equipment Description

### 3.1. The recirculating flume

The majority of laboratory experiments undertaken as part of the present study were conducted at the Southampton Oceanography Centre (SOC), within the School of Ocean and Earth Science, of the University of Southampton, U.K. The experiments utilised an S6 tilting flume, available commercially from *Armfield Ltd.*, U.K. (see Figure 3.1 and Figure 3.2, for general layout and dimensions). In practical terms, the flume provides either a channel for unidirectional flows or (in the case of the present study) a chamber of still water, within which the oscillating trolley apparatus (Section 3.2) can be mounted. This particular flume had a rectangular cross section channel, 0.3m wide and 0.45m deep. The base of the channel was a painted metal surface, whilst the walls were toughened glass along a 5m working section. Moulded fibreglass riser tanks, at either end of the working section, acted as stilling chambers for the turbulent water being either pumped in to, or drained out of, the flume. The flume utilised freshwater, stored at room temperature in separate reservoir tanks. When in use, the water was pumped to the upstream riser tank by a constant-output electric pump. The rate of flow was determined using a computer-actuated butterfly valve between the pump and riser tank inlet. This flume equipment, together with various aspects of flow structure and flow capabilities when simulating unidirectional and (simple) oscillatory flows, have been described in detail by Paphitis and Collins (2001a,b).

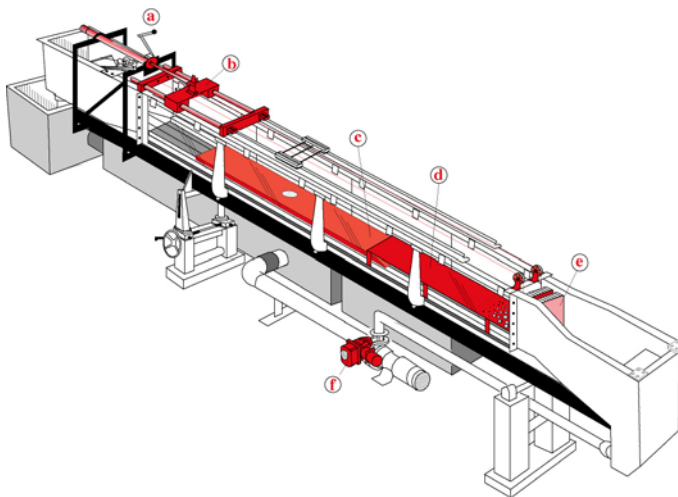


Figure 3.1. The recirculating flume and oscillating trolley, located at SOC. Key: (a) hydraulic ram; (b) linear carriage; (c) oscillating plate; (d) raised upstream bed; (e) flow-straightening tiles.

The flume described herein was used previously for sediment dynamics investigations, by several authors (Hammond and Collins, 1979a,b; Tomlinson, 1993; and Voulgaris *et. al.*,

1995). During these previous investigations, the flume provided unidirectional channel flows; it served also as the fluid chamber for a flywheel driven oscillating trolley, simulating both oscillatory and combined flows. When simulating unidirectional flows, the flume would be filled with water until a base-hinged weir at the downstream end was overtopped; water would then return to the reservoir tanks, via a gravity drain in the downstream riser tank. The equilibrium flow rate was achieved when the rate of overtopping was equal to the input of water at the upstream end.

## 3.2. The oscillating trolley

### 3.2.1. General description

The principle of using an oscillating trolley to simulate oscillatory flow of water, at the seabed, has been introduced in Section 1.1. In the present study, an oscillating trolley was mounted within the recirculating flume, described previously in Section 3.1 (Figure 3.1 and Figure 3.2).

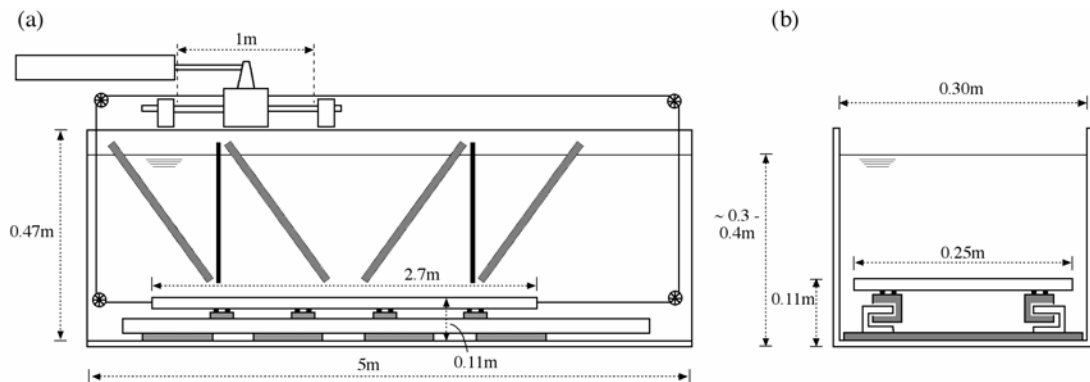


Figure 3.2. The oscillating trolley equipment mounted within the recirculating flume (not to scale): (a) side and (b) cut-away along flume views. Note: see text for a description of the various components.

The main apparatus consisted of a flat, heavy, aluminium alloy plate ( $2.7\text{m} \times 0.25\text{m} \times 0.02\text{m}$ ), mounted on ‘C-section’ aluminium rails; these ran parallel to the bed and were aligned with the long axis of the flume. The plate was supported upon the rails by steel ball bearings contained within a framework of machined ‘Orkot’ (water-lubricated, high-density plastic) blocks.

The plate oscillation was driven by a hydraulic ram, mounted on a rigid framework above the downstream riser tank of the flume. The hydraulic arm produced: a maximum stroke

length of 1m; a maximum outward stroke velocity of  $0.7\text{ms}^{-1}$ ; and a maximum return stroke velocity of  $0.45\text{ms}^{-1}$ . The hydraulic arm was coupled to the flume via a solid carriage mounted on linear bearings. Translation of the ram motion to the carriage was through a short vertical fin, made fast by a pin, through a socket and rubber bush. In turn, the plate and carriage were connected using a (parallel) twin-rigging loop of 4mm gauge stainless steel wire; this was guided over high-density plastic sheaves, mounted on metal spindles, at each corner of the working section of the flume. Strong springs were used to reduce shock loading of the equipment, created by any sudden motion of the ram; these were incorporated, in series, into the wire loop, at the point where the wires terminate on the linear carriage.

In order to prepare the flume tank for use with the oscillating trolley, the water outlet in the downstream riser tank of the flume was plugged using an appropriate rubber ‘O-ring’ and a solid metal plate. The flume was filled with water to the maximum possible depth, 2cm below the top edge of the flume, i.e. 33cm above the level of the plate; the valve was then closed and the water was allowed to become still. Slight leakage through the plug, caused the water level to drop very slowly ( $\sim 2\text{cm}/\text{hour}$ ); consequently, water levels were topped up on a regular basis, allowing adequate time for the main body of water to become still after each addition. Still water was maintained throughout the experiment by the placement of vertical solid plates and oblique porous mats (see also Plate 3.1); these acted as baffles, to dampen residual and resonant flows within the tank.



Plate 3.1. The configuration of the central porous mats and solid plates used as flow baffles to maintain still water above the plate.

To allow the possibility of combined flow studies (not undertaken as part of the present study), an additional fixed bed, raised to the height of the trolley, was installed; this provided a continuous flat surface, from the start of the working section to the end of the oscillating plate. This additional bed remained in place during the oscillatory flow experiments, but caused no significant effect on the resulting flows in the test section.

---

### 3.2.2. Control software

The motion of the hydraulic ram and as such, the plate itself, was controlled by PC windows-based user interface program; this was written for the present study using *National Instruments* LabVIEW software (an example ‘screen shot’ is shown in Plate 3.2). This control software allowed the user to specify the oscillatory period, degree of asymmetry and value of  $U_1$ ; a corresponding value of  $U_2$  was obtained using Eq. 2.10. The position of the ram (hence, the plate) was calculated as

$$x_t = (-U_1 / \omega) \sin \omega t + (-U_2 / 2\omega) \sin 2\omega t \quad \text{Eq. 3.1}$$

The calculated signal was outputted as a voltage between 0-10V, from a Data Acquisition Card (DAC), commercially available from National Instruments. The resolution of the ram arm motion, following conversion of the digital signal to analogue, was better (finer) than 1mm. During the initial testing, the ram arm position (in relation to the voltage) was calibrated by making 10 coincident observations and performing a linear regression.

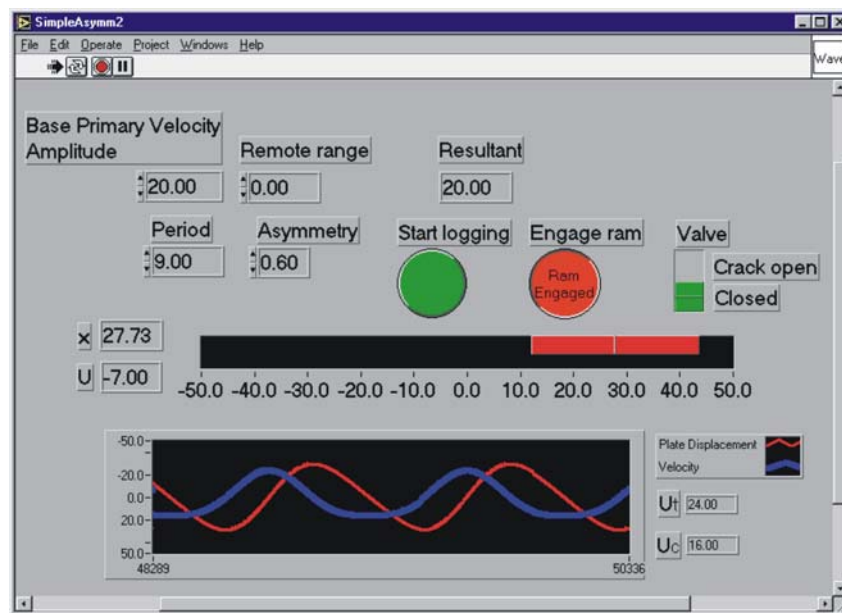


Plate 3.2. An example of the user interface screen for controlling the oscillating trolley, during the present study.

### 3.2.3. Plate positioner

A positioner device (shown in Plate 3.3) was designed, in order to measure the absolute motion of the plate. A 10-revolution potentiometer was attached to a spindle (a strong metal rod), spanning the top of the downstream riser tank, adjacent to the turning blocks of the main rigging loop. Mounted also on the spindle were two drums, with guiding grooves for a

thin, light rope with minimal stretch characteristics. One such line was connected to the plate, via a small turning block at the base of the flume; the other was attached initially to a lead counterweight and, latterly, to a thick elastic cord, placing the system into constant tension.

The system was constructed in such a way that the maximum travel of the plate (1m) caused the spindle to rotate approx. 9.5 revolutions (near the full range of the potentiometer). This produced a voltage ranging between 2.85 and 5 volts, where the voltage was a non-linear function of the number of rotations and, hence, the position of the oscillating plate. The analogue voltage signal from the potentiometer was interpreted, via the DAC and LabVIEW software.

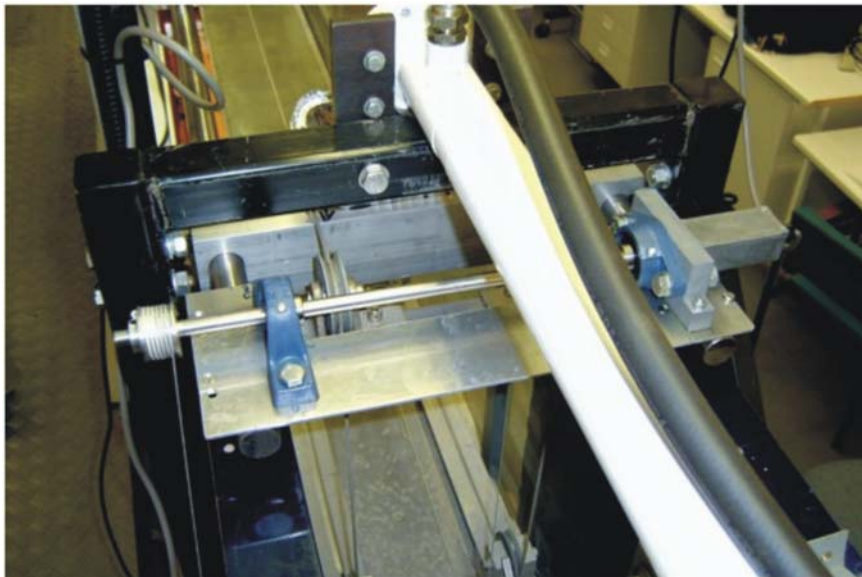


Plate 3.3. The plate positioner system, located (beneath the hydraulic ram) within the flume.

#### *3.2.4. Calibration of the plate positioner*

Initial calibration of the potentiometer was carried out, by gradually moving the ram over a 1m stroke in both directions; this generated continuous and coincident measurements of the potentiometer voltage. A calibration algorithm was determined using a second-order polynomial regression. Following conversion of the analogue signal, via the DAC, the resolution of the potentiometer was 0.005V; this corresponded to a position resolution of 2-3mm, including non-linearity of the voltage response. Additional instrument noise was observed in some cases; this was of the order of  $\pm 0.005V$  ( $\pm 2-3mm$ ).

#### *3.2.5. Calibration/validation of the oscillating trolley*

The accuracy of the system, in reproducing the prescribed oscillatory motion, was tested by measuring separately, the motion of the ram arm and of the oscillating plate. The position of

---

the ram arm was recorded as the desired position (as calculated by the control software). The actual position of the plate was then measured independently, using the plate positioner equipment described in Section 3.2.3. Calibration of voltage to actual position for the ram and plate positioner, was carried out separately (see Sections 3.2.2 and 3.2.4, respectively).

The positions of the ram and the plate were recorded simultaneously at 100Hz, over a range of sinusoidal and asymmetric oscillatory motions; the separately recorded positions and calculated velocities were compared over the oscillatory cycle. The measured position of the plate followed closely the position of the ram arm, over time; however, some deviation was observed in the form of a sinusoidal variation (amplitude 2cm). The peaks in deviation coincided with the phases of peak velocity, when resistance due to drag and friction are greatest. Hence, this deviation was attributed to extension of the springs in the wire rigging loop. The plate velocity calculated over time from the plate position data, followed closely the velocity of the ram arm. After applying a low-pass filter to remove instrument noise from the plate position data, the ram arm and plate velocities did not differ by more than 1.5%.

The data show also, that at the time of initial testing, a small amount of ‘play’ (~2.2cm) was observed in the connection between the ram and the oscillating plate. This play was attributed to: (i) the non-rigid connection between the ram arm end and the linear carriage; and (ii) extension of the springs incorporated in the wire rigging loop. Deviation due to play occurred in the ~0.1s, immediately following the point of flow reversal; this was due to the negligibly low velocity and acceleration around that time. This effect was not considered to be significant in terms of flow development.

### *3.2.6. Sediments used in the present study*

Thirteen non-cohesive, uniform, sand-sized sediment samples were prepared for testing, in the threshold experiments of the present study. A number of the measured grain parameters are summarised in Table 3.1.

$D_{50}$ ( $\mu\text{m}$ )	Material	$\rho_s$ ( $\text{kgm}^{-3}$ )	$D$ Interval ( $\mu\text{m}$ )	Shape	Comment (see Plate no.)
275	Aragonite	2750	250-300	Sub angular spherical	Plate 3.5e
327.5	Aragonite	2750	300-355	Sub angular spherical	Plate 3.5d
390	Aragonite	2750	355-425	Sub angular spherical	Plate 3.5c
472.5	Aragonite	2750	425-500	Sub angular spherical	Plate 3.5b
550	Aragonite	2750	500-600	Sub angular spherical	Plate 3.5a&f
275	Quartz	2650	250-300	Sub rounded spherical	Plate 3.4e
327.5	Quartz	2650	300-355	Sub rounded spherical	Plate 3.4d
390	Quartz	2650	355-425	Sub rounded spherical	Plate 3.4c
472.5	Quartz	2650	425-500	Sub rounded spherical	Plate 3.4b
550	Quartz	2650	500-600	Sub rounded spherical	Plate 3.4a&f
925	Bakelite	1400	850-1000	Angular spherical	Plate 3.6d&e
1200	Bakelite	1400	1000-1400	Angular spherical	Plate 3.6c
1550	Bakelite	1400	1400-1700	Angular spherical	Plate 3.6b
1850	Bakelite	1400	1700-2000	Angular spherical	Plate 3.6a

Table 3.1. Characteristics of the sediments used in the present study.

Quartz samples (Plate 3.4) were prepared from commercially available builders sand. Dry sieving techniques were used, using ‘research quality’ sieve stacks to separate the appropriate grain size fractions. The quartz grains used in subsequent experiments were generally spherical and sub-rounded in shape.

Aragonite samples (Plate 3.5) were prepared from ‘hard coral sand’, commercially available through aquarium and tropical fish suppliers. The original material was composed of roughly broken hard coral fragments, harvested in a ‘sustainable manner’; clasts were angular, with an estimated mean long-axis length of 4mm. A conical grinder (in the SOC) was used to progressively crush the material. The resulting mix of finer grains was dry sieved, in the same way as the quartz sediments; they were washed then, in water, to remove any fine residue. The prepared aragonite clasts were angular in shape. Aragonite is a form of calcium carbonate ( $\text{CaCO}_3$ ) and its density is listed as  $\rho_s=2950 \text{ kgm}^{-3}$ . It was intended originally that, in combination with quartz and Bakelite grains, this would provide a range of  $\rho_s$  in the sediment samples. However, laboratory tests using a simple displacement method, to measure the volume of a known mass of sample, indicated that the actual density was closer to that of calcite (also  $\text{CaCO}_3$ ) at  $\rho_s=2750 \text{ kgm}^{-3}$ . The Aragonite grains used in the present study were generally sub-spherical and angular in shape.

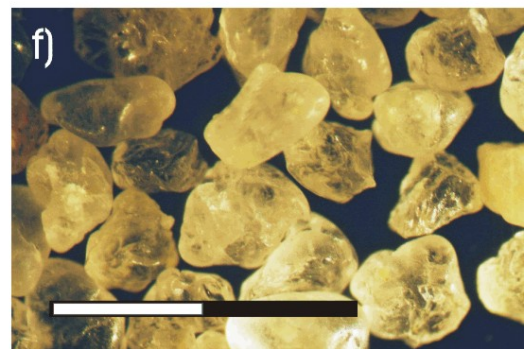
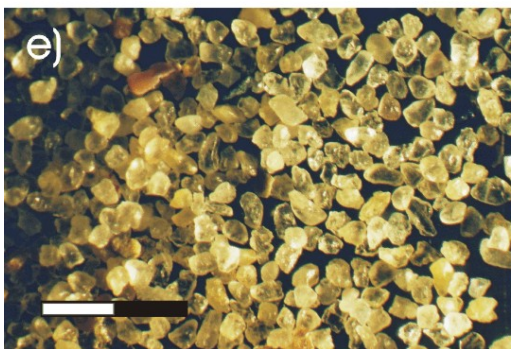
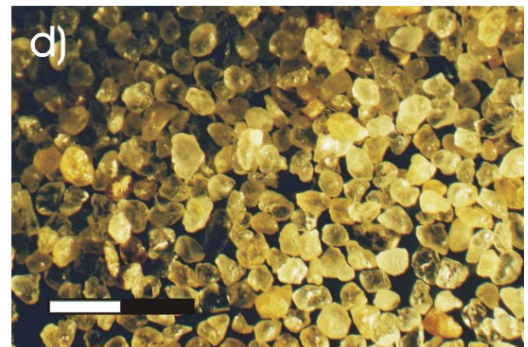
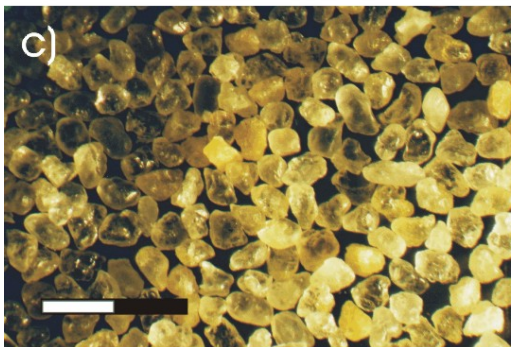
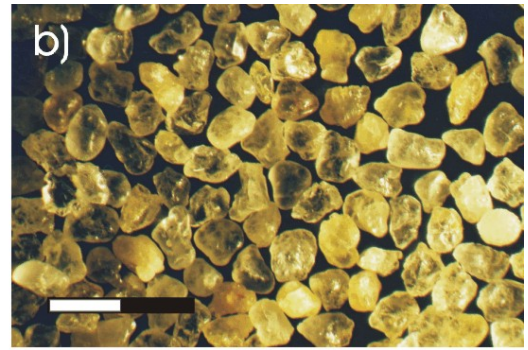
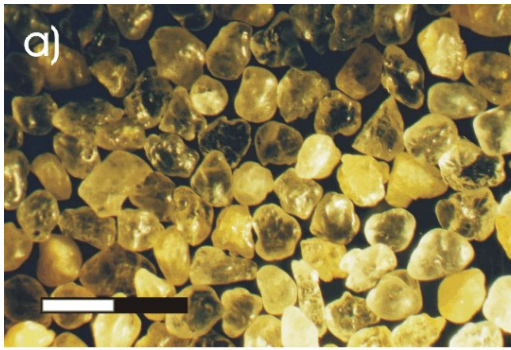


Plate 3.4. Quartz sediments used in the present study, of median diameter: (a) and (f) 550 $\mu\text{m}$ ; (b) 472.5 $\mu\text{m}$ ; (c) 390 $\mu\text{m}$ ; (d) 327.5 $\mu\text{m}$ ; and, (e) 275 $\mu\text{m}$ . Note: scale bar = 2mm.

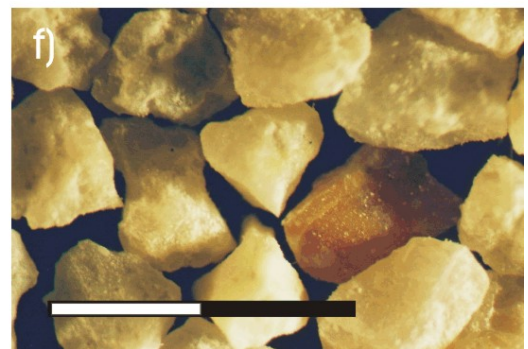
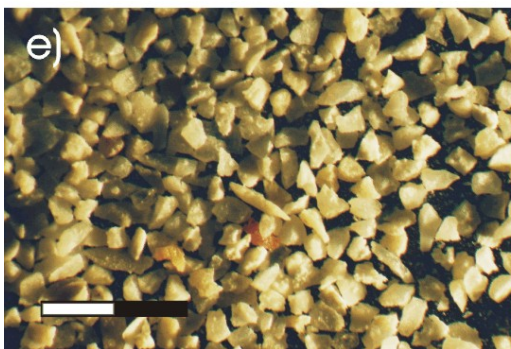
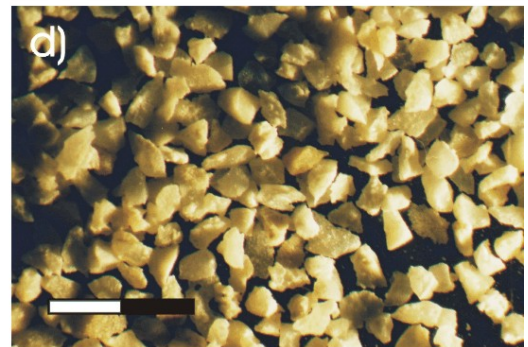
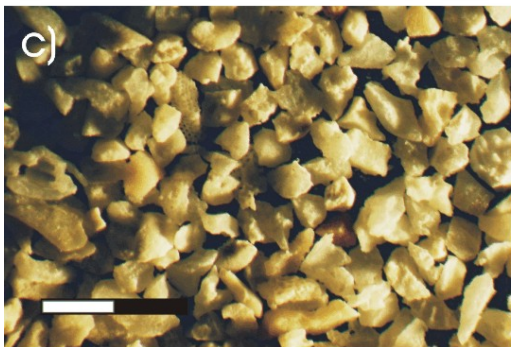
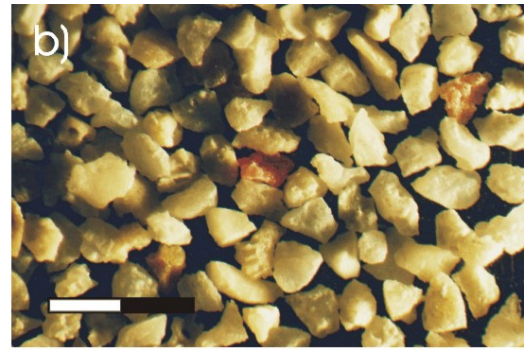
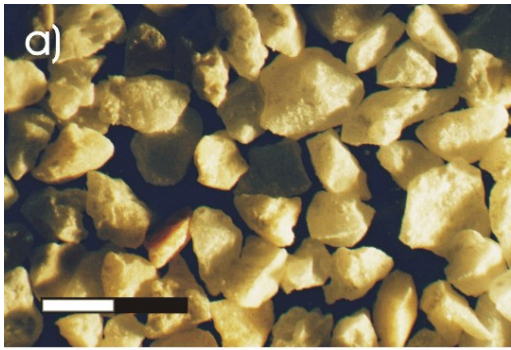


Plate 3.5. Aragonite sediments used in the present study, of median diameter: (a) and (f) 550 $\mu\text{m}$ ; (b) 472.5 $\mu\text{m}$ ; (c) 390 $\mu\text{m}$ ; (d) 327.5 $\mu\text{m}$ ; and, (e) 275 $\mu\text{m}$ . Note: scale bar = 2mm.

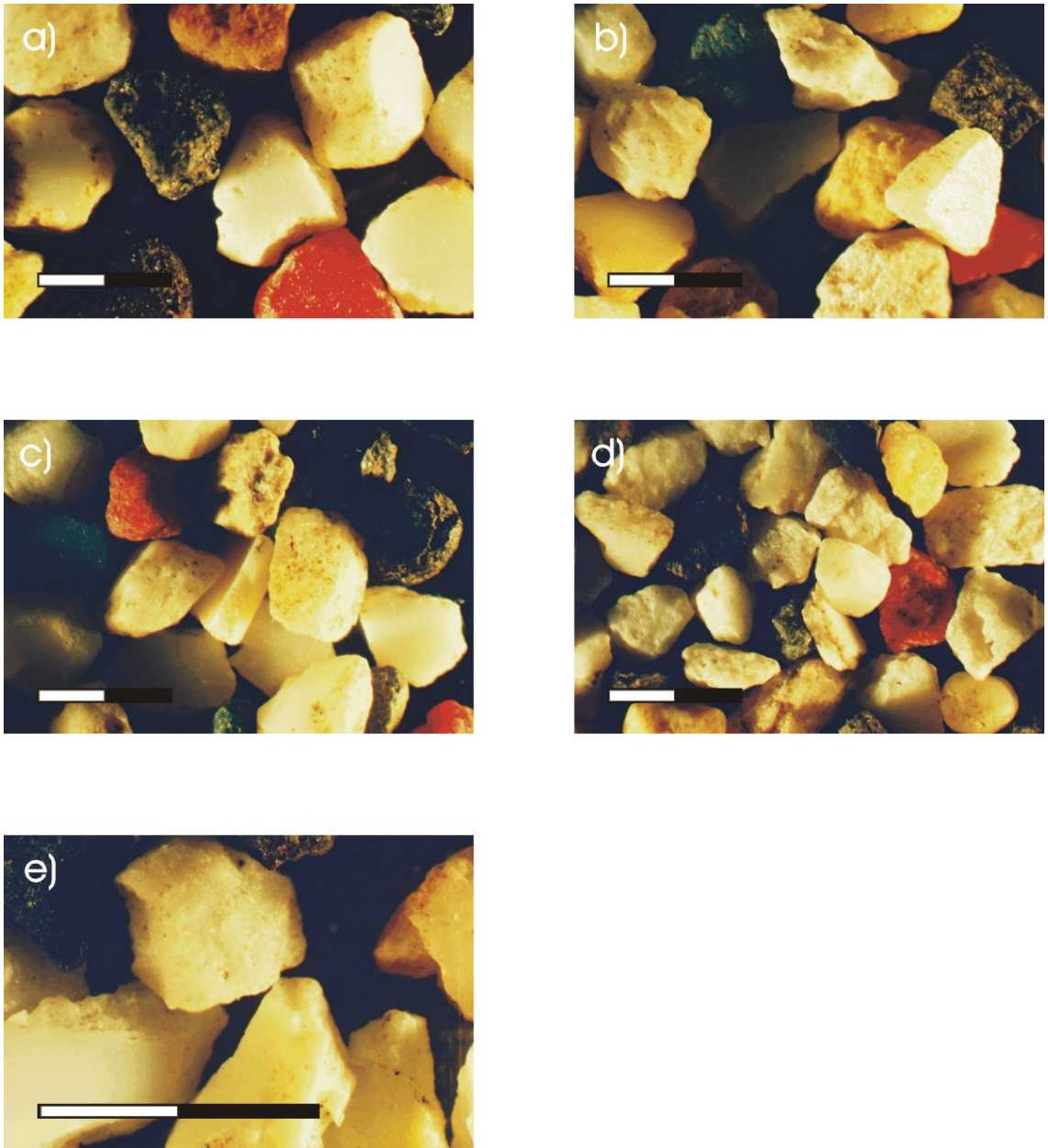


Plate 3.6. Bakelite sediments used in the present study, of median diameter: (a) 1850 $\mu\text{m}$ ; (b) 1550 $\mu\text{m}$ ; (c) 1200 $\mu\text{m}$ ; (d) and (e) 925 $\mu\text{m}$ . Note: scale bar = 2mm.

Bakelite samples (Plate 3.6) were dry sieved from a bulk sample, provided by the Department of Civil and Environmental Engineering, at the University of Southampton. Before use, all of the Bakelite samples were soaked in water, with some added surfactant (photographic wetting agent was used); this reduced the hydrophobic properties of the Bakelite material, which would otherwise cause some grains to float, due to surface tension effects. The Bakelite grains used in the present study were generally spherical but angular in shape.

---

### 3.2.7. *Smooth and fixed granular beds*

During each of the experiments undertaken in Southampton, an additional bed surface providing a flat and horizontal bed with smooth or roughened texture, was fixed rigidly to the upper surface of the oscillating plate. An hydraulically smooth bed was created, using a flat sheet of polished glass 1.2m long, 0.2m wide and 5mm thick. For the rough bed experiments, two fixed-roughness beds were prepared by carefully gluing a layer of uniform quartz sand to similar sheets of glass; the mean grain diameter for each bed was 275 $\mu$ m and 550 $\mu$ m, respectively. The sand samples used to create these beds are described in Section 3.2.6. All of the beds provided a continuous flat surface, of a length in excess of the maximum stroke length simulated.

## 3.3. Flow velocity measurement

### 3.3.1. *The LDV system*

Detailed flow measurements were carried out in a number of the experiments undertaken within the present study, using a Laser Doppler Velocimeter (LDV) instrument (Plate 3.7). Loan of the equipment and subsequent support for the LDV system was provided by the EPSRC equipment pool. The LDV system, as used in the present study, was a 5 Watt argon-ion laser, measuring two components of flow in a backscatter mode. The source beam was provided by a *Spectra Physics* laser source (Model 2017); this was passed into a ‘Colorburst’ unit, providing laser light in green (514.5nm) and blue (488.0nm) wavelengths. A ‘ColorLink’ module was used to condition two additional frequency-shifted beams at these wavelengths; all four beams were subsequently transmitted, via fibre optic cables, to a 9832 optic head. From the optic head, the two pairs of beams were focused upon a point 350mm distant (in air), perpendicular to the face of the optic head. The optic head was mounted upon a computer controlled three-axis traverse system, allowing accurate positioning of the optic head and, hence, of the sampling volume (see Section 3.3.2, for further details of spatial accuracy and resolution of the beams). The ColorLink module and an IFA650 signal processor were used to interpret the Doppler shift information in the backscattered signal. All aspects of LDV equipment control and data logging were performed using the TSI software provided with the system (named ‘Ffw16.exe’).

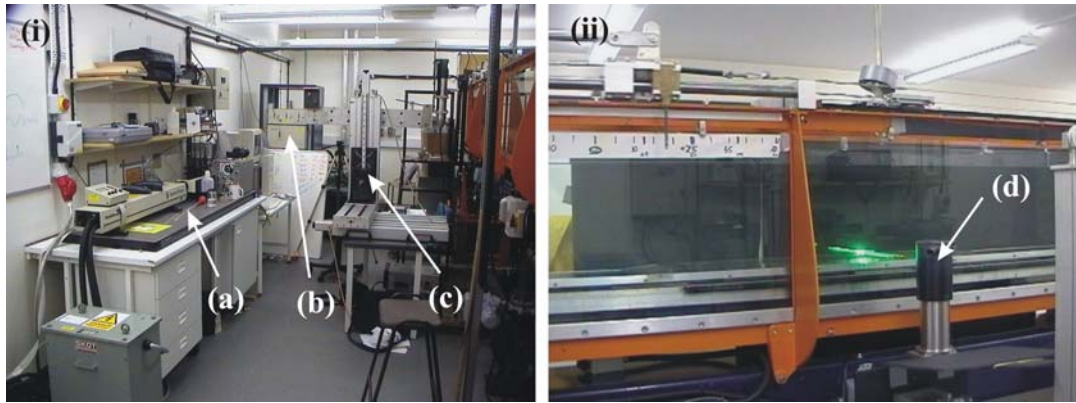


Plate 3.7. The LDV system: (i) placement within the laboratory; and (ii), in use during a velocity profiling experiment. Key: (a) optic bench, laser source and beam splitter; (b) ‘ColorLink’ module; (c) 3D traverse; (d) optic head.

### 3.3.2. Resolution and accuracy of the LDV

The sampling volume for each component of flow was formed by the intersection of two circular beams at a half crossing angle of  $3.95^\circ$ ; this had dimensions of maximum diameter =  $0.0905\text{mm}$  and length =  $1.3\text{mm}$ . The position of the sampling volume was fixed, in relation to the location and orientation of the optic head (Section 3.3.1). However, the refractive index of water is greater than that of air; hence, a small motion of the optic head in the cross flume direction,  $\Delta y$ , caused an actual displacement of the sampling volume in the water  $\approx 1.3\Delta y$ . This effect was taken into account, when performing traverse motions in a cross-flume direction.

The mounting of the optic head, on a three-axis traverse, enabled accurate positioning of the optic head; hence, the sampling volume, over the full height and practically the full width of the flume. Measurements were not possible within  $2\text{cm}$  of the nearest side wall, due to excessive interference, and outside of  $35\text{cm}$  either side of the main observation area. The absolute resolution and accuracy of the traverse was better than  $0.1\text{mm}$ .

In addition, the optic head could be tilted in a vertical plane, to permit measurement of the vertical component of flow, in regions very near to the bed; this would otherwise be restricted by the relative geometry of the intersecting beams and the bed. Measurements of flow described as being in the vertical plane ( $w$ , perpendicular to the horizontal plane of the oscillating trolley) were, as such, made at an angle of  $5^\circ$  from the vertical, tilted about the  $x$ -axis; hence, the  $w$  component of flow was actually  $[w \cos(5^\circ) + v \sin(5^\circ)]$ . Observations of  $u$  were unaffected. Assuming that velocity fluctuations due to flow caused by plate motion and by turbulent eddies were two-dimensional in the  $x$  and  $z$  plane (i.e.  $v=0$ ), this corresponded to

a consistent 8.7% decrease in  $w$ . This reduction in  $w$  did not significantly affect any of the experiments undertaken in the present study; values of  $\nu$  and  $w$  are either inconsequential under laminar flow conditions (Equation A.6), or are only important in terms of relative amplitude (Section 4.2.4).

## Chapter 4. Experimental Methodology

### 4.1. Velocity profiling

#### 4.1.1. Introduction

Combinations of oscillatory period and stroke length were selected (Table 4.1 and Appendix B), to provide simulations of wind-induced waves (6s period) and larger storm (swell) waves (9s and 12s period) using the oscillating trolley equipment in Southampton (Section 3.2).

Differences in stroke length were used to simulate variations in the orbital amplitude, representative of a range of theoretical water depth and wave height combinations.

Theoretical combinations of wave height and water depth for selected experiments, derived on the basis of small amplitude wave theory, are shown in Figure 4.1. Similar combinations of period and stroke length were used for the non-linear experiments, together with a superimposed asymmetry of  $R=0.55$ ,  $0.6$  or  $0.7$ . The range of  $R$  selected for these experiments was not designed to represent specific theoretical conditions; rather, values were selected to test the robustness of the laminar flow field model. Flows were simulated over the smooth bed and two fixed-roughness beds, as described in Section 3.2.7.

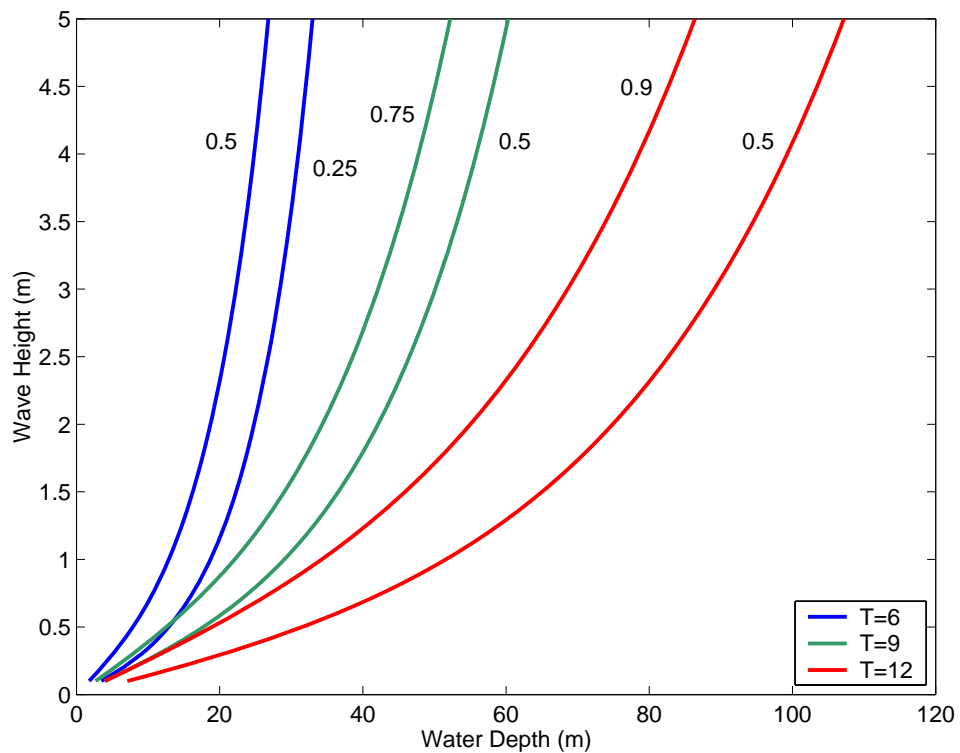


Figure 4.1. Theoretical combinations of wave height and water depth relating to the simulated conditions listed in Table 4.1 ( $R=0.5$ ). The values were derived on the basis of linear wave theory. Note: the text labelling indicates the stroke length (m).

Bed type	$R=0.5$	$R=0.55$	$R=0.6$	$R=0.7$
Smooth	6s (25, 50cm) <sup>1</sup> 9s (50, 75cm) <sup>1</sup> 12s (50, 90cm) <sup>1</sup>		6s (50cm) <sup>1</sup> 9s (50cm) <sup>1</sup> 12s (50cm) <sup>1</sup>	9s (50cm) <sup>1</sup>
275 $\mu$ m	6s (25, 50cm) <sup>2</sup> 9s (50, 75cm) <sup>2</sup> 12s (50, 90cm) <sup>2</sup>	9s (50cm) <sup>2</sup> 12s (50cm) <sup>2</sup>	6s (50cm) <sup>2</sup> 9s (50cm) <sup>2</sup> 12s (50cm) <sup>2</sup>	
500 $\mu$ m	6s (25 <sup>2</sup> , 50cm <sup>2,3</sup> ) 9s (50, 75cm) <sup>2,3</sup> 12s (50, 90cm) <sup>2,3</sup>	9s (50cm) <sup>2</sup> 12s (50cm) <sup>2</sup>	6s (50cm) <sup>2</sup> 9s (50cm) <sup>2</sup> 12s (50cm) <sup>2</sup>	

Table 4.1. Summary of the velocity profiles measured (wave period and stroke length). Key: (1), high-resolution data set; (2), low-resolution data set; (3), medium-resolution data set. (see also, Section 4.1.2 and Appendix B).

#### 4.1.2. General methodology

Oscillatory flows were simulated using the oscillating trolley equipment described in Section 3.2. Coincident time-series of the horizontal ( $u$ ) and vertical ( $w$ ) components of velocity were measured in a vertical profile, using the LDV system described in Section 3.3. Measurements were obtained at 200Hz for 2 min duration at each of the heights. The phase referencing of individual velocity time-series, relative to the plate motion, was undertaken manually at the time of data collection. This operation was achieved by the operator initiating data collection at the point of plate reversal. Automation of this operation was not possible, due to limitations of the LDV equipment, i.e. the system did not support an external trigger to initiate data collection.

In total, 42 velocity profiles were obtained: 10 over a smooth bed; 11 over the 275 $\mu$ m fixed roughness bed; and 21 over the 550 $\mu$ m fixed roughness bed. All of the smooth bed profiles were collected at ‘high-resolution’, where measurements were obtained at 50 positions above the bed. Depending upon the (wave) period, 32-38 of these measurements were obtained within the boundary layer. In addition, 5 of the 550 $\mu$ m profiles were collected at ‘medium-resolution’ where measurements were obtained at 32 positions above the bed. Depending upon the period, 23-26 of these measurements were made within the boundary layer. Spatial

resolution for all types of measurement was greatest close to the bed; this was reduced progressively with height above the bed. However, the ‘high-‘ and ‘medium-resolution’ data sets required some considerable time for their collection and exhibited important phase lag errors (described in more detail in Section 5.5) due to the methodology; as such, they had no significant advantage over data collected at a lower resolution. Hence, subsequent investigations utilised a ‘low-resolution’ profile, measuring at only 14 heights above the bed; 9-10 of these were within the boundary layer. In order to further improve experimental efficiency, phase referencing of the time-series for measurement of phase lag was discontinued in the ‘low-resolution’ experiments. The precise locations of measurements made using high-, medium- or low-resolution profiles are listed in Table B.3.

#### *4.1.3. Data analysis*

The velocity time-series in each of the experiments were analysed; this was to derive a single representative (mean) velocity cycle, at each of the heights above the bed. Using the oscillatory period for the observed flow conditions, together with the sampling frequency (200Hz), the full length time-series were bin-averaged; the bin width was defined as  $T/100$ . Corresponding bins (phases), within each wave period, were then averaged (mean of bins [1, 101, 201, 301... etc.]), to generate a single representative wave cycle, 100 values in length. Within the ‘high-‘ and ‘medium-resolution’ data sets, all of the resulting velocity cycles were phase-referenced, relative to the plate motion (and to each other, see Section 4.1.2). On the basis of improving experimental efficiency, data collection was undertaken continuously, without pause between the time-series. Hence, the ‘low-resolution’ observations were not phase-referenced.

In addition to the horizontal time series, the phase-referenced data could be analysed further in order to yield: a time-series of vertical velocity profiles; vertical profiles of phase lag; and vertical profiles of velocity amplitude. The non-phase referenced data could be analysed to yield only vertical profiles of velocity amplitude. These data were compared subsequently with the theoretical distribution, as predicted by Eq. 2.14.

## **4.2. Transition to turbulence**

### *4.2.1. Introduction*

A broad range of oscillatory parameters was simulated over the three prepared beds, as described in Section 3.2.7 (one hydraulically smooth bed surface; together with two of fixed

---

granular roughness,  $D=275\mu\text{m}$  and  $550\mu\text{m}$ ); a full list of the conditions simulated can be found in Appendix B. The flow variable combinations of  $T$ ,  $R$  and  $S$  simulated were in the same range as, and were representative of, those used later in the observation of the threshold of sediment motion (Chapter 7). In addition, the combinations were comparable to those used by other major contributors to the field of transition to turbulence included herein (Li, 1954; Manohar, 1955; Vincent 1957; Lhermitte, 1958; and Tanaka *et al.*, 2000) (Section 7.1).

Oscillatory flows were simulated using the oscillating trolley equipment described in Section 3.2. The hydrodynamic conditions were observed and interpreted subsequently using three methods, namely: ‘visual observation’; ‘velocity time-series’; and ‘turbulent intensity’ (Sections 4.2.3, 4.2.4 and 4.2.5, respectively).

#### *4.2.2. General methodology*

The oscillatory period and degree of asymmetry were set (over one of the artificially prepared beds); these then remained constant throughout the experimental run. Initial stroke lengths were determined on the basis of relationships proposed previously (Sleath, 1984); these were such that initial conditions would be within the laminar flow regime, but close to the point of transition. The initial flow conditions were confirmed as being laminar, either by visual observation (for the visual observation method), or by inspection of the initial velocity time-series (for the velocity time-series and turbulent intensity methods, described below).

During each experimental run, the stroke length was increased incrementally, by between 1-2cm (corresponding to an increase of  $\sim 1\text{cm s}^{-1}$  in velocity amplitude), until the ‘transition to turbulence’ occurred. At least three further increments and observations were undertaken, beyond the first signs of transition occurring. At each of the stroke lengths, the flow was allowed to adjust over three full oscillatory cycles, prior to observations being made or to the initiation of the data collection. For the ‘velocity time-series’ and ‘turbulent intensity’ methods, flow velocity measurements were undertaken at a height of 3mm above the bed, over 1 min, following each stroke length increment and allowing time for flow adjustment. A minimum of six time-series were collected, during each of the experiments.

#### *4.2.3. Visual observation method*

Visual observations of the transition to turbulence were performed by initially placing a small crystal of potassium permanganate on the central part of the oscillating plate. Under laminar flow conditions, a ‘stable’, longitudinal streak of dye was formed close to the bed,

---

i.e. initial dye dispersion from the streak was by molecular diffusion processes only. As the flow (stroke and/or velocity) amplitude was increased, instability waves were observed to develop at the top of the dye streak. Latterly, tongues of dye were ejected from within the boundary layer at the point of flow deceleration and reversal; these became more regular and widespread with further incremental increases in the flow amplitude. Immediately following this condition, eddy diffusion processes dispersed the dye streak rapidly. The observation of this dispersion was designated as the transition to turbulence. The progressions of such instability events under oscillatory flows have been described previously elsewhere (e.g. Bagnold, 1949, Li, 1954; Vincent, 1957; George and Sleath, 1978).

#### *4.2.4. Velocity time-series method*

The measured time-series of the horizontal ( $u$ ) and vertical ( $w$ ) components of velocity, corresponding to laminar flow, appeared as a smooth harmonic signal (Figure 4.2a) and as a small-amplitude (uniform variability) signal within a narrow envelope ( $\pm 0.005\text{ms}^{-1}$ ) (Figure 4.2b), respectively. These observations were in accordance with laminar flow theory (Appendix A). As the flow was increased, the signal began to deviate from the laminar solution. Both components of velocity exhibited evidence of high-frequency fluctuations ( $\pm 0.05\text{ms}^{-1}$ ) (Figure 4.2c&d); these were attributed to the periodic ejection of eddies, from within the boundary layer. Such a condition was designated as the ‘point of transition’; as such, it is consistent with the ‘visual observation’ method (Section 4.2.3). The transition occurred, typically, over a narrow range of velocity amplitudes ( $1\text{-}2\text{cms}^{-1}$ ).

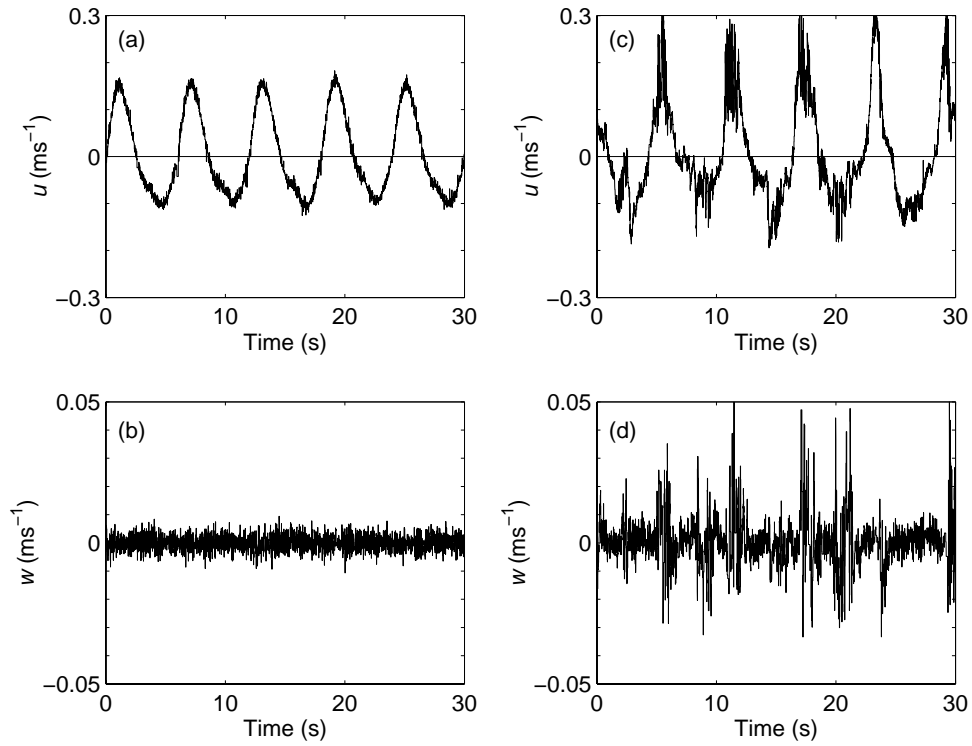


Figure 4.2. Recorded velocity time-series, corresponding to: (a) & (b) laminar (stroke length = 66cm, and  $RE = 573$ ); and, (c) & (d) transitional/turbulent, (stroke length = 82cm, and  $RE = 712$ ) flows, over a smooth bed ( $T = 6\text{s}$ ,  $R=0.6$ ,  $z=3\text{mm}$ ).

#### 4.2.5. Turbulent intensity method.

Using the measured velocity data (Section 4.2.2), the vertical component of the turbulent intensity,  $E$ , was calculated for each time-series, using,

$$E = \overline{\rho w'^2} \quad \text{Eq. 4.1}$$

where,  $\rho$  is the density of the fluid and  $w'$  is the fluctuating component of  $w$ . The horizontal component of velocity,  $u$ , was not utilised as the mean of the fluctuating component varies with asymmetry, even in the case of pure laminar flow, and would therefore present additional unnecessary complication.  $E$  was plotted then against stroke length, for each combination of bed type, oscillating period and asymmetry. A particular case [ $D=275\mu\text{m}$ ,  $T=6\text{s}$  and  $R=0.55$ ] is presented as an example of this approach, in Figure 4.3.

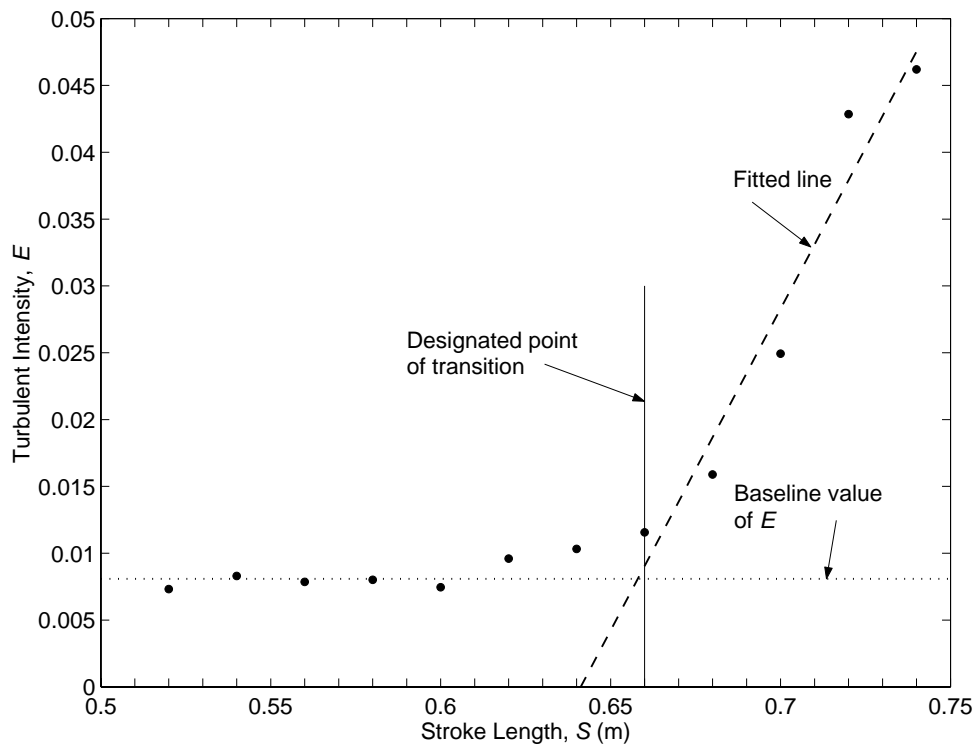


Figure 4.3. Turbulent intensity,  $E$ , at  $z=3\text{mm}$ , with increasing stroke length, demonstrating the transition to turbulence. ( $D=275\mu\text{m}$ ,  $T=6\text{s}$  and  $R=0.55$ ).

The computed value of  $E$ , derived from the experimental runs, was observed to remain constant (a ‘baseline value’, with only slight variability) until increasing suddenly. A straight line was fitted to those data exhibiting elevated  $E$  (taken as where,  $E > \text{baseline value} + 0.005$ ). The ‘critical’ stroke length, corresponding to the transition to turbulence, was defined as the point where the fitted curve increased by more than 0.005 units, above the mean baseline value of  $E$ , observed during each of the experiments. The critical stroke length was expressed to the nearest centimetre. This method was consistent with the observation of ‘significant eddy formation’, as used in the visual observation and velocity time-series methods (Sections 4.2.3 and 4.2.4, respectively).

### 4.3. Threshold of motion

#### 4.3.1. Introduction

A broad range of hydraulic conditions was simulated, using the oscillating trolley equipment (as described in Section 3.2), in order to investigate the effect of asymmetry on the threshold of motion for non-cohesive uniform sands, under oscillatory flow. Thirteen uniform sediments were tested in the present study; these are described in more detail in Section

3.2.6. Depending upon the sediment used, wave periods of between 3-12s and asymmetry values between  $R=0.5-0.7$  were simulated, at varying stroke lengths (up to a maximum of 1m).

Previous researchers, investigating aspects of sediment dynamics under asymmetric oscillatory flows, (e.g. Manohar, 1955; Sato and Horikawa, 1986; Ribberink and Al-Salem, 1994, 1995; and Davies and Li, 1997) used typically, values of  $R$  of between 0.5 and 0.65. Manohar simulated also higher asymmetry values, in some cases up to  $R=0.88$ . However, the equipment used by Manohar utilised a flywheel, where the duration of each half cycle was set independently. Hence, this equipment did not simulate second-order Stokes flows.

#### 4.3.2. *General methodology*

Sub-samples of the sediment were wetted initially with tap water, in a suitable container; these were subsequently ‘poured’, underwater, into a conical pile, at the cross-flume mid-point of the oscillating plate and beneath the access gap in the flow baffles. A shaping tool, made of a rectangular piece of sheet aluminium with straight edges was used to shape the sediment patch. ‘Spacer’ wedges, at either end of the shaping tool and constructed of multiple layers of tape, were used to hold the tool at a fixed height above the bed. The tool was drawn smoothly and gradually over the sediment. The resulting ellipsoid or teardrop-shaped patch measured approximately 25cm long ( $x$ -axis), 15cm wide ( $y$ -axis), and 3mm deep (providing  $>3$  layers of mobile grain-on-grain contact, in most of the experiments). Due to the method, a small step was formed initially around the edges of the patch; this step became tapered rapidly, during the first two plate oscillations.

Once the equipment and sediment were prepared, an initial oscillatory flow was applied, with given parameters of oscillatory period and asymmetry. An initial value of  $U_1$  was selected, such that conditions were close to, but below, the threshold of motion of the sediment sample. The hydraulics control software was modified to include a remote dial, adjacent to the flume; this allowed the operator to manually increase  $U_1$ , whilst maintaining continuous and close visual observation of the sediment sample. Although the input was essentially analogue,  $U_1$  was incremented by approximately  $1\text{cm s}^{-1}$  at the end of each of the wave cycles in the early stages of each of the experiments; latterly, once every three wave cycles in anticipation of threshold. Once the point of threshold was observed (Section 4.3.3), the operator observed the: critical stroke length; water temperature; and orbital diameter of parasitic flows in the upper water column.  $U_1$  was then reduced by around  $2\text{cm s}^{-1}$ , or until initial motion had ceased; following this,  $U_1$  was, once again, increased slowly and by a

---

similar amount, to confirm that the previously noted values corresponded actually to the threshold of motion, i.e. rather than grain motion affected by the pattern of flow increase. The experiment was deemed to be finished, either: (a) when threshold conditions had been observed and confirmed (using the method described above); or (b) if significant disturbance of the mobile sediment surface was observed, necessitating the resetting of the sediment patch.

During the experiments, the sediment patch became gradually dispersed, or distorted, by: (i) sediment transport of ‘vulnerable’ grains on the margins of the patch, either located on the side slope or not resting on a bed of similar grains; and (ii) the development of small bedforms which, once initiated, were enlarged rapidly and caused localised scouring of the sediment. Hence, the sediment was recollected, supplemented (if necessary) and reshaped (using the method described above), before and/or (if required) during, each new experiment.

Initially, the 275 $\mu$ m fixed roughness bed was used as the plate surface, but osmosis blistering of the glue began to cause significant rippling of the bed; latterly, the hydraulically smooth bed was used. Since the experiments were being undertaken preferably under laminar or near-laminar conditions, the relative roughness of the surrounding bed was unimportant; this was provided that the bed was sufficiently smooth so as not to cause transition to turbulence, at lesser flows than required by the sediment patch.

#### *4.3.3. Definition of threshold*

Throughout the present study, the Yalin Criterion (Section 2.12.2) was used to provide a quantifiable (visual) definition for the threshold of motion; this was expressed in terms of a critical number of grains in motion per unit area, per unit time. However, in practice, sediment motion was observed rarely to be uniform across the sediment surface; rather, to exhibit a sudden transition between a state of ‘zero’ grain motion and one of the conditions outlined below.

- (i) *Bursts of multiple grain motion in an ellipsoid area with the long-axis orientated flow parallel; this was approximately 2.5cm long, 1.5cm wide, incorporating all of the surface grains in that area.* Typically, between 2-3 such bursts occurred during one half cycle (the erosive half cycle, in the case of asymmetric flows). Based upon analysis of video footage (Section 7.5), under such conditions, grains are transported in traction mode (as bedload). Once initiated, this erosive process appeared to be augmented locally by ‘ballistic momentum flux’ (BMF), a grain impact force

(described in more detail in Section 4.4.6). These sediment burst events occurred typically, approximately 0.5-1.5s ( $20^{\circ}$ - $40^{\circ}$ ) after the peak in the fluid shear stress. It is suggested that this type of grain motion is initiated either by: localised unstable patches of sediment; or, by localised turbulent downward burst events, brought about by slight (and unavoidable) undulations in the fixed bed, or, in the mobile bed geometry following short durations of exposure to the flow.

- (ii) *'General bed motion', in excess of that established on the basis of the Yalin Criterion.* Based upon analysis of video footage, this type of grain motion was initiated typically at the point of flow reversal; it ceased at around the same point as the 'burst-type' event, as described in (i) above. Transport was dominantly as bedload, with some limited saltation during the high-energy portions of the wave cycle; as such, erosive processes were augmented by BMF. It is suggested that relatively large acceleration forces, caused by the motion of the trolley, can initiate this type of bed motion at below critical fluid shear amplitudes (see Section 4.4.4, for a discussion of acceleration forces). Once initiated, this motion is perpetuated then by fluid shear.
- (iii) *Limited uniform motion in quantities comparable to that calculated by the Yalin Criterion:* Based upon analysis of video footage, this motion was initiated typically around or soon after the peak in shear stress (according to laminar theory); it ceased at around the same point as the events described in (i) and (ii), above. Transport was dominantly as bedload. It is suggested that fluid shear forces (rather than acceleration or burst like events) at the bed dominate this type of grain motion.

Observations of threshold, undertaken during the present study, were typically some combination of the three conditions described above. However, condition (iii), in conjunction with the Yalin Criterion, was upheld as the preferred condition within the context of the definition of threshold; this was observed as the main mode of threshold, in the majority of cases.

Under condition (i), burst events tended to be restricted to certain areas of the sediment patch; the location of these areas was, typically, similar between wave cycles. As such, these areas and other parts of the bed immediately downstream were excluded from the area being considered by the operator. The experiment was continued until threshold, as defined by condition (iii), was achieved over the remaining area.

If condition (ii) dominated, it was decided that a dual set of conditions should be met. As the flow amplitude was increased, two phases of sediment erosion were observed at the point of threshold: a primary phase, which corresponded to condition (ii); and a secondary phase of motion, which corresponded to condition (iii). The operator determined visually this dual condition. However, observations made under these conditions were significantly subjective and were influenced by unwanted secondary forces, e.g. acceleration, BMF, etc.

Observations made under condition (ii) were quite rare, occurring during less than 5% of the total. The repeatability of observations under condition (ii), was tested for the case of a single observer; it was shown to be as repeatable as observations made under combinations of conditions (i) and (iii). However, due to the subjective nature of this condition, such observations are less likely to be repeatable between independent observers, without prior collaborative work to standardise the visual criteria for observation.

#### **4.4. Quantities of interest**

The quantities of interest, whilst investigating the threshold of motion for sediment using an oscillating trolley, include: the angle of repose; fluid velocity amplitude outside the boundary layer; the fluid shear stress at the bed; and the acceleration, or inertial forces, imparted to the grains by the motion of the trolley. It is important to quantify these factors, as they will all contribute to the balance of forces acting upon individual grains and hence, the threshold of motion.

##### *4.4.1. Angle of repose*

Mobile, non-cohesive grains at the surface of the prepared sediment patch (as described in Section 3.2.6) are located within a loose matrix of other grains; individual grains are supported by inter-granular contact with the surrounding grains. The angle of contact (with respect to the vertical) between grains will vary greatly, depending upon parameters such as the packing configuration (including porosity), grain shape, bed slope angle and pore fluid pressure gradients that may create additional vertically orientated forces on the grains.

During the present experiments, the pore fluid pressure gradient and bed slope angle were negligible due to the experimental set-up; both were considered to be equal to zero. The mean value of the contact angle, incorporating bed packing and grain shape is termed the angle of repose,  $\phi$ . This value is representative of the ‘angle of initial yield’, or ‘angle of internal friction’ i.e. the angle at which sediment slope failure occurs, as the sample is gradually tilted; this is distinct from the ‘residual angle of shearing’, which describes the

equilibrium slope angle, following slope failure. Results from previous investigations as to the value of  $\phi$ , are discussed elsewhere (e.g. Sleath, 1984). Based upon the wide range of results reported, the value ( $\phi=32^\circ$ ) suggested by Soulsby (1997), for natural sediments in investigations such as those presented here, will be used.

#### 4.4.2. Velocity and stroke amplitude

The velocity amplitude ( $U_c$ ) of the moving plate and therefore of fluid outside of the boundary layer may be calculated directly for the sinusoidal case using

$$U_\infty = \frac{S\pi}{T} \quad \text{Eq. 4.2}$$

In the present study, only  $S$ ,  $T$  and  $R$  were used to record critical flow conditions. In order to calculate  $U_c$  from these parameters for  $R>0.5$ , an iterative model was used in conjunction with

Eq. 3.1. Using values from this model,  $U_c$  may be calculated empirically for  $0.5<R<0.7$  using

$$U_{c,R} = \frac{S\pi}{T} \times (-2.33R^2 + 4.35R - 0.59) \quad \text{Eq. 4.3}$$

[accuracy  $\pm 0.3\%$ ]

or

$$U_{c,R} = \frac{S\pi}{T} \times (1.58R + 0.22) \quad \text{Eq. 4.4}$$

[accuracy  $\pm 1.2\%$ ]

If the stroke length is required and the velocity amplitude and period are the only known parameters (e.g. in the control software), then the above relationships for  $U_c$  may be rearranged easily to provide this particular value.

#### 4.4.3. Fluid shear stress

The fluid shear stress at the bed, under laminar flow conditions, may be calculated directly as,

$$\tau = \mu \left( \frac{\partial u}{\partial z} \right)_{z=0} \quad \text{Eq. 4.5}$$

---

Thus, for simple harmonic flows the bed shear stress over the wave cycle is,

$$\tau = \mu U_0 \beta \sqrt{2} \cos\left(\omega t + \varphi + \frac{\pi}{4}\right) \quad \text{Eq. 4.6}$$

yielding the important quantity of peak shear stress,

$$\tau_0 = \mu U_0 \beta \sqrt{2} \quad \text{Eq. 4.7}$$

Fluid shear stress under asymmetric (laminar) flows may be calculated analytically using Eq. 4.5, by solving the boundary layer velocity equations for a very small value of  $z$ , with axes fixed in the moving plate (Eq. 2.14). The quantity  $\tau_0$  may be calculated also using the wave friction factor,  $f_w$ , where

$$\tau_0 = 0.5 \rho f_w U_c^2 \quad \text{Eq. 4.8}$$

Under laminar flow conditions, second-order Stokes theory yields the following analytical and empirical relationships for the wave friction factor, for sinusoidal and asymmetric flows (associated with the wave crest), respectively,

$$f_w = \frac{c}{\sqrt{\text{Re}}} \quad \text{Eq. 4.9}$$

where,

$$c = 2 \quad \text{for } R = 0.5 \quad \text{or}$$

$$c = -13.38R^3 + 28.00R^2 - 19.58R + 6.46 \quad \text{for } 0.5 < R < 0.8$$

where the asymmetric solution is accurate to  $\pm 0.25\%$ . Solutions for  $f_w$  over smooth beds and under waves in shallow water (water depth  $< 35\text{cm}$ ) were calculated using stream function theory and compared to observed values by Kuo and Chen (1990). Diagrams for the laminar wave friction factor under cnoidal flows may be found in Tanaka, *et al.* (1998). In these references, the degree of asymmetry was expressed in terms of the Ursell parameter ( $\text{Ur} = HL^2/d^2$ ).

---

Under rough turbulent flow conditions (as  $Re \rightarrow \infty$ ),  $f_w$  becomes independent of  $Re$  (see Figure 4.4). Often quoted are the implicit relationships of Jonsson (1966),

$$f_w = \frac{1}{4\sqrt{f_w}} + \log_{10} \frac{1}{4\sqrt{f_w}} = -0.08 + \log_{10} \left( \frac{a}{k_s} \right) \quad \text{Eq. 4.10}$$

where  $k_s$  is the Nikuradse equivalent sand roughness and is taken usually to be  $k_s = 2.5D$  (Soulsby, 1997). Also, the implicit relationship of Kamphuis (1975),

$$f_w = \frac{1}{4\sqrt{f_w}} + \log_{10} \frac{1}{4\sqrt{f_w}} = -0.35 + \frac{4}{3} \log_{10} \left( \frac{a}{k_s} \right) \quad \text{For } a/k_s \geq \sim 5 \quad \text{Eq. 4.11}$$

or

$$f_w = 0.4 \left( \frac{a}{k_s} \right)^{0.75} \quad \text{For } a/k_s \leq 100 \quad \text{Eq. 4.12}$$

The following explicit approximation of Eq. 4.10 was proposed by Swart (1974) and is often used by present day researchers,

$$f_w = 0.00254 \exp \left[ 5.213 \left( \frac{a}{k_s} \right)^{-0.194} \right] \quad \text{For } a/k_s > 1.57 \quad \text{Eq. 4.13}$$

or

$$f_w = 0.3 \quad \text{For } a/k_s \leq 1.57 \quad \text{Eq. 4.14}$$

The relationship of Jonsson (1966) and, hence, that of Swart (1974) are based upon the interpretation of other well known boundary layer equations, rather than observed data. These relationships provided a good visual fit to the data used by Kamphuis (1975), for approximately  $a/k_s < 25$ ; beyond this value,  $f_w$  is slightly overestimated. Soulsby (1997) provided an alternative empirical relationship,

$$f_w = 0.237 \left( \frac{a}{k_s} \right)^{-0.52} \quad \text{For all } a/k_s \quad \text{Eq. 4.15}$$

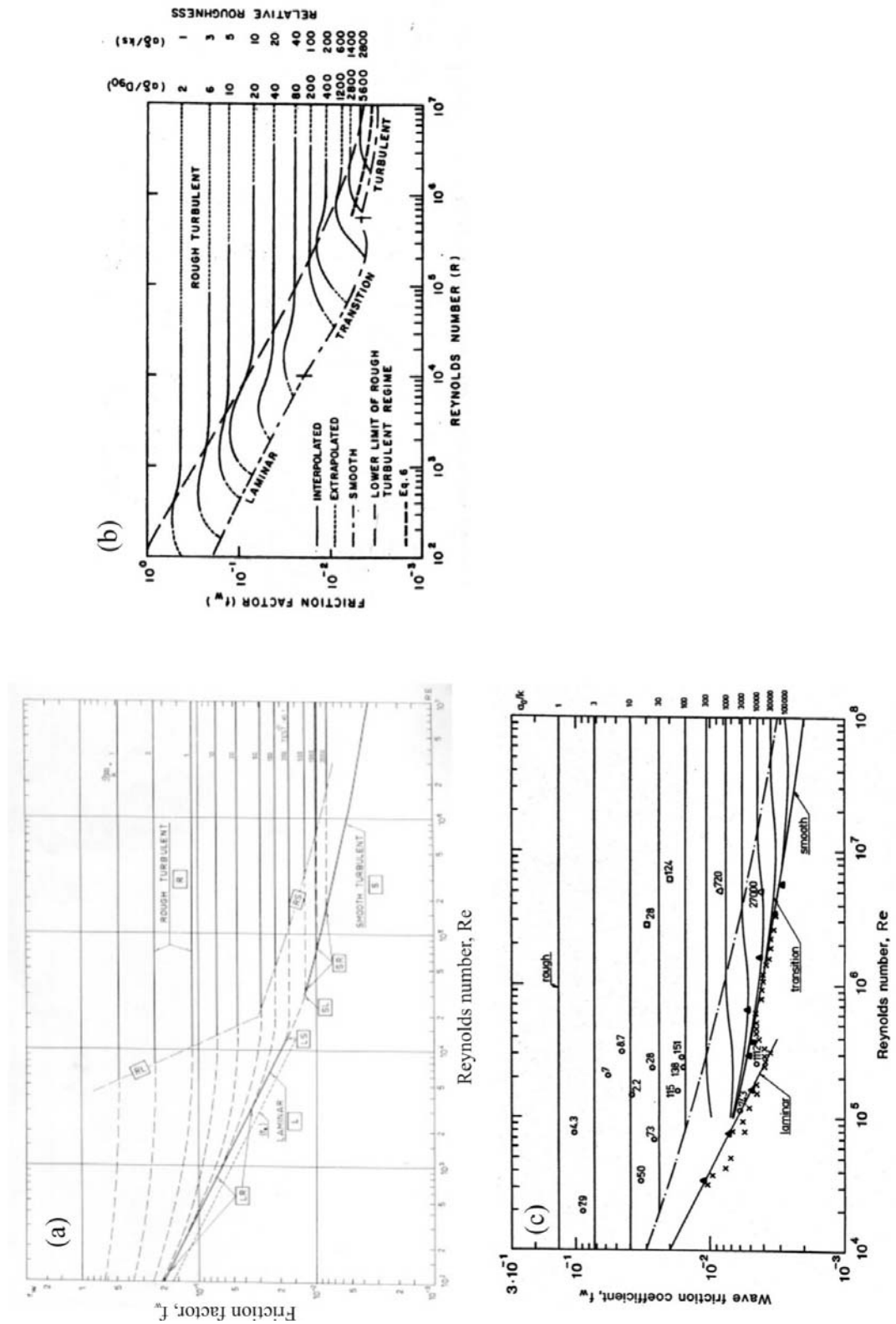


Figure 4.4. Wave friction factor diagrams: (a) Jonnson (1966); (b) Kamphuis (1975); and (c) Myrhaug (1989).

This expression provided the best fit (at the time of publication, 1997) to seven laboratory data sets, five of which became available only following the publication of the relationships of Jonsson (1966) and of Kamphuis (1975). Kamphuis suggested that the lower limit of rough turbulent flow (the smallest value of Re at which rough turbulent solutions apply) lies at approximately

$$\text{Re} = \frac{200}{\sqrt{\frac{f_w}{2} \left( \frac{k_s}{a} \right)}} \quad \text{Eq. 4.16}$$

for  $a/k_s \leq 100$ . For larger values of  $a/k_s$ , the constant in the numerator tends towards 70, which is the value for unidirectional flow. In the rough-transitional region between this limit and the laminar solution and in the smooth-transitional region, the relationship between  $f_w$  and Re was simply ‘estimated’ by Jonsson (1966) and ‘extrapolated’ through gaps in the (‘less ordered’) data by Kamphuis (1975). Myrhaug (1989) provides an explicit solution for the smooth-transitional region, based upon transitional boundary layer theory. In each of these examples, the solution for a given  $a/D$  is extrapolated as a single line; the general form of the extrapolation in each case is shown diagrammatically in Figure 4.4

Relationships describing the wave friction factor over smooth turbulent flows may also be found in the references described above. Often used is the relationship of Kajiura (1968),

$$\frac{1}{8.1\sqrt{f_w}} + \log \frac{1}{\sqrt{f_w}} = -0.135 + \log \sqrt{\text{Re}} \quad \text{Eq. 4.17}$$

Most recently, Le Roux (2003) describes a new method by which  $f_w$  can be calculated using the unidirectional shields parameter. This is intended to reduce the uncertainty surrounding parameters such as the boundary layer thickness or  $k_s$ . This method is not presented here, due to concerns raised by the present study about the transfer of the Shields type analysis to oscillatory flows (Chapter 7).

Fluid shear stress forces,  $F_\tau$ , acting upon individual grains may be calculated by multiplying the shear stress (essentially a fluid pressure) by the area of effect. Assuming that the shear forces act upon the full cross-sectional area of a spherical grain gives,

$$F_\tau = \text{Area} \times \tau = \pi(0.5D)^2 \times \tau \quad \text{Eq. 4.18}$$

---

Grain area and, hence,  $F_\tau$ , are likely to be overestimated by this method; this is due to the effect of shape and relative grain protrusion, on the area of effect. However, this does enable the investigator to estimate the magnitude of fluid shear forces being experienced by individual grains.

#### 4.4.4. Acceleration of the bed and of mobile grains

Acceleration of the plate and, as such, the mobile grains resting upon it is simply the first derivative of the plate velocity, over time. In the simple harmonic case ( $R=0.5$ ) this becomes,

$$Acc_{(t)} = \frac{\partial u}{\partial t} = -\omega U_1 \sin(\omega t + \varphi) \quad \text{Eq. 4.19}$$

Including second order terms gives

$$Acc_{(t)} = \frac{\partial u}{\partial t} = (-\omega U_1 \sin(\omega t + \varphi_1)) + (-2\omega U_2 \sin(2\omega t + \varphi_2)) \quad \text{Eq. 4.20}$$

Acceleration terms in oscillating trolley experiments are often expressed as a fraction of the gravitational acceleration constant,  $g$  ( $=9.81\text{ms}^{-2}$ ); they refer to the acceleration of the plate and the mobile sediment, as a whole. Hammond and Collins (1979) suggested that for mobile grain studies, such horizontal inertial forces become insignificant in comparison to vertical forces, when the acceleration of the plate and grains is less than an arbitrary value of  $0.05g$ . Based upon numerical arguments, Davies and Wilkinson (1977) proposed that for mobile bed experiments using oscillating trolleys with a sinusoidal motion, acceleration forces would be negligible in proportion to fluid shear forces if

$$0.82D\sqrt{\frac{2\pi}{Tv}} < 1.0 \quad \text{Eq. 4.21}$$

This equation places a limit on the magnitude of the inertial force, in relation to the fluid force. Both of the above relationships were intended for application in experiments undertaken using quartz grains, with sinusoidal flows. However, the acceleration force under asymmetric oscillations may be calculated easily and compared to the limit of Hammond and Collins (1979) as a first approach. The maximum acceleration as a fraction of  $g$  and the result of Eq. 4.21, for all threshold of motion data used in the present study, are plotted in Figure 4.5. The arbitrary value of Hammond and Collins is exceeded in approximately 28%

---

of the cases; the majority of these were part of the asymmetric flow data set and/or associated with small wave periods. The limit of Davies and Wilkinson (1977) was exceeded by 18% of the data; however, this was attributed mostly to observations at large grain sizes where, typically, reduced grain density (therefore an effective reduction in inertial forces) is not accounted for by the relationship.

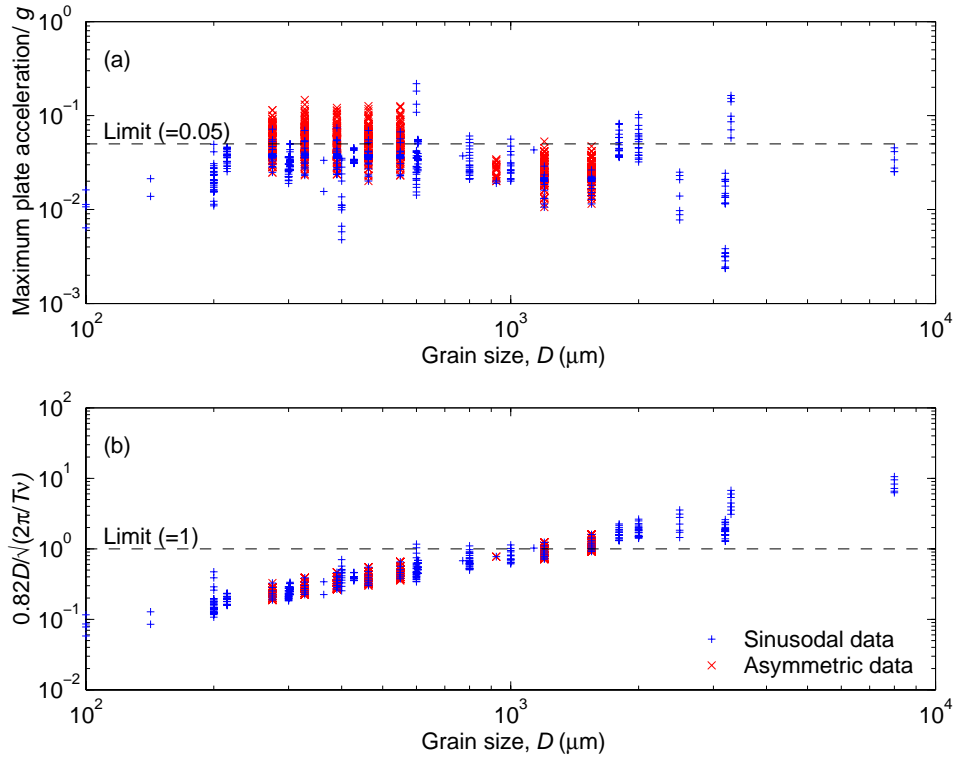


Figure 4.5. Acceleration limits of Hammond and Collins (1979) (a) and Davies and Wilkinson (1977) (b), in comparison to the threshold of motion data used in the present study.

Inertial forces due to acceleration acting upon individual grains may be calculated by Newton's Second Law; this, assuming a spherical grain shape, gives,

$$F_{acc} = \text{Mass of grain} \times \text{Acc} = (\rho_s - \rho) \frac{3}{4} \pi (0.5D)^3 \times \text{Acc} \quad \text{Eq. 4.22}$$

Grain mass and, hence,  $F_{acc}$  are likely to be overestimated by this method; this is due to the effect of shape on the volume of grains. However, this does enable the investigator to estimate the magnitude of acceleration forces being experienced by individual grains.

#### 4.4.5. Resistive forces

In the absence of fluid and inertial forces, the grains experience a net vertical (downwards) acceleration due to gravity, this can be resolved into force vectors through the points of contact with other grains. The resistive force experienced by individual grains,  $F_g$ , is calculated using Newton's Second Law,

$$F_g = \text{Mass of grain} \times \text{Acc} = (\rho_s - \rho) \frac{3}{4} \pi (0.5D)^3 \times g \quad \text{Eq. 4.23}$$

Grain mass and, hence,  $F_g$  are likely to be overestimated by this method; this is due once again, to the effect of shape on the volume of grains. However, this does enable the investigator to estimate the magnitude of the resistive forces being experienced by individual grains. This force acts then about the pivoting angle made between adjacent grains, i.e. the angle of repose. The resulting effective resistive force is given by

$$\text{effective } F_g = F_g \tan \phi \quad \text{Eq. 4.24}$$

#### 4.4.6. Ballistic momentum flux

Ballistic momentum flux (BMF) is the additional force transferred to a grain at rest on the bed, as a result of impact from other moving grains. Because grains in motion are likely to be moving in the same direction as the mean flow (hence, in the direction of the fluid shear force), the BMF tends to act as an erosive force in conjunction with the flow. The effective destabilising force transferred directly to the impacted grain depends upon the momentum and angle of attack of the moving grain; energy will be transferred also to grains surrounding those impacted, by inter-granular contact. Therefore, the actual destabilising force (as a result of the BMF) is a complex quantity and is not easily represented mathematically. Investigations into the mechanisms and importance of BMF have been undertaken in relation to both non-cohesive (e.g. Bagnold, 1936, 1966; Abbot and Francis, 1977; Leeder, 1979) and mixtures of cohesive and non-cohesive sediments (e.g. Amos *et al.*, 1998).

### 4.5. Phase and duration of sediment motion

In a separate investigation as part of the present study, the phase of the onset of sediment motion (at the threshold of motion condition), together with the duration of the subsequent motion, were measured. Observations were made for quartz grains ( $D=550\mu\text{m}$  and  $250\mu\text{m}$ ), over a range of wave periods [ $T=4,5,6,7\text{s}$ ] and degrees of asymmetry [ $R=0.5, 0.6, 0.7$ ]. The

---

observations made under asymmetric flows were made only during the positive flow half cycle. Sediment samples were brought to the threshold of motion using the methodology described in Section 4.3.2. Visual recordings of sediment motion were made using the digital video camera, mounted on a moving bracket outside of the flume. The bracket was attached in such a way that the motion of the camera was equal and simultaneous to that of the plate; this permitted a static view of the mobile bed, throughout the oscillatory cycle. Video recording was made of at least 5 full oscillatory cycles, during each experiment.

The video data were interpreted subsequently visually, using the threshold criteria described in Section 4.3.3. The slow play function of the digital camera allowed the user to accurately define the initiation and cessation of sediment movement. The time-resolution of the video record was 1/25s and the time stamp (including the sub-second frame number) was visible on the monitor, during video analysis. A minimum of three observations were made for each experiment. Observations of the time of sediment motion were then made relative to the phase of plate motion, hence other related fluid parameters ( $U_c$  and  $\tau_c$ ), by establishing visually the time reference of zero plate motion at either end of the plate motion half cycle.

## Chapter 5. Velocity Profiling

### 5.1. Introduction

Time-series measurements of velocity were undertaken in a vertical profile, over a wide range of flow conditions, as described in Section 4.1. These measurements provided observational data, for comparison with the laminar flow model described in Sections 2.4 and 2.5. Comparisons were made in order to determine the validity and accuracy of the model and the equipment, in predicting and simulating such flows, throughout the oscillatory cycle and for known wave parameters. The potential effects of secondary flows, in the overlying body of relatively still water, were also considered. A number of theoretical (numerical) studies were undertaken, to quantify the direct effect of asymmetry within the boundary layer. Likewise, to assess the importance of additional higher harmonics, as might be found in wave channels or in the field.

### 5.2. Results: The outer layer

#### *5.2.1. The form of outer layer oscillations*

The laminar boundary layer theory of Schlichting (1968) makes the assumption that the fluid remains still, in regions far from the plate surface ( $z \gg \delta_{0.99}$ ). However, it has been noted by all previous users of oscillating trolley equipment, that it is difficult to reduce (and almost impossible to avoid) the presence of a ‘parasitic’ resonant oscillation, or wave, within the tank. This condition caused (limited) deviation between the observed and predicted results, in areas outside and, to some extent, inside the boundary layer (Section 5.4.1).

During the collection of the smooth bed data in the present study, simple porous mats were used in conjunction with solid plates to dampen resonant oscillations within the tank. Despite these adopted measures, parasitic oscillations were observed to develop during flow simulations; the amplitude and form of which varied with combinations of period and stroke length (Tables B.1 and B.2).

A number of sample time-series from the outer region are shown in Figure 5.1. These flows can be described closely by a simple first-order harmonic (sinusoidal) pattern, for oscillatory periods of  $T=6s$  and  $12s$ . These periods coincide with multiples of the estimated resonant frequency of free oscillation within the tank ( $\approx 6s$ ). A second harmonic of significant amplitude is observed also in the  $T=9s$  example; this suggests that energy is being transmitted to higher harmonics, in non-resonant modes of oscillation. Due to time

---

limitations on the duration of availability of the LDV equipment (on loan from the EPSRC), data were not collected at other intermediate periods (e.g.  $T=7s$  or  $8s$ ), to establish the harmonic content in these cases.

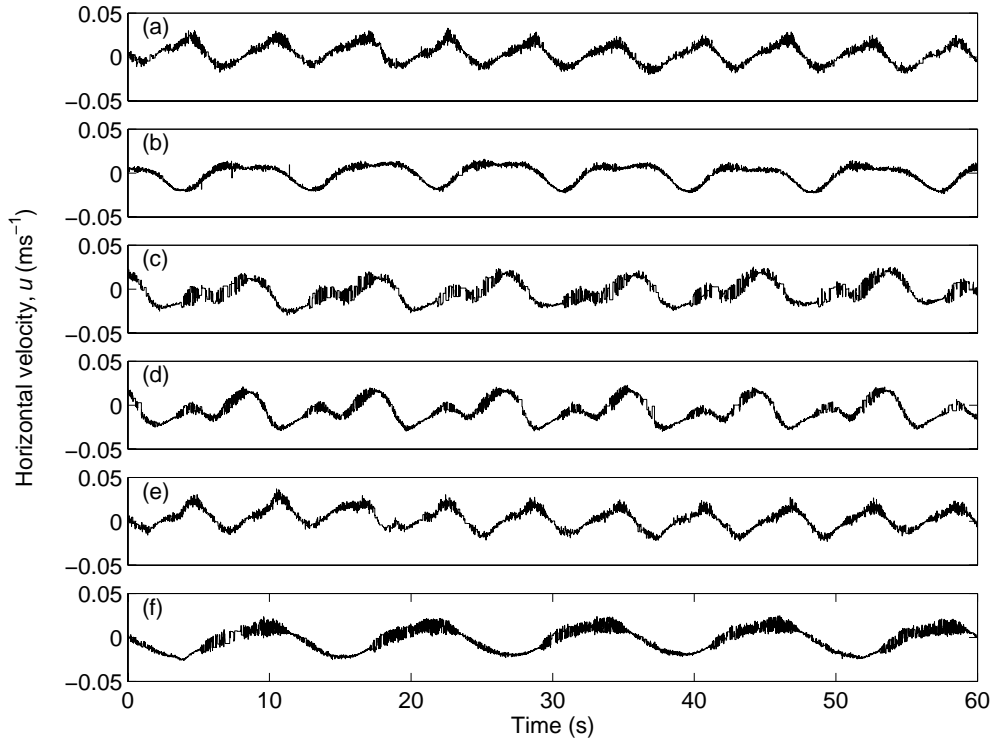


Figure 5.1. Representative time-series of velocity outside the boundary layer ( $z=20\text{mm}$ ), illustrating the presence of the ‘parasitic’ oscillatory flow for: (a) [ $T=9s$ ,  $S=0.5m$ ,  $R=0.5$ ]; (b) [ $T=9s$ ,  $S=0.75m$ ,  $R=0.5$ ]; (c) [ $T=9s$ ,  $S=0.5m$ ,  $R=0.6$ ]; (d) [ $T=9s$ ,  $S=0.5m$ ,  $R=0.7$ ]; (e) [ $T=6s$ ,  $S=0.5m$ ,  $R=0.6$ ]; and (f) [ $T=12s$ ,  $S=0.5m$ ,  $R=0.6$ ].

The amplitude of the first and second harmonics of parasitic oscillation were measured using Fourier analysis, for all of the velocity profiling experiments (Figure 5.2 (a) & (b)). The phase lag of the first two harmonics were also measured, for the 10 phase-referenced velocity profiling experiments (Figure 5.2 (c) & (d)). The value presented for each condition is the mean value for all time-series outside of the boundary layer, this reduces the effect of ‘erroneous phase referencing’. Erroneous phase referencing is caused when the investigator is consistently slightly late or early, when initiating data collection with the LDV. When the resulting data sets are assembled vertically, the phase is then offset at several heights. This causes an apparent deviation from the expected value; this persists throughout the wave cycle.

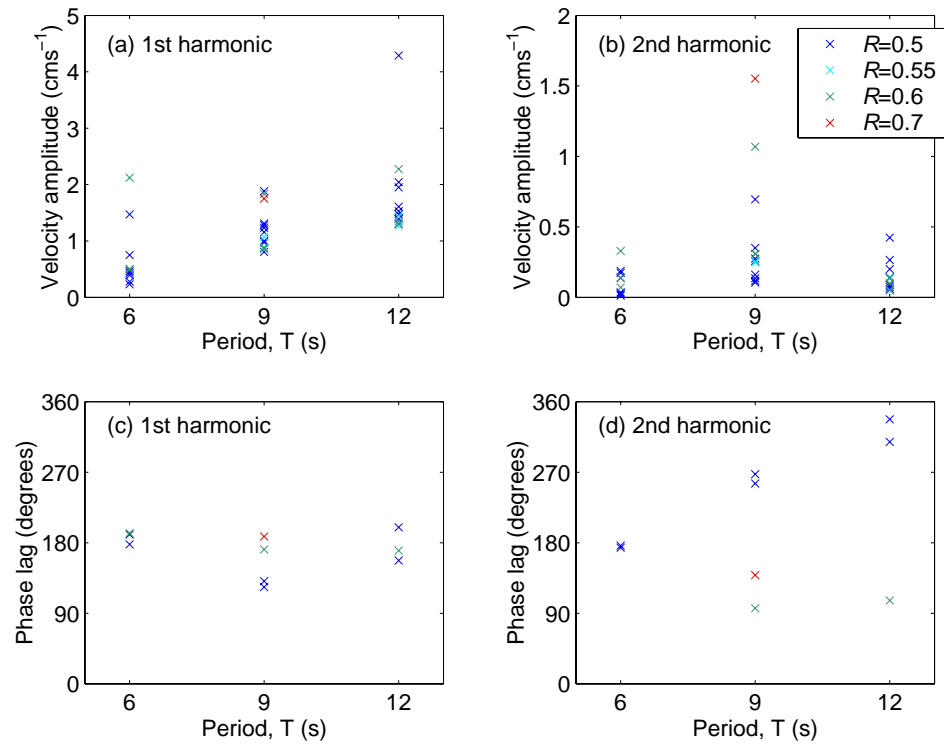


Figure 5.2. Outer layer (parasitic) oscillatory flows: velocity amplitude (a) & (b); and phase lag (c) & (d), of the principle and second harmonics, respectively.

In the early (smooth bed) cases, the mean amplitude of the principle harmonic of oscillation was  $1.6\text{cm s}^{-1}$ ,  $2.0\text{cm s}^{-1}$  and  $2.8\text{cm s}^{-1}$  (6.3%, 7.5% and 15.6% of  $U_\infty$ ) for  $T=6\text{s}$ ,  $9\text{s}$  and  $12\text{s}$ , respectively. However, higher values of up to  $4.0\text{cm s}^{-1}$  (16.9% of  $U_\infty$ ) were also observed. The flow baffles were redesigned subsequently, prior to the ‘rough bed’ experiments; this was to reduce the absolute amplitude of the parasitic oscillation. Errors due to parasitic oscillations, in these cases, typically did not then exceed  $0.6\text{cm s}^{-1}$ ,  $1.3\text{cm s}^{-1}$  or  $1.8\text{cm s}^{-1}$  (1.9%, 6.7% and 12.1% of  $U_\infty$ ) for  $T=6\text{s}$ ,  $9\text{s}$  and  $12\text{s}$  respectively. The amplitude and form of the parasitic oscillation was observed to be nearly constant with height outside of the boundary layer, in all cases. The amplitude of the second harmonic is typically of the order  $<0.4\text{cm s}^{-1}$  ( $<1\%$  of  $U_\infty$ ) but becomes slightly larger in some cases (at larger values of  $R$ ) where  $T=9\text{s}$ ; this is greatest in the case of  $[T=9\text{s}, S=50\text{cm}, R=0.7]$ , at  $1.5\text{cm s}^{-1}$  (9% of  $U_\infty$ ).

The phase of the primary harmonics, for the cases of  $T=6\text{s}$  and  $12\text{s}$ , are in the region of  $\varphi_\infty=180^\circ \pm 5^\circ$  and  $\pm 20^\circ$ , respectively. The greatest variability in  $\varphi_\infty$  is observed in cases  $[T=9\text{s}]$ , where  $\varphi_\infty$  was on average lower ( $=160^\circ$ ) and ranged between  $125^\circ$  and  $190^\circ$ .

However, in these cases, the contribution of the higher harmonics was more significant and tended to skew the resultant flow back towards  $\varphi_\infty=180^\circ$ .

An additional low frequency ( $T \approx 60\text{s}$ ) harmonic, of the order of  $1\text{-}2\text{cm s}^{-1}$ , was observed in a few of the outer layer time-series. The vertical coherence of such oscillations could not be easily quantified, due to the inability to phase reference this particular harmonic. This phenomenon may have contributed to the vertical variation in phase lag of the mean (bin-averaged) signal.

### 5.2.2. Comparison with the model

The combined use of flow baffles, together with the extended theory (Section A.3), has resulted in good general correlation, in all cases, between the observed and predicted velocity for the region outside the boundary layer. When the extended solution by Du Toit and Sleath (1981) was applied to the phase-referenced velocity profile data, errors unaccounted for by the model in the outer layer were reduced to less than  $0.5\text{cm s}^{-1}$ , i.e. less than 3% of  $U_{\infty}$ , in all cases. Residual deviation from the predicted velocity, for measurement axes in the still water, was consistent with erroneous phase offset, of up to  $\pm 30^\circ$  from that predicted, between adjacent time-series.

## 5.3. Discussion: The outer layer

On the basis that the dominant phase of flow in the upper layer was  $180^\circ$  out of phase with the motion of the plate, together with the information that the velocity amplitude is constant with height in the tank, it is suggested that the parasitic oscillation is dominated by a gravity current, i.e. rather than a progressive or standing free surface gravity wave. This current is driven by the water slope, induced by periodic vertical displacement of the water surface by the moving plate. Provided that the assumption of laminar flow is valid and the flow at the upper edge of the boundary layer is known, the resulting velocity field within the boundary layer is the same, in either case.

For the purposes of velocity profile data analysis undertaken in the present study, the outer layer flow may be expressed adequately by the summation of two harmonic components. In the case of phase-referenced time-series, Fourier analysis was used to obtain the velocity amplitudes and phases (relative to the plate motion); by taking mean values over a number of heights, the error attributed to erroneous phase-referencing was reduced. In the case of non-phase referenced time-series, only the amplitude of the two harmonics and their phase, relative to each other, may be calculated using this method. On the basis of an analysis of the phase referenced data, the phase of the primary harmonic is best represented by a value of

---

180° and the phase of the second harmonic by either 90° or 270° (a visual or numerical test should be performed to determine the most appropriate value).

Based upon numerous observations of the outer layer orbital amplitude, during threshold of motion experiments, the outer layer flow can be estimated using a simplified model; this assumes that the principle harmonic is dominant, discarding the second harmonic component. If the orbital diameter in the outer layer,  $S_\infty$  is known, then the velocity amplitude may be calculated directly, using,  $U_\infty = S_\infty \pi / T$ . If the orbital diameter is not known, then an estimate of  $U_\infty$  in the outer layer may be made using the following relationships:

$$\begin{aligned} \text{for } T \leq 7 \quad S_\infty &= 0.01m & U_\infty &= [-0.0012T + 0.013]ms^{-1} \\ \text{for } 8 \leq T \leq 12 \quad S_\infty &= [0.024T - 0.182]m & U_\infty &= [0.0055T - 0.0406]ms^{-1} \end{aligned}$$

Eq. 5.1

The phase lag in both cases was assumed to be 180° ( $\pi$  rad). The use of the above model, instead of observed  $S_\infty$ , produced error in the calculated  $\tau_0$  of the order of 0.025% (within the range of experimental parameters investigated in the present study). If the outer layer is excluded altogether from the calculation of  $\tau_0$  ( $S_\infty=0$ ), the predicted value is 1-4% larger (mean value 1.7%) for  $T \leq 8s$  and 2-12% larger (mean value 6.8%) for  $9s < T < 12s$ ; these include the full range of asymmetry, simulated as part of the present study.

## 5.4. Results: The inner layer

### 5.4.1. Comparison with the model

Incorporating the outer flow model developed in Section 5.3, theoretical vertical profiles of velocity amplitude, phase lag (for phase-referenced experiments) and instantaneous velocity were calculated from the model; these were compared to the observed data, for the regions within the boundary layer ( $z < \delta_{0.99}$ ). For the high-resolution profiles, the phase of the observed data was maintained ‘as observed’, i.e. from the methodology,  $t=0$  in the observed velocity time-series corresponded to a known phase of the plate (and hence, outer layer) motion and this information was preserved throughout the data processing. For the purposes of comparison, the phase lag of individual time-series was fitted to that of the modelled data before analysis of the low-resolution profile data. Figure 5.3 provides an example of the

---

form and visual fit between the observed and predicted data sets, for sinusoidal and asymmetric oscillations, under laminar flow conditions (high-resolution profiles).

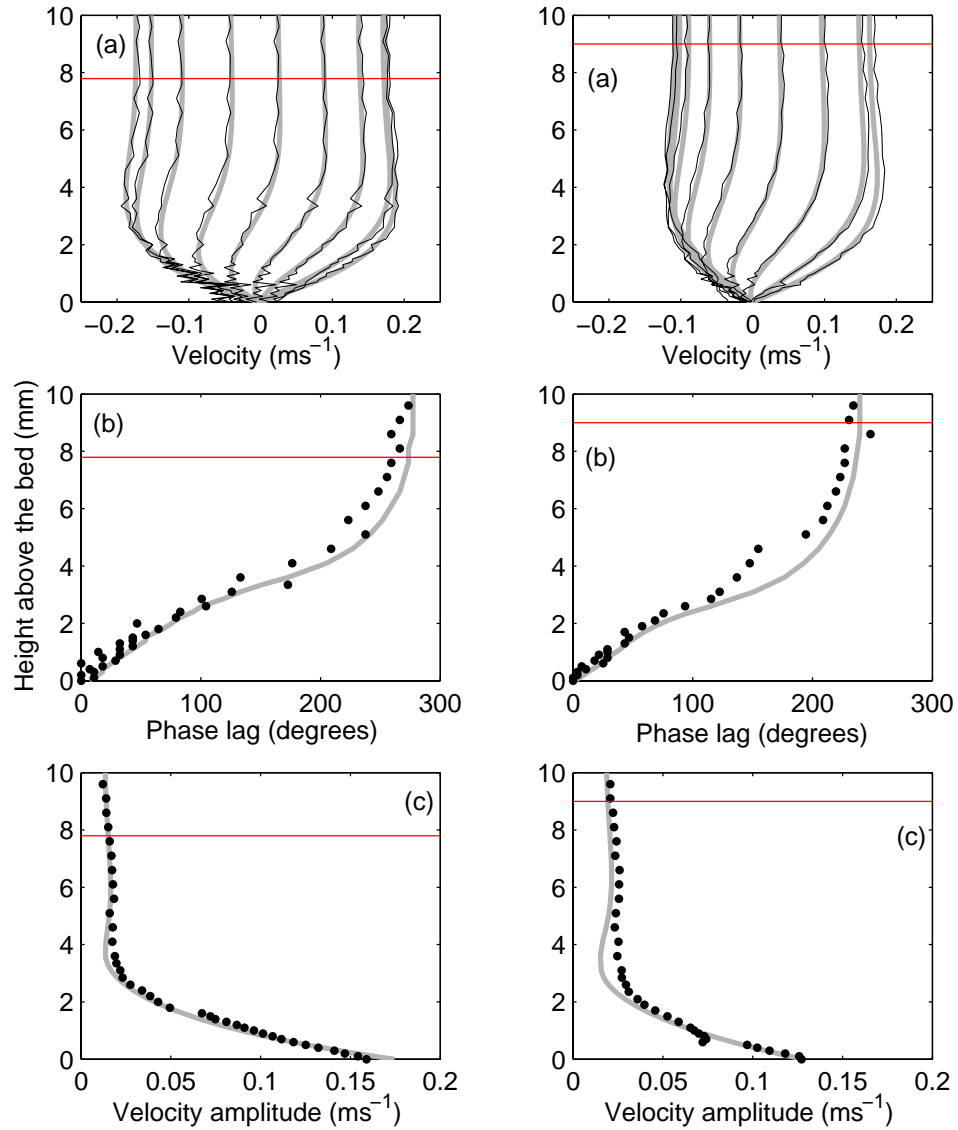


Figure 5.3. Flow structure of the outer flow and the boundary layer, for oscillation of  $[T=9\text{s}, S=50\text{cm}, R=0.5]$  (left side) and  $[T=12\text{s}, S=50\text{cm}, R=0.6]$  (right side) over a smooth bed.

Vertical profiles of: (a) instantaneous velocity from  $\omega t=0-\pi$  with axes of measurement fixed in the moving plate; (b) phase lag; and (c) velocity amplitude with the axes of measurement fixed in the still water. **Key:** grey lines – theoretical distribution (Du Toit and Sleath, 1981; see also Eq. A.8 and A.12); black lines and points – observed distribution; and red line – boundary layer extent ( $\delta_{0.99} = 4.6052/\beta = 7.8\text{mm}$ ).

The observed profiles of instantaneous velocity (with axes fixed in still water) follow closely the general form of the predicted profile, but with some superimposed variability. Two types of departure from the smooth profile may be observed, namely: larger, vertically coherent ‘deviations’; and smaller ‘fluctuations’ (Figure 5.4). Deviations are typically manifestations of erroneous phase-referencing, whilst fluctuations are caused when a step or jump in the mean velocity signal occurs at a certain height, but does not persist for more than 20-30° of phase.

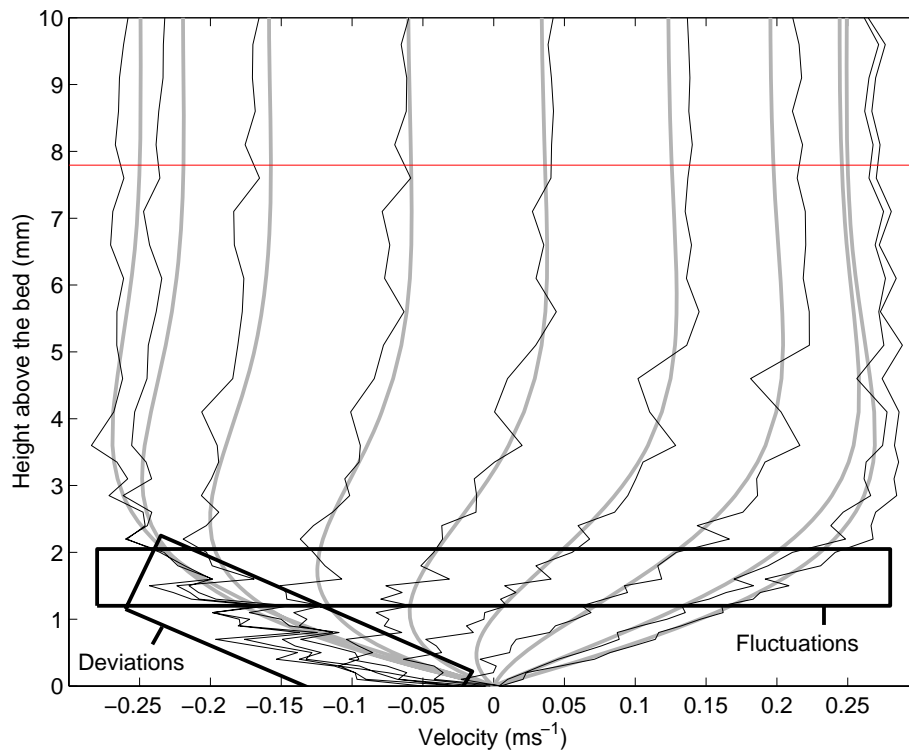


Figure 5.4. Deviations and fluctuations observed in the velocity profiles. Data for [ $T=9s$ ,  $S=75cm$ ,  $R=0.5$ ] Key as Figure 5.3.

The maximum amplitudes of the deviations and fluctuations, observed in each of the experimental case are listed in Tables B.1 and B.2. Vertically-coherent deviations are typically between  $2-6cm s^{-1}$  (i.e.  $\sim 10-40\%$  of  $U_\infty$ ). Instantaneous fluctuations are smaller, of the order of  $1-2cm s^{-1}$  (i.e.  $\sim 8-15\%$  of  $U_\infty$ ). In the low-resolution data set, fluctuations are typically of the order of  $0.5-1cm s^{-1}$  (i.e.  $\sim 5-8\%$  of  $U_\infty$ ), rising to  $2-3cm s^{-1}$  (i.e.  $\sim 10-15\%$  of  $U_\infty$ ) in 20% of cases and up to  $4cm s^{-1}$  (i.e.  $\sim 15-25\%$  of  $U_\infty$ ) in only 10% of cases. Such fluctuations (especially at higher flow velocities) were very short time-scale features, lasting between 0.1s and 0.5s ( $\sim 5^\circ-25^\circ$  phase duration).

When the axes of reference for the high-resolution data were transferred to the moving plate, a significant impact on the correlation was observed. The correlation coefficient between observed and modelled data values improved in terms of the instantaneous velocity, but decreased in terms of both the phase lag and velocity amplitude profiles. This effect became more pronounced closer to the bed. On the basis of more detailed analysis, it can be shown that this is a purely numerical phenomenon caused by small anomalies contained in the original phase lag profile; these affect then many aspects of the transformed data. The manual method used for phase-referencing (see Section 4.1.2) was the primary source of such error, throughout analysis of the high-resolution data; as such, this did not reflect the actual deviation of the velocity profile from the laminar case. Based upon an assumed operator inaccuracy of  $\pm 0.2s$ , the maximum amplitude of the phase error attributed to the methodology was estimated to be within the range of  $\pm 6-12^\circ$ , depending upon the period.

The observed and predicted velocity data, for values of  $z$  less than  $\delta_{0.99}$  and with axes fixed in the still water, were plotted against each other; a linear regression was applied. In such an analysis, an ideal fit between the two data sets is represented by a correlation coefficient of 1.0 and a regression gradient of  $45^\circ$ . The calculated correlation coefficients were between 0.943 and 0.999 (with a mean value of 0.979); regression gradients were between  $38.3^\circ$  and  $49.2^\circ$ , with a mean value of  $44.3^\circ$ . However, it should be noted that the smallest regression gradient value of  $38.3^\circ$  is an outlier, whilst the next nearest value is  $40.9^\circ$ . Overall, these values confirm that the model describes the flow field well in terms of both velocity amplitude and phase, at all heights above the bed. Residual deviation from the model was considered to be representative of experimental noise only.

## **5.5. Discussion: The inner layer**

### *5.5.1. Summary of the sources of error*

The first data to be collected (all at high-resolution) exhibited significant deviations and fluctuations from the flow field predicted by the extended theory of Du Toit and Sleath (1981). Deviations between the predicted and the observed data, occurred typically at the point of flow reversal and were attributed to a number of factors (see below).

- (i) Vertically-coherent phase lag errors, caused by the observational methodology.
- (ii) A short pause or ‘play’ in the mechanical linkage, between the hydraulics and the plate, during direction reversal.

- (iii) Slight (unavoidable) imperfections in the surface of the perspex plate (of the order 1mm, over the maximum stroke length  $S=1\text{m}$ ), used in the velocity profiling experiments only.
- (iv) Slight inaccuracies in the numerical representation of the outer layer flow.
- (v) Difficulty of the LDV in resolving flow at low instantaneous velocities, due to the frequency-shift settings necessary to resolve the larger, peak velocity amplitudes.

Errors in actual or measured velocity, caused by imperfections in the bed surface, were greatest in the steep velocity gradient region, i.e. very close to the bed. Latterly, during the collection of the medium- and low-resolution data, sources of error (i) and (ii) above were addressed by removing the dependence upon phase lag during analysis; likewise, by identifying and subsequently reducing the error due to play in the mechanical linkage. Deviations were observed then to be most significant around the phase of the peak flow amplitude. Detailed analysis showed that these small errors were mostly due to the phase lag errors, either in the main data set or in the phase of the outer layer flow.

The amplitude of these errors was considered to be insignificant under most circumstances, in the subsequent experimental programme undertaken in the present study.

### *5.5.2. Use of the model for description of the boundary layer*

Previous researchers, using oscillating trolley equipment to study transition to turbulence or threshold of motion, have not apparently included outer layer fluid motions in the calculation of fluid flow parameters, in relation to the processes being observed. The inclusion of outer layer parasitic flows, during the interpretation of transition to turbulence data (described in Chapter 6), reduced  $U_\infty$  in the order of 1.5-2.5%; this was considered insignificant in relation to the data analysis. The inclusion of outer layer parasitic flows, in the calculation of  $\tau_0$  from the threshold of motion data (described in Chapter 7), caused a mean reduction in the calculated value of only 2%. The relative difference was greater than 10% in only 1.5% of cases; it was greater than 5% in only 4.6% of cases. Greater disagreement corresponded, typically, with observations made at large wave periods.

Hence, to maintain a standard methodology between the present and previous studies, it was considered appropriate to exclude outer layer flows, from the analysis of the transition to turbulence and threshold of motion data.

Other potential sources of error identified in this Chapter were addressed, prior to the start of subsequent experimental work described herein. Disturbance of the flow, caused by undulations in the plastic plate or rubber overlays, were reduced further in later experiments by replacement of such surfaces with a rigid glass plate. Outer layer flow baffles were checked regularly and secured, to ensure efficiency in minimising parasitic flows. Error in the measurement of the phase lag was ignored, as only the amplitude of the plate oscillation and oscillatory period (set by the control software) were needed to quantify adequately the necessary flow parameters; similarly, no phase referencing was needed for the subsequent data analysis.

Ultimately, these analyses have demonstrated that the second-order Stokes model was constructed correctly; therefore, it is acceptable for use in describing the flow field above the oscillating trolley, when simulating such flows under laminar conditions.

## **5.6. Results: Comparison between wave theories**

In this Section, laminar flow fields of unit value  $U_c$  and normalised  $z$  were created, for a range of flow asymmetry ( $R=0.5, 0.55, 0.6, 0.65$  and  $0.7$ ) using second-order Stokes and cnoidal flow models. Laminar boundary layer flow fields were calculated for sinusoidal, second-order Stokes and cnoidal flows, using the models described in Sections 2.4, 2.5 and 2.6, respectively. These data were used to compare: (i) the sinusoidal case with second-order Stokes solutions of increasing  $R$ , to determine the effect of asymmetry in the present study; and (ii) second-order Stokes with cnoidal solutions, at the same value of  $R$ , to investigate the effect of additional harmonics. The data were compared in terms of absolute velocity, fluid acceleration and velocity shear gradients at all heights above the bed within the boundary layer and at all phases in the wave cycle. The focus of this Section is upon the boundary layer characteristics around the phase of the wave crest, i.e. the peak in positive velocity, as this is the primary region of interest in subsequent Chapters.

### *5.6.1. First order vs second order theory*

Each of the plots in Figure 5.5 illustrates the distribution of the flow parameters, for a given  $R$ . Values varied differently throughout the wave cycle at different  $R$ , but the general location and polarity of the signal are similar. The location and intensity of patterns around the trough becomes slightly more complex (bimodal) for  $R \geq 0.63$ , due to the presence of the secondary hump.

Flow velocities throughout the boundary layer, at phases on either side of the crest, are lower under asymmetric flows (when  $U_\infty = U_c$ ). The maximum decrease (e.g. 39% for  $R=0.7$ ) is located at approximately 30% of  $\delta_{0.99}$  above the bed and the ‘no slip’ condition causes the relative difference to decrease gradually, to zero at the bed. As a result, both fluid acceleration and deceleration on either side of the crest are progressively stronger under asymmetric flows; phases of fluid acceleration occur over a shorter period of time and are phase-shifted towards the peak in the outer layer velocity. Maximum fluid acceleration/ deceleration occurs at approximately  $\pm 90^\circ$  about the peak in velocity, for  $R=0.5$  and  $\pm 55^\circ$  for  $R=0.7$ ; it is located approximately 50% of  $\delta_{0.99}$  above the bed, for all values of  $R$ . Fluid shear is uniformly small throughout the wave cycle, at heights greater than 15% of  $\delta_{0.99}$  above the bed. However, below this height and at a phase prior to the peak in velocity, the fluid shear increases progressively towards the bed, to a maximum value (which was 55% greater than the sinusoidal case, for  $R=0.7$ ) at the phase of peak shear stress (which moves closer to the phase of peak velocity, with  $R$ ). A region of increased fluid shear is observed to propagate away from the bed following the peak in shear stress; this represents the zone of flow inflection. In this condition of equal  $U_\infty$ , the relative increase in fluid shear with asymmetry in the mid- to upper-boundary layer is small. The amplitude of peak shear stress at the bed and under the crest becomes only slightly larger with asymmetry (by 7.6% for  $R=0.7$ ); it becomes also narrower in phase. The bed shear stress is reduced typically for much of the duration of the flow under the trough.

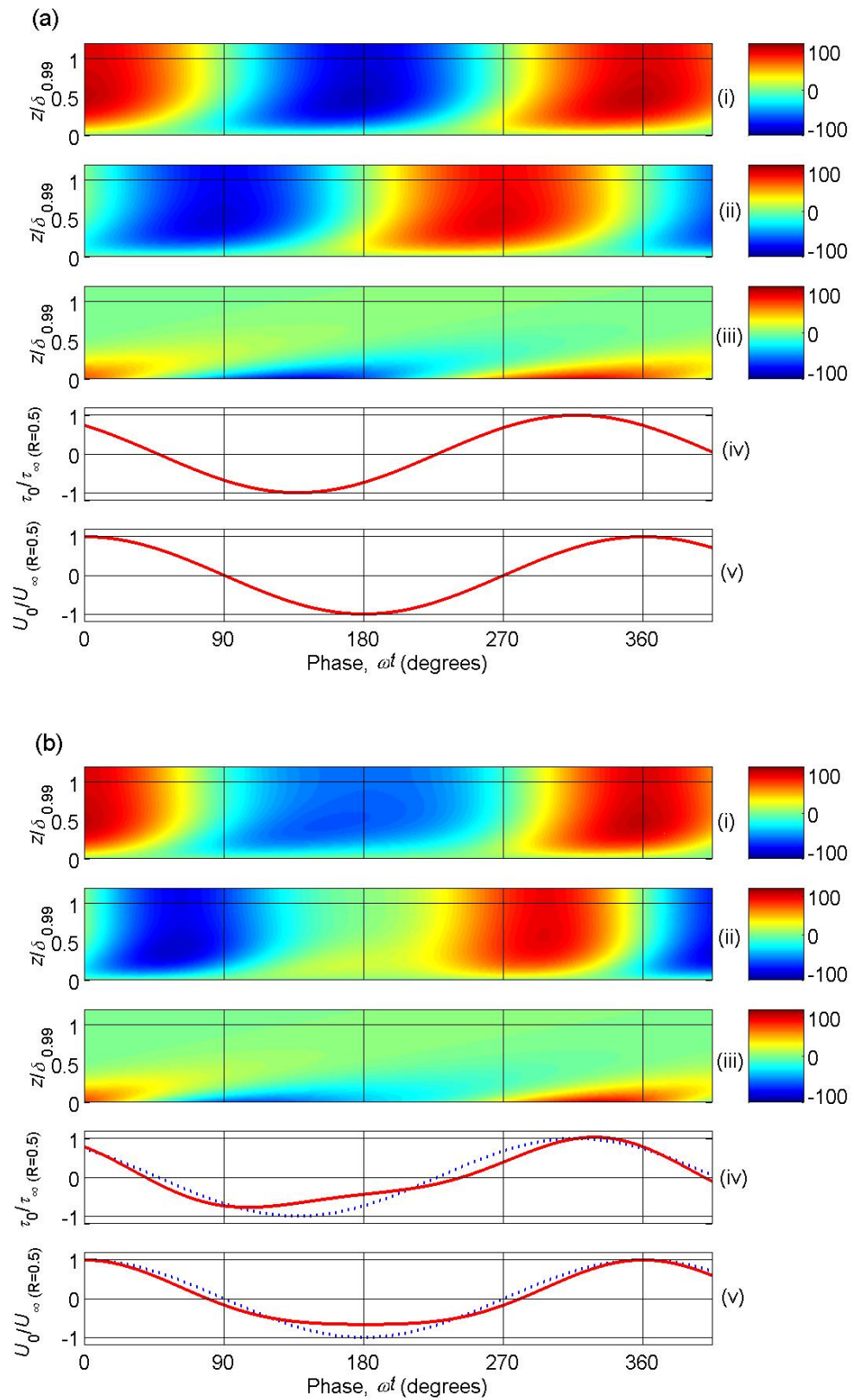


Figure 5.5. *continued overleaf...*

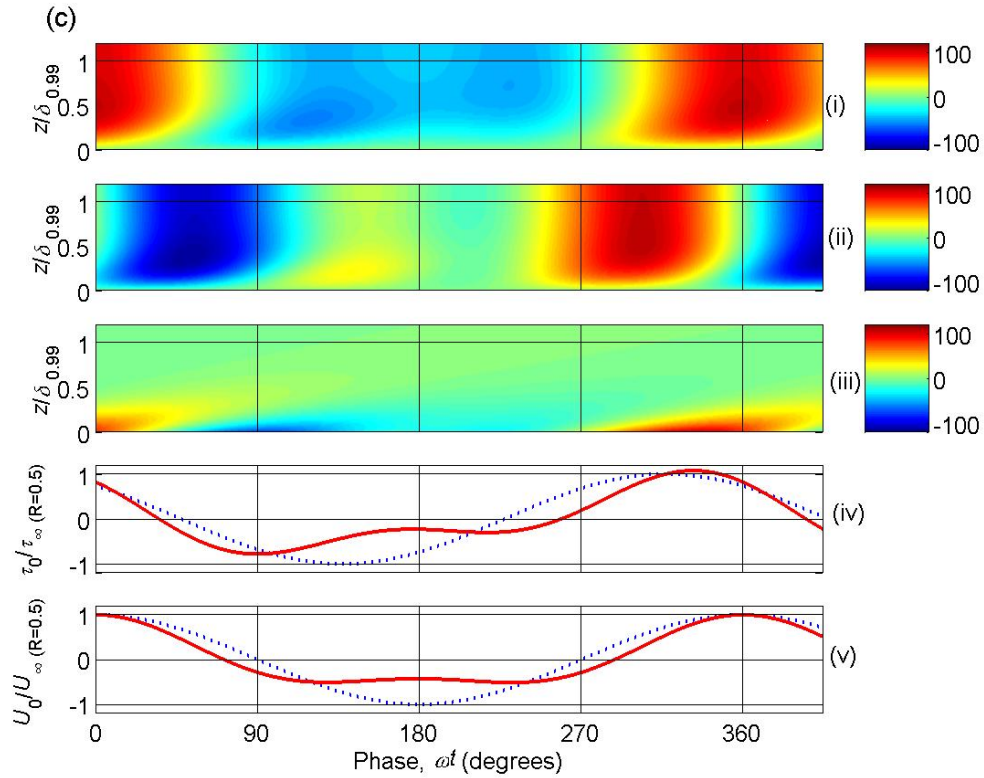


Figure 5.5. Wave boundary layers calculated using second-order Stokes theory. Subplots illustrate the vertical and temporal distribution of: (i) absolute velocity; (ii) fluid acceleration; fluid shear (iii) in the boundary layer; and, (iv) at the bed. These are in relation to the velocity cycle at the edge of the boundary layer (v). Values are shown as a percentage of the maximum value in the sinusoidal case for: (a)  $R=0.5$ ; (b)  $R=0.6$ ; and (c)  $R=0.7$ . Key: blue lines – sinusoidal case (for comparison); red lines – asymmetric case.

### 5.6.2. Second order vs Cnoidal theory

Second-order Stokes theory produces a secondary hump in the trough, at large asymmetry ( $R > 0.65$ ); cnoidal theory maintains a smooth trough, without inflection. Consequently, the two theories compare closely for  $R \leq 0.6$ ; under these conditions, maximum deviation for any of the three parameters (absolute velocity, fluid acceleration and fluid shear) did not exceed 5%. Significant deviation was observed then at larger values of asymmetry; this is described below.

The plots in Figure 5.6 show the relative difference in the flow parameters, as calculated by the two theories; these are expressed as a percentage of the maximum value of that parameter from the second-order Stokes solution. Flow velocities are reduced generally under cnoidal flows. These reductions occur almost symmetrically, on either side of the crest and trough.

The maximum reduction in velocity around the crest (e.g. -17% for  $R=0.7$ ) occurs at  $\pm 50^\circ$ ; this is located approximately 30% of  $\delta_{0.99}$  above the bed. Because the absolute peak velocity is the same in both of the data sets, acceleration and deceleration of fluid around the crest are consequently larger, under cnoidal flows. Fluid acceleration prior to the crest has a slightly larger maximum increase than the deceleration phase following the crest; the maximum increases occurs at around  $\pm 23^\circ$ , located at approximately 30% of  $\delta_{0.99}$  above the bed. Differences in the predicted fluid shear are limited to regions close to the bed. Patterns observed in the vertical distribution of fluid shear are dominated by a small phase shift of shear stress between the two solutions; therefore, they are not included in the Figure. The peak value of bed shear stress is relatively unaffected by the addition of higher harmonics, but is slightly negatively phase-shifted. The positive peak in bed shear stress is slightly narrower under cnoidal flows; it is not symmetrical about the peak.

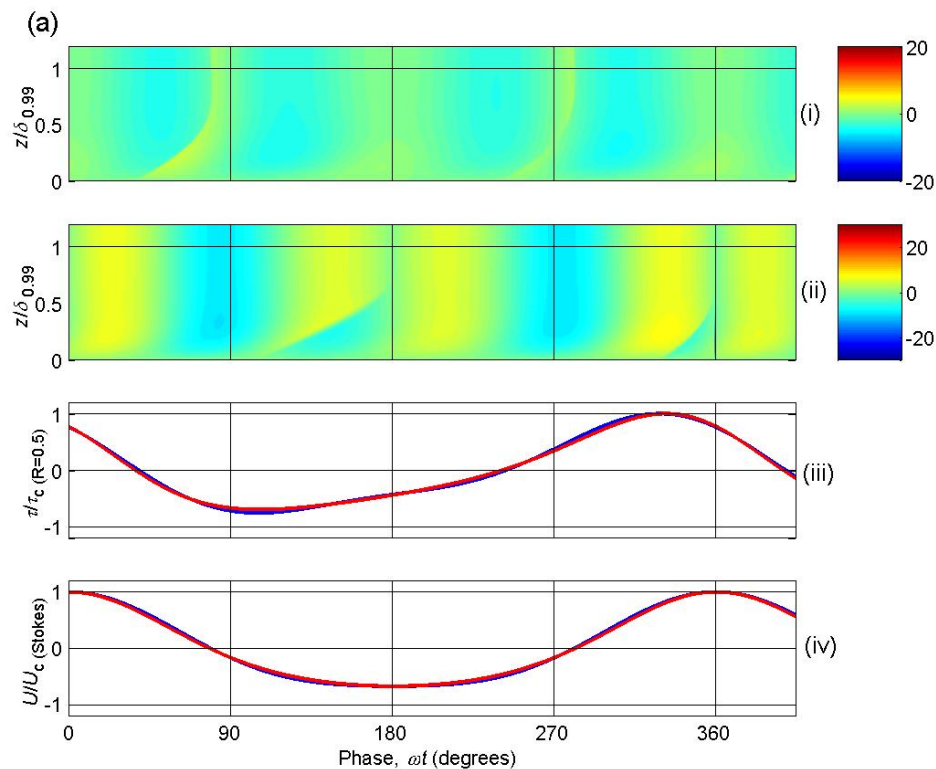


Figure 5.6. *continued overleaf...*

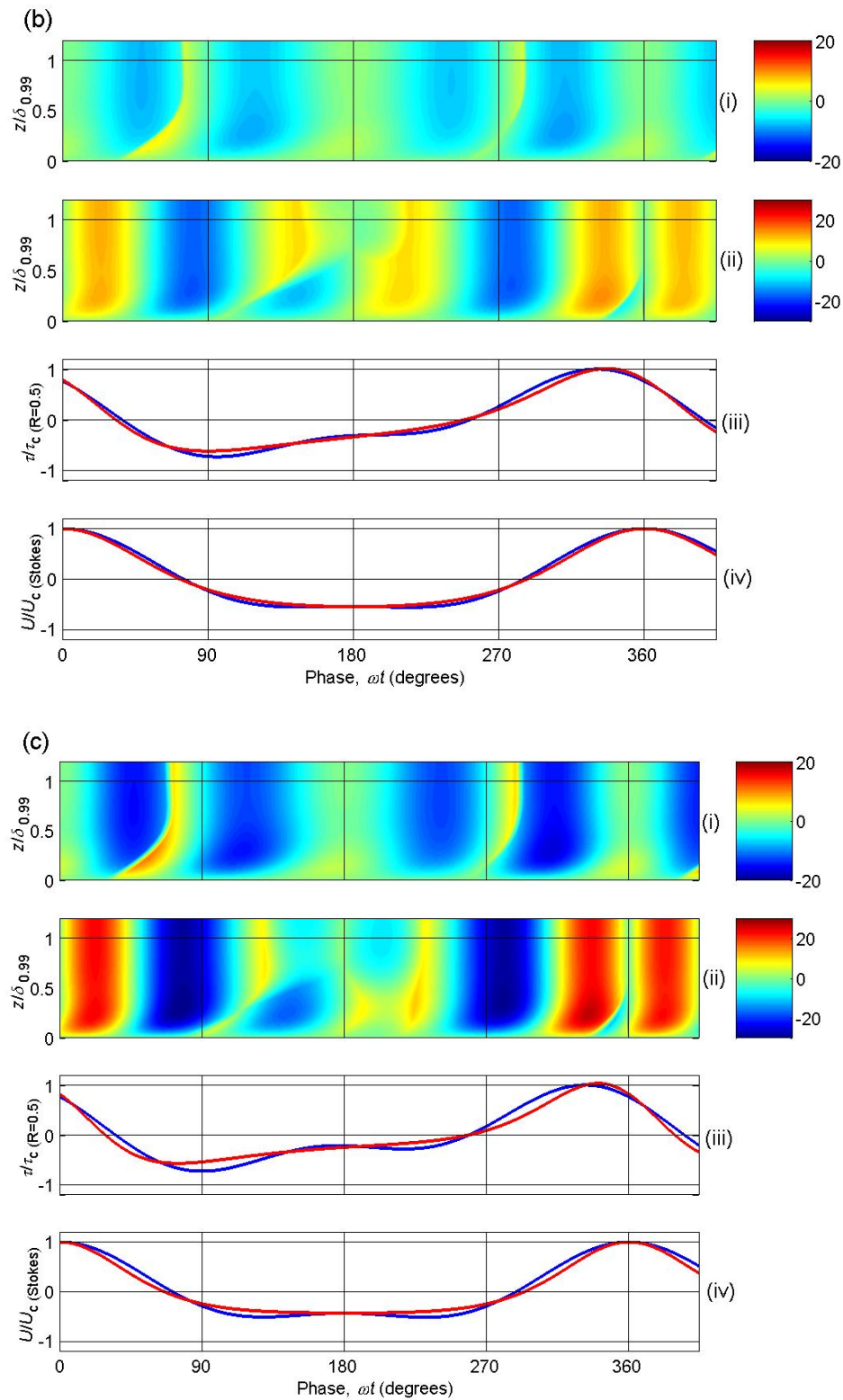


Figure 5.6. Comparison of second-order Stokes and cnoidal wave boundary layers: (i) absolute velocity; (ii) fluid acceleration; and (iii) fluid shear at the bed, relative to the outer layer velocity (iv). Percentage deviation from the second-order Stokes solution: (a)  $R=0.6$ ; (b)  $R=0.65$ ; and (c)  $R=0.7$ . Key: blue lines – second-order Stokes theory; red lines – cnoidal theory.

### **5.7. Discussion: Comparison between wave theories**

In Chapter 6, it was proposed that the increase in rates of fluid acceleration, associated with flow asymmetry, act to stabilise the boundary layer; this delays the onset of turbulence under such flows. It has been shown here that increasing asymmetry corresponds to larger rates of fluid acceleration and deceleration, in phases prior to and following the crest. This region corresponds also to the zone of flow inflection. Both of these factors are considered to be important directly in regulating the initiation of flow instability in the laminar boundary layer, over relatively smooth beds.

In Chapter 7, both the peak value of fluid shear stress at the bed and the development of such forces, over time, are considered to be important in regulating the threshold of motion for sediment. It has been shown here that the shear cycle produced by an asymmetric flow may be of similar shear amplitude, but will be narrower than that of a sinusoidal flow of similar velocity amplitude. This is shown later to necessitate a larger peak shear stress value, in order to cause the threshold of motion for sediments under asymmetric waves.

The comparison between second-order Stokes and cnoidal wave theory was designed to test the sensitivity of the asymmetric model used in the present study, to the inclusion of additional higher harmonics. In this case, the cnoidal model represents a total of 10 harmonic components. The difference between the two models was negligible for  $R \leq 0.6$ ; the following discussion relates to flows of greater  $R$ . The most noticeable difference between such flows, at equal peak velocity amplitude, was that flow velocity was typically reduced over much of the wave cycle when using cnoidal theory. This pattern suggests that cnoidal waves of similar  $U_c$  represent a lower energy boundary layer; this may increase the peak velocity required to initiate sediment motion and to maintain any subsequent sediment transport. Based upon the findings described in Chapter 6, it is likely that cnoidal boundary layers are relatively more stable than an equivalent second-order Stokes case; this is partly as a result of the increased rates of fluid acceleration. Based upon the findings of Chapter 7, it is likely that a slightly higher peak velocity and/or shear stress (together with other associated parameters) may be necessary to cause the threshold of motion, under cnoidal waves.

This analysis has demonstrated that the degree of asymmetry in oscillatory flow is an important parameter, in order to quantify properly both the magnitude and the distribution of fluid velocity, fluid acceleration and fluid shear forces. As shown in the following Chapters, such information should now be considered necessary in order to interpret observations of

---

the transition to turbulence and the threshold of motion for sediment. The effect of asymmetry may be incorporated adequately, as a first approximation, by the use of Stokes second-order solution. Higher-order solutions provide a lesser, fine-tuning effect only; in turn, they tend to accentuate the general findings, that asymmetry acts to stabilise the boundary layer and delay the onset of sediment transport.

# Chapter 6. Transition to Turbulence

## 6.1. Introduction<sup>1</sup>

In total, 37 conditions were simulated and interpreted using the velocity time-series and turbulent intensity methods. In addition, the visual observation method was incorporated into 14 of these conditions. All of the results have undergone careful screening to exclude certain conditions which: (i) exceeded the theoretical limitations of the oscillating trolley equipment in terms of maximum velocity amplitude; and/or (ii) did not extend sufficiently into the transitional regime to provide a clear transitional point. Of 88 possible observations, 68 were considered to be acceptable; of these, 15 were collected over a smooth bed. Although three distinct methods were used to define and observe transition, the observed critical flow parameter values compared well between the various methods. This indicated that the various methods represent a consistent and comparable set of hydrodynamic conditions. As such, all the screened data were used in the overall analyses to reduce bias introduced by any single method.

Parameters describing the flow conditions present during each experiment were calculated from the recorded values of  $T$ ,  $S$ ,  $R$  and temperature, using the laminar flow model described in Section 2.5.

## 6.2. Results: Critical flow parameters

Observations of transition were compared in terms of four critical flow parameters, namely: stroke length; peak outer layer velocity; peak shear stress; and the mid-boundary layer velocity gradient. This Section summarises the general trends observed in these parameters; the main analysis of data is undertaken in subsequent Sections using these same parameters combined into various Reynolds numbers.

### 6.2.1. Sinusoidal flow

Patterns observed in the critical parameters could be grouped according to the bed roughness,  $D$  (Figure 6.1). For  $D \geq 421 \mu\text{m}$ , the critical stroke length,  $S_{\text{crit}}$ , increases in proportion with  $T$  and the critical velocity amplitude,  $U_{\infty \text{crit}}$ , is approximately constant over

---

<sup>1</sup> Note: The main results and discussion from this Chapter may be found also in Lambkin, D.O., Collins, M.B. and Paphitis, D. (In press) Wave period and flow asymmetry effects on the transition to turbulence in relation to sediment dynamics. *Journal of Geophysical Research*. (Appendix E).

---

the range of  $T$ , i.e.  $\delta U_{\infty \text{ crit}}/\delta T \approx 0$  and therefore,  $\delta S_{\text{crit}}/\delta T \propto U_{\infty \text{ crit}}$ . However, for  $D \leq 275 \mu\text{m}$ , including smooth beds,  $S_{\text{crit}}$  increases in the manner described above only for small values of  $T$ , with the gradient subsequently becoming  $\delta S_{\text{crit}}/\delta T \approx (1.66 \times 10^5 \nu)/1.5\pi$ . This corresponds to the smooth bed limit for transition to turbulence (indicated in the Figure by dashed lines), discussed further in Section 6.3.1.

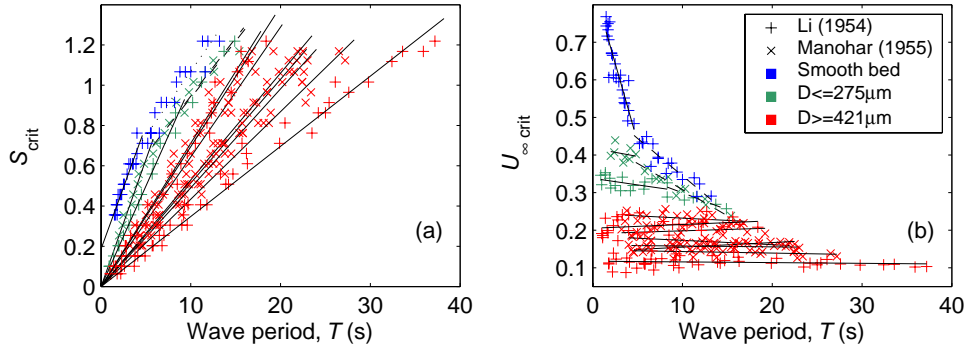


Figure 6.1.  $S_{\text{crit}}$  (a) and  $U_{\infty \text{ crit}}$  (b) causing transition to turbulence over uniform, fixed granular beds under sinusoidal flows. See text for more details.

The peak bed shear stress at the point of transition,  $\tau_{0 \text{ crit}}$ , calculated using laminar theory, is higher under smaller wave periods (Figure 6.2). This value then decreases smoothly in a non-linear fashion for all values of  $D$ , becoming almost constant at large wave periods. Absolute values of  $\tau_{0 \text{ crit}}$  are larger at smaller  $D$ ; this is most pronounced at grain sizes  $D \leq 275 \mu\text{m}$ .

The velocity gradient parameter,  $\delta u/\delta z$ , is the maximum velocity gradient (shear) associated with the boundary layer velocity profile in the mid-boundary layer. This parameter is significant as it represents one of the primary destabilising forces (fluid shear) directly. The location of this region moves upwards from the bed during the phase range proposed by Jensen *et al.* (1989), over which initial transition occurs (Figure 6.3a). The velocity gradient in this region is related fundamentally to the velocity gradient at the bed and, therefore, with  $\tau_0$ ; hence, the observed pattern in  $(\delta u/\delta z)/\delta T$  is similar to that observed for  $\delta \tau/\delta T$  (Figure 6.3b). As such, the velocity gradient parameter is typically larger at the point of transition, for smaller  $T$  and/or  $D$ ; this was greatest for grains  $D \leq 275 \mu\text{m}$ .

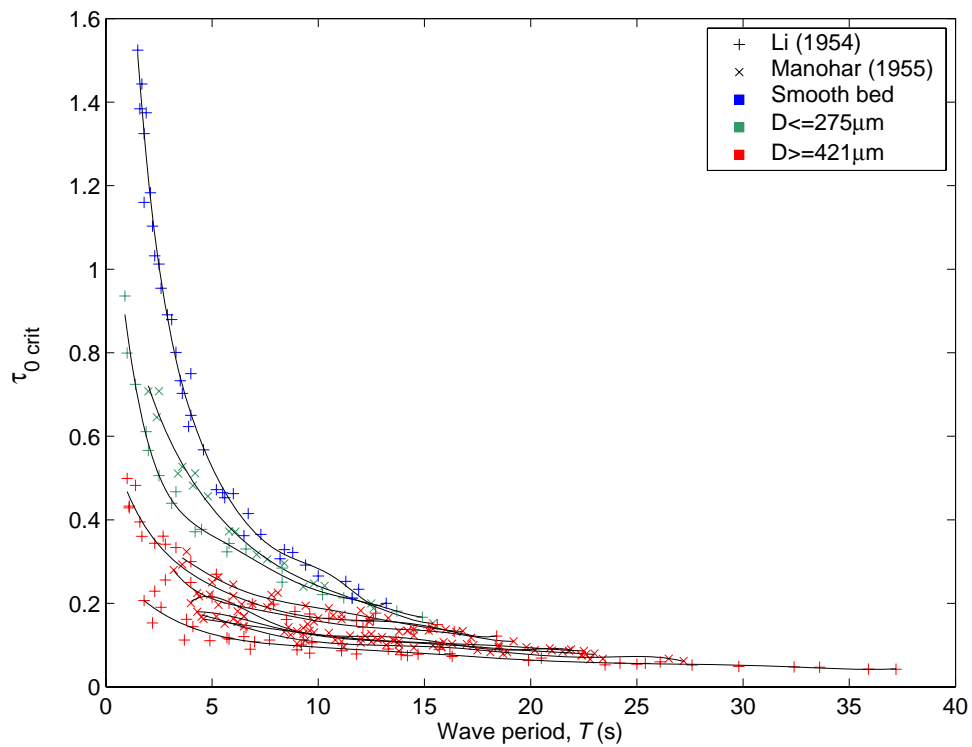


Figure 6.2. Trends in the values of  $\tau_{0\text{crit}}$  causing transition to turbulence over uniform, fixed granular beds under sinusoidal flows.

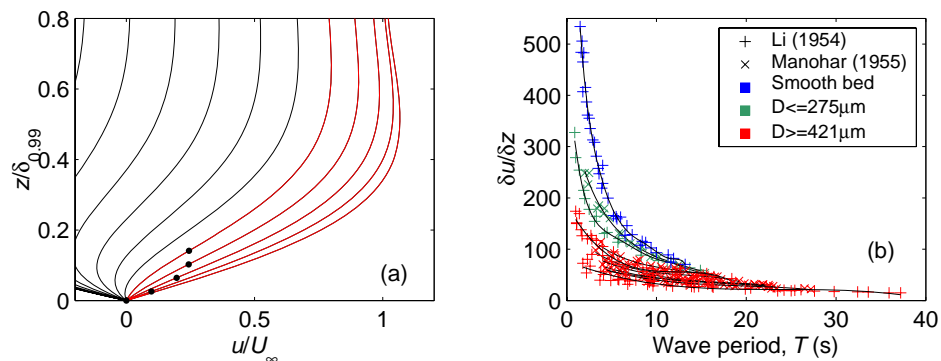


Figure 6.3. (a) Velocity distribution in the sinusoidal boundary layer and the location of the maximum velocity gradient (black points) through the phase range of the onset of transition (red lines); and (b) maximum observed values in sinusoidal flows causing transition to turbulence over uniform, fixed granular beds.

### 6.2.2. Asymmetric flow

The value of  $S_{\text{crit}}$  did not vary significantly from the sinusoidal case, as a result of flow asymmetry, for any of the beds investigated (Figure 6.4 -

Figure 6.6). Therefore, the effect of greater asymmetry is to cause an increase in absolute  $U_{c\text{crit}}$ , following Eq. 4.3. The gradient  $\delta U_{c\text{crit}}/\delta T$  for all  $R$  was variable with  $D$ , following the same general patterns described above for sinusoidal flows (Figure 6.1b).

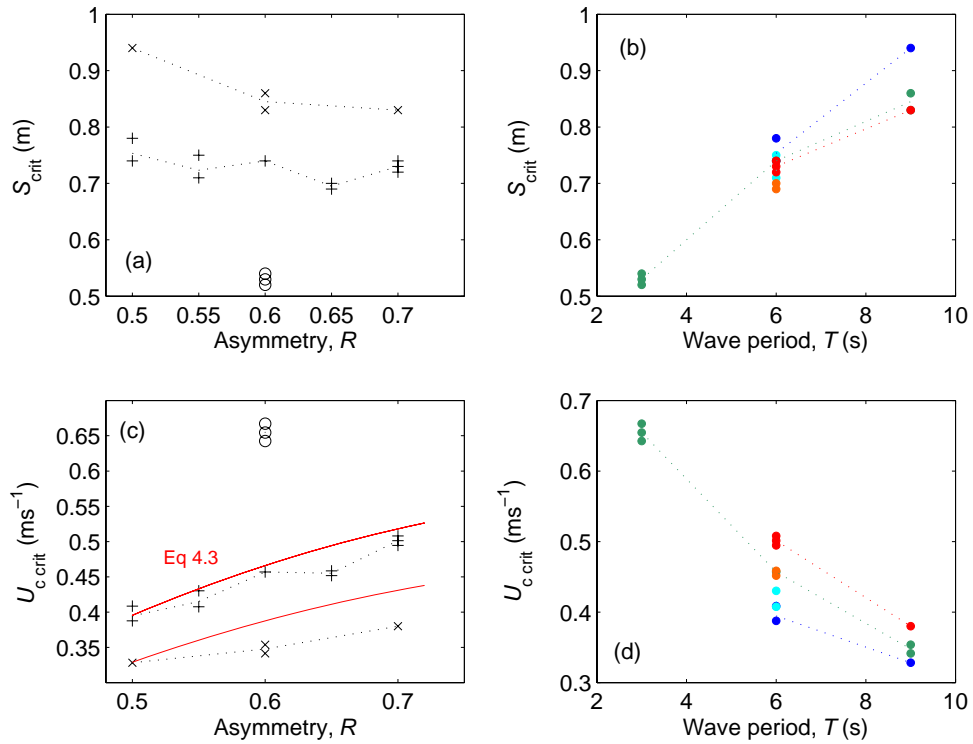


Figure 6.4. Trends in the values of  $S_{\text{crit}}$  ((a) and (b)) and  $U_{c\text{crit}}$  ((c) and (d)), in relation to asymmetry and wave period, respectively, causing transition to turbulence over smooth beds under asymmetric flows.

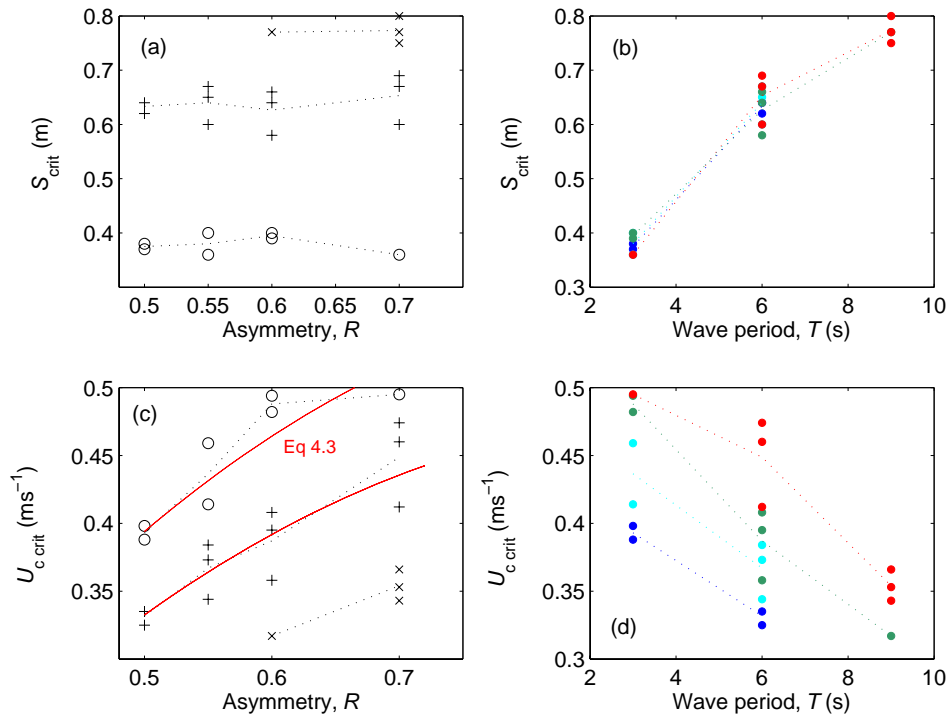


Figure 6.5. Trends in the values of  $S_{\text{crit}}$  ((a) and (b)) and  $U_{\text{crit}}$  ((c) and (d)), in relation to asymmetry and wave period, respectively, causing transition to turbulence over uniform, fixed granular beds ( $D=275\mu\text{m}$ ) under asymmetric flows.

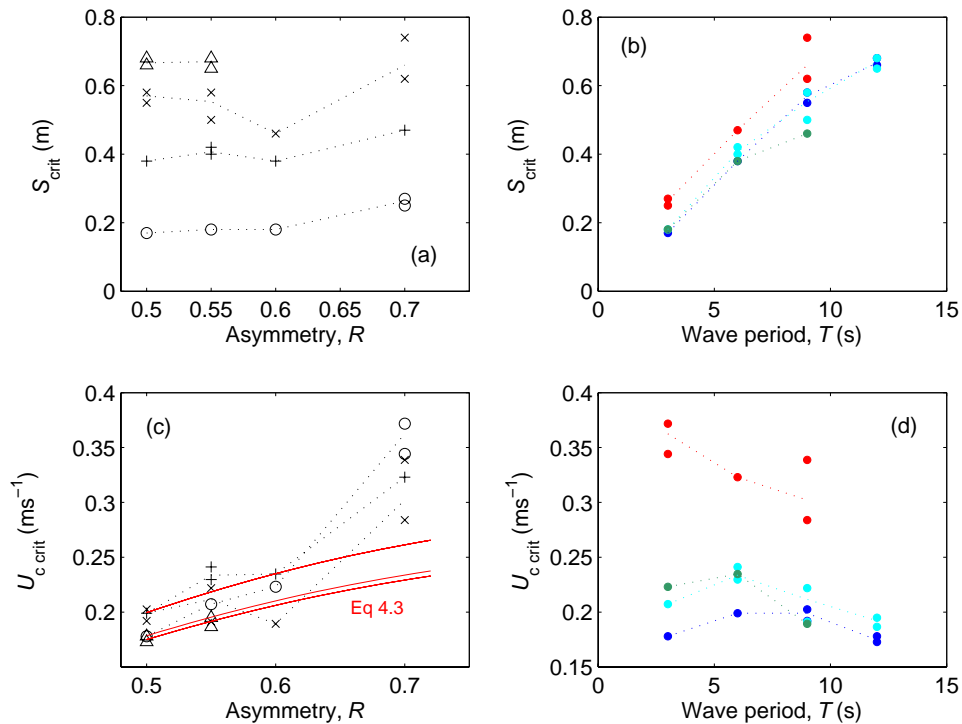


Figure 6.6. Trends in the values of  $S_{\text{crit}}$  ((a) and (b)) and  $U_{\text{crit}}$  ((c) and (d)), in relation to asymmetry and wave period, respectively, causing transition to turbulence over uniform, fixed granular beds ( $D=550\mu\text{m}$ ).

The critical value of  $\tau_0$  was observed to increase steadily with  $R$ , in all cases (Figure 6.7); this increase is of the order 25% across the range  $0.5 < R < 0.7$ . The relative increase in  $\tau_{0 \text{ crit}}$ , due to asymmetry, is approximately proportional to  $R$  and is similar at all wave periods. For the two rough beds considered in the present study, differences in the absolute values of  $\tau_{0 \text{ crit}}$  may be attributed almost equally to differences in asymmetry and wave period, over the range of values that were investigated.

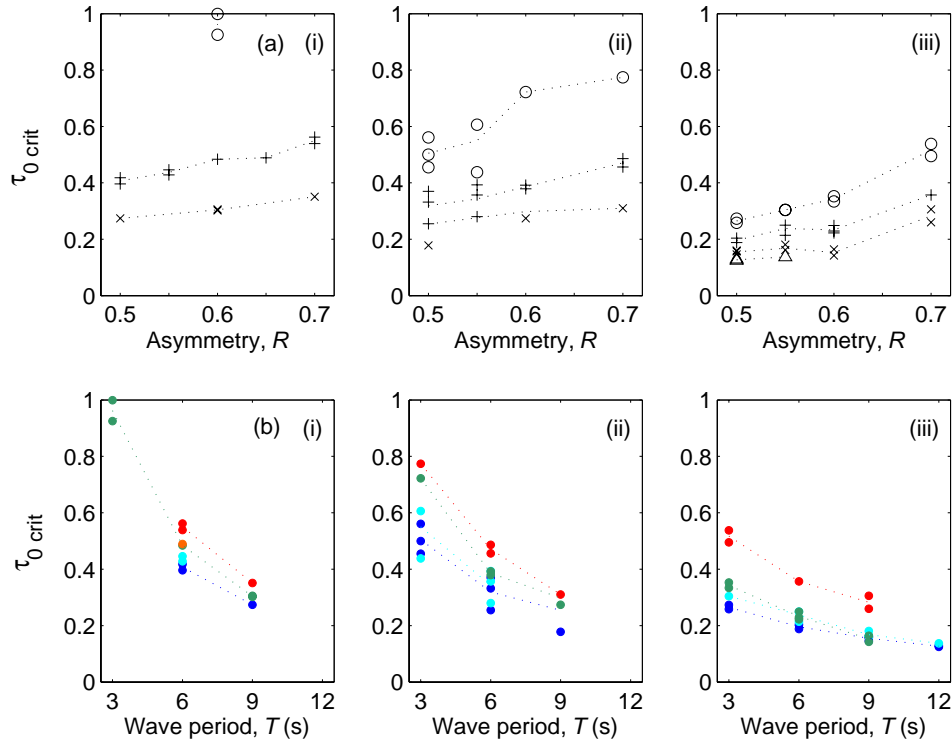


Figure 6.7. Trends in the value of  $\tau_{0 \text{ crit}}$  in relation to asymmetry (a) and wave period (b), causing transition to turbulence. Observations made over smooth beds (i) and uniform, fixed granular beds,  $D=275\mu\text{m}$  (ii) and  $D=550\mu\text{m}$  (iii). Key for (a):  $T=3\text{s}$  (o);  $T=6\text{s}$  (+);  $T=9\text{s}$  (×);  $T=12\text{s}$  ( $\Delta$ ). Key for (b):  $R=0.5$  (blue);  $R=0.55$  (turquoise);  $R=0.6$  (green);  $R=0.65$  (orange);  $R=0.7$  (red).

The similarity between the patterns relating to  $\tau_{0 \text{ crit}}$  and  $\delta u/\delta z$  under sinusoidal flows are presented in Section 6.2.1; patterns in the critical values of these parameters are described therein also, in relation to  $T$  and  $D$ . From this baseline, the effect of asymmetry is to increase slightly the absolute value of the critical velocity gradient in the mid-boundary layer (Figure 6.8). This increase is relatively small over smooth beds; however, it becomes larger with

increasing bed roughness. On the basis of the data available, the increase associated with larger grain sizes is uniform over all wave periods, at a given  $D$ .

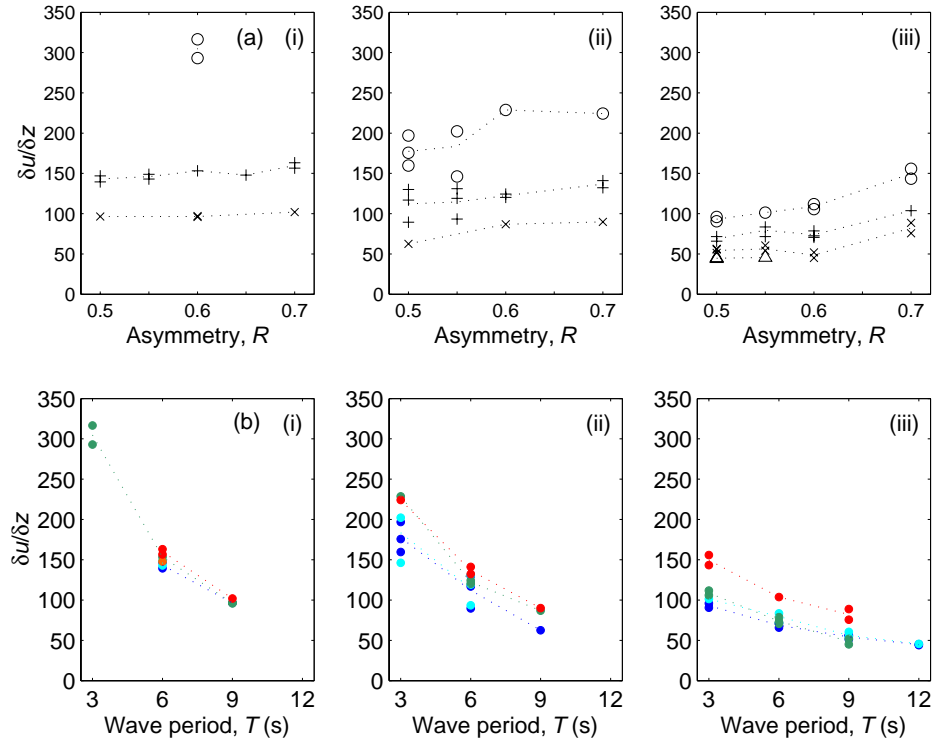


Figure 6.8. Trends in the value of the velocity gradient parameter,  $\delta u / \delta z$  (a measure of a destabilising fluid force), in relation to asymmetry (a) and wave period (b), at the transition to turbulence. Observations made over smooth beds (i) and uniform, fixed granular beds,  $D=275\mu\text{m}$  (ii) and  $D=550\mu\text{m}$  (iii). Key: (a)  $T=3\text{s}$  (o);  $T=6\text{s}$  (+);  $T=9\text{s}$  (x);  $T=12\text{s}$  ( $\Delta$ ); and (b)  $R=0.5$  (blue);  $R=0.55$  (turquoise);  $R=0.6$  (green);  $R=0.65$  (orange);  $R=0.7$  (red).

### 6.2.3. Comparison of methods and estimation of error

The three observational methods used to quantify and define the transition to turbulence have been described in Section 4.2. These methods identify commonly the initiation of turbulence by observing the onset of significant transport of fluid by eddies within the boundary layer. This observation is accomplished using two distinct approaches, i.e. visual (qualitative) and measured velocity time-series (quantitative) approaches. Data at coincident values of  $T$ ,  $R$  and  $D$  provided by the three methods are compared directly, in terms of  $S_{\text{crit}}$ , in Figure 6.9. No significant, consistent bias or offset is found between the two velocity measurement methods and the absolute disagreement is small (of the order of  $\pm 6\%$ ). In comparison to the former methods, the visual method consistently underestimates the value of  $S_{\text{crit}}$ , by a small

margin (~7-10%). In only a few cases, typically for observations made over the smooth bed when comparing the visual method with either of the velocity measurement methods, this value may be higher (+20-40%).

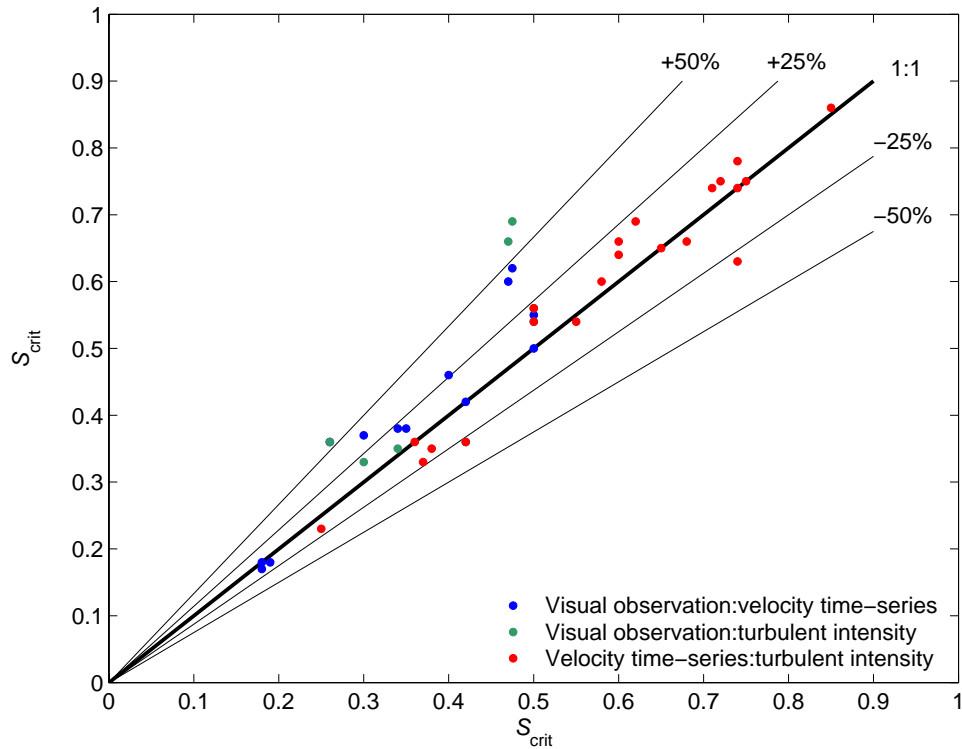


Figure 6.9. Relative error between methods used in the present study for observation of the transition to turbulence.

During the data collection, the incremental step increase in  $S$  and, therefore, the resolution of  $S$  in the results, was 1-2cm. The mean absolute difference in observed  $S_{crit}$  between the two velocity profiling methods and between these and the visual method, is 3.1cm; this corresponds approximately to only 2-3 increments of  $S$ . In some cases, typically those made over smooth beds when comparing the visual method with either of the velocity profiling methods, this value is larger (12.3cm).

### 6.3. Results: Smooth beds

#### 6.3.1. Sinusoidal flows

Smooth beds are a limiting case that may be representative of featureless mudflats or possibly very fine sand beds. On the basis that no roughness element should be present on the smooth bed, only the velocity time-series and turbulent intensity methods were used

during the present experimental programme. Li (1954) provides 54 observations of the transition to turbulence over smooth beds, within the range  $T=0.6-13.2s$ . Following selective filtering of the smooth bed data, collected during the present study, only three data points remained in relation to smooth beds; consequently, this data is not intended to provide significant addition to that of Li, but does demonstrate favourable comparison in terms of the magnitude of the results. Together, these data were used to investigate the dependency of  $Re_{crit}$  on the flow parameters for sinusoidal flows. A positive linear relationship with  $T$  was observed, following

$$\begin{aligned}
 RE_{crit} &= 41T + 430 \quad \text{or} \quad Re_{crit} = 2.1 \times 10^4 T + 9.25 \times 10^4 && \text{for } T \leq 3.5s \\
 \text{and} & && \\
 RE_{crit} &= 576 && \text{or} \quad Re_{crit} = 1.66 \times 10^5 && \text{for } T > 3.5s
 \end{aligned}$$

Eq. 6.1

This relationship and the observed data of Li (1954), together with those of the present study, are shown in Figure 6.10.

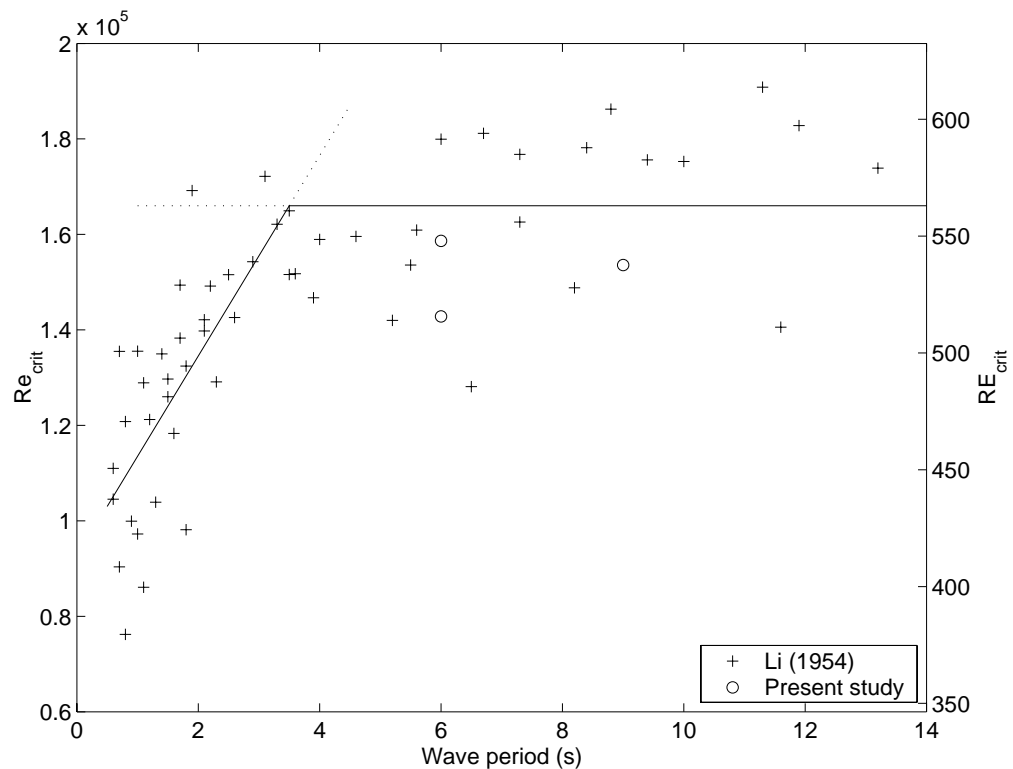


Figure 6.10. The observed transition to turbulence over smooth beds, under sinusoidal oscillatory flows. The suggested fit to the data (Eq. 6.1) is superimposed.

Although the described pattern is clearly visible in the data, it has been suggested by Sleath, (*Pers. Comm.*) that this might be caused potentially by a deviation from true sinusoidal motion ('jerkyness' or play in the mechanism) by oscillating trolley equipment when simulating very small wave periods (e.g.  $T < 3s$ ).

### 6.3.2. Asymmetric flows

The relationship for the transition to turbulence, over hydrodynamically smooth beds under asymmetric flows, proposed on the basis of the results of the present study, is shown in Figure 6.11. Asymmetric flow conditions are described in terms of a boundary Reynolds number, RE, defined as:

$$RE_{c,t} = \frac{U_{c,t} \sqrt{2\nu/\omega}}{\nu} \quad \text{Eq. 6.2}$$

where the length scale is  $\delta$  (a measure of boundary layer thickness) and, for these and all parameters used subsequently, the subscripts 'crit', 'c' and 't' identify critical values of parameters at the phase of the crest and the trough, respectively. In Figure 6.11, open and filled circles represent all of the observed time-series data that have been classified as either 'laminar' or 'transitional/turbulent' under the crest only, according to the criteria described in Section 4.2. It should be noted that some conditions (from different experimental runs) may be identified simultaneously as being laminar and transitional/turbulent (possibly due to differences in wave period); in this case, the dot and circle may overlap, giving the appearance of a larger dot. In addition, individual points indicating the transition to turbulence have been identified separately as crosses, for observations under the crest and under the trough. An empirical curve representing the boundary between laminar and transitional/turbulent conditions was fitted to the crest data in Figure 6.11, using a least squares method. An envelope representing the 99% confidence interval is also shown. The form of the relationship was

$$RE_{c,crit} = i + j(R - 0.5)^k \quad \text{Eq. 6.3}$$

where  $i$ ,  $j$  and  $k$  are fitting coefficients, summarised in Table 6.1.

	Fitting coefficients		
	i	j	k
Present study	566	3500	2.133
Tanaka (2000)	550	8880	2.16

Table 6.1. Fitting coefficients for Eq. 6.3, describing the transition to turbulence over smooth beds, for second-order Stokes (present study) and cnoidal flows (Tanaka *et al.*, 2000)

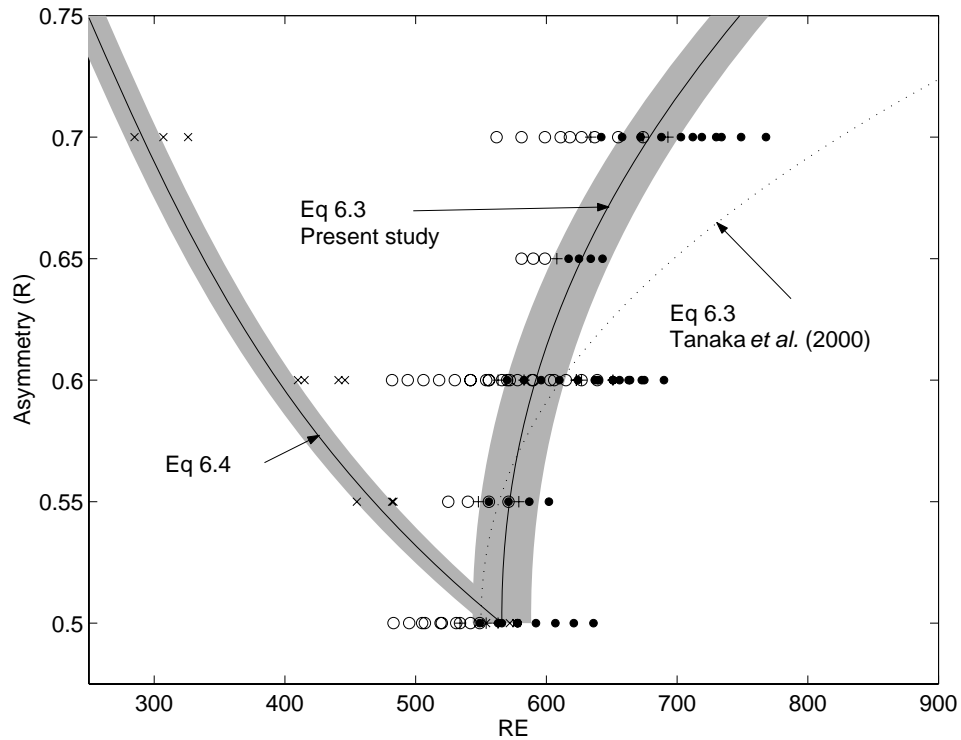


Figure 6.11. Stability of the oscillatory boundary layer over a flat, smooth bed. **Key:** Laminar (O) and transitional/turbulent (●) conditions and flows at initial transition under the crest (+) and trough (x) half cycles, as observed in the present study; solid line and envelope – least squares fit to crest data (and corresponding curve for the trough) and 99% confidence interval; dotted line – relationship for cnoidal flows, as proposed by Tanaka *et al.* (2000). See text for more details.

For second-order Stokes formulations,  $U_c$  and other values proportional to changes in  $U_c$  (e.g. Reynolds numbers) may be calculated interchangeably under the crest and the trough using

$$x_t = \frac{x_c}{R} \times (1 - R) \tag{Eq. 6.4}$$

where  $x_c$  and  $x_t$  are the values of the parameter under the crest and under the trough, respectively. Using this method, a corresponding curve for flows under the trough was drawn from the relationship fitted to the crest data. This curve was found to describe the trough data well in most cases but, on average,  $RE_{t\text{crit}}$  was slightly underestimated. This suggested that, in some cases, transition occurs initially under the crest and only then under the trough at greater overall flow amplitudes (i.e. a larger orbital amplitude  $a=S/2$ ), for the same  $T$  and  $R$ .

Scatter in the observations obtained from the present study can be attributed to: (i) slight differences between the observational methods; (ii) slight disturbances (vibrations or play), associated potentially with the mechanical action of the oscillating plate; and (iii) natural variability in the complex hydrodynamic processes involved. The data appear also to indicate a possible sensitivity to the period of oscillation. However, following data screening, insufficient data points were available to draw firm conclusions on this particular observation.

For comparison, the curve for cnoidal waves proposed by Tanaka *et al.* (2000), based primarily on the results of a  $\kappa$ - $\varepsilon$  boundary layer model, is shown on Figure 6.11. The two curves are somewhat similar in shape, as both demonstrate an increase in the critical value of  $RE$  with progressively higher asymmetry; however, in absolute terms they exhibit several differences also. The laboratory and numerical studies of Hino *et al.* (1976) and Tanaka *et al.* (2000) respectively, identified that transition at very low asymmetry ( $R=0.5$ ) occurs at  $RE=550$  ( $Re=1.51\times 10^5$ ). In the present study, an alternative value of  $RE=566$  was used as a fixed origin in the fitted curve corresponding to the generally accepted value of  $Re=1.6\times 10^5$ , for transition over smooth beds (Sleath, 1984). From Eq. 6.1, the latter may not accurately represent transition for flows  $T<3.5s$ , but is still suitable for larger  $T$ . The value of Tanaka *et al.* is lower still and is more representative of small  $T$  ( $\sim 2.8s$ ) in the data sets presented herein. As it is not clear whether the form of the asymmetric relationship should vary with  $T$  (as well as  $R$ ) it is possible that the curve of Tanaka *et al.* is more representative of small values of  $T$ . The second-order Stokes and cnoidal curves also exhibited stronger disagreement at  $R\geq 0.65$ , at which point cnoidal flows appeared to stabilise the boundary layer to a greater extent than the equivalent second-order Stokes flow.

## 6.4. Results: Rough beds

### 6.4.1. Sinusoidal flows

The observations of Li (1954) and Manohar (1955), relating to sinusoidal flows, were used in combination with the asymmetric crest and trough data of the present study to provide 308 observations of the transition to turbulence. These represent 10 grain sizes within the range  $D=0.025\text{-}1.38\text{cm}$  and oscillatory periods in the range  $T=0.9\text{-}15\text{s}$  for all grain diameters (but in some cases as high as  $T=34\text{s}$ ). In the experiments of Li and of Manohar, transition was determined by observing the dispersion of dye over a fixed granular bed, using an oscillating trolley apparatus, i.e. a variation upon the visual observation method. These data were analysed for sensitivity to the experimental parameters using two methods, namely: ‘critical length-scale’; and ‘critical time-scale’ methods.

#### 6.4.1.a. Critical length-scale method

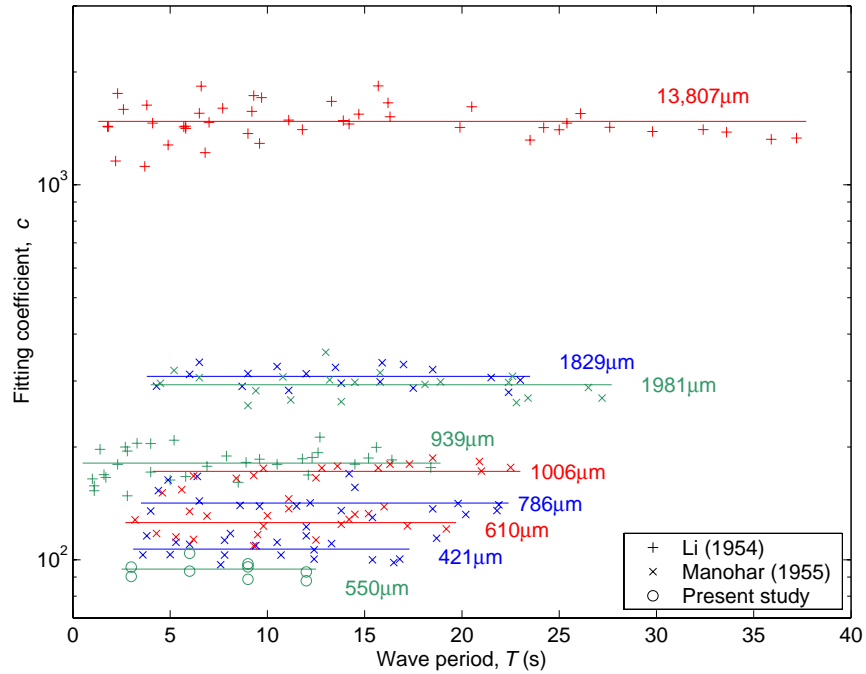
It was observed that the coefficient  $c=\text{Re}_{\text{crit}}/(a/D)$  was nearly constant with  $T$ , for all  $D\geq 421\mu\text{m}$  (Figure 6.12); likewise, that the mean value of  $c$  increased linearly then with  $D$  (Figure 6.13). A significant negative linear correlation was observed between  $c$  and  $T$ , for  $D\leq 275\mu\text{m}$ , within the experimental range (Figure 6.14). From these relationships,  $\text{Re}_{\text{crit}}$  was described by

$$\begin{aligned} \text{Re}_{\text{crit}} &= \left( (1.32 \times 10^5 D) + 46 \right) \times (a/D) && \text{for } 421\mu\text{m} \leq D \leq 13807\mu\text{m} \\ \text{and} &&& \\ \text{Re}_{\text{crit}} &= \left( (-2.4T) + 107 \right) \times (a/D) && \text{for } 235\mu\text{m} \leq D \leq 275\mu\text{m} \end{aligned} \tag{Eq. 6.5}$$

Rearranging Eq. 6.5, this relationship may be expressed instead in terms of a critical grain Reynolds number,

$$\begin{aligned} \frac{U_{\infty} D}{\nu} &= \left( 1.32 \times 10^5 D \right) + 46 && \text{for } 421\mu\text{m} \leq D \leq 13807\mu\text{m} \\ \text{and} &&& \\ \frac{U_{\infty} D}{\nu} &= \left( -2.42T \right) + 107 && \text{for } 235\mu\text{m} \leq D \leq 275\mu\text{m} \end{aligned} \tag{Eq. 6.6}$$

This approach avoids the explicit use of  $a$  in both the predictive and resultant equations. This is advantageous, as the quantity  $a$  is not always easily extracted from field or laboratory observations, especially in the presence of flow asymmetry.



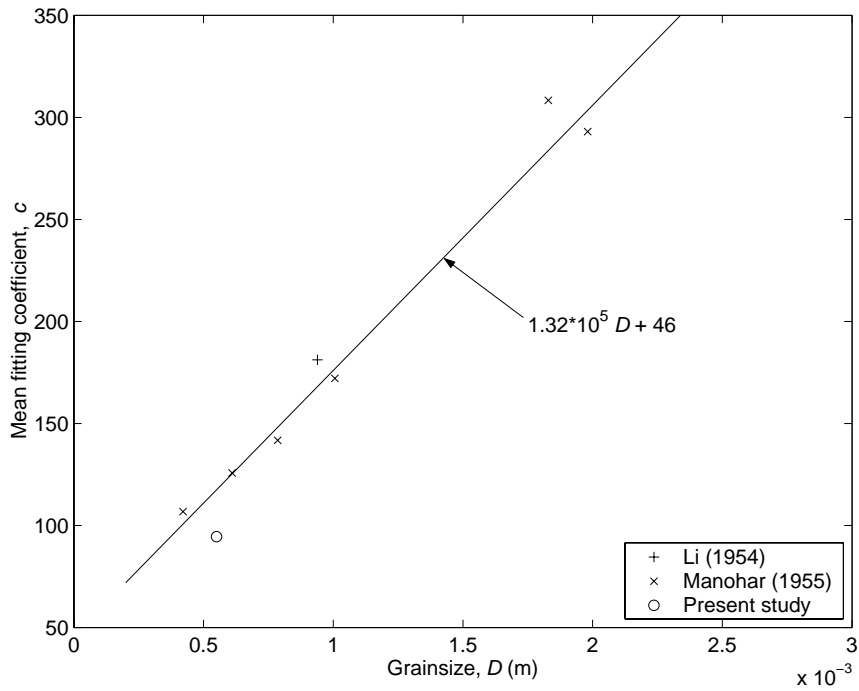


Figure 6.13. The observed transition to turbulence over rough beds, under sinusoidal oscillatory flows for  $D \geq 421 \mu\text{m}$ : trend analysis of the mean value of  $c$  with  $D$ .

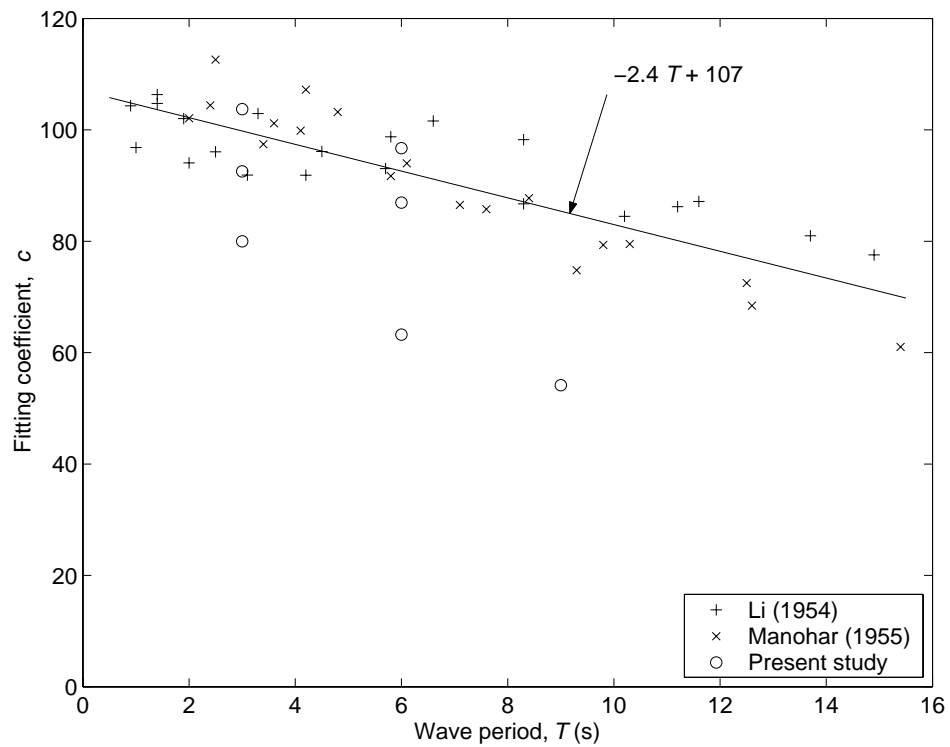


Figure 6.14. The observed transition to turbulence over rough beds, under sinusoidal oscillatory flows for  $D \leq 275 \mu\text{m}$ . The linear dependence of  $c$  on  $T$ , together with the suggested fit to the data are shown.

Predicted values of  $Re_{crit}$  (using Eq. 6.1 and Eq. 6.5 for smooth and rough bed observations, respectively) are compared to the observed data in Figure 6.15. The error was of the order  $\pm 8.2\%$  of the observed value, for the data sets of Li (1954) and Manohar (1955). A similar degree of scatter ( $\pm 10\%$ ) was observed for the asymmetric data from the present study; however, the results were, on average, over-predicted by approximately 20%. If the predicted values of  $Re_{crit}$  were used then to calculate values of  $S_{crit}$ , this corresponded to error of only 4% and 8%, respectively.

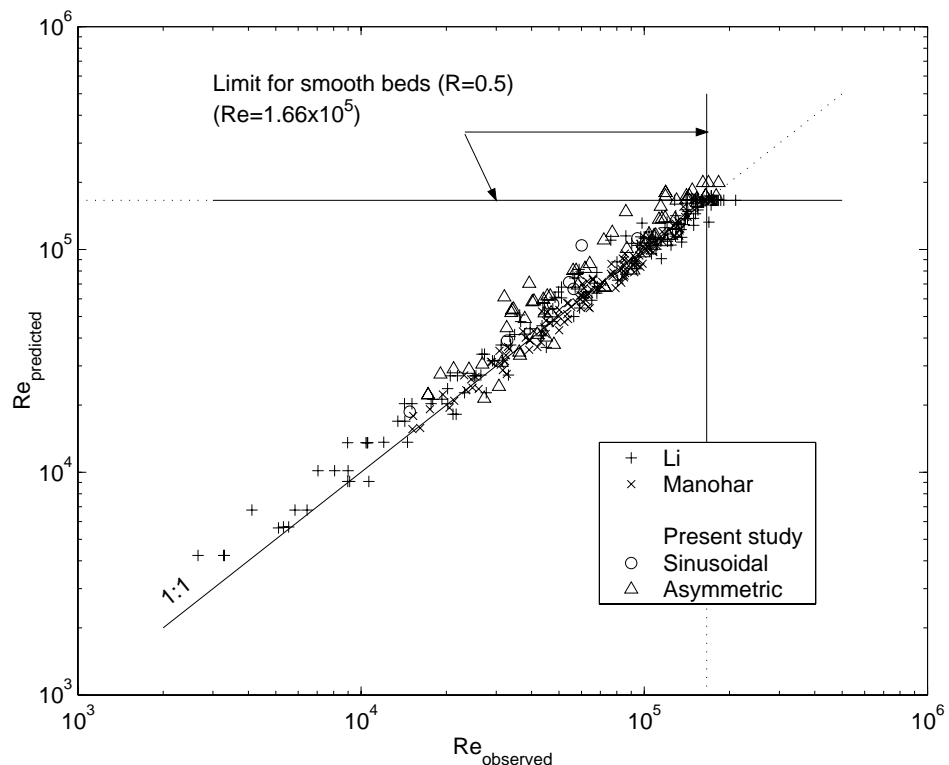


Figure 6.15. Comparison of observed values of  $Re_{crit}$  over flat, rough (granular) beds and those predicted using Eq. 6.5.

#### 6.4.1.b. Critical time-scale method

Direct correlation between  $Re_{crit}$  and the parameters  $T$  and  $D$  was investigated separately. As illustrated in Figure 6.16, all the rough beds in the range of the experimental data exhibited a linear relationship with  $T$ , up to a maximum value ( $Re=1.66 \times 10^5$ ). In this diagram, data subsets representing experiments undertaken over beds of different  $D$  are highlighted. The gradient of each linear fit is plotted, against  $D$ , in Figure 6.17 and a regression line was drawn using a least squares method. These relationships can be summarised by

$$Re_{crit} = T \left( 2400 \times e^{5.73 \times 10^{-4} / D} \right) \quad \text{for } 240 \mu\text{m} < D < 13807 \mu\text{m} \quad \text{Eq. 6.7}$$

with an upper limit of  $1.66 \times 10^5$ . Eq. 6.7 reflects a positive linear relationship between  $Re_{crit}$  and  $T$ , where the gradient decreases with  $D$  but the intercept remains constant (zero). This gradient increases sharply with decreasing  $D < 421 \mu\text{m}$  but becomes almost constant for  $D > 2000 \mu\text{m}$  with a smooth transition between the two conditions. Eq. 6.7 attempts to combine the two conditions observed in Eq. 6.5.

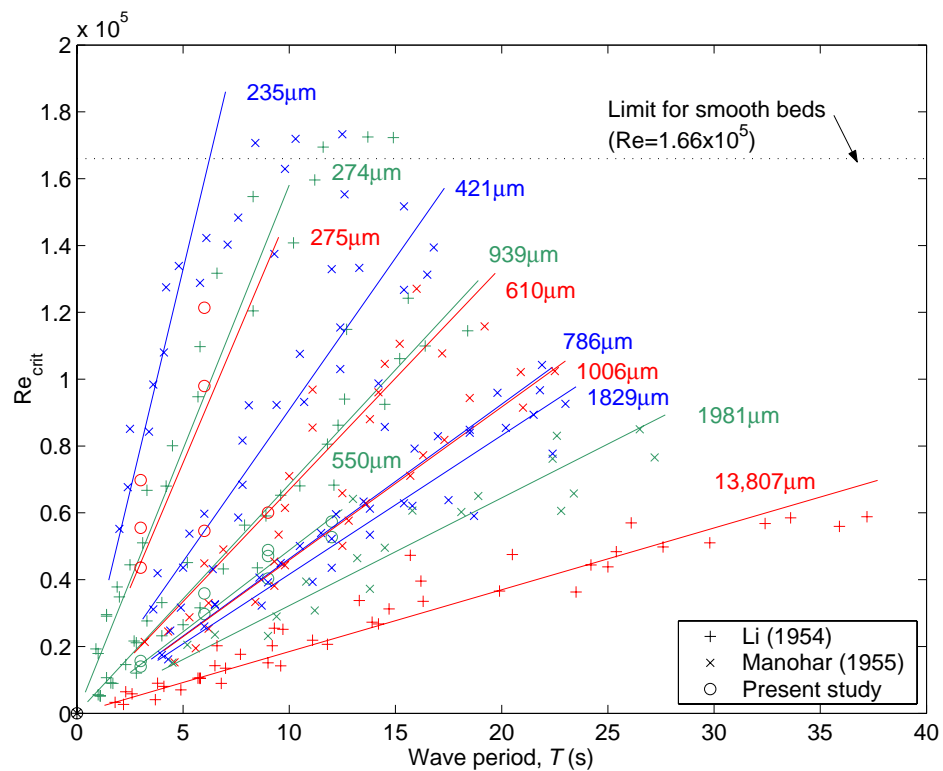


Figure 6.16. The observed transition to turbulence over rough beds, under sinusoidal oscillatory flows, for all values of  $D$ : linear dependency of  $Re$  with  $T$  and the limiting ‘smooth bed’ condition are demonstrated. Colours have been used to differentiate between groups of data, corresponding to different values of  $D$  (as indicated).

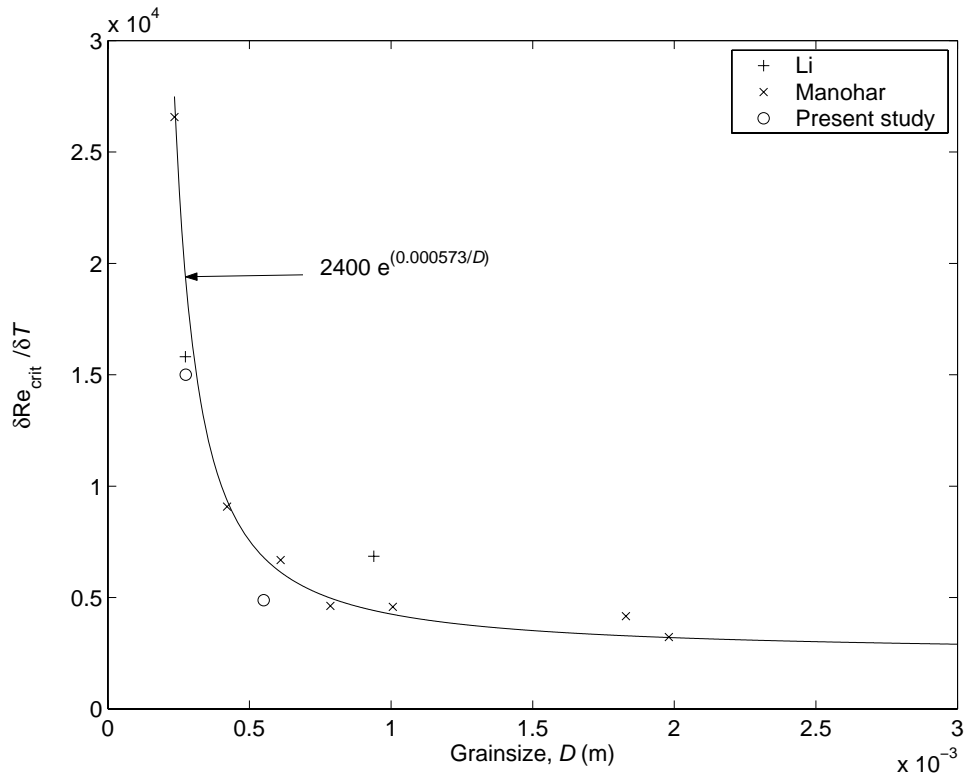


Figure 6.17. The observed transition to turbulence over rough beds, under sinusoidal oscillatory flows, for all  $D$ : variation of the gradient ( $\delta Re / \delta T$ ) with  $D$  is illustrated.

Predicted values of  $Re_{crit}$  (using Eq. 6.1 and Eq. 6.7 for smooth and rough bed observations, respectively) are compared to the observed data in Figure 6.18. Although the trend analysis highlighted clear relationships, the mean scatter in absolute error of predicted values from Eq. 6.7 was increased by a factor of 2, over that from Eq. 6.5.

The observed trends in transition to turbulence over smooth and rough beds, for sinusoidal flows (as described by Eq. 6.1 and Eq. 6.7), are summarised graphically in Figure 6.19.

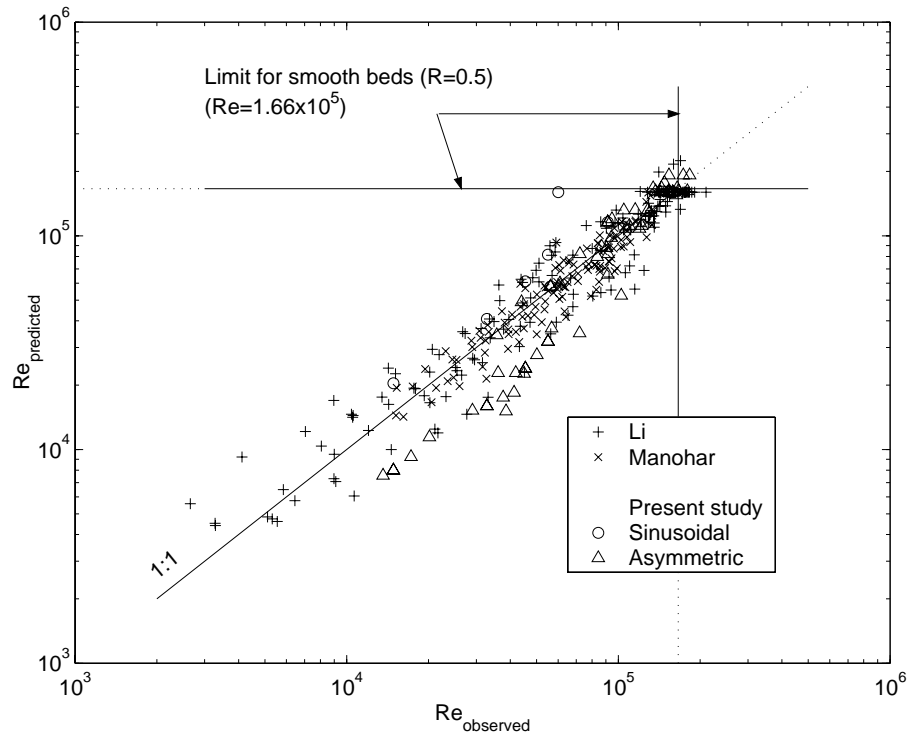


Figure 6.18. Comparison of the observed values of  $Re_{crit}$  over flat, rough (granular) beds and those predicted using Eq. 6.7, incorporating the sinusoidal data of Li (1954), Manohar (1955) and the present study.

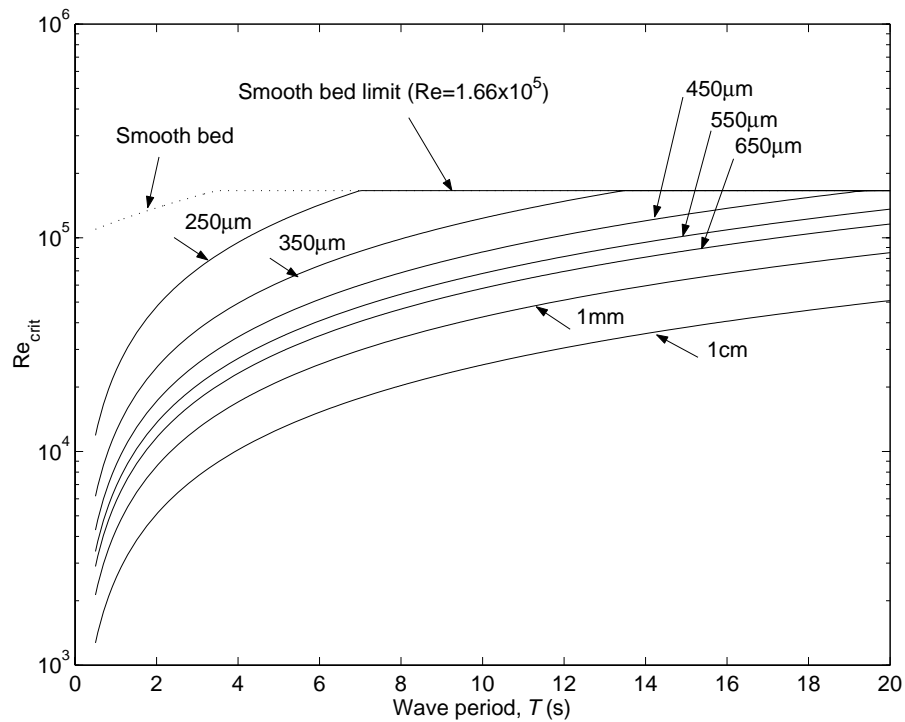


Figure 6.19. The predicted transition to turbulence under sinusoidal oscillatory flows (Eq. 6.3 and Eq. 6.7).

## 6.4.2. Asymmetric flows

The transition to turbulence data collected over hydrodynamically rough beds, under asymmetric flows, are shown in Figure 6.20; these were constructed in the same manner as Figure 6.10. For clarity, these Figures contain only those observational data identified as being the transition to turbulence; they are sub-grouped in relation to  $T$ . The data from the  $D=275\mu\text{m}$  experiments contain extensive scatter; as such, it was deemed inappropriate to fit curves to these data in this format. The data from the  $D=550\mu\text{m}$  experiments demonstrate clearer relationships and, as such, curves were fitted using a least square analysis applied to Eq. 6.3. The resulting fitting coefficients may be found in Table 6.2. Scatter in these data increased at larger values of  $T$ , [Note: the  $T=12\text{s}$  curve is fitted to only a small range of data ( $R=0.5-0.55$ )].

$T$ (s)	Fitting coefficients		
	i	j	k
3	181	3500	1.971
6	243	2337	1.553
9	279	3138	1.722
12	311	3440	1.472

Table 6.2. Fitting coefficients for Eq. 6.3, describing the transition to turbulence over a rough bed ( $D=550\mu\text{m}$ ), for second-order Stokes flows as observed in the present study.

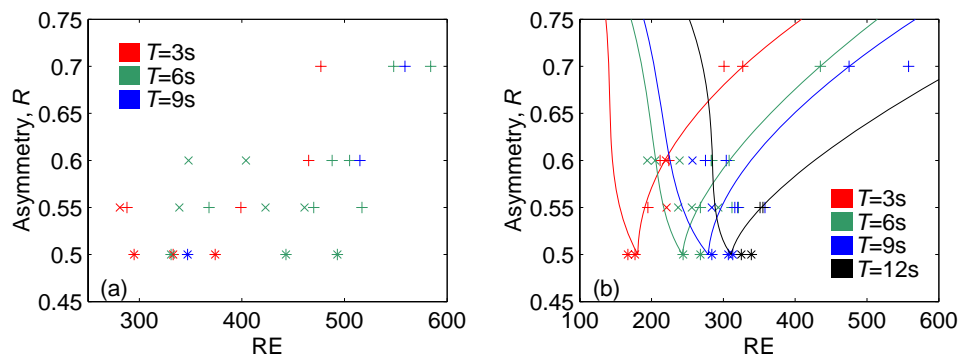


Figure 6.20. Stability of the oscillatory boundary layer over a flat, rough (granular) bed: (a)  $D=275\mu\text{m}$ ; (b)  $D=550\mu\text{m}$ . **Key:** Transition to turbulence observed under the crest (+) and trough (x) half cycles, in the present study; solid line – least squares fit to crest data (Eq. 6.3 and Table 6.2, incorporating Eq. 6.5) and corresponding curve for the trough (Eq. 6.4 – not based on data). Colours are used to identify data subsets of different  $T$ .

In Figure 6.20b, it was noted that the shape of the curves, for any  $T$ , was similar. By extending this assumption to all grain sizes, the effect of flow asymmetry was reanalysed subsequently; it was described as a scalar increase in  $Re_{crit}$ , from the equivalent  $R=0.5$  case (calculated using Eq. 6.1, Eq. 6.5 or Eq. 6.7), which varied then with  $D$ . The data were normalised to the  $R=0.5$  case and fitted to a relationship of the form

$$Re_{c\ crit} = Re_{crit} \times (1 + j(R - 0.5)^k) \quad \text{Eq. 6.8}$$

and

$$Re_{t\ crit} = (Re_{c\ crit} / R) \times (1 - R)$$

The fitting coefficients  $j$  and  $k$ , for the normalised data, are summarised in Table 6.3; they are shown graphically in Figure 6.21. This empirical approach had the advantage of making fewer assumptions about the nature of the inter-relationships between  $Re$ ,  $R$ ,  $T$  and  $D$ .

Bed	Fitting coefficients	
	j	k
Smooth bed	6.2	2.133
$D=275\text{mm}$	12.7	1.960
$D=550\text{mm}$	12.7	1.470

Table 6.3. Fitting coefficients for Eq. 6.8, describing the transition to turbulence for second-order Stokes flows, as observed in the present study.

Of the three beds investigated, the relationship derived for the  $D=275\mu\text{m}$  bed coincided most closely with the case where  $S_{crit}$  remains roughly constant; at the same time, all other related parameters ( $U_c$  and  $Re$ ) increase simply as a function of  $R$ . This idealised relationship is approximated closely by [ $j=1.23$ ,  $k=0.840$ ]. In comparison,  $S_{crit}$  decreased with  $R$  in the smooth bed case; it increased with  $R$  in the  $D=550\mu\text{m}$  case. Over smooth beds, transition takes place initially during the crest half cycle; only then, under the trough, following further increases in the flow amplitude. On some occasions over the  $D=550\mu\text{m}$  bed, transition was observed to occur under the trough at a lower value of  $RE$  than predicted by the second part of Eq. 6.8, i.e. at smaller  $a_{crit}$  for a given  $T$  and  $R$ . The significance of this observation is that transition is occurring initially in the trough, whilst flow under the crest remains laminar. Insufficient observations of this occurrence were made in order to be able to quantify the conditions where this would occur.

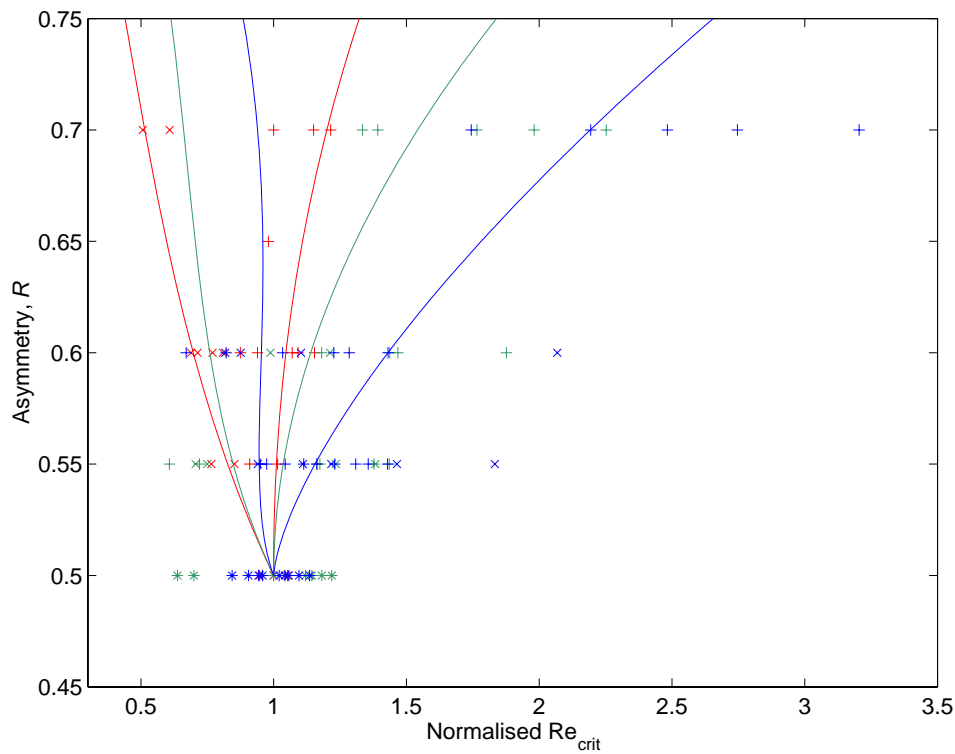


Figure 6.21. Normalised increase in  $Re_{crit}$  caused by flow asymmetry for observations made under the crest (+) and trough (x) half-cycles. Best fit curves for data from the smooth bed (red lines and data),  $D=275\mu\text{m}$  (green lines and data), and  $D=550\mu\text{m}$  (blue lines and data) experiments (Eq. 6.8 and Table 6.3).

### 6.5. Discussion: Processes regulating the transition to turbulence over smooth and rough beds.

Differences in the smooth and rough bed relationships suggest that the balance between rates of fluid acceleration, sources of initial flow perturbation, velocity distribution and time-scales are important in regulating the development of turbulence. Over relatively smooth beds, the initial source of flow perturbation is fluid shear in the vertical velocity profile. When destabilising shear becomes large, with respect to other stabilising forces, turbulence is initiated. It follows that, under laminar flows, the vertical gradient in horizontal velocity and, therefore, the transition to turbulence are proportional to  $T$ . Conversely, over very rough beds, initial flow perturbation is caused by eddies shed from individual roughness elements. In this case, the strength of eddy development and, therefore, the transition to turbulence are proportional to  $D$ . From Eq. 6.7, smooth bed processes dominate for  $D < 400\text{--}500\mu\text{m}$ , whilst rough bed processes dominate for  $D > 2000\mu\text{m}$ . Intermediate grain sizes experience a balance between both processes. A similar pattern (without reference to wave period effects) has

been observed for transition over rippled beds, of increasing ripple steepness (Sleath, 1975). As analogous processes, these observations are likely to be related by similar mechanisms but are made at different length-scales.

The above arguments may be applied also to the less straightforward case of asymmetric flows. Under the crest, there is an increase in vertical gradients of horizontal velocity and flow rates around roughness elements (the principle destabilising processes over smooth and rough beds, respectively (see above)) with smaller  $T$  and/or larger  $R$ . These destabilising processes are balanced by the associated increases in flow acceleration (a known stabilising process); likewise, by corresponding decreases in the time available for the development of turbulence in the deceleration phase. The opposite pattern can be identified, when considering the transition to turbulence under the trough. Here, vertical gradients in horizontal velocity and the flow rate around individual grains are reduced, but are associated also with lower rates of fluid acceleration and a longer time-frame for the development of turbulence. The data show that the balance of forces is primarily grain size-dependent; it is likely also to be period dependant. As  $R$  increases, it seems that stabilising processes increase at a lower rate than destabilising processes for smooth beds; the opposite is true for rough beds. This balance is apparently maintained over beds of  $D \approx 275 \mu\text{m}$ . It is anticipated that a larger data set, with a greater range and resolution of flow parameters, will demonstrate non-linear relationships similar in form to that for smooth beds as shown in Figure 6.4; these are a function of both  $T$  and  $D$ .

The relationship proposed by Tanaka *et al.* (2000), together with the relationship derived on the basis of the present study, exhibit stronger disagreement at  $R \geq 0.65$ , at this point, cnoidal flows appeared to stabilise the boundary layer to a greater extent, than the equivalent second-order Stokes flow. On the basis of comparison between second-order Stokes and cnoidal flow theory (described in Sections 2.5 and 2.6, respectively, see also Section 5.6.2), under second-order Stokes flows, the rates of fluid acceleration/deceleration are typically lower around the crest, than under the equivalent cnoidal flow; mid-boundary layer velocity gradients are slightly larger. These differences are initially very small, prior to the development of the secondary ‘hump’ in the trough part of the velocity cycle of the second-order Stokes model; latterly, they increase abruptly. This deviation is apparent initially at  $R=0.63$ , but does not become significant until approximately  $R=0.65$ . The coincidence of the above observations suggests that the inclusion of additional harmonics may have an enhanced, stabilising, effect in the case of smooth beds; it supports further the proposed importance of fluid acceleration, in the regulation of turbulence. The appropriate inclusion of

---

higher harmonics in different conditions and the relative validities of water wave theories are discussed elsewhere (e.g. Dean, 1970; Le Mehaute, 1976; Sleath, 1984).

### **6.6. Discussion: Implications for the interpretation of previous studies concerning the transition to turbulence.**

The strong relationships highlighted in the present study, particularly in relation to wave period but also with grain size, do not appear to have been included in studies relating to the transition to turbulence, or in the formulation of other equations related to the presence of turbulence, e.g. the wave friction factor, or the threshold of motion for sediment.

Previous studies that do not represent the effect of wave period typically use data sets representing only a small range of  $T$ . Numerical modelling studies tend to select arbitrary values of  $T$ ; indeed, they may not state the value used at all. As such, it is not clear from the existing literature whether the period dependency observed in the laboratory data, would be replicated by modelling a range of  $T$ . Similar limitations in the range of  $T$  are present in the detailed, high-resolution laboratory studies of Jensen *et al.* (1989) and Lodahl *et al.* (1998), for smooth beds. In these studies, almost all of the experiments were undertaken using  $T=9.72$ s and 10s, respectively. However, because smooth beds were used, the present study suggests that the results presented therein are representative of all sinusoidal flows, for  $T>3.5$ .

The ‘ $LS$ ’ and ‘ $LR$ ’ design curves of Jonsson (1966), for the onset of transition over smooth and rough beds, respectively, were based upon observations made by other researchers using wave channels; these would permit only a limited range of  $T$  (typically <4-5s) and, furthermore, the data represented only a small range of  $D$ . A range of  $Re_{crit}$  was observed in the smooth bed data used to create these curves (as would be expected, given the range of  $T$ ); however, only the mean value was used. The rough bed data followed a relationship similar to that of Manohar (1955), where  $Re_{crit}=(constant \times a/D)$ ; once again, this does not allow for variation of the solution with  $D$  or  $T$ . Jonsson (*op. cit.*) presents the smooth bed limit suggested by Li (1954) for comparison; however, neither this value, nor the large data sets of Li or of Manohar, are incorporated into the diagrams. The reason given for this was that differences existed in the methodology used for the definition of threshold, although no specific argument was presented.

As a third example, the relationship proposed by Manohar (1955) exhibited clear disagreement between both its own observations and those of Li, at large  $D$ ; this is even

---

though a large data set, with a broad range of flow and sediment variables, was available. This limitation may be attributed in part to the lack of (personal) computing power available in the 1950's. In contrast, during the present study, the ability to rapidly manipulate and plot large data sets has been invaluable.

The findings of the present study are relevant when comparing the findings of studies undertaken at small values of  $T$  (i.e. most wave channel or wave basin experiments) and/or  $D$ , to those at large values of  $T$  (oscillating trolleys or water tunnels and field observations) and/or  $D$ . However, these effects alone are not sufficient to explain the difference between the observations of transition made using an oscillating trolley (Li, 1954; Manohar, 1955) and a wave channel (Vincent, 1957; and, Lhermitte, 1958) (see Section 2.9.1). Therefore, differences in observational methodology or, to a lesser extent, the selection of flow simulation equipment, may still cause disagreement between the results. Insufficient data were available from the literature, to investigate whether the patterns observed in oscillating trolley data could be transferred to such observations under surface gravity waves, either in the laboratory or in the field. The principle physical difference between the two situations is the absence of the (correct) horizontal pressure gradient, when using an oscillating trolley; also, to some extent, an oscillating water tunnel. Whilst it is not likely that this additional force will affect significantly the observed period dependency, the absolute values of  $Re_{crit}$  may be reduced. As such, the design diagram of Jonsson (1966) might be considered to better describe conditions resulting from free surface gravity waves in some circumstances, even though wave period dependency is not accounted for explicitly.

### **6.7. Discussion: Implications for future studies concerning the transition to turbulence.**

The accurate estimation of the initial transition to turbulence is important, in almost all areas of study in the field of sediment dynamics. However, detailed observations and analysis of flow parameters within the transitional range are presently limited. Once it is possible to define the Reynolds number at which transition will occur, it becomes possible to analyse experimental data (e.g. threshold of motion or transport rates for relatively fine sediments) in terms of relative position in the transitional range. It becomes also possible to calculate values of characteristic flow variables (e.g. flow velocity or shear stress) from laminar theory corresponding to the marginal laminar-transitional case. These may be used then, with greater confidence, in conjunction with equations predicting the corresponding value at the marginal transitional-turbulent case, to aid investigation of the change in such parameters over the transitional range. Knowledge relating to, and the ability to predict the characteristic

---

boundaries of the transitional range might be considered important in a variety of fluid- and sediment-dynamics applications. This principle is applied to the effect of wave period and asymmetry on the wave friction factor in Sections 7.3.5 and 7.4.3.

In order to represent accurately the differences associated with  $T$  when investigating the transition to turbulence, smooth bed experiments similar to those described herein should be undertaken using  $T > 3.5$ s. Smooth bed experiments using  $T < 3.5$ s, together with all rough bed experiments should be conducted over a wide range of  $T$ . The results should be analysed in terms of  $\delta/\delta T$ , as well as differences attributed to other experimental variables, e.g.  $R$  or sediment roughness properties. Future laboratory investigations considering the effect of wave asymmetry should be similarly broad in the range of  $R$  studied; results should be analysed in terms of both  $\delta/\delta R$  and  $\delta/\delta T$ . Investigators should consider carefully the selection between second-order Stokes and cnoidal or other higher-order theories. This selection is made on the basis of model validity for the particular shallow water conditions being investigated; results will likely differ for values of  $R > 0.65$ , if comparison is made with observations made using a different wave model.

These suggestions are based upon the findings of the present study. Therefore, until further work has been undertaken to compare these with data collected using other equipment (wave channels and basins, in particular), these are best suited to experiments undertaken using oscillating trolleys and possibly oscillating water tunnels. It is not clear to what extent the absolute values and relationships presented herein may be applied to wave channels, wave basins or to the field. However, the evidence predicting strong effects of wave period and flow asymmetry, in oscillatory flows, however created, is compelling.

## Chapter 7. Threshold of Motion

### 7.1. Introduction

Observations of the threshold of motion, made under sinusoidal oscillatory flows during the present study, were used in conjunction with similar observations collected previously in the laboratory studies of: Bagnold (1946); Manohar (1955); Hammond and Collins (1979); and Tomlinson (1993). All of these latter observations were made using various designs of oscillating trolley, similar to that used in the present study. These data have provided 516 observations of the threshold of motion for sand in the range  $100 < D < 8000 \mu\text{m}$  and  $1050 < \rho_s < 7900 \text{kgm}^{-3}$ . Simulated conditions were in the range  $0.76 < T < 26.1 \text{s}$  and maximum  $S = 1.27 \text{m}$ , corresponding to  $0.04 < U_\infty < 0.47 \text{ms}^{-1}$ . In addition, the present study provided an additional 537 observations of the threshold of motion under asymmetric (second-order Stokes) oscillatory flows; of these, approximately half the number represented standard observations, repeated periodically for the analysis of observational continuity and/or error. These data were in the range  $275 < D < 1550 \mu\text{m}$ ,  $1450 < \rho_s < 2750 \text{kgm}^{-3}$ ,  $3 < T < 10 \text{s}$ ,  $0.5 < R < 0.7$  and maximum  $S = 1.00 \text{m}$ , corresponding to  $0.16 < U_c < 0.45 \text{ms}^{-1}$ .

In this Chapter, patterns observed in the critical flow parameters are presented. Investigations are described which were undertaken in order to better understand the processes causing changes in  $\tau_{\text{crit}}$ , observed herein and in a small number of previous investigations, to be associated with wave period and flow asymmetry; these were conducted primarily to extend the understanding of the processes controlling the threshold of motion for sand. However, at the same time, they provide new relationships to predict such conditions and other related flow parameters.

### 7.2. Results: Critical flow parameters

Threshold observations were compared in terms of three critical flow parameters, namely: stroke length; peak outer layer velocity; and peak bed shear stress. This Section summarises the general trends observed in the critical stroke length and outer layer velocity data. Patterns in peak shear stress are addressed, in more detail, in Sections 7.3 and 7.4.

#### 7.2.1. Sinusoidal flows

The critical stroke length,  $S_{\text{crit}}$ , causing the threshold of motion was proportional to  $T$  for a given grain size,  $D$  (Figure 7.1a). Therefore, the ratio  $S/T$  was nearly constant for given  $D$ . As a result, the critical outer flow speed amplitude,  $U_{\infty \text{crit}}$ , was also nearly constant over a

---

broad range of  $T$  (Figure 7.1b). Increased deviation from this pattern ( $\delta U_{\infty \text{ crit}}/\delta T > 0$ ) can be seen for observations where the intercept value of  $T$  (where  $S_{\text{crit}}$  approaches zero, see Section 2.13) becomes significant; this coincided typically with large sediment grains of low density and an associated shift in the intercept of the curve  $S_{\text{crit}}$  against  $T$  (see below). Although this pattern is clearly visible in the data, it has been suggested by Sleath, (*Pers. Comm.*) that (for similar experiments relating to the transition to turbulence over smooth beds) this observation might be influenced potentially by an increase in acceleration forces or deviation from true sinusoidal motion by oscillating trolley equipment when simulating very small wave periods (e.g.  $T < 3\text{s}$ ); this effect is not considered to affect the observed trends in the data at longer wave periods. Figure 7.1 illustrates these patterns for a selection of the available data; these incorporate observations from each of the independent investigators and represent the full range of flow and grain parameters. It should be noted also that the relationship between  $U_{\infty \text{ crit}}$  and  $S_{\text{crit}}$  causes the critical Reynolds number ( $Re$ ) to follow a proportional positive linear relationship with  $T$ . You (2000) has provided previously an empirical relationship (Eq. 2.36) for  $S_{\text{crit}}$ , based upon a number of threshold data sets; these include some of those utilised here. For the majority of the data,  $s_*$  values were sufficiently small that the intercept of the linear relationships was considered to be zero, in most of the cases (e.g.  $T_0=0.5\text{-}0.63\text{s}$  for quartz grains). Exceptions occur at very low sediment density (e.g.  $T_0=6.1\text{s}$  for  $\rho_s=1050$  and  $T_0=1.7\text{-}2.0\text{s}$  for  $\rho_s=1300$ ).

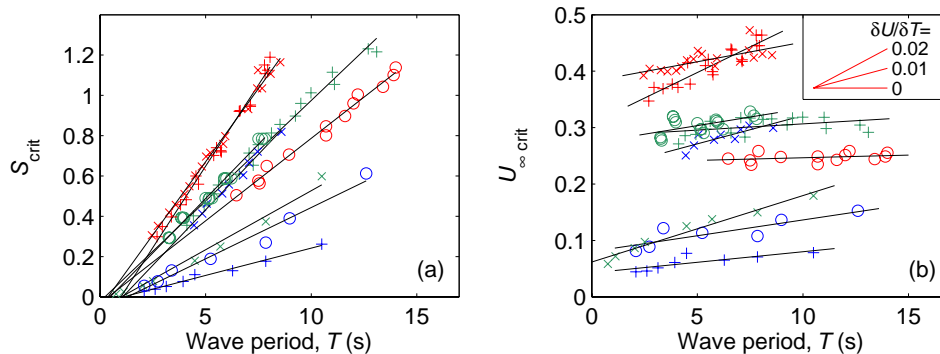


Figure 7.1.  $S_{\text{crit}}$  (a) and  $U_{\infty \text{ crit}}$  (b) causing threshold of motion in sands, representative of the range of  $D$  and  $\rho_s$  in the main dataset. Data are sourced from Li (1954) and Manohar (1955), different grain types are identified in no order using a variety of colours and marker shapes.

The gradient  $\delta S_{\text{crit}}/\delta T$  typically increased with  $D$  and  $\rho_s$  (Figure 7.2); the majority of this was attributable to  $\rho_s$ . Further analysis has shown that the residual scatter in the values is not related to any of the remaining flow or grain parameters. The direct implication of this

observation is that a larger value of  $U_{\infty \text{ crit}}$  is necessary, to achieve the threshold of motion for larger and/or denser grains. Predictive curves for the data range using Eq. 2.36 are shown also.

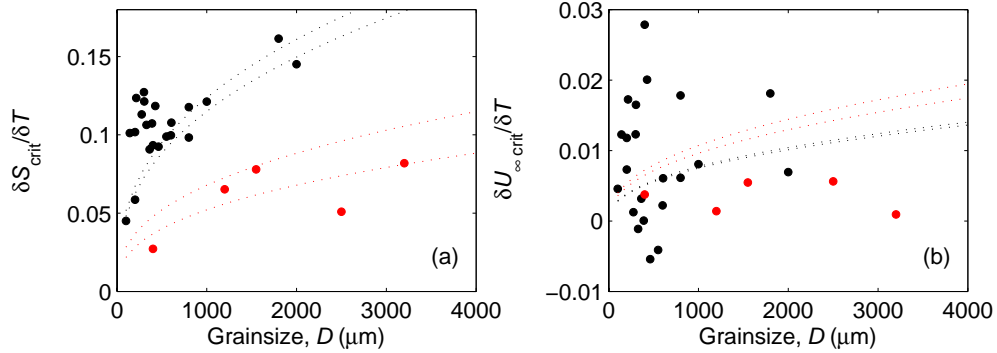


Figure 7.2. Variation of  $\delta S_{\text{crit}}/\delta T$  (a) and  $\delta U_{\infty \text{ crit}}/\delta T$  (b) with grain size for uniform sediments of density:  $2450 < \rho_s < 2700$  (black points and lines); and  $1260 < \rho_s < 1460$  (red points and lines). Also shown are the predictive curves of You (2000) (Eq. 2.36).

### 7.2.2. Asymmetric flows

The critical stroke length causing the threshold of motion is unchanged with varying  $R$ , for  $R \leq 0.65$  and given  $T$ ,  $D$  and  $\rho_s$ ; however, for  $R > 0.65$ , it tends to decrease by approximately 5-10% of  $S_{\text{crit}, R=0.5}$ . In cases where  $S_{\text{crit}}$  was considered to remain constant, the increase in  $U_{\text{c crit}}$  is, therefore, a direct function of  $R$  and followed closely Eq. 4.3.

Examples of the observed trends are shown in Figure 7.3 for quartz grains of  $D=390\mu\text{m}$ ; similar trends were observed in all cases, for the experiments undertaken in the present study. As shown in Figure 7.4, the gradient  $\delta U_{\text{c crit}}/\delta R$  increases with  $T$  and decreases with  $D$ . In the absence of observations at a similar  $D$ , the effect of  $\rho_s$  is not entirely clear; however, if the visual trend over  $D$  was extrapolated, then the effect of  $\rho_s$  was minimal (i.e.  $D$  was the dominant variable).

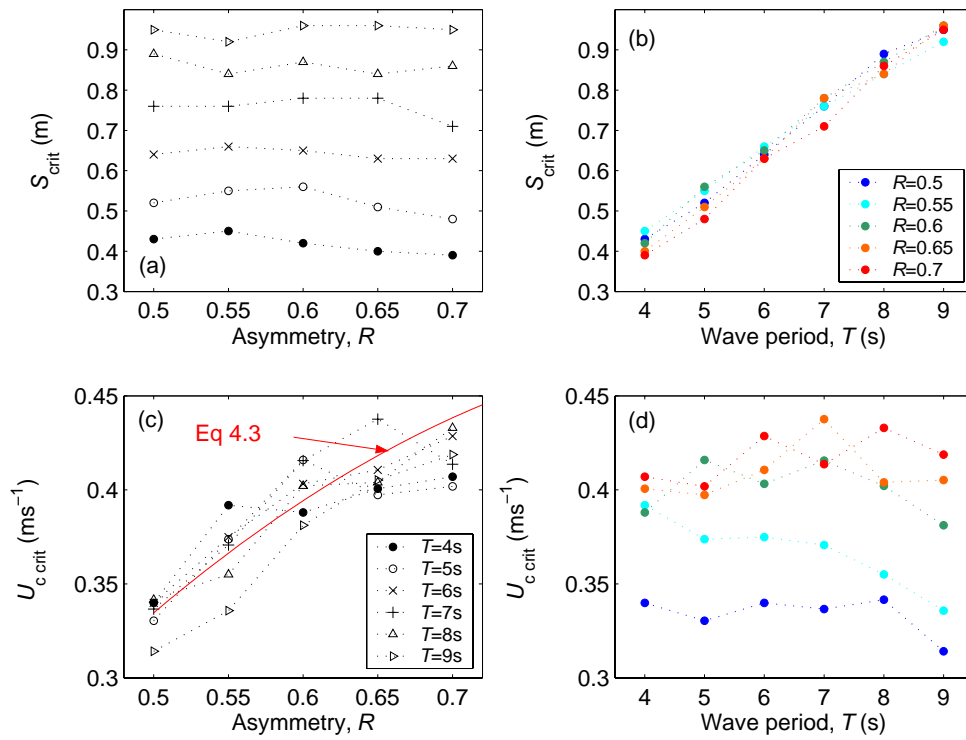


Figure 7.3. Trends in  $S_{crit}$  ((a) and (b)) and  $U_{c,crit}$  ((c) and (d)) causing threshold of motion in quartz sand,  $D=390\mu m$ , in the presence of flow asymmetry.

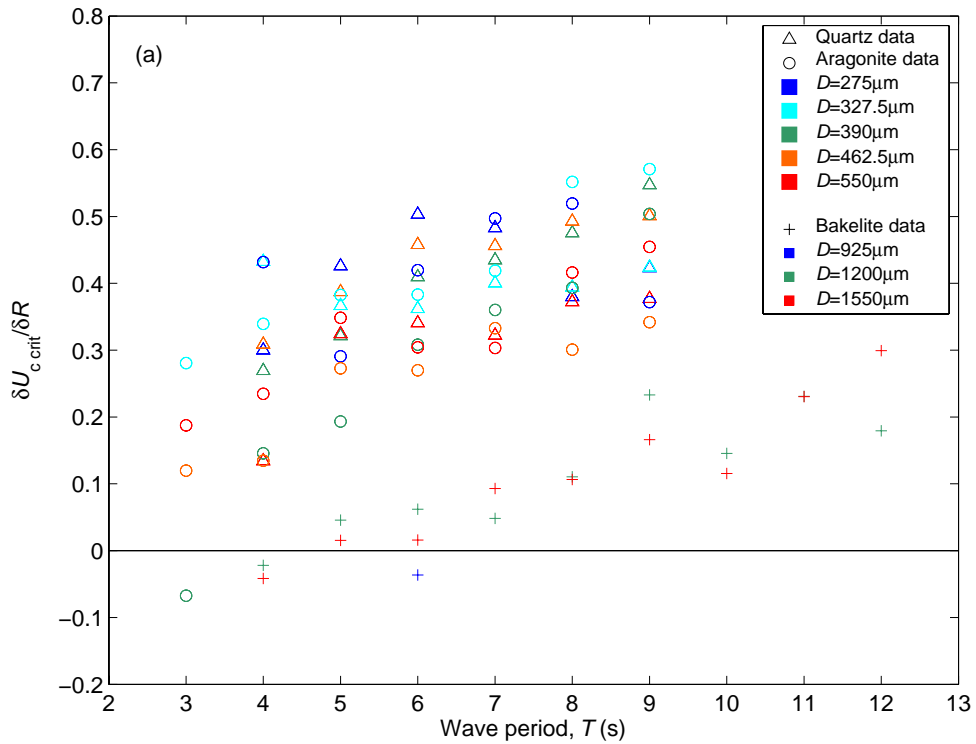


Figure 7.4 continued overleaf...

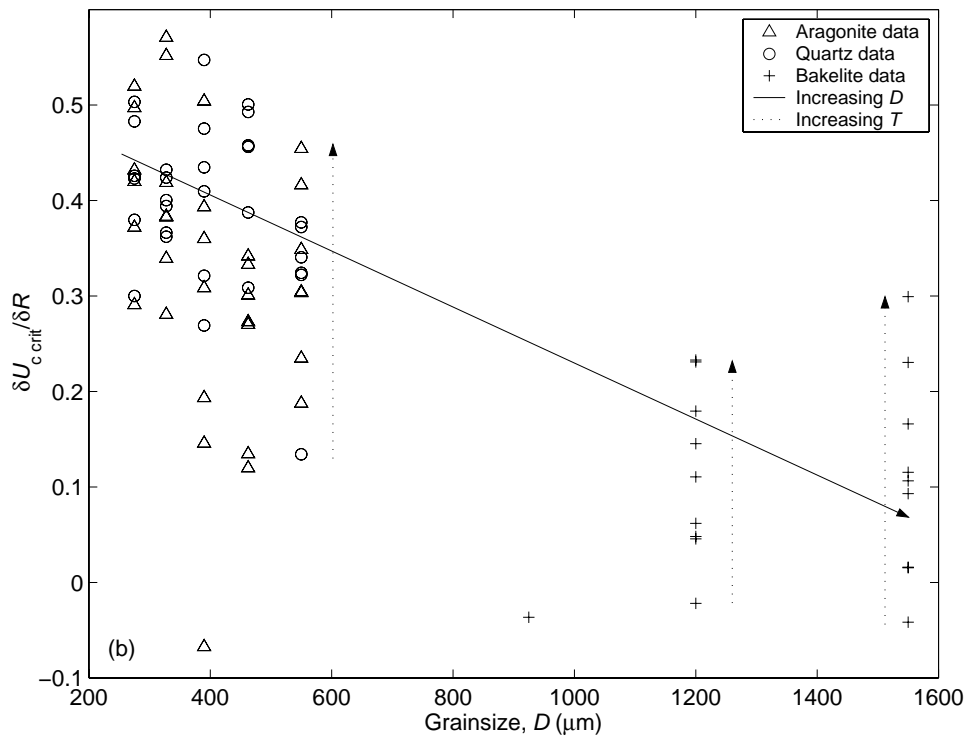


Figure 7.4. Observed  $\delta U_{c,crit}/\delta R$  with respect to wave period (a) and grain size (b).

### 7.2.3. Estimation of error.

Throughout the experimental programme, observations were made repeatedly at standard flow parameter combinations, in order to assess the magnitude of any scatter or trend in the data (reproducibility) associated potentially with the methodology. During the data collection, for any given sediment, experimental conditions were varied sequentially from  $R=0.5$  to  $0.7$  in increments of  $0.05$ . For each value of  $R$ , the wave period was then increased incrementally from small to large  $T$  over the range investigated. The actual range adopted was dependent on the response of the particular sediment within the limitations of the equipment (i.e. maximum stroke length). Additional observations were made at the following parameter combinations: for experiments  $R=0.5$ , three additional observations were made at  $T=6\text{s}$ ,  $R=0.5$ ; for  $R>0.5$ , two additional observations were made at  $T=6\text{s}$ ,  $R=0.5$  and a further three observations were made at the given value of  $R$  and  $T=6\text{s}$ . For each sediment, this provided 12 observations at  $T=6\text{s}$ ,  $R=0.5$  and 4 observations at  $T=6\text{s}$  for every value of  $R>0.5$ . Such standard observations were made at regularly-spaced intervals, throughout the experimental schedule.

For all the values of  $R$ , the variance in observed  $S_{\text{crit}}$  was within the range  $\pm 1.5$ - $2.6$ cm (2.4-4.2% of the mean of  $S_{\text{crit}}$ ) for the quartz and aragonite sediments; it was  $\pm 2.6$ - $3.2$ cm (7.6-10.3%) for the Bakelite sediments. These values correspond also to variation in  $U_{c \text{ crit}} \pm 0.8$ - $1.4$ cms<sup>-1</sup> (2.4-4.2%) and  $\pm 1.4$ - $1.7$ cms<sup>-1</sup> (7.6-10.3%); likewise, to variation in  $\tau_{0 \text{ crit}} \pm 0.034$ - $0.047$ Nm<sup>-2</sup> (8.7-11.7%) and  $\pm 0.006$ - $0.012$ Nm<sup>-2</sup> (3.0-5.8%), respectively. These values did not show any trend over time (i.e. over hours, days or weeks); as such, this would not suggest any progressive change in the visual perception (or interpretation of the threshold condition), on the part of the investigator.

### **7.3. Results: The effect of wave period on $\tau_{0 \text{ crit}}$**

#### *7.3.1. Introduction*

Voulgaris *et al.* (1995) commented that, for sinusoidal flows, a larger peak shear stress is necessary to cause the threshold of motion of sands under smaller wave periods. This observation was/has not been incorporated, latterly, by similar studies. This may be due in part to a discussion paper by You (1997) in which several of the analytical assumptions of the original paper are challenged, but were successfully repealed by Voulgaris *et al.* (1997). Values of  $\tau_{0 \text{ crit}}$ , calculated using laminar theory, normalised to the mean value observed at  $T=6$ s, using observations under both sinusoidal and asymmetric flows, is plotted in Figure 7.5 against wave period, to illustrate the general relationship. These data include all of the observations available from present and past studies. In the Figure, the effect of  $T$  is shown also to be independent of  $R$ ; this is addressed in more detail in Section 7.4.

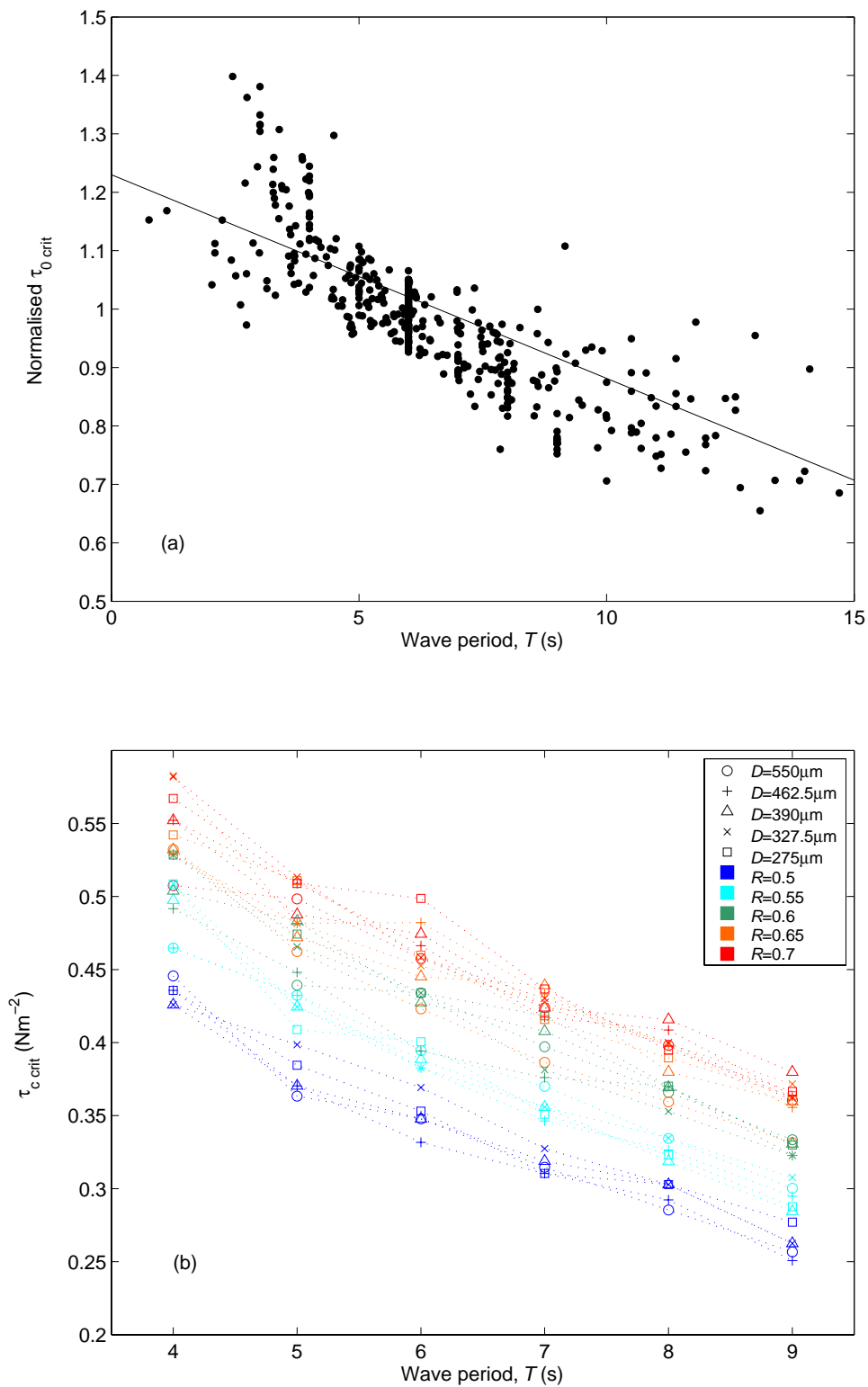


Figure 7.5.  $\tau_{c \text{ crit}}$  causing threshold of motion for: (a) all of the sinusoidal flow observations (sources listed in Section 7.1) showing values normalised to the mean of all data  $T=6\text{s}$ , also line of best fit; and (b) for selected sinusoidal and all the asymmetric flow experiments undertaken using quartz sand during the present study (actual values).

The gradient  $\delta\tau_{0\text{ crit}}/\delta T$  is strongly dependant upon the presence of turbulence within the flow. When threshold occurred under laminar flow conditions, only a small decrease in  $\tau_{0\text{ crit}}$  (5-10%) is observed with large increases in  $T$ . Marginal laminar/transitional flows exhibit a larger decrease (20-25%), whilst transitional flows decrease significantly (35-40%) over a relatively small range of  $T$ . These observations are quantified in Figure 7.6, which shows the gradient  $\delta\tau_{0\text{ crit}}/\delta T$ , against the presence of turbulence (the location of the observations in relation to laminar, transitional or fully turbulent flow has been calculated using Eq. 6.5 and Eq. 2.26).

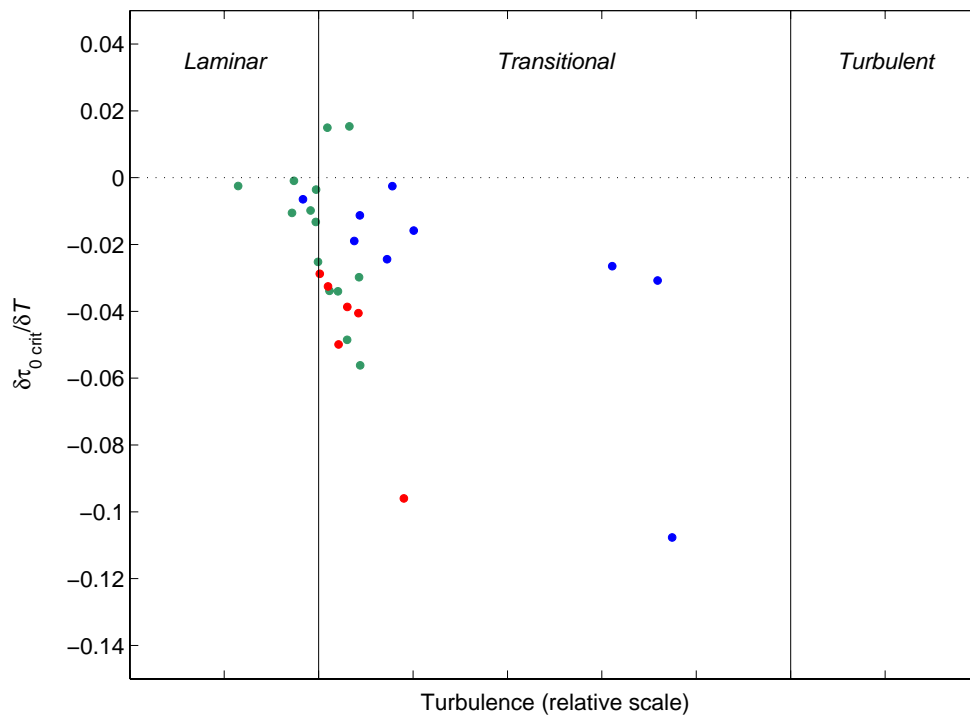


Figure 7.6. The magnitude of  $\delta\tau_{0\text{ crit}}/\delta T$  under sinusoidal flows (including all data used in the present study). Data points represent particular grain sizes, of density:  $\rho_s < 2650 \text{ kgm}^{-3}$  (blue);  $\rho_s = 2650 \text{ kgm}^{-3}$  (green);  $\rho_s > 2650 \text{ kgm}^{-3}$  (red).

On the basis of the balance of forces approach to the threshold of motion, i.e. that a single value of critical peak shear stress is necessary to erode any particular grain, the peak shear forces at threshold should be the same at all values of  $T$  for any given sediment. Agreement with this concept was closest, but not complete, in the observations made under laminar flow conditions. However, significant deviation is evident when using methods incorporated

previously into the interpretation of transitional and turbulent flows. Consequently, an alternative explanation is required.

Four general areas for study are summarised in Table 7.1, below and are addressed in turn in the following Sections. These study areas investigate the potential causes of the observations described above, either by: (a) reducing the effect of wave period on  $\tau_{0 \text{ crit}}$ , supporting the balance of forces approach; or (b) explaining the observed relationships in terms of alternative processes not accounted for by traditional approaches, (accepting such observations as a real phenomenon).

<p><u>A larger value of <math>\tau_{0 \text{ crit}}</math> is observed to be required at progressively smaller wave periods. This effect is enhanced in threshold of motion occurring under transitional flow conditions.</u></p> <p><u>Causes include potentially:</u></p>		
<b>Observational errors</b>	Observational techniques are somehow inconsistent, between small and large wave periods.	
<b>Experimental errors</b>	Inertial forces, brought about by acceleration of the grains resting on the oscillating trolley, affect the observed value of $\tau_{0 \text{ crit}}$ .	
<b>Numerical errors</b>	<i>(Laminar flow conditions)</i> Because analytical solutions for $\tau_{0 \text{ crit}}$ are used, period dependence is not likely to be due to incorrect calculation of this value.	<i>(Transitional flow conditions)</i> The difference in $\tau_{0 \text{ crit}}$ is an artefact in the data, a result of the incorrect calculation of the peak value of $\tau$ by using methods that do not include dependence on wave period.
	<b>Physical mechanisms</b> (1) The stochastic distribution of instantaneous $\tau$ under turbulent flows allows the similar occurrence of high shear events under a range of wave periods, corresponding to the observed range of $\tau_{0 \text{ crit}}$ . (2) The initial dislodgement and motion of an individual grain occurs in response to the mean or cumulative force applied over a finite time period; hence, this process is dependent upon $T$ .	

Table 7.1. Summary of potential causes of the observed dependency on wave period and flow asymmetry.

### 7.3.2. *Observational errors*

A progressive bias could have been introduced as a result of the relatively subjective visual interpretation of the threshold condition. Under shorter wave periods, grain motion might arguably be observed over a shorter time-span. As such, it is possible that the observer might interpret this as a lesser state of motion, awaiting more significant transport; this would correspond to a larger flow amplitude and, hence, larger  $\tau_0$ . However, it is unlikely that such observational errors are the primary cause of the dependency on  $T$ , for the reasons outlined below.

1. The duration of sediment transport at the threshold of motion is similar over a range of  $T$  (Section 7.5).
2. A linear relationship between  $\tau_{0 \text{ crit}}$  and  $T$  is observed over a wide range of values. Such observational errors would be largest at small  $T$ ; they would become progressively lower (latterly, insignificant) with increasing  $T$ .
3. The gradient  $\delta \tau_{0 \text{ crit}} / \delta T$  increases in the presence of turbulence. Such observational errors would likely be of similar magnitude, under different flow conditions.
4. With the various methods and individual observers represented by the combined dataset, any error in the methodology would have been apparent also as a variation between the data subsets.

### 7.3.3. *Experimental errors*

It was considered that the physical mechanism of grain motion may have been affected by additional (period dependant) forces, produced by the oscillating trolley. When using oscillating trolley equipment to investigate the motion (initial or otherwise) of mobile granular beds, an additional inertial force caused by the periodic acceleration of the plate is imparted to the grains (Section 4.4.4). Although the inertial force is not in phase with the shear force, the inertial force vector acts in the same direction as the shear force, at its peak. As such, acceleration could provide an additional destabilising or eroding force. It has been argued that if inertial forces are small in relation to the fluid shear forces, they may be discounted from such experiments. However, it is unlikely that inertial forces are a primary cause of the observed dependence on  $T$  for the reasons given below.

1. Inertial forces are typically larger, in relation to fluid shear forces, at smaller  $T$ . If inertial forces were consistently significant, then the opposite effect would be

observed, i.e. the secondary force aiding grain motion would apparently reduce  $\tau_{0 \text{ crit}}$  at smaller  $T$ .

2. Similarly large  $\delta \tau_{0 \text{ crit}} / \delta T$  were observed for grains of both low and high density. Low density grains have a reduced mass for a particular grain size; as such, they are eroded at lower velocity/acceleration amplitudes and, therefore, should be less affected by inertial forces.

The influence of inertial forces might be investigated further by using data collected using equipment which is not associated with such secondary forces, i.e. wave flumes or oscillating water tunnels. However, appropriate datasets were not readily available, from the literature available to the author.

#### 7.3.4. Numerical errors

Threshold of motion data have been evaluated, traditionally, using values of shear stress calculated from other flow parameters, i.e. rather than by direct measurement. It is proposed that previously excluded wave period dependency, in relationships for the wave friction factor ( $f_w$ ) causes the observed pattern, simply as a result of the ‘incorrect’ calculation of  $\tau_{\text{crit}}$ . An alternative method for the calculation of  $f_w$  in the rough-transitional regime is described and the effect on  $\delta \tau_{0 \text{ crit}} / \delta T$  is discussed, below.

A broad range of empirical relationships is available to describe  $f_w$ , as a function of flow and sediment parameters over (flat) rough beds. Typically, the (analytical) laminar solution is used in relation to laminar flow conditions whereas various fully turbulent solutions are used for both transitional and turbulent conditions (e.g. Jonsson, 1966; Kamphuis, 1975; Justesen, 1988; Voulgaris *et al.*, 1995, and references contained therein). In these diagrams, the transitional region was interpolated as a single line for given  $a/D$ ; data and observations in this region are considered to demonstrate significant scatter (Kamphuis, 1975). As highlighted in Voulgaris *et al.*, none of the relationships suggested previously explain, or substantially reduce, the gradient  $\delta \tau_{0 \text{ crit}} / \delta T$ ; nor do they reproduce the period dependence, observed in the transition to turbulence (as described in Chapter 6).

The friction factor diagrams presented by Jonsson (1966), Kamphuis (1975) and Justesen (1988) show  $f_w$  increasing throughout the transitional region from a single point of departure from the laminar solution, i.e. assuming a single value of  $Re$ , for all  $T$  at the transition to turbulence. An apparently near-linear interpolation is used between the laminar and fully turbulent conditions (which appears curved on log-log axes). In addition, previous authors

---

have not reported variation in  $f_w$ , as a result of  $T$ , in fully turbulent flows. Therefore, it was assumed that any differences caused by  $T$  in the transitional region become asymptotic with the fully turbulent solution, as  $Re \rightarrow Eq. 4.16$  (see Figure 7.8). Other, more detailed studies of  $f_w$  in the transitional regime, such as those undertaken by Jensen *et al.* (1989) and Lodahl *et al.* (1998) using smooth beds, did not incorporate a sufficient range of conditions in order to observe the effect of  $T$ .

A simple numerical model has been constructed, to apply the new transition to turbulence relationships from the present study to the prediction of  $f_w$  under transitional flow conditions. To this end, a number of assumptions were made, as outlined below.

That

1. Eq. 4.9 for the laminar friction factor can be applied to all (sinusoidal) laminar flows ( $Re \leq Re_{crit}$ ).
2. That Eq. 6.1 and Eq. 6.5 represent the transition to turbulence and that this condition corresponds closely to initial deviation from Eq. 4.9.
3. That the relationship of Kamphuis (1975) (Eq. 4.11) can be used for the prediction of  $f_w$  under rough turbulent flow conditions, for all values of  $T$ .
4. That the transitional region takes the form of a linear interpolation, between  $f_w$  at the point of departure from the laminar solution and the corresponding rough turbulent value.

The second part of 2 (above) was made on the basis of the modified friction coefficient diagram of Jensen *et al.* (1989) (Figure 2.7); this suggests that (for smooth beds), initial deviation of  $f_w$  from the laminar solution at the phase of peak  $\tau_o$  occurs at the same condition identified as transition over such beds ( $Re \approx 1.6 \times 10^5$ ), in the present study. However, the patterns of transition were presented graphically only in this reference and no data were found to describe, either quantitatively or qualitatively, such patterns over rough beds or the variation of such a pattern with  $T$ . The initial departure from the laminar solution for given  $a/D$  over a range of  $T$  was calculated then using the following model approach outlined below.

1. A value of  $f_w$  was chosen and the corresponding value of  $a/D$  for rough turbulent flow was calculated using Eq. 4.11.
  2. An arbitrary starting value of  $D$  (close to the expected final value) was used, to establish the corresponding value of  $a$ .
-

3. A value of  $T$  was selected and linear wave theory used to calculate  $U_\infty$  and, subsequently,  $Re$ , using  $\nu=10^{-6}$ .
4. Using Eq. 6.5, the parameters  $a/D$  and  $T$  or  $D$  were used to calculate a second value of  $Re$ , corresponding to the predicted transition to turbulence. At this stage, the two values of  $Re$  are not the same, but vary at different rates with the value of  $D$  (Figure 7.7).
5. Using solution-finding software, the variable  $D$  was then altered incrementally, until the two values of  $Re$  were identical, i.e. the combination of flow and grain parameters corresponded simultaneously to the predicted transition to turbulence, also, to the selected value of  $a/D$ . The corresponding value of  $f_w$  was calculated subsequently using Eq. 4.9.
6. Stages 2-5 were then repeated for other values of  $T$ .

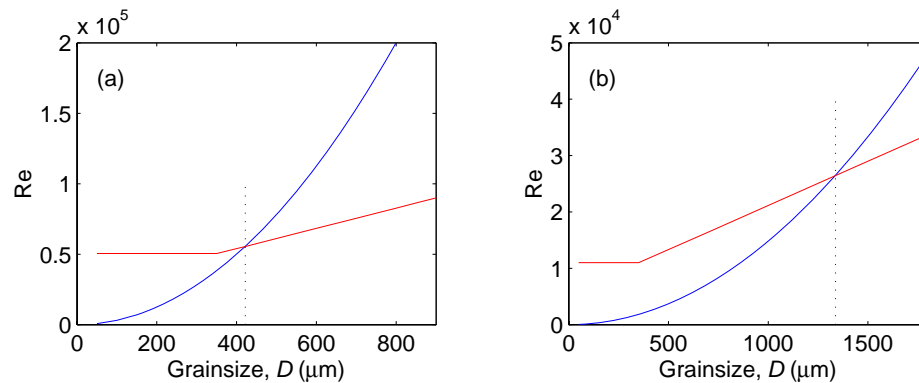


Figure 7.7. Variation of  $Re$  with  $D$  in the wave friction factor model ( $T=6s$ ): (a) [ $f_w=0.01$  ( $a/D=545.7$ ),  $R=0.5$ ]; (b) [ $f_w=0.02$  ( $a/D=118.8$ ),  $R=0.5$ ]. Key: blue line – flow  $Re$  (stage 3); red line –the transition to turbulence.

The resulting effect on the wave friction factor, of period dependence in the transition to turbulence, is shown in Figure 7.8; this was constructed on the basis of the diagram of Kamphuis (1975). Shown also in the Figure are: the analytical solution for laminar flows; the empirical relationship for smooth turbulent conditions; and the empirical limit for fully developed rough turbulent flow (Kamphuis, 1975). Solutions for four values of  $a/D$  are shown, corresponding to four (constant) values of  $f_w$  in rough turbulent flow conditions; the selected values reflect the range of flow and sediment parameters upon which the transition to turbulence relationships were empirically-based.

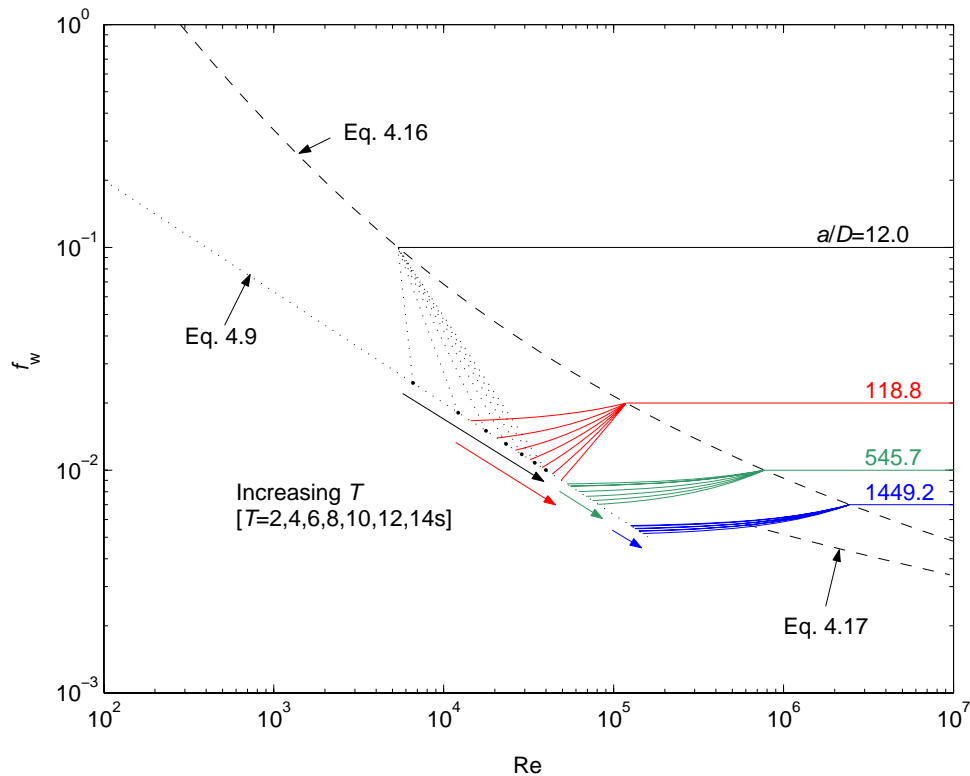


Figure 7.8. The effect of wave period on the wave friction factor coefficient. Coloured arrows indicate the effect of increasing  $T$ . See text for more details.

Over rough beds, the value of  $Re_{crit}$  for initial transition to turbulence varies with  $T$  (Eq. 6.5); consequently, so does the value of  $f_w$  at the initial deviation from the laminar solution (Eq. 4.9). At small  $a/D$  (e.g.  $a/D = 12$ ), calculations showed that initial departure from the laminar solution occurred at a value of  $Re$  larger than is required for fully developed turbulence. This situation cannot exist in real flows, but may arise numerically in this case, either: (a) as a result of an unaccounted for period dependence in the relationship between  $a/D$  and  $f_w$  in rough turbulent flows (Eq. 4.11); or (b) as a result of the overestimation of  $Re_{crit}$  by Eq. 6.5 (transition to turbulence), at large grain sizes. The former explanation appears to be more likely, because data within the range  $2 < a/D < 15$  were incorporated into Eq. 6.5, this then provided equally good representation of such data, when compared to larger values of  $a/D$ . At smaller values of  $a/D$ , the range of  $Re_{crit}$  (and  $f_w$ ) calculated by using this approach, for the same range of  $T$ , was broader. Values of  $f_w$  at all  $T$  were less than the equivalent rough turbulent value. Similarly, the range of  $Re$  over which transition occurred was reduced (this effect was enhanced at larger  $T$ ). At very large  $a/D$  ( $\approx > 1500$ ): the range of  $Re_{crit}$  was reduced to a constant value at the smooth bed limit ( $Re = 1.66 \times 10^5$ ), with an associated single value of  $f_w$ ; predicted values of  $f_w$  in the rough turbulent regime were almost equal to the laminar case initially but, subsequently, are less (reducing progressively down to the smooth turbulent

limit); and, the range of  $Re$  over which transition occurred was larger, relative to the previous example.

New values of  $f_w$  were calculated for the threshold of motion data. Observations made under either fully laminar or rough turbulent conditions were interpreted, using Eq. 4.9 or Eq. 4.11 directly, as appropriate; transitional values were calculated by fitting the observed values of  $Re_{crit}$ ,  $a/D$  and  $D$  to the model described above. The difference in the predicted  $f_w$  between the laminar and transitional solutions was calculated for each case; the results are shown in Figure 7.9. These data represent the relative increase in the calculated  $\tau_{0\text{crit}}$  over that calculated using the laminar solution alone. The new model typically increased the predicted value of  $f_w$  at larger  $T$  and  $D$ . However, at small grain sizes (approximately  $D < 300\mu\text{m}$ ), corresponding to large values of  $a/D$ , the friction factor in rough turbulent flow was equal to, or less than, that in the laminar case.

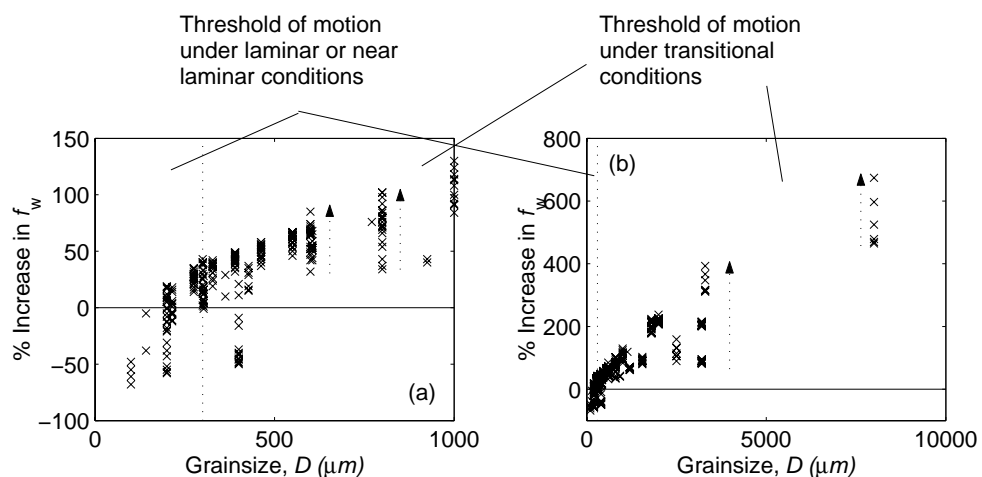


Figure 7.9. Percentage difference in  $f_w$  between the fully turbulent (Eq. 4.11) and laminar (Eq. 4.9) solutions at the threshold of motion: (a)  $D < 1\text{mm}$ ; and (b)  $D < 1\text{cm}$ . Dotted arrows indicate the effect of increasing wave period.

It was anticipated originally that  $\delta\tau_{0\text{crit}}/\delta T$  might be reduced through the use of the new model by causing  $f_w$ , hence,  $\tau_{0\text{crit}}$ , to increase at a greater rate under longer wave periods through the transitional regime. However, this effect was offset by an increase in  $a/D$ ; this was associated also with increasing wave period, at threshold. Although  $\delta\tau_{0\text{crit}}/\delta T$  was reduced in some cases, the new model had generally the opposite effect, producing a mean increase in the gradient steepness of 25%; there was also a corresponding increase in the

scatter of predicted  $\tau_{0 \text{ crit}}$  (see Figure 7.10), which somewhat negated the significance of any change in the observed gradient.

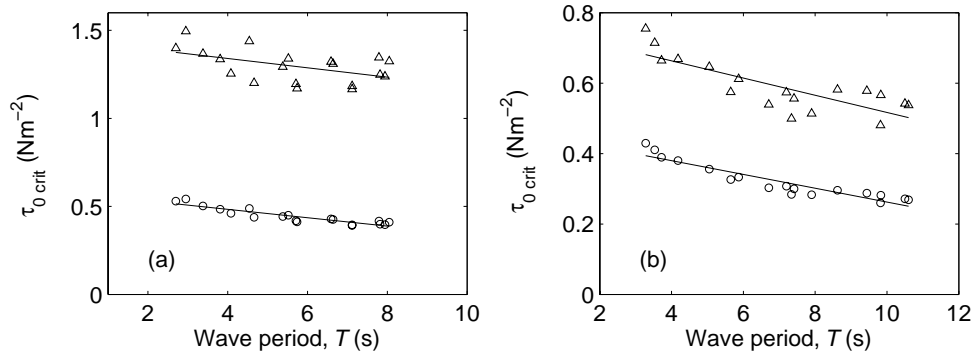


Figure 7.10. Comparison of  $\tau_{0 \text{ crit}}$  for threshold of motion under sinusoidal flows, calculated using the laminar solution (O) and the transitional model ( $\Delta$ ) for (a) [ $D=1800\mu\text{m}$ ,  $\rho_s=2600 \text{ kgm}^{-3}$ ]; and (b) [ $D=800\mu\text{m}$ ,  $\rho_s=2630 \text{ kgm}^{-3}$ ].

By manipulating the pattern of  $\delta f_w / \delta \text{Re}$  in the transitional region, this model could modify  $\delta \tau_{0 \text{ crit}} / \delta T$ , potentially reducing the gradient to zero. However, this would be an empirical adjustment for the transitional region only and significant  $\delta \tau_{0 \text{ crit}} / \delta T$  would still exist for laminar flows. This approach makes the assumption also that  $\delta \tau_{0 \text{ crit}} / \delta T$  should equal zero, in transitional or even laminar flows; this is an assumption challenged below.

### 7.3.5. Physical mechanisms

The mechanical action of eroding a single grain, from within a bed of similar grains, is recognised as a highly complex process involving many more variables than are considered within the present study. It is the balance and interaction of these processes that regulate ultimately, the erosion of such grains. The relative magnitudes of the opposing forces are compared traditionally on an instantaneous time scale. It is assumed that, at the threshold of motion, the destabilising fluid shear forces locally balance, or slightly exceed, the resistive forces of the individual grain.

Two physical mechanisms are presented here that consider the potential direct and indirect mechanisms by which wave period may influence the instantaneous balance of forces, namely: an apparent shear stress offset; and ‘cumulative force effects’.

7.3.5.a. *Apparent shear stress offset*

If the balance of forces approach is applied strictly to turbulent flows, on an essentially instantaneous time scale, then it must be the case that traditional methods are somehow inaccurate in representing the instantaneous flow. Similarly, that this misrepresentation varies with  $T$ . Following the stochastic approach to threshold of motion under unidirectional flows, it is suggested that this error is introduced by the incomplete representation of the turbulent flow, by means of a single value of  $\tau_{0 \text{ crit}}$ . The accuracy of the calculation of this single value is discussed in Section 7.3.4, but is assumed here to be accurate. At the onset of grain motion under turbulent flows, the most susceptible particles, with the lowest characteristic critical shear stress (in relation to differences in grain size or relative protrusion) are moved by the highest shear stresses occurring in the shear stress distribution, applied to the bed by the background flow (Grass, 1970, for unidirectional flows). The instantaneous horizontal component of velocity, throughout the oscillatory cycle, is more accurately represented by

$$u = \bar{u} + u' \quad \text{Eq. 7.1}$$

where  $\bar{u}$  is the mean value of  $u$  at that phase and  $u'$  is a fluctuating component, with a (positively skewed) lognormal distribution (Lopez and Garcia, 2001); similarly in the vertical and horizontal, flow perpendicular planes,  $w = \bar{w} + w'$  and  $v = \bar{v} + v'$ , respectively. For laminar flows,  $u'=v'=w'=0$ . However, for turbulent flows or turbulent portions of transitional flows,  $[u',v',w'] \neq 0$ , corresponding to the migration of fluid eddies across streamlines and through the boundary layer. Three-dimensional coherence of these eddies, in contact with the bed, means that turbulent shear stress may be represented in a similar manner

$$\tau = \bar{\tau} + \tau' \quad \text{Eq. 7.2}$$

Relationships such as the wave friction factor provide the mean value  $\bar{\tau}$ , but do not include  $\tau'$ . The amplitude of this fluctuating component of velocity was measured at a range of heights over beds of sediment by Sleath (1991), yielding the empirical relationship

$$\frac{1}{w'} = b \cdot z \quad \text{where} \quad b = 6.29a^{-3/2}k_s^{-1/2}T \quad \text{Eq. 7.3}$$

where  $w'$  is the cycle mean rms fluctuation in the vertical component of velocity (approximately equivalent to the magnitude of variation in  $u'$ ). If this equation is applied to

---

the threshold of motion observations, in order to maintain the observed ratio of  $a$  to  $T$ , an increase is observed in the amplitude of  $w'$  with increasing  $T$ . This is likely to reflect the extended time frame for the development of physically-large eddies under longer wave periods. Such an increase may be transferred qualitatively to the calculation of  $\tau$ , where it is now reasonable to assume that  $\tau'$  will be increased under larger  $T$ .

The combined effect of these observations, on the threshold of motion, is illustrated diagrammatically in Figure 7.11, assuming a simplified normal distribution of velocity and shear stress. In the Figure, the balance of forces for individual grains is satisfied at a single value of  $\tau_0$  (for an idealised sediment of uniform grain-size, -shape, -density and bed packing), but could be represented alternatively also as a normal or log-normal distribution. The width of this distribution corresponds to the ranges in grain size and individual grain instability, within the sediment being considered. Figure 7.11 assumes that the threshold of motion under turbulent flow conditions occurs in response to instantaneous, localised, high shear events; these, in turn, are statistically more probable under longer wave periods. As such, longer wave periods with smaller  $\tau_0$  may still provide a sufficient number of high shear events to cause the threshold of motion condition.

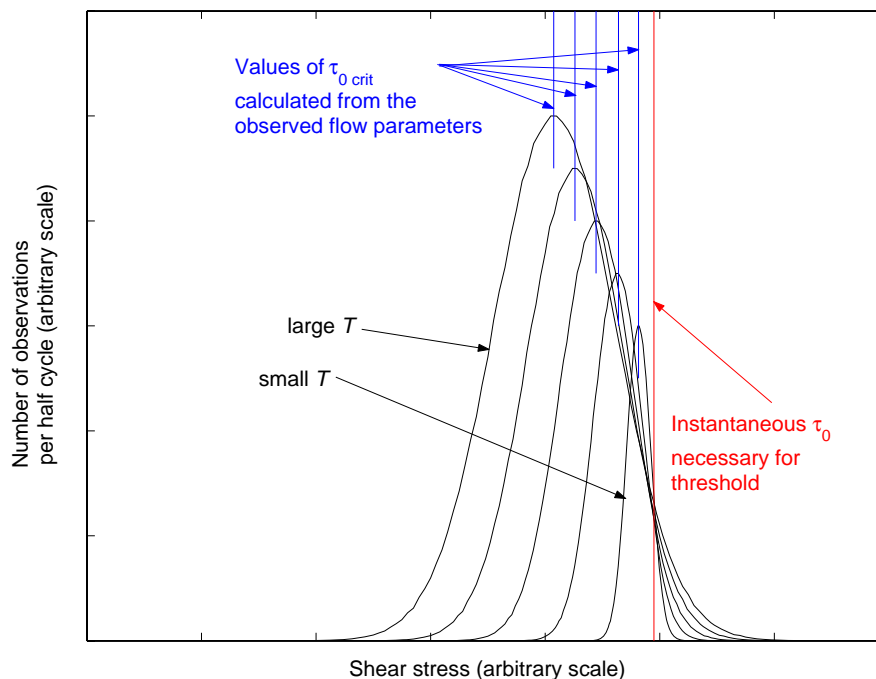


Figure 7.11. Theoretical shear stress distribution causing threshold of motion.

In order to test the conceptual model described above, a simple model was created to provide theoretical observations of shear stress, incorporating the observed flow parameters causing threshold of motion in sand [ $\rho_s=2540\text{kgm}^{-3}$  and  $D=600\mu\text{m}$ ]. The results are shown in Figure

7.12. In the model, a random number generator was used to produce normally-distributed values with mean=0, variance  $\sigma^2=1$ , and standard deviation  $\sigma=1$ . These values were scaled initially to mean= $\tau_{0 \text{ crit}}$ , calculated using  $f_w$  from the linear interpolation model (Section 7.3.4). Secondly, the range of values was scaled to  $\sigma=\tau'$ , calculated using Eq. 7.3 and the same value of  $f_w$ . The final result was found to be highly sensitive to  $z$ ; in Eq. 7.3,  $y=0$  could not be used whilst no alternative length scale has been suggested in the literature. The Figure shows that results follow closely the proposed mechanism, if  $z$  is set to an arbitrary small value (1mm). However, the individual curves become small and separated, if a larger value of  $y$  is used (e.g.  $z=\delta_{0.99}$ ); they become larger and with significant overlap, when a smaller arbitrary value is used (e.g.  $z=0.5\text{mm}$ ).

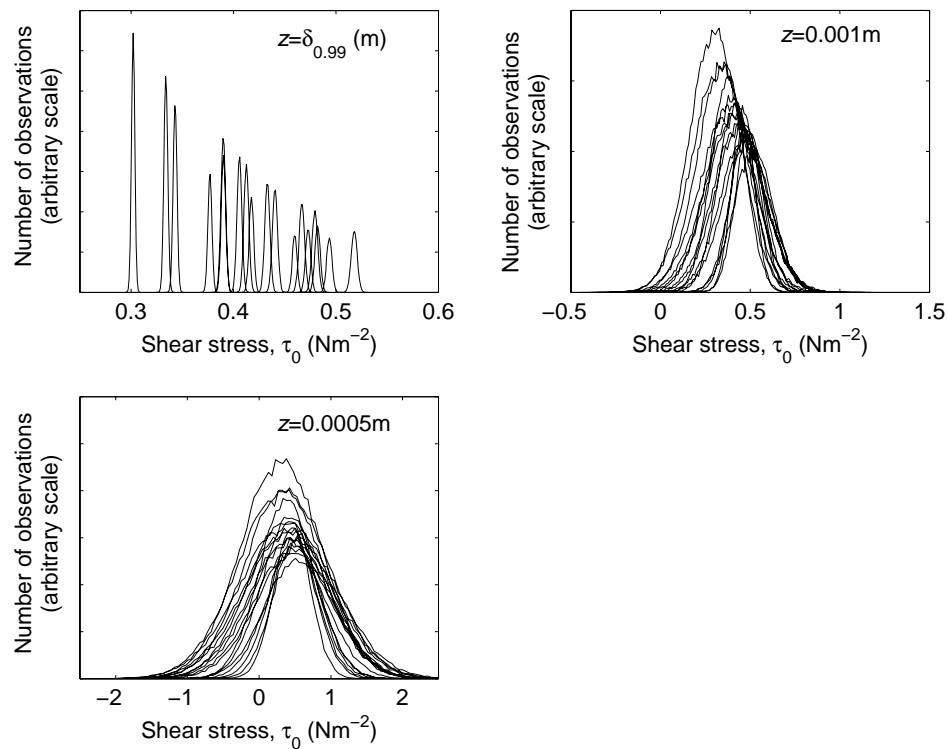


Figure 7.12. Modelled observations of instantaneous shear stress, for flow conditions at the threshold of motion for sand [ $\rho_s=2540\text{kgm}^{-3}$  and  $D=600\mu\text{m}$ ] under sinusoidal flows. The effect of variation in the parameter  $y$  is illustrated.

This analysis lends some merit to the proposed mechanism. However, the arbitrary use of  $z$  and the suitability of the scaling  $\tau'=\sigma$  need to be investigated further.

## 7.3.5.b. Cumulative force effects

It is proposed that, in the case of transitional and possibly laminar flows, the absolute amplitude of the peak in shear stress is not strictly important. Rather, that the physical mechanism for dislodging, subsequently eroding, a single grain requires a time-mean or cumulative force occurring over a finite period of time; as such, it is a function of  $T$ . In the present study, the mean force was represented by the time-mean shear stress, measured over a variable time-frame,  $\Delta t$ , centered on the peak shear stress (see Figure 7.13). The cumulative force (per unit area) may be represented by the time-integrated shear stress ( $= \bar{\tau}_0 \times \Delta t$ ). However, this varied considerably in magnitude with  $\Delta t$ , making it unsuitable for numerical or graphical interpretation. Hence, only the mean shear stress approach is presented here.

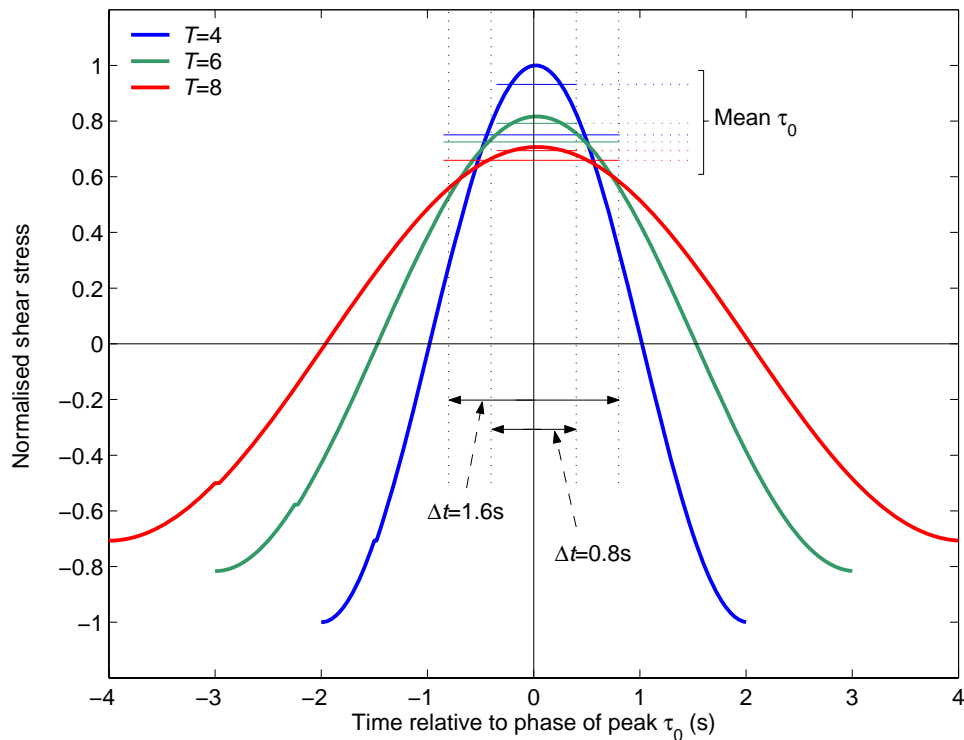


Figure 7.13. Definition of the mean force calculation variables for sinusoidal flows.

At very small values of  $\Delta t$ ,  $\bar{\tau}_0 \approx \tau_0$ . Subsequently, as  $\Delta t$  increased,  $\bar{\tau}_0$  decreases at a non-linear rate, inversely proportional to the period. As a result, the difference in the mean values tended to be reduced, with the converging eventually to a varying degree. Two examples, representing the clearest results of such an analysis, are shown in Figure 7.14.

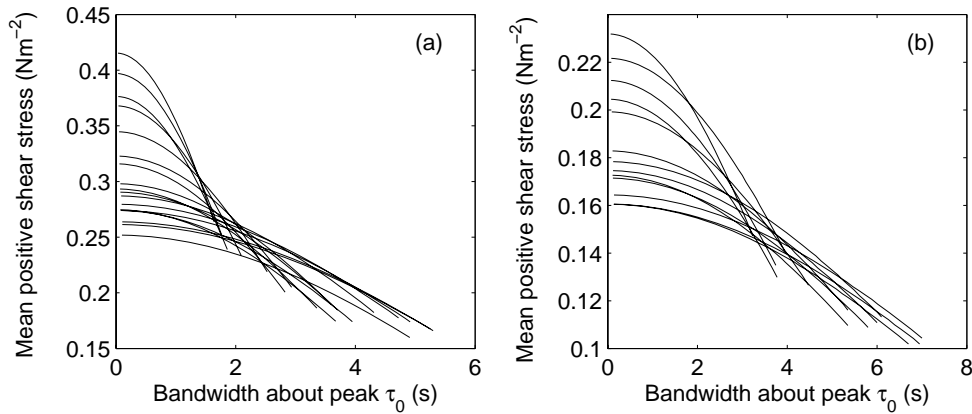


Figure 7.14. Mean shear stress causing threshold of motion in sands: (a)  $\rho_s=2630\text{kgm}^{-3}$ ,  $D=800\mu\text{m}$ ; and (b)  $\rho_s=1280\text{kgm}^{-3}$ ,  $D=3200\mu\text{m}$ .

For observations obtained using other grain sizes and densities, a similar pattern was observed; however, with a less well defined zone of convergence. In all cases, the convergence zone was typically in the region  $\Delta t=1.5\text{-}3.5\text{s}$ ; this reduced the range of the parameter representing the flow ( $\bar{\tau}_{0\text{ crit}}$ ), by a factor 2-4. The characteristic value (or range) of  $\Delta t$  did not appear to vary, with  $D$  or  $\rho_s$ .

## 7.4. Results: The effect of flow asymmetry on $\tau_{c\text{ crit}}$

### 7.4.1. Introduction

The threshold of motion under asymmetric flows was identified nearly always in relation to the flow associated with the wave crest. Hence, the critical shear stress is identified here as such, using  $\tau_{c\text{ crit}}$ , which is equal to  $\tau_{0\text{ crit}}$  for the case  $R=0.5$ . From the baseline observations undertaken relating to sinusoidal flows (Section 7.3), the effect of flow asymmetry was to increase the value of  $\tau_{c\text{ crit}}$  for given sediment ( $D$ ,  $\rho_s$ ) and flow parameters ( $T$ ). The relative increase of  $\tau_{c\text{ crit}}$  with  $R$  (calculated using laminar theory) is shown in Figure 7.5b and Figure 7.15, for each of the three sediment material types investigated. For quartz and aragonite grains, relatively large asymmetry ( $R=0.7$ ) caused  $\tau_{c\text{ crit}}$  to increase; this was by up to  $\sim 30\%$  of the observed value, under sinusoidal flows; this was only slightly lower ( $\sim 25\%$ ) for grains of Bakelite. The relative increase in  $\tau_{c\text{ crit}}$ , with  $T$ , was the same at all values of  $R$  for the more rounded quartz grains; however, it varied slightly with  $T$ , at larger  $R$ , for the more angular aragonite and Bakelite grains. The relative increase in the effect of  $R$  ( $\delta\tau_{c\text{ crit}}/\delta R$ ) was greatest between the cases of sinusoidal flow and  $R=0.55$ , for all three material types.

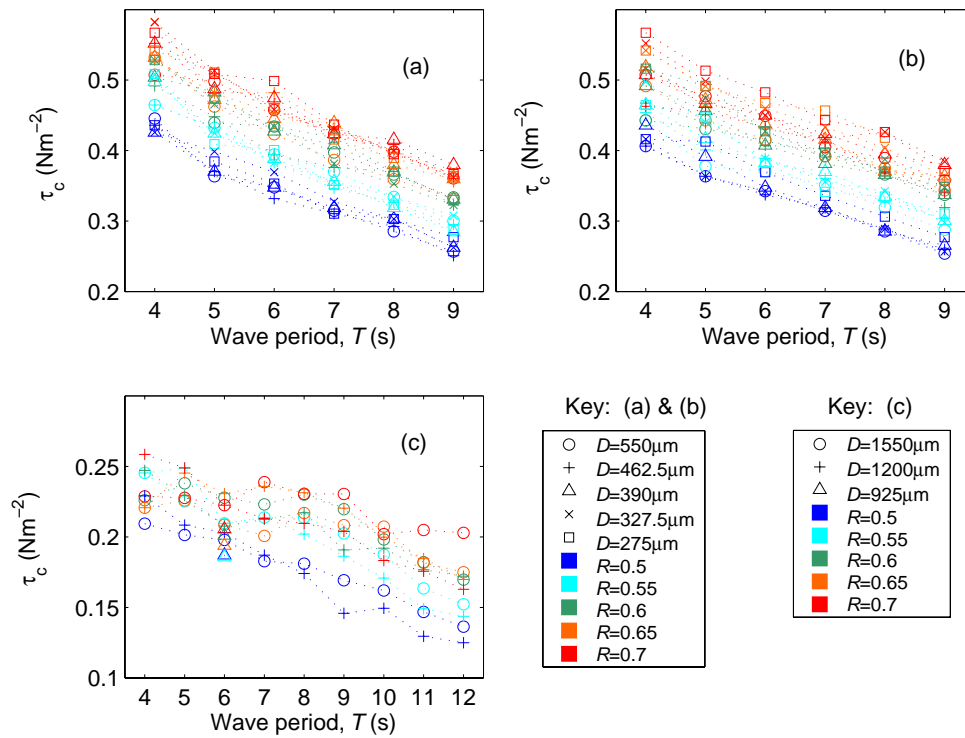


Figure 7.15. Bed shear stress causing threshold of motion in sediments investigated during the present study, consisting of: (a) quartz (b) aragonite and (c) Bakelite. The result of increasing flow asymmetry is demonstrated.

The gradient  $\delta\tau_{c\text{ crit}}/\delta R$  (for any given  $T$ ), calculated using laminar theory, was similar ( $\approx 0.5 \pm 0.175$ ) for the quartz and aragonite sands (see Figure 7.16a); however, it was generally smaller ( $\approx 0.2 \pm 0.1$ ) for the Bakelite sands. The mean  $\delta\tau_{c\text{ crit}}/\delta R$  decreased progressively, with increasing grain size; this coincided with the increasing presence of turbulence, at threshold, for such grains. Also, the gradient decreased slightly with increasing wave period. The observations did not extend sufficiently into the transitional region to comment fully on the pattern of increase in  $\delta\tau_{c\text{ crit}}/\delta R$  with the presence of turbulence (Figure 7.16b). It may be noted, from this Figure, that the majority of the data represent near laminar conditions; only the larger quartz and aragonite grain sizes are affected significantly by (transitional) turbulence.

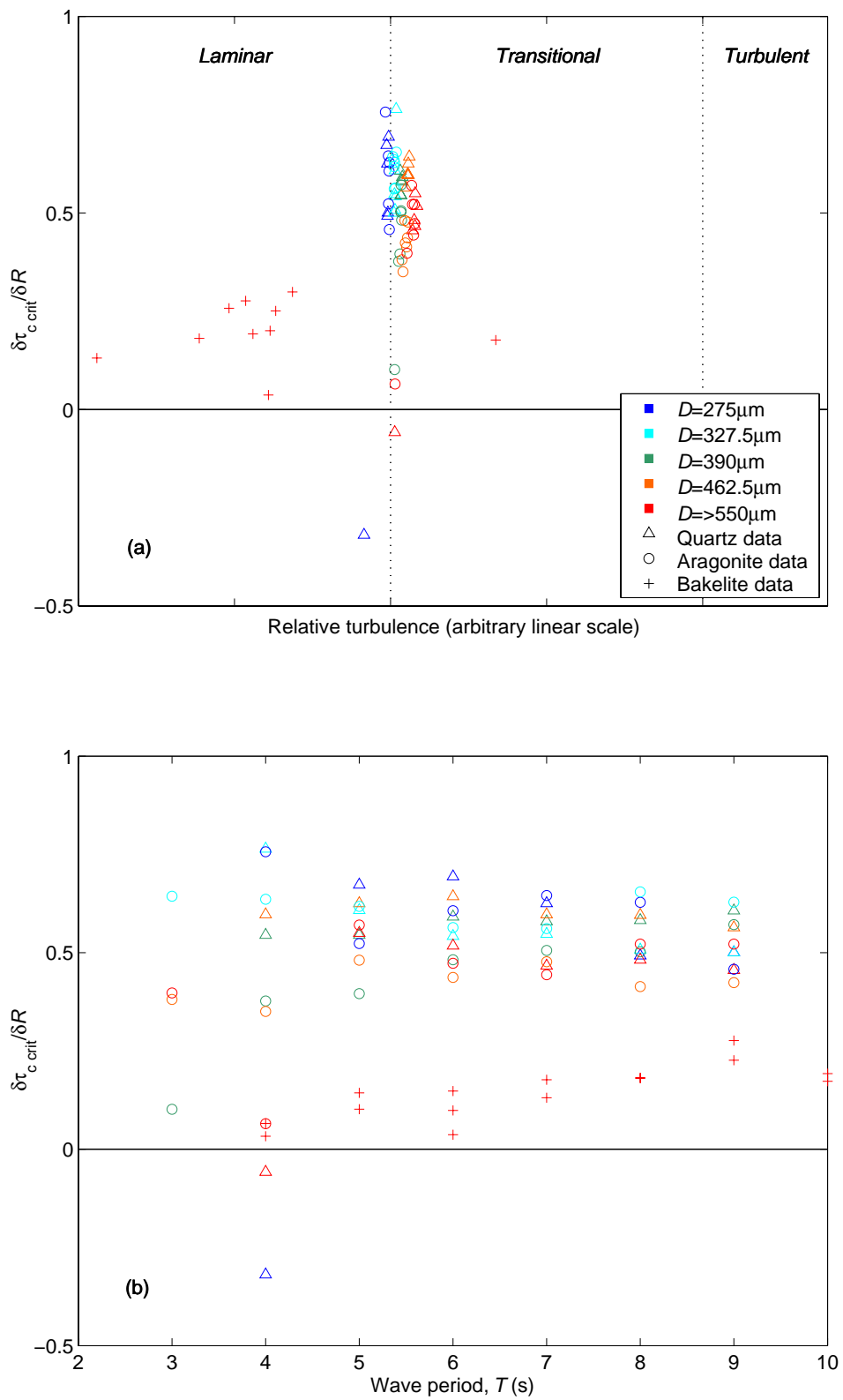


Figure 7.16. Variation in  $\delta\tau_{c\text{crit}}/\delta R$  calculated using laminar theory: (a) over the transitional range; and (b) in relation to wave period. Colours highlight differences in grain size, whilst symbols differentiate between the granular materials.

In order to explain the patterns described above, the errors and mechanisms described in Section 7.3 were used to incorporate the effect of flow asymmetry. Asymmetry dependence, caused by observational errors, was unlikely to be the primary source of error, for the same reasons described previously. Acceleration forces were typically larger at the point of threshold, under flows with greater asymmetry; these would have the opposite effect of reducing observed  $\tau_{c \text{ crit}}$ . Hence, experimental error may be discounted also, as a primary source of the observed dependency.

#### 7.4.2. Numerical error

This Section follows the principles and methods applied previously to the issue of wave period dependency (Section 7.3). From Eq. 4.9, the wave friction factor for laminar asymmetric flow becomes smaller, with increasing  $R$ . This difference is relatively small and is shown in Figure 7.17.

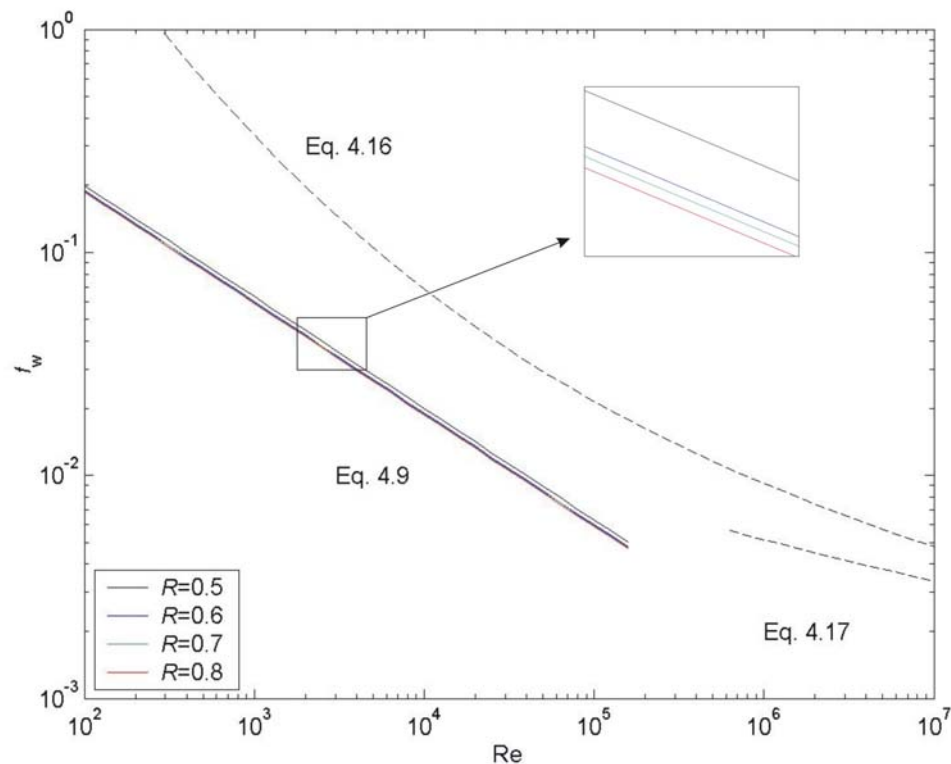


Figure 7.17. The laminar wave friction factor, under asymmetric oscillatory flows.

Using the model outlined in Section 7.3.4, in conjunction with the asymmetric solution for Eq. 4.9, the limiting cases of initial deviation from the laminar solution and the fully turbulent case were calculated, over a range of  $R$  for fixed  $T=6s$ , using (2) typical values of  $a/D$ . In the absence of any further information, an additional assumption was made that the

relationship between  $a/D$  and  $f_w$ , in rough turbulent flow, is the same for all  $R$ . However, for large values of  $T$  and/or  $R$ , and/or small values of  $a/D$ , the solutions of  $Re_{crit}$  for initial transition and for fully turbulent flows do not converge (Figure 7.18). This pattern indicates that this particular assumption may not be valid. The results of this model are shown in Figure 7.19.

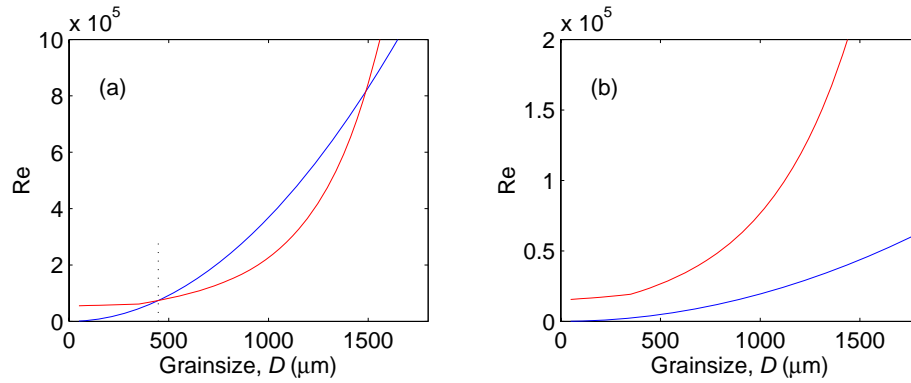


Figure 7.18. Variation of  $Re$  with  $D$  in the wave friction factor model ( $T=6s$ ): (a) [ $f_w=0.01$  ( $a/D=545.7$ ),  $R=0.6$ ]; (b) [ $f_w=0.02$  ( $a/D=118.8$ ),  $R=0.7$ ]. Key: blue line – flow  $Re$ ; red line – the transition to turbulence.

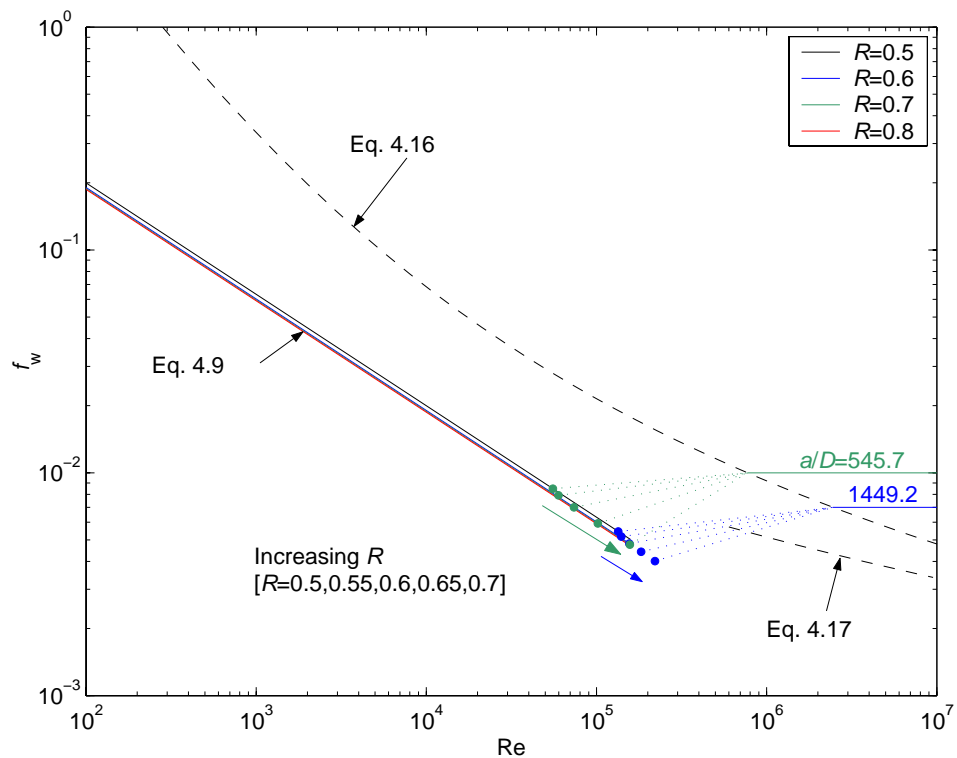
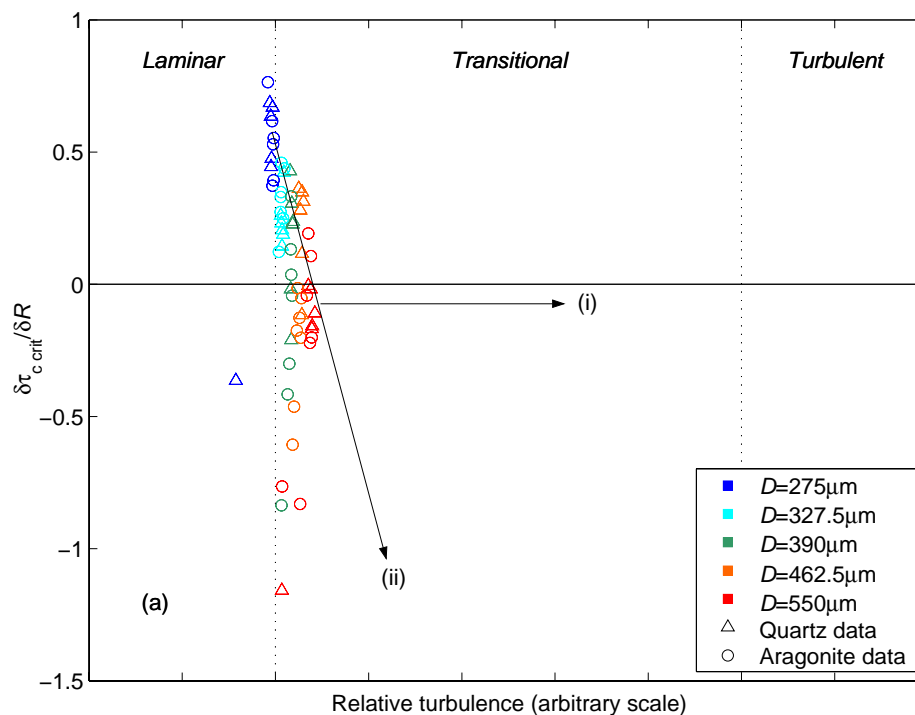


Figure 7.19. The wave friction factor, under asymmetric laminar flows. Arrows indicate the effect of increasing  $R$  on the point of departure from the laminar solution. Values are based on a fixed value of  $T=6s$ .

Values of  $f_w$  and the resulting values of  $\tau_{c\text{crit}}$  were calculated, using the model for the threshold of motion data observed under asymmetric flows. The model was applied successfully to only the quartz and aragonite sand data, as the Bakelite data often did not converge to a solution; this was considered to be due to small values of  $a/D$ , causing non-convergence as described above. The resulting  $\delta\tau_{c\text{crit}}/\delta R$  are shown in Figure 7.20 and selected examples of values calculated using laminar theory and using the model are compared in Figure 7.21. The observed  $\delta\tau_{c\text{crit}}/\delta R$  was reduced at the larger grain sizes investigated, i.e. similar values of  $\tau_{c\text{crit}}$  were observed to cause threshold of motion under flows of any asymmetry, for given  $T$ . This coincides also with larger grains reaching threshold, at values of  $Re$  further into the transitional flow regime; smaller grain sizes remain dominated by laminar processes. It is not clear from these data whether the reduction in  $\delta\tau_{c\text{crit}}/\delta R$  will stabilise at  $\delta\tau_{c\text{crit}}/\delta R=0$  (indicated by arrow 'i'), or alternatively, if it will continue to decrease, resulting in an increasingly strong negative gradient at large  $D$  (indicated by arrow 'ii'). Because the model calculates  $\tau$ , hence  $\delta\tau_{c\text{crit}}/\delta R$ , using a numerical model with an associated set of assumptions, both of these outcomes are considered to be numerical effects only. To resolve this question, more accurate direct measurements of shear stress in the transitional regime are required.



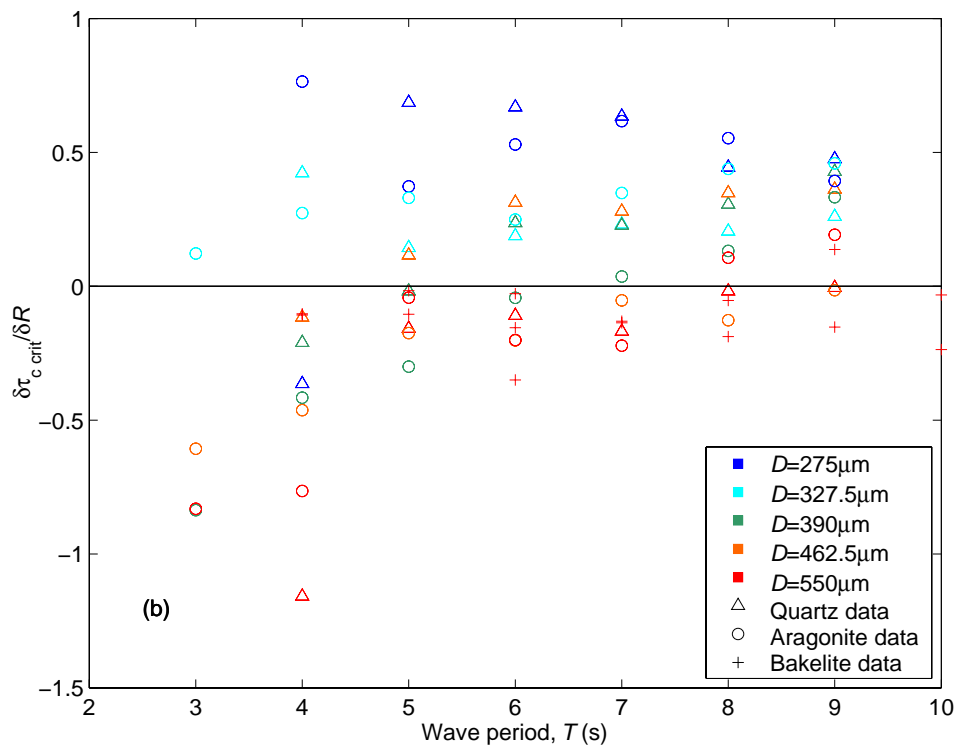


Figure 7.20. Variation in  $\delta\tau_{c\text{ crit}}/\delta R$  calculated using the transitional model: (a) over the transitional range; and (b) with wave period. Colours highlight differences in grain size whilst symbols differentiate between the granular materials, also see text for more details.

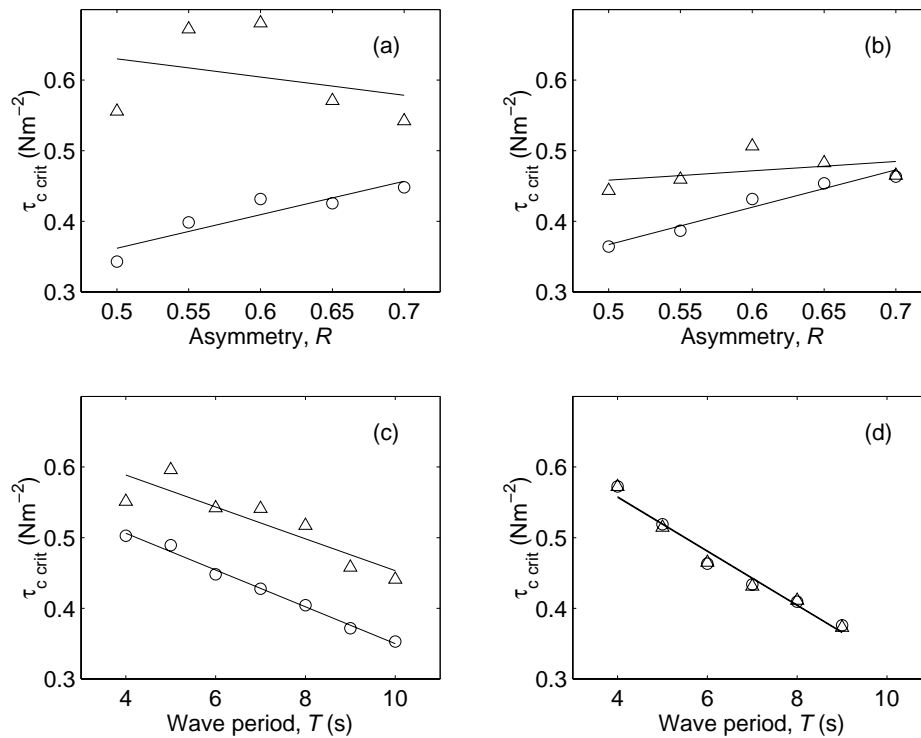


Figure 7.21. Comparison of  $\tau_{c \text{ crit}}$  for threshold of motion under asymmetric flows, calculated using the laminar solution (O) and the transitional model ( $\Delta$ ), for quartz sediment ( $\rho_s=2650 \text{ kgm}^{-3}$ ). Variation with asymmetry (for  $T=6\text{s}$ ) and with wave period (for  $R=0.7$ ) for (a) & (c),  $D=550\mu\text{m}$ ; and (b) & (d),  $D=327.5\mu\text{m}$ .

### 7.4.3. Physical Mechanisms

#### 7.4.3.a. Apparent shear stress offset

This Section follows the principles and methods applied previously to the concept of wave period dependency (Section 7.3.5). It was identified in Section 7.3.5.a that once a flow has become partially or wholly turbulent, turbulent fluctuations in the form of eddies are shed into the boundary layer; the size and velocity amplitude of these eddies are (partially) limited by the time-scale for their development. At greater flow asymmetry, the time frame for development of physically-large eddies is shortened, potentially reducing  $u'$ . However, as  $R \Rightarrow 0.5$ , the time-frame is extended; it becomes then more probable that larger eddies will form, yielding relatively larger  $u'$  at a similar flow amplitude outside of the boundary layer. The above assumptions are summarised in Figure 7.22. The Figure shows that the calculated value of  $\tau_{c \text{ crit}}$  may appear to increase with  $R$ , although the statistical distribution of instantaneous local flow conditions, causing motion, are essentially the same.

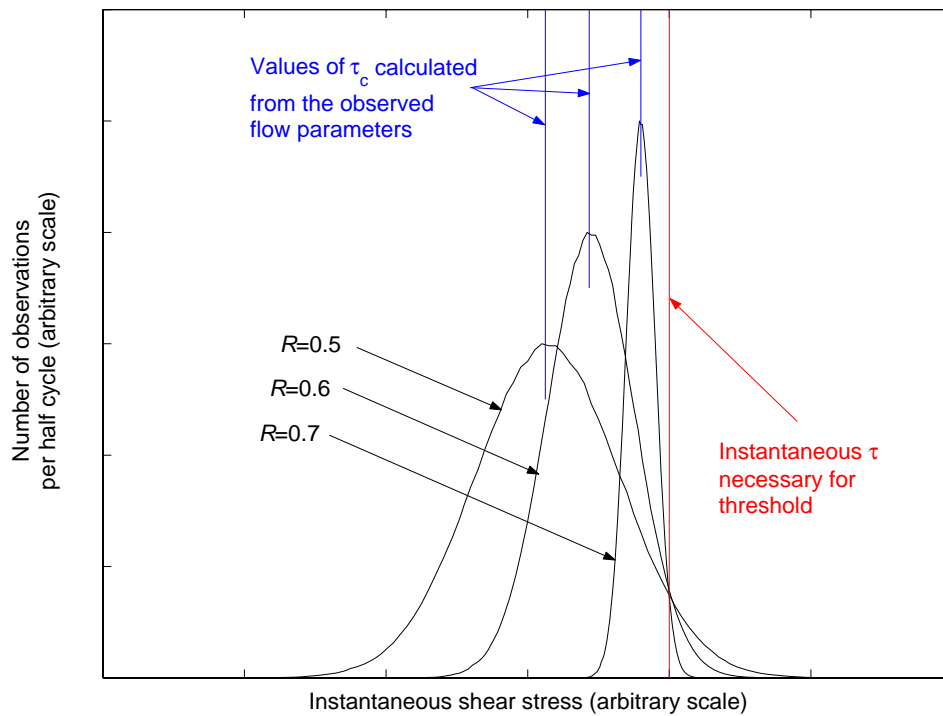


Figure 7.22. Theoretical shear stress distribution causing threshold of motion; the observation frequency of  $\tau$  during the positive shear stress half-cycle for a range of  $R$ .

Tanaka *et al.* (1998) discuss a limited number of turbulence intensity observations, made over smooth beds under cnoidal oscillatory flows. However, an insufficient range of  $R$  values (together with no range in  $D$ ) was presented with which to draw conclusions (either qualitatively or quantitatively) regarding the effect of asymmetry on such observations. In the absence of alternative information, it was not possible to analyse quantitatively the observed data to test this theory. However, it is anticipated that similar results would be observed to those shown for the sinusoidal case.

#### 7.4.3.b. Cumulative force effects

An example of the observed shear stress cycles (calculated using laminar theory), that were observed to cause the threshold of motion in quartz sands, is shown in Figure 7.23. This diagram reiterates previous observations in this Section, i.e. that a larger  $\tau_{c \text{ crit}}$  is needed to cause threshold under flows of greater flow asymmetry. The Figure highlights also differences in the temporal distribution of shear stresses, where: (a) under a sinusoidal flow, the peak is broad and relatively flat; and (b), under asymmetric flows, the peak becomes narrower and of larger amplitude. This same pattern was observed consistently, at all combinations of  $D$ ,  $\rho_s$  and  $T$ .

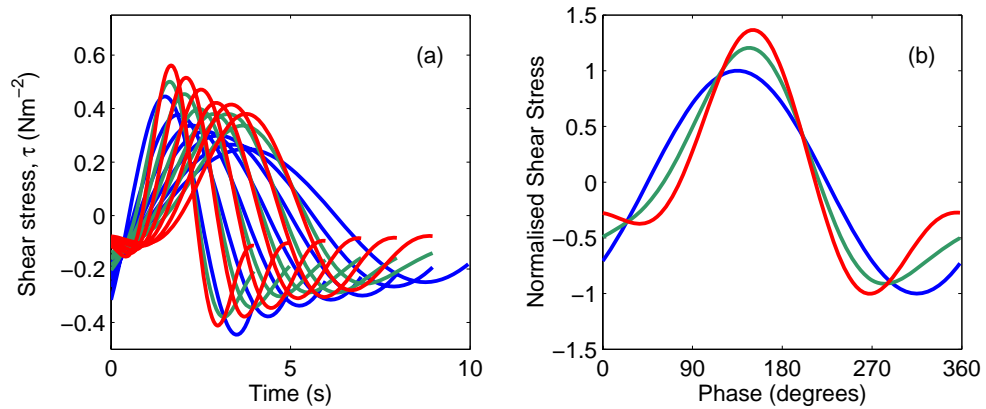


Figure 7.23. Shear stress cycles calculated using laminar theory, causing threshold of motion in quartz sand ( $D=327.5\mu\text{m}$ ): (a)  $4\text{s} < T < 10\text{s}$ ; and (b)  $T=6\text{s}$ . Key: blue lines ( $R=0.5$ ); green lines ( $R=0.6$ ); red lines ( $R=0.7$ ).

In terms of the nature of the flow asymmetry considered herein, the duration of the positive shear stress half cycle decreased with greater asymmetry. Hence, as a first approach, it was considered that the asymmetric flow might possibly be better represented by a wave period equal to twice the duration of the positive velocity half cycle. Figure 7.24 demonstrates that scatter in the quartz sand data, caused by  $R$ , is reduced but not eliminated by plotting  $\tau_{c \text{ crit}}$  against such a modified period,

$$T_{\Delta\omega t} = T \times \left[ \frac{180^\circ}{(\Delta\omega t)_{\max}} \right] \quad \text{Eq. 7.4}$$

Where,  $180^\circ$  is the bandwidth of the positive peak under sinusoidal flow and  $(\Delta\omega t)_{\max}$  is the corresponding value under asymmetric flow ( $168^\circ$ ,  $154^\circ$ ,  $145^\circ$  and  $135^\circ$  for  $R=0.55$ ,  $0.6$ ,  $0.65$  and  $0.7$ , respectively). The reduction in scatter was similar for the aragonite and Bakelite data sets.

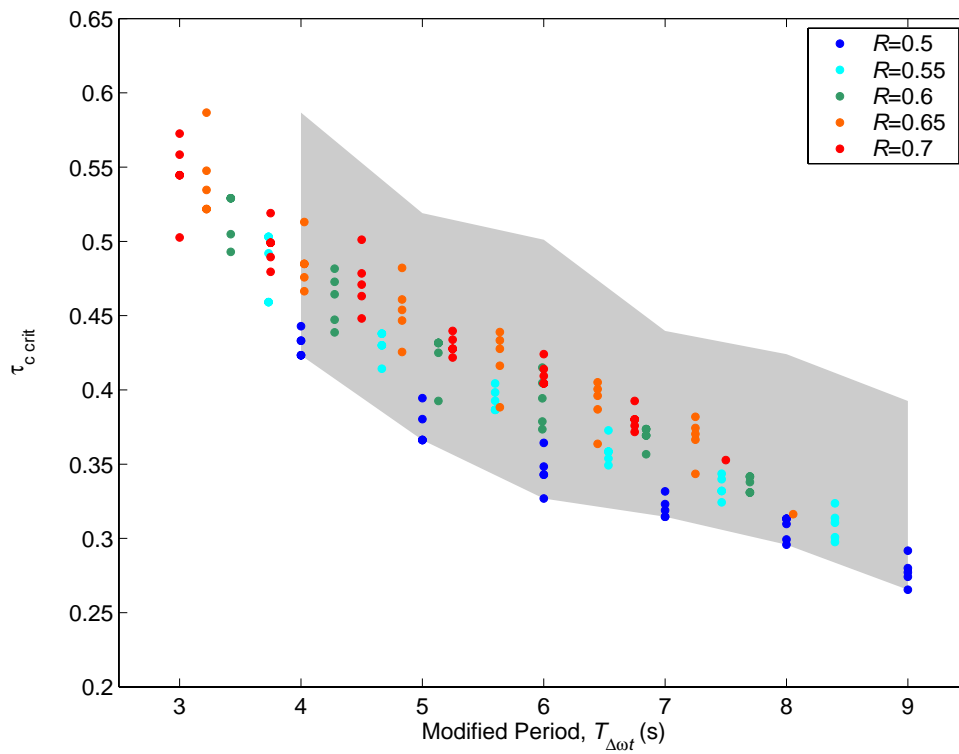


Figure 7.24. Peak shear stress causing threshold of motion in quartz sands ( $275\mu\text{m} < D < 550\mu\text{m}$ ) plotted in relation to the modified period (Eq. 7.4). The shaded area on the Figure represents the spread of the data, when plotted directly against  $T$ .

The data were reanalysed, in order to investigate the potential similarity between the shear stress cycles, in terms of the mean shear stress over a variable phase bandwidth,  $\Delta\omega t$ , centered on  $\tau_c$  (Figure 7.25).

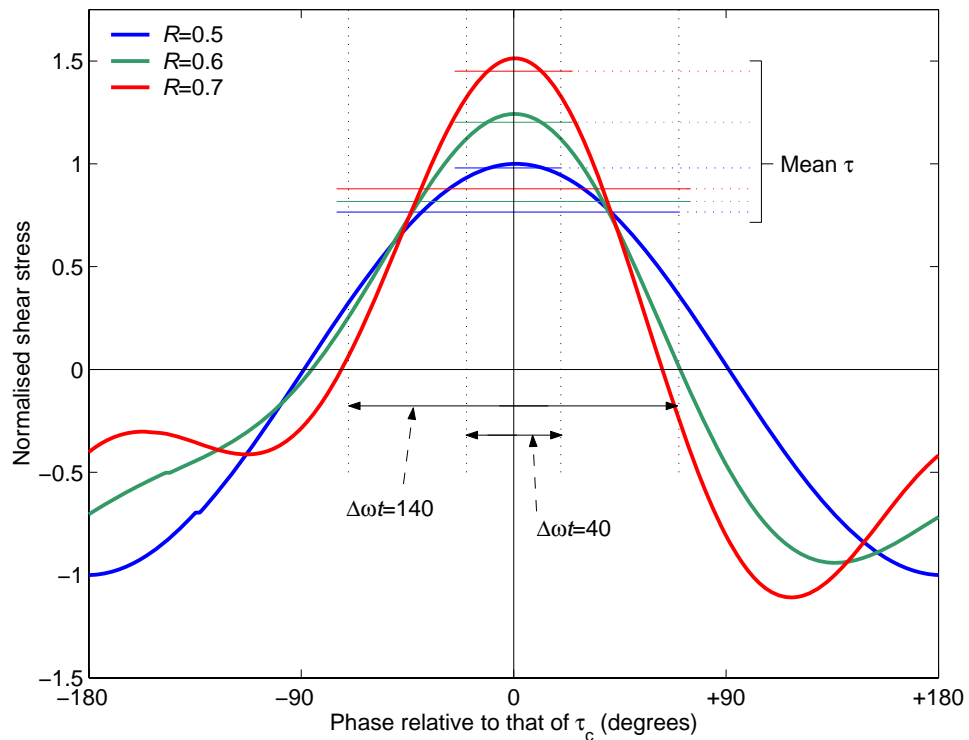


Figure 7.25. Definition of the cumulative force calculation variables for asymmetric flows.

Using the same data as presented in Figure 7.23, the mean shear stress was calculated over increasing phase bandwidth; selected results are shown in Figure 7.26. The data shown in the Figure represent an integration bandwidth, up to the maximum width of the positive shear stress peak (e.g.  $180^\circ$  for  $R=0.5$  and  $\sim 135^\circ$  for  $R=0.7$ ). For clarity, data are shown for only two values of  $T$ . However, very similar patterns pertaining to differences in  $R$  were found, for all values of  $T$ ,  $D$  and  $\rho_s$ . Bakelite grain data demonstrated similarity in the pattern of the results, but at smaller absolute values. Plotting against phase bandwidth on the ordinate axis removed the effect of  $T$ ; it was found that the characteristic value of  $\Delta\omega t$  was not period-dependant. The effect of wave period (Section 7.3) was evident in the data (for all values of  $R$ ) as an overall decrease in the characteristic shear stress (mean or peak) with increasing  $T$ .

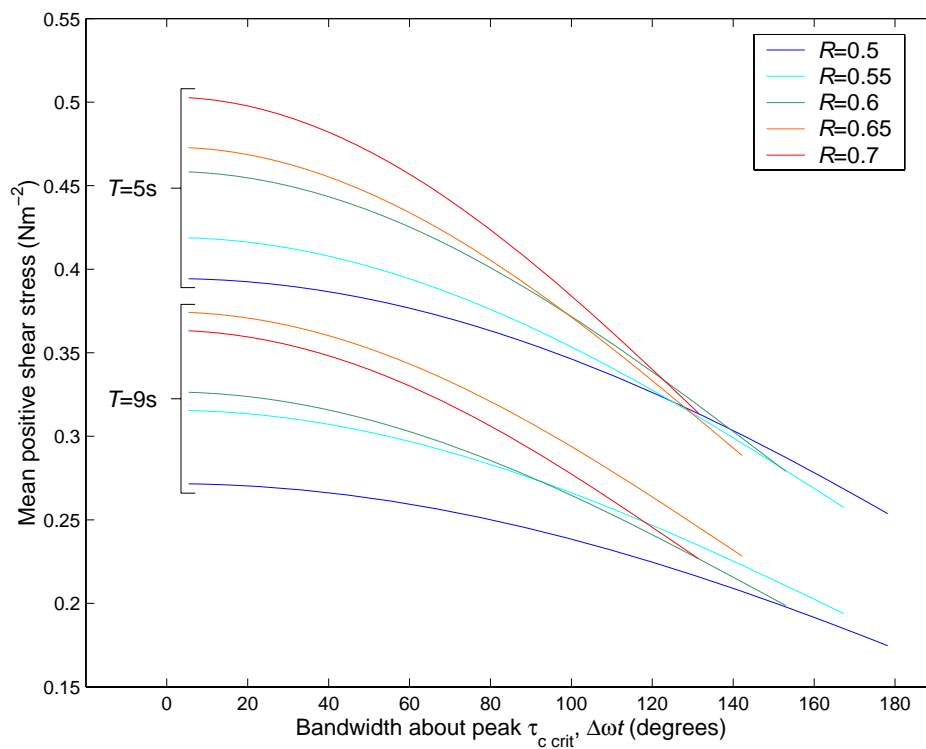


Figure 7.26. Mean shear stress causing threshold of motion in quartz sand ( $D=327.5\mu\text{m}$ ), for  $T=5\text{s}$  and  $9\text{s}$ . Data are truncated at the width of the positive shear stress peak, for each value of  $R$ , accordingly.

Figure 7.26 shows that the values of mean shear stress, for the range of  $R$ , tend to converge in a manner similar to that described in Section 7.3.5.b, relating to differences in wave period. For observations made using other grain sizes and densities and at other values of  $T$ , a similar pattern was observed; there was an equal degree of convergence. In all cases, the convergence zone was typically in the region  $\Delta\omega t=120^\circ\text{-}140^\circ$ ; this reduced the range of  $\tau_{c\text{ crit}}$ , by a factor 2-4. Using  $\Delta\omega t=130^\circ$ , this corresponds to  $\Delta t=1.44\text{s}$  and  $2.53\text{s}$  for  $T=4\text{s}$  and  $7\text{s}$ , respectively.

Because this observation was made at a consistent phase bandwidth (not time-frame), it is suggested that the asymmetric component of the mechanisms controlling threshold of motion may reflect the influence of variations in fluid acceleration and vertical gradients of horizontal velocity within the boundary layer flow. Although these parameters tend to vary significantly only in the mid-boundary layer flow, they do vary (nearly) linearly with  $R$ , whilst remaining proportional to  $T$ .

## 7.5. Results: The phase and duration of sediment motion at threshold.

### 7.5.1. The presence of turbulence

Using the model described in Section 7.3.4, the relative position of each observation within the transitional range was estimated; the results are shown for all observations in Figure 7.27. The Figure shows that, over the  $D=275\mu\text{m}$  bed, flow conditions were close to the beginning of the transitional range (to the point of transition). On the basis of the definition of transition made in the present study, it is likely that no significant eddies were present within the boundary layer; similarly, that shear stress followed, reasonably closely, the laminar solution at the onset of motion. However, observations made over the  $D=550\mu\text{m}$  bed and, in particular, under sinusoidal flows, extended further into the transitional regime. In this case, the presence of significant turbulence is more likely, but only in the phase of flow deceleration following the peak in velocity. Therefore, the onset of motion can be considered to be occurring in conditions of relatively low turbulence.

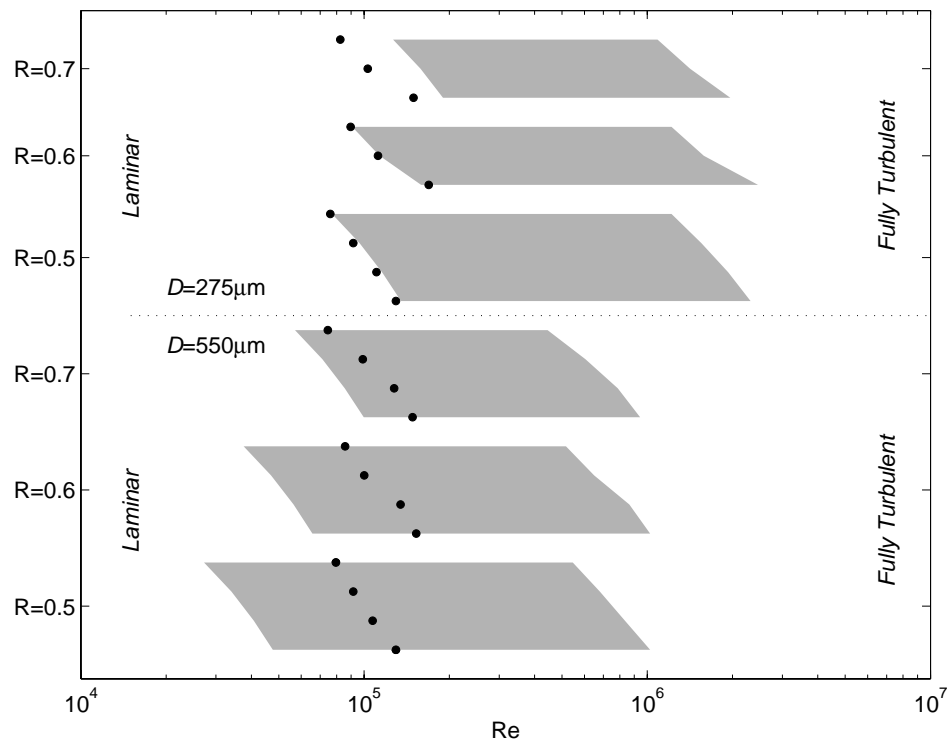


Figure 7.27. Flow conditions for visual observation data of the onset and duration of sediment motion, at threshold. Key: data points – observed conditions; shaded area – the transitional range.

Under sinusoidal flows over smooth beds, the phase lag of peak shear stress (behind the peak in outer layer velocity) decreases steadily through the transitional regime, from 45° in the laminar case to approximately 10° in the fully turbulent case (Fredsoe and Deigaard, 1992). Numerical models have provided the two limiting values whilst laboratory data have suggested that initial deviation does not occur until  $Re \approx 10^5$ . Similar information was not available for rough beds, or asymmetric flow over any beds. From Eq. 2.14 and Eq. 4.5, laminar asymmetric flows have a smaller phase lag between peak shear stress and velocity. This value would be reduced further in fully turbulent flow, but it is assumed that the asymptotic value should not be markedly different from sinusoidal flows ( $\varphi \approx 10^\circ$ ). Because the processes controlling the phase lag in the limiting cases are theoretically independent of grain size, these relationships should approximately apply to the transitional range at any bed roughness. It is also not clear at what value of  $Re$  initial deviation would occur over rough beds. However, it is presumed that this value should lie close to that for the transition to turbulence. In the absence of any more accurate information, a simple expression is proposed for the phase lag in the sinusoidal case:

$$\varphi = 45 - \left[ \frac{35(Re_{observed} - Re_{transition})}{Re_{turbulence} - Re_{transition}} \right] \quad \text{Eq. 7.5}$$

Using this expression, e.g. at the threshold of motion for  $D=550\mu\text{m}$ , the phase lag of peak shear stress is reduced from 45° to a mean value of  $42.2^\circ \pm 0.6$ . Depending upon the oscillatory period, this would correspond to a shift in the actual position of the shear stress peak by 0.05-0.2s. Within this range, the phase lag was greatest under sinusoidal flows and least under flows with  $R=0.7$ . The phase lag was unaffected theoretically, in all cases where  $D=275\mu\text{m}$ , as threshold occurs under laminar flow conditions. However, both grain size data sets exhibited similar delay in the onset of sediment motion following the peak in shear stress that was calculated using linear theory ( $\varphi=45^\circ$ ). A model of greater accuracy could be created, by taking into account the smaller value of  $\varphi$  for laminar asymmetric flows. However, this would not change the qualitative results, but would typically reduce further the value of  $\varphi$  predicted by the laminar solution.

### 7.5.2. Sinusoidal flows

Under sinusoidal flows, at the condition defined as the threshold of motion, the onset of sediment motion occurred after the peak in the shear stress, in all cases. Although significant scatter was present in the data, the mean offset increased generally with  $T$  (Figure 7.28a).

The mean phase of onset, relative to the phase of  $\tau_0$ , ranges from  $\omega t=22^\circ$  for  $T=4\text{s}$ , to  $\omega t=44^\circ$  for  $T=7\text{s}$ . These correspond to a progressively longer time delay between  $\tau_c$  and the onset of motion, of the order 0.25-0.86s, over the same range of  $T$ . Because similar patterns are observed for the  $D=275\mu\text{m}$  and  $550\mu\text{m}$  beds (where threshold occurred at different stages of transition), the phase shift of  $\tau_0$  (Section 7.5.1) is not considered to be a primary factor in the observed phase lag of the onset of motion. For both grain sizes, sediment was in motion typically for 0.6-0.9s (Figure 7.28b) and almost all observations were in the range 0.5-1s. This corresponds to a gradual reduction in the phase duration, with increasing  $T$ . Scatter in either the phase of onset or the duration of sediment motion is not apparently associated with any of the other flow variables, e.g. the magnitude of  $U_{c\text{crit}}$  or fluid temperature, etc.

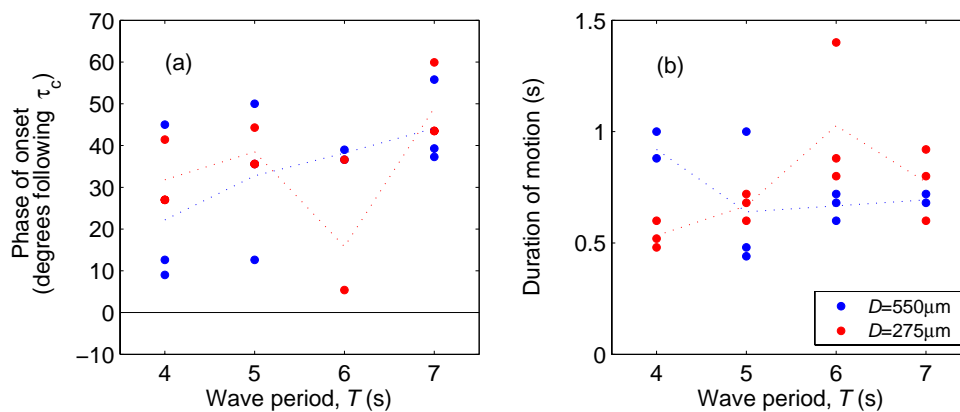


Figure 7.28. Quartz sediment motion under sinusoidal flows: (a) the phase of onset relative to the phase of  $\tau_0$ ; and (b), the duration of motion. Key: dotted lines show the mean trend.

The observations described above, are shown in (phase) relation to the velocity, shear stress and grain acceleration (inertial) force cycles in Figure 7.29; the inertial forces were calculated using Eq. 4.22. In all cases, sediment motion was initiated only some time after the peak in shear stress. The subsequent duration of sediment motion was centered typically upon the peak in plate (outer flow) velocity; this is in agreement with similar observations of bedload transport made in a laboratory by Sleath (1978) and in the field by Davies (1980). Acceleration forces were minimal at the onset of grain motion, in all cases.

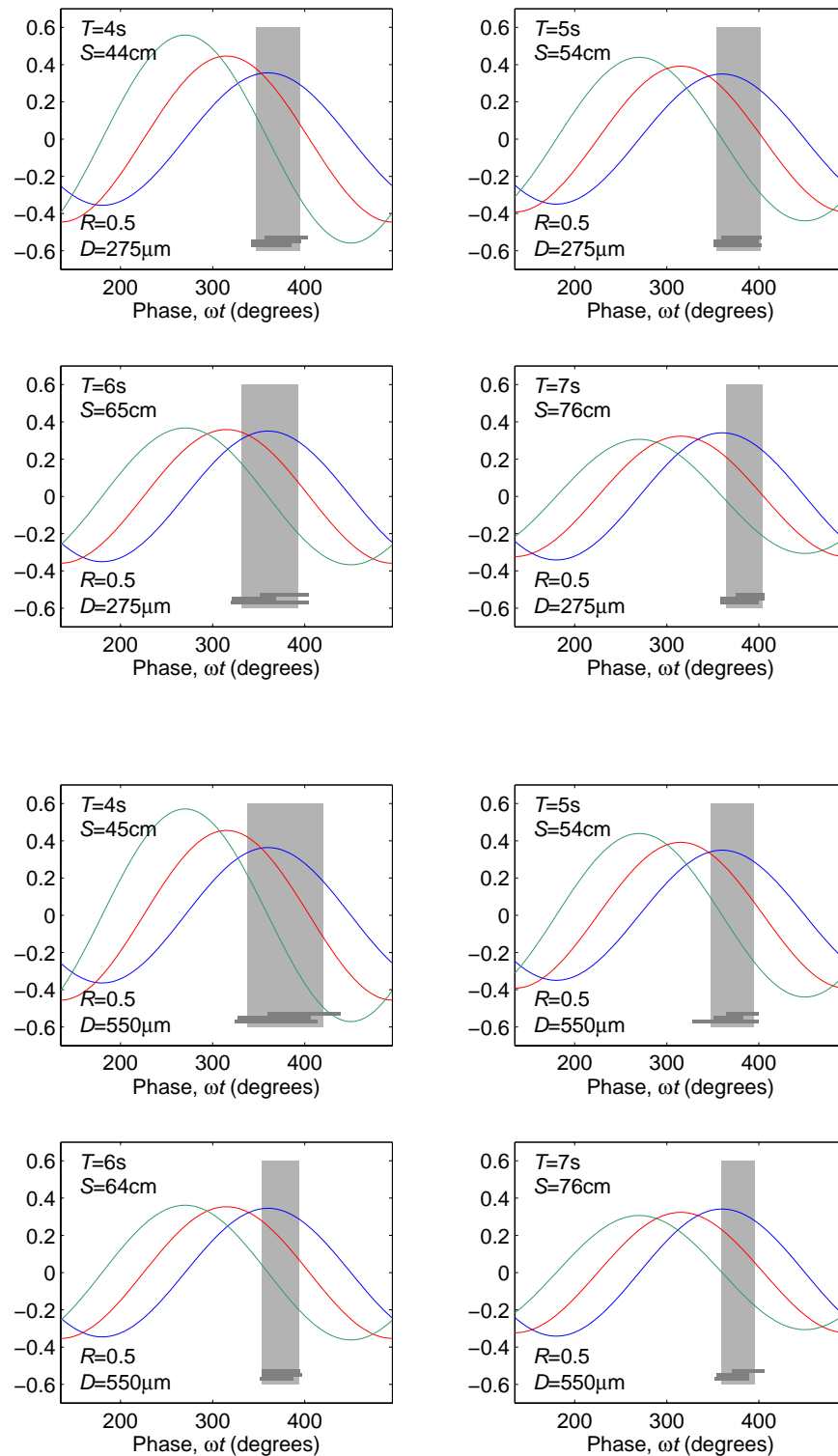


Figure 7.29. Observations of the phase of onset and duration of quartz sand motion at the threshold of motion condition, under sinusoidal flows. Key: blue lines – outer flow velocity ( $\text{ms}^{-1}$ ); red lines – laminar shear stress ( $\text{Nm}^{-2}$ ); green lines – plate (grain) acceleration forces ( $\text{ms}^{-2}$ ); shaded area – period of observed grain motion.

## 7.5.3. Asymmetric flows

From the baseline provided for sinusoidal flows in the previous Section, the effect of asymmetry was to cause earlier onset of motion, at all  $T$  (Figure 7.30a&b). For sediment  $D=550\mu\text{m}$ , asymmetry caused the phase of the onset to be brought closer to the phase of  $\tau_c$ . This effect was greater at large  $R$  ( $=0.6-0.7$ ) and small  $T$  ( $=4-5\text{s}$ ), where onset occurred  $-30^\circ$  prior to  $\tau_c$ . Values increased then with  $T$ , becoming closer to the sinusoidal case ( $\omega t=20-40^\circ$ ) over the range of  $T$ . The  $D=550\mu\text{m}$  data are considered to have been affected by acceleration forces, which are discussed in more detail in the following paragraphs. In addition, it was noted that acceleration forces were relatively much smaller, prior to and at the instant of onset in these observations.

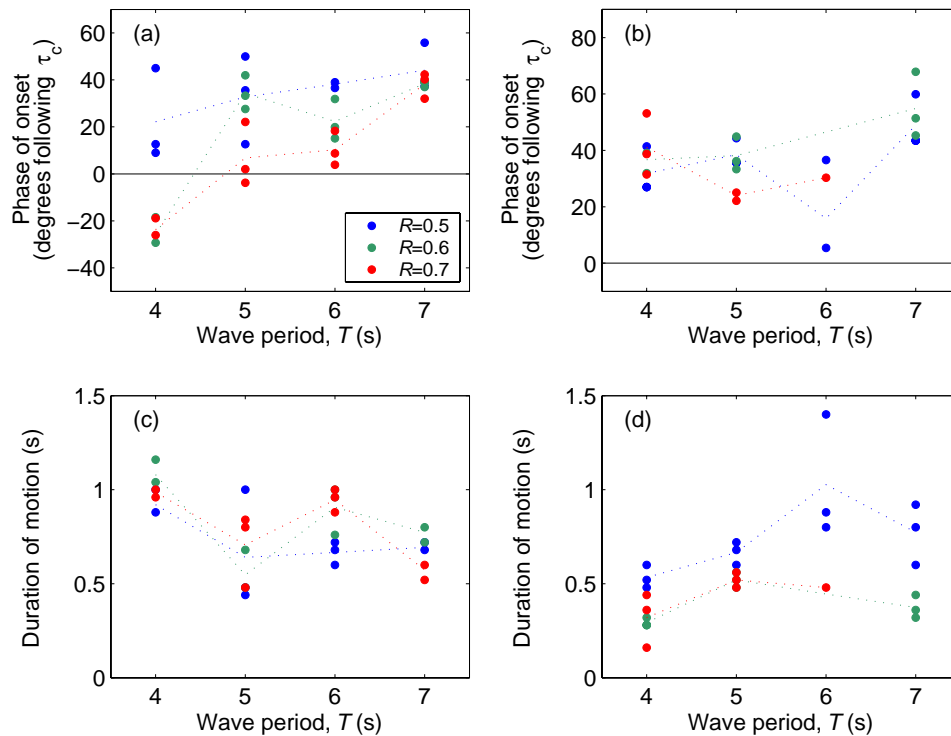


Figure 7.30. Sediment motion under asymmetric flows: (a) & (b) the phase of onset relative to the phase of  $\tau_c$ ; and (c) & (d), the duration of motion for quartz sands  $D=550\mu\text{m}$  and  $D=275\mu\text{m}$ , respectively. Key: Dashed lines – mean trend.

For sediment  $D=550\mu\text{m}$ , grains were in motion for 0.5-1s; they exhibited a similar range of scatter, at all values of  $R$ . However, a slight negative trend in mean duration, with  $T$ , was observed (Figure 7.30c&d). For sediment  $D=275\mu\text{m}$ , the duration of motion was reduced generally in the presence of significant wave asymmetry ( $R=0.6$  and  $0.7$ ) to 0.3-0.5s; in this case, a slight positive trend in the mean duration was observed, with increasing  $T$ .

The observations of sediment motion, described above, are shown in relation to the velocity, shear stress and inertial force cycles in Figure 7.31. In most cases, sediment motion was initiated only following the peak in the shear stress. However, for  $D=550\mu\text{m}$  and small  $T$ , the onset of motion occurs closer to the phase of  $\tau_c$ , to the extent that at [ $D=550\mu\text{m}$ ,  $T=4\text{s}$ ,  $R=0.6,0.7$ ], onset occurs prior to the phase of  $\tau_c$ . Onset in these asymmetric cases coincides with significant acceleration (inertial) forces; these may have initiated sediment motion independently of, or in conjunction with, fluid shear forces. At such times, absolute acceleration of the bed was  $0.85g$  and  $0.1g$ , respectively. Similar patterns were not observed in the  $D=275\mu\text{m}$  cases, even though absolute acceleration forces were slightly greater. It was noted at the time of experimentation that the  $T=4\text{s}$  cases, in particular, did not appear to follow visually the pattern of erosion resulting from fluid shear alone. In most cases, the subsequent duration of sediment motion was typically centered upon the peak in plate (outer flow) velocity. Acceleration forces were minimal at the onset of grain motion in all cases (with the exception of [ $D=550\mu\text{m}$ ,  $T=4\text{s}$ ,  $R=0.6,0.7$ ]); as such, onset occurred substantially after the peak in the acceleration force in the vast majority of cases. This re-emphasises the importance of: 1) the consideration of inertial forces; and 2) the limitation of such forces by experimental planning or data exclusion, if necessary.

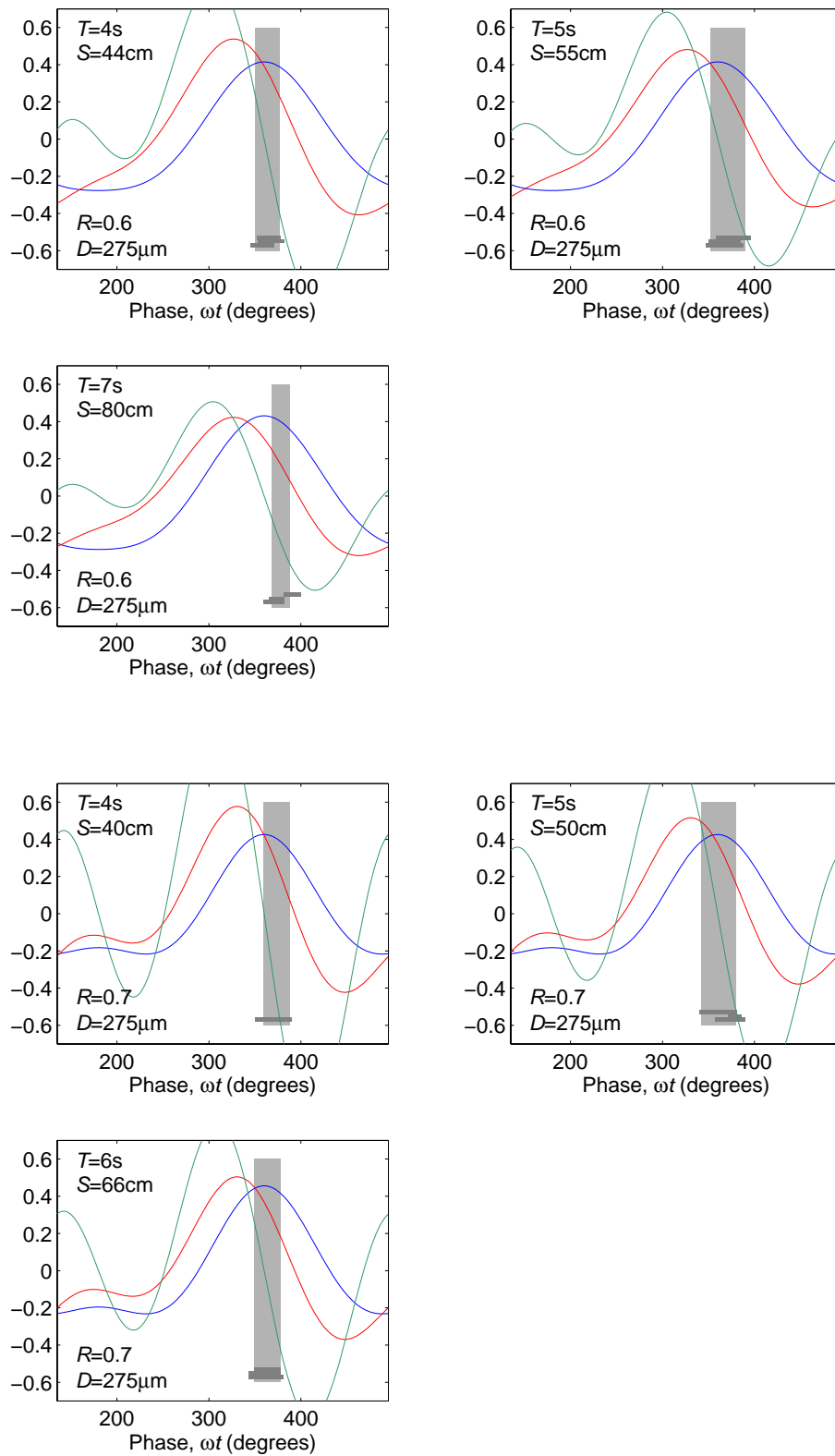


Figure 7.31. *continued overleaf...*

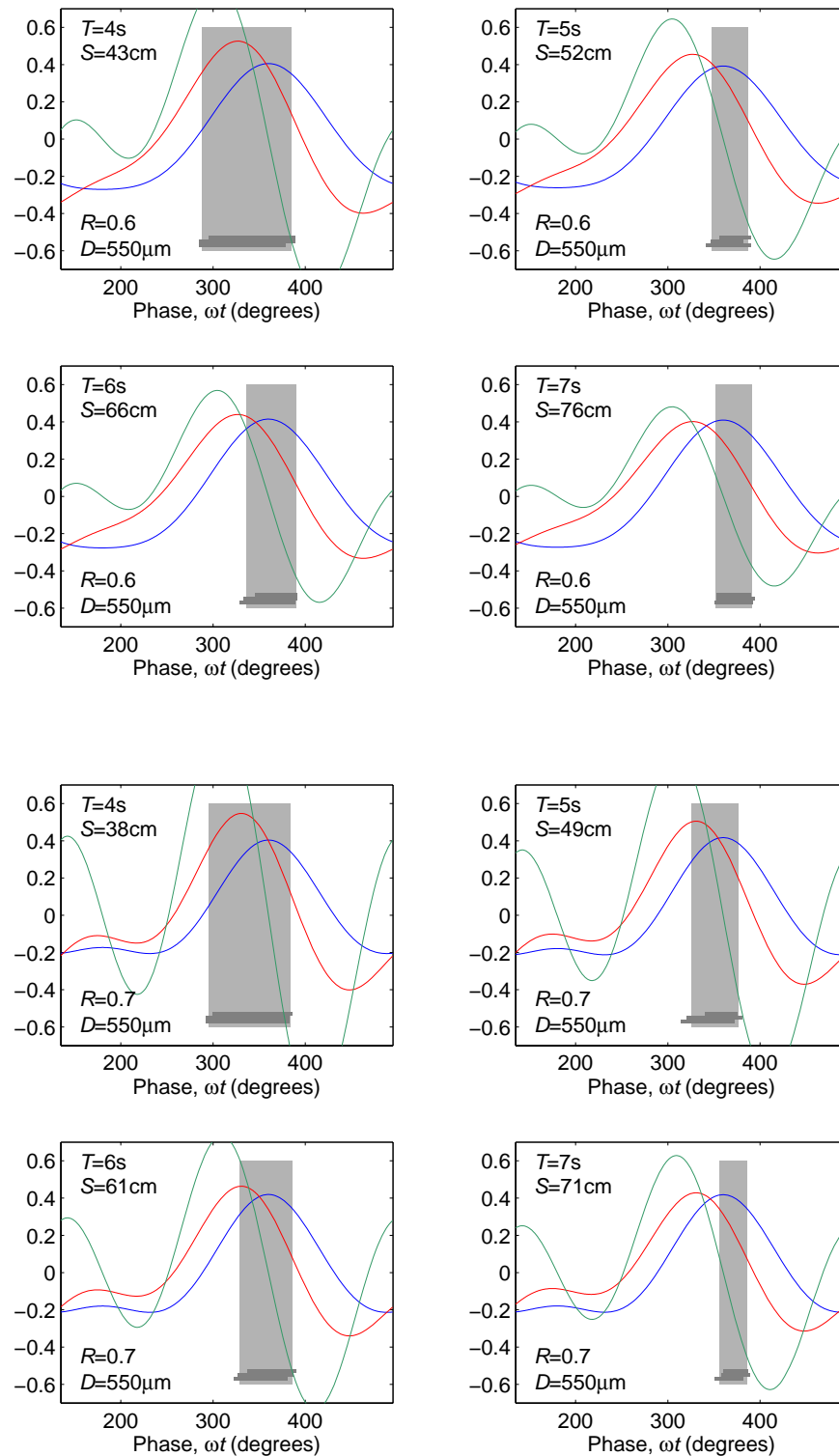


Figure 7.31. Observations of the phase and duration of quartz sand motion, at the threshold of motion condition under asymmetric flows. Key: blue lines – outer flow velocity; red lines – laminar shear stress; green lines – grain inertial forces; shaded area – period of observed grain motion (lighter shade – mean duration; darker shade – individual observations).

## 7.6. Discussion: The effect of wave period and asymmetry on $\tau_{c \text{ crit}}$ under laminar and transitional flow conditions.

A larger peak shear stress appears to be necessary in order to cause the threshold of motion for sand under smaller oscillatory flow periods. Under transitional or fully turbulent flows, this statement applies to the cycle-mean shear stress, as used typically in sediment dynamics studies. This effect was observed in relation to both laminar and transitional turbulent flow conditions; however, it was less significant in the former. In a parallel investigation, it has been shown also that a larger peak shear stress is needed to cause threshold, under oscillatory flows of greater asymmetry. A number of possible mechanisms have been proposed in order to explain these observations. Sources of observational and experimental error have been examined; these were shown subsequently to have no significant or coherent effect. Of the three remaining mechanisms, two relate to variation previously unaccounted for in the derived time-mean and instantaneous shear stresses, used to represent such turbulent flows. The third argues the importance of time-integrated forces (the ‘work’ done to move individual grains). Successful application of any of the proposed mechanisms should account also for the observed delay in the onset of motion, following the peak in the shear stress.

### 7.6.1. Laminar flow conditions

The observation of wave period and asymmetry effects under laminar flow conditions is significant, as it excludes the relatively unpredictable or stochastic effect of turbulence; this, in turn, reinforces the potential importance of cumulative, or time-dependant, forces. In the present study, only one mechanism (arguing the importance of time integrated forces) is presented, by which  $\delta \tau_{c \text{ crit}}/\delta T$  and  $\delta \tau_{c \text{ crit}}/\delta R$  may be explained under laminar flow conditions. As part of the present study, consideration was given also to the importance of vertical length scales (e.g.  $D/\delta_{0.99}$ ) and other aspects of the middle/upper flow (e.g. maximum velocity gradients ( $\delta u/\delta z$ ) or fluid acceleration ( $\delta u/\delta t$ )); such studies were discontinued as variation in these parameters tended to be insignificant on the scale of an individual grain in the lower part of the boundary layer.

For sinusoidal flows of varying  $T$ , time-mean shear forces were observed to converge at  $\Delta t \approx 2.5$ s. This time-step was approximately a factor 1.5-5 longer than the delay in the onset of motion under near-transitional conditions, which occurred 0.25-0.86s following the peak in  $\tau$ , i.e. this time frame corresponds to  $\Delta t = 0.5-1.7$ s. Under asymmetric flows, the time-mean shear forces were observed to converge at  $\Delta t \approx 1.44$ s and 2.53s for  $T=4$ s and 7s, respectively. This was a factor 3-5 longer than the delay in the onset of grain motion ( $\sim 0.25-0.86$ s, for

---

$D=275\mu\text{m}$ , at all values of  $R$ ). [Note: the early onset observed in the asymmetric  $D=550\mu\text{m}$  data should be ignored, because of the issues highlighted in relation to acceleration forces. Because onset occurred some time before the convergence of the time-mean shear stress values, this did not provide particularly convincing evidence in support of this mechanism; however, it should not be discounted altogether.]

The mechanism by which energy is somehow stored within the bed, prior to the onset of motion, is not clear. Based upon Hinze (1975), Soulsby (*pers comm.*) suggested that the characteristic time-scale for the development of flow and shear forces, around individual grains, is of the order  $\sim 0.05\text{s}$ . This value is in better agreement with the concept of instantaneous shear stress causing the erosion of individual grains. However, there remains conflict between this relatively small time-scale and the longer delay observed in the onset of grain motion (0.25-0.86s). It is proposed that this process is only initiated at sufficiently large instantaneous or time-mean value of  $\tau$  (a function of  $\tau_c$  and  $\Delta t$ ); likewise, that a subsequent time period ( $\sim 0.25\text{-}0.86\text{s}$ ) of sufficiently large  $\tau$  is required then to cause a critical mass or rate of initial dislodgement of the grains. The additional ballistic momentum flux (BMF), a grain impact force, (Section 4.4.6) causes then a chain reaction of grain dislodgment. Grains are transported in either traction or limited saltation modes; these receive kinetic energy from BMF and the horizontal fluid pressure related to fluid velocity (the magnitude of  $\tau$  at the bed surface or elsewhere is less important). Hence, the time-frame of grain motion is centered around the peak in horizontal velocity. New grain dislodgment ceases when the combined shear stress and BMF are reduced. Subsequently, sediment motion decreases and ends when the horizontal velocity in the lower-middle boundary layer is no longer sufficient to support grains already in motion. A similar pattern has been reported in Figures by Davies (1980, 1984, 1985), on the basis of field observations, where the duration of sediment motion was (visually) centered upon the peak in the near-bed velocity.

### 7.6.2. Transitional/turbulent flow conditions

In addition to the laminar mechanisms described in Section 7.6.1, the presence of turbulence exaggerates the gradients  $\delta\tau_{c\text{ crit}}/\delta T$  and  $\delta\tau_{c\text{ crit}}/\delta R$ . The general importance of turbulence may be addressed by considering separately, the cases of laminar and fully turbulent flow conditions. It may be assumed that there is then a gradual merging of the two states within the transitional flow regime. In order to simplify the initial approach to this discussion, the assumption is made that the threshold of motion is controlled by the balance of forces approach, i.e. assuming a single critical instantaneous shear value to cause threshold.

---

However, this assumption should be treated with caution, as discussed in the previous Section.

Under laminar flow conditions for sinusoidal or asymmetric flows, the outer flow amplitude interacts with the bed via viscous shear through the full thickness of the boundary layer. Because  $\delta \propto T$ , a larger value of  $U_c$  is needed at larger  $T$ , to generate the same value of  $\tau_c$  at the bed. Therefore, in the laminar case,  $\tau_{c \text{ crit}}$  is (nearly) constant and, in theory,  $U_{c \text{ crit}} \propto \sqrt{T}$ . Under fully turbulent flow, periodic eddies with fluid velocities equal or near to that of  $U_c$  will penetrate to the bed; these cause a localised, instantaneous shear stress, proportional to  $U_c^2$ . Therefore, in the turbulent case,  $U_{c \text{ crit}}$  and the peak instantaneous  $\tau$  may both remain nearly constant over a range of  $T$ . However, instantaneous  $\tau$  is represented instead by the peak mean value ( $\tau_{c \text{ crit}}$ ) and, because  $U_{c \text{ crit}}$  remains constant,  $\tau_{c \text{ crit}} \propto \sqrt{(1/T)}$  and has a positive linear relationship with  $R$ . These patterns described for laminar and turbulent flow were observed, to some extent, in the data; however, laminar flows exhibited a small gradient  $\delta \tau_{c \text{ crit}} / \delta T$  and (transitional) turbulent flows contained a small gradient  $\delta U_c / \delta T$ . Clearly, a number of additional processes are occurring to cause deviation from this simplistic analysis.

Two mechanisms have been presented, in order to investigate changes in the gradients  $\delta \tau_{c \text{ crit}} / \delta T$  and  $\delta \tau_{c \text{ crit}} / \delta R$  as a result of the presence of turbulence. The first suggests that variation in  $\tau_{c \text{ crit}}$  is simply a result of a period- or asymmetry-dependant error in its calculation in the transitional regime. In order to investigate this concept, a new model for the wave friction factor under rough transitional flows has been proposed; this was based upon the ‘transition to turbulence’ results described in Chapter 6. Due to lack of data, it was not possible to test some of the important assumptions made in the model, such as: the form of the fit between laminar and fully turbulent solutions in the transitional regime (e.g. linear, logarithmic, etc); or the validity of a single solution for given  $a/D$  in the rough turbulent regime for all  $T$  and  $R$ . It was noted also that the model was unsuccessful when applied to large grain sizes under asymmetric flows; this is because the implicit relationship did not converge between the laminar and fully turbulent solution. However, in some cases, it was observed that some reduction was made in the gradients  $\delta \tau_{c \text{ crit}} / \delta T$  and  $\delta \tau_{c \text{ crit}} / \delta R$ . Thus, it is possible that incorrect calculation of  $\tau_c$  may, to some extent, anomalously introduce or exaggerate such gradients. This area is considered to be important for future study, as transitional flow conditions correspond typically to: (a) the threshold of motion for quartz sands ( $D > 400\text{-}500\mu\text{m}$ ); and (b) transport conditions for finer-grained material.

---

The second mechanism presented, highlights the fact that the derived  $\tau_{c \text{ crit}}$  value is the peak of the cycle-mean shear stress. Likewise, that the probability of localised instantaneous higher shear events is greater under longer wave periods. It is proposed that, in combination, these may bring about similar hydrodynamic conditions, causing the threshold of motion, although the (cycle-mean) peak in shear stress may apparently vary with wave period. In order to test this hypothesis, a simplified model was designed. The model was limited in its accuracy by: (i) the representation of velocity fluctuation using the half cycle rms value ( $u'$ ) which did not describe time-dependant velocity fluctuation around the phase of  $\tau_c$ ; and also (ii) by the absence of information relating to the variation of  $u'$  with  $R$ . The arbitrary selection of the representative length-scale  $y$  and its impact on the results was considered also to be indicative of the limited practical use of the model. However, the proposed mechanism was fitted successfully to the data in a qualitative sense, as shown in a few examples. Therefore, it is also possible that the observed gradients  $\delta\tau_{c \text{ crit}}/\delta T$  and  $\delta\tau_{c \text{ crit}}/\delta R$  are real features of the data, in the presence of turbulence.

## **7.7. Discussion: The suitability of various methods to predict the threshold of motion for sand under waves.**

Aspects of the data highlighted in this Chapter are discussed now, within the context of the methods commonly used previously to predict the threshold of motion, namely: critical velocity approaches; the approach of Shields (1936); Moveability Number approaches; and stochastic approaches. The scope of this discussion is focused upon uniform sands, with  $D$  and  $\rho_s$  within the range of the data analysed in the present study. As such, this range refers generally to sediment that achieves threshold of motion under either laminar or transitional, but not fully turbulent, oscillatory flows.

### *7.7.1. The critical velocity approach*

The critical velocity approach, as used by previous researchers, is described in Section 2.13. The majority of critical velocity equations make the same assumption as that of the Shields diagram, i.e. that a single critical value of  $\tau_{c \text{ crit}}$  is sufficient to describe threshold of motion, for a given uniform sediment, under oscillatory flows, at all  $T$ ; this implies that  $U_{c \text{ crit}} \propto \sqrt{T}$ . However, for reasons discussed previously (Section 7.6.1), the observed gradient  $\delta U_c/\delta T$  was smaller than would be expected in the laminar regime; it became even smaller in progressively (transitional) turbulent flows, to the extent that in some cases  $\delta U_c/\delta T \Rightarrow 0$ . Only a small number of researchers have proposed such relationships that yield constant  $U_c$  with  $T$ , e.g. the turbulent solution of Manohar (1955) and the general solution of Vincent (1957).

---

Data from the present study were fitted to the general empirical relationship,

$$c_1 = \frac{U_{crit} V^{c_2}}{\left[ \left( \frac{\rho_s - \rho}{\rho} \right)^{c_3} g^{c_4} D^{c_5} T^{c_6} R^{c_7} \right]^{c_8}} \quad \text{Eq. 7.6}$$

The structure of this relationship is based upon the wide range of such critical velocity equations previously proposed; in addition, this utilises the full range of parameters previously used. Least error analysis was used to determine the fitting coefficients  $c_n$  ( $n=1-8$ ) (Table 7.2) for: all of the data; all the sinusoidal data from the present and previous studies (excluding the parameter  $R$ ); and all the sinusoidal and asymmetric data collected during the present study.

n	All data <sub>1</sub>	Sinusoidal data <sub>2</sub>	Present study <sub>3</sub>
1	24.108	4.032	28.598
2	0.810	-0.173	-0.519
3	0.674	3.107	0.513
4	-9.958	1.527	1.387
5	0.025	1.049	-0.139
6	0.107	1.086	0.084
7	0.982	0.000	0.734
8	0.671	0.165	0.674

Table 7.2. Fitting coefficients for Eq. 7.6, predicting  $U_{crit}$  for the threshold of motion. (1) all the data used in the present study; (2) all the sinusoidal data from the present and previous studies (excluding the parameter  $R$ ); (3) and all the sinusoidal and asymmetric data collected during the present study.

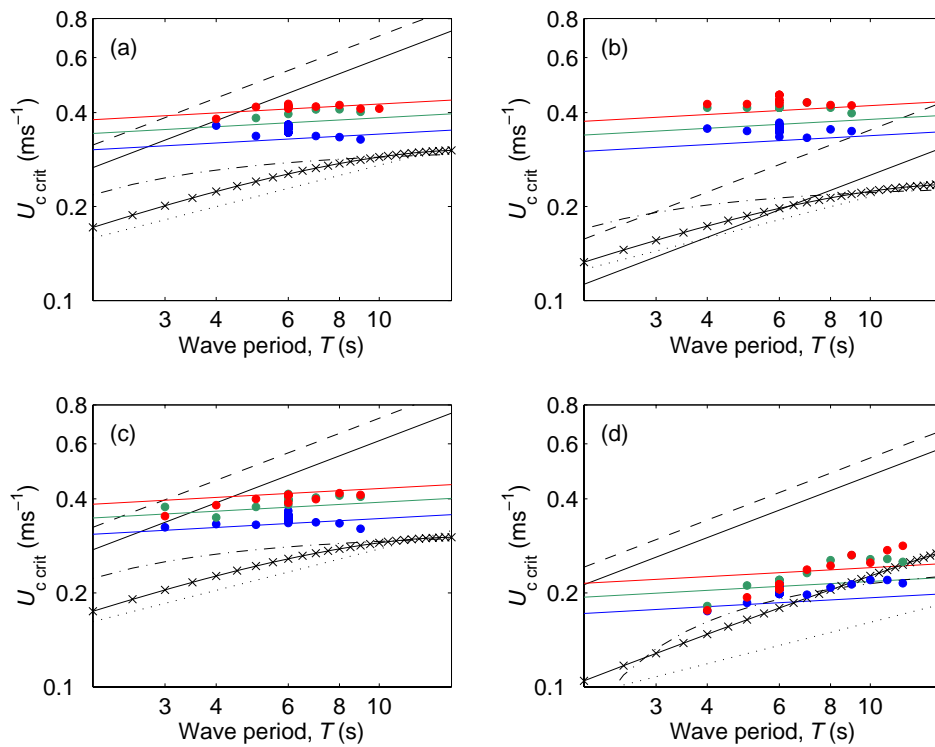


Figure 7.32. Critical outer flow velocity amplitude observed in the present study, for threshold of motion in: (a) quartz sediment,  $D=550\mu\text{m}$ ; (b) quartz sediment,  $D=275\mu\text{m}$ ; (c) aragonite sediment,  $D=550\mu\text{m}$ ; and (d) Bakelite sediment,  $D=1500\mu\text{m}$ . Key: blue, green and red lines and data points – Eq. 7.6 using coefficients for all data, and observed data for  $R=0.5$ ,  $0.6$  and  $0.7$ , respectively; black lines – predictive equations of Shields (1936) [solid line], Manohar (1955) [dashed line], Komar and Miller (1973, 1974) [dotted line], You (2000) [dot-dashed line] and Le Roux (2001) [solid line with crosses].

Selected results from the present study are shown, in relation to a range of predicted values, in Figure 7.32. The error in the computed values of  $U_{c\text{crit}}$  was small, in all cases. For all of the data, error  $> \pm 10\text{cms}^{-1}$  occurred in 1.6% of observations, whilst error  $> \pm 5\text{cms}^{-1}$  occurred in 11.5% of observations; the mean error was  $\pm 2.5\text{cms}^{-1}$  (typically 9.5% of observed  $U_{c\text{crit}}$ ). These values increased slightly when considering only the sinusoidal data, to 2.9% and 16.3%, respectively; the mean error was  $\pm 2.2\text{cms}^{-1}$  (typically, 11.8% of the observed  $U_{c\text{crit}}$ ). The asymmetric relationship provided a better description of the data; the maximum error was  $\pm 6.9\text{cms}^{-1}$  and the mean error was only  $\pm 1.4\text{cms}^{-1}$  (typically 4.3% of observed  $U_{c\text{crit}}$ ). The significant reduction in error, when using data from only a single source and over a relatively narrow range of parameters, is indicative, at least partly, of the scatter introduced by differences in experimental methodologies. Similarly, there is difficulty in incorporating variation in  $\delta U_{c\text{crit}}/\delta T$  across a much broader range of grain and flow parameters, within the

larger data sets. As such, the new relationships presented herein do not necessarily represent the slope of the Bakelite data as well as that of others, e.g. You (2000) or Le Roux (2001).

A wide range of critical values was obtained on the basis of the selection of the relationships presented in Figure 7.32; this corresponded to significant error, when compared to the observed data. These relationships tended generally to generally either over- or under-estimate the value of  $U_{c \text{ crit}}$  (with little or no overlap). In addition, the difference between the observed and predicted gradients of  $\delta U_{c \text{ crit}} / \delta T$  were such that, even if an overlap of values occurred, the relationships proportional to  $\sqrt{T}$  tended to over- and under-predict  $U_{c \text{ crit}}$  at larger and smaller values of  $T$ , respectively, i.e. the gradient of the predicted curve is too steep. The relationships of You (2000) and Komar and Miller (1973, 1974) were closest to that of the present study, in terms of the effect of  $T$ .

Provided that the critical velocity is predicted accurately for the sinusoidal case (in terms of the mean value and with respect to  $T$ ), the effect of asymmetry may easily be incorporated by calculating the corresponding critical stroke length; this, then remains approximately constant with  $R$ .

### 7.7.2. *The approach of Shields (1936)*

The approach of Shields (1936), together with subsequent developments of this approach, are described in Section 2.14. The construction of the Shields parameter and diagram, for unidirectional and oscillatory flows, implies that for any given uniform sediment, the threshold condition is represented by a single value of  $\tau_{c \text{ crit}}$ . This condition precludes the assumption that the critical value of  $U_c$  varies then, with  $T$ . However, the present study has shown that for oscillatory data, within the range investigated, the negative gradient  $\delta \tau_{c \text{ crit}} / \delta T$  is significant, becoming more pronounced into the transitional/turbulent regime for observations relating to any given sediment (Section 7.3). Consequently, the positive gradient  $\delta U_{c \text{ crit}} / \delta T$  is correspondingly smaller than would otherwise be predicted. This effect was less (closer to the assumptions of Shields), but was still clearly present in those data that were deemed to have been collected under laminar flow conditions; it increased as the flow became progressively more (transitionally) turbulent.

The direct result of this failure in the assumptions is to introduce scatter in oscillatory flow data about the Shields curve, as was demonstrated for sinusoidal flows in Figure 2.11. Values of the Shield parameter are scattered vertically by the effect of wave period (larger values correspond to smaller  $T$ ). Scatter is least when  $\theta_{\text{crit}}$  is plotted against  $D^*$  (Eq. 2.42),

---

where the scatter is limited to differences in  $\theta_{\text{crit}}$ . However, if  $\theta_{\text{crit}}$  is plotted against  $\text{Re}_*$ , then an additional lateral scatter away from the Shields curve is included also; this is due to variation in  $u_*$  (a component parameter in  $\text{Re}_*$ ) with  $T$ . The apparent scatter is greatest for threshold around the transitional region of the curve, for two reasons: (1) because  $\delta\tau_{c \text{ crit}}/\delta T$  and, therefore, the range of  $\theta$  is larger for threshold occurring under transitional flows (in comparison to laminar flows); and (2) this larger range is further exaggerated visually by the logarithmic (vertical) scaling of the diagram.

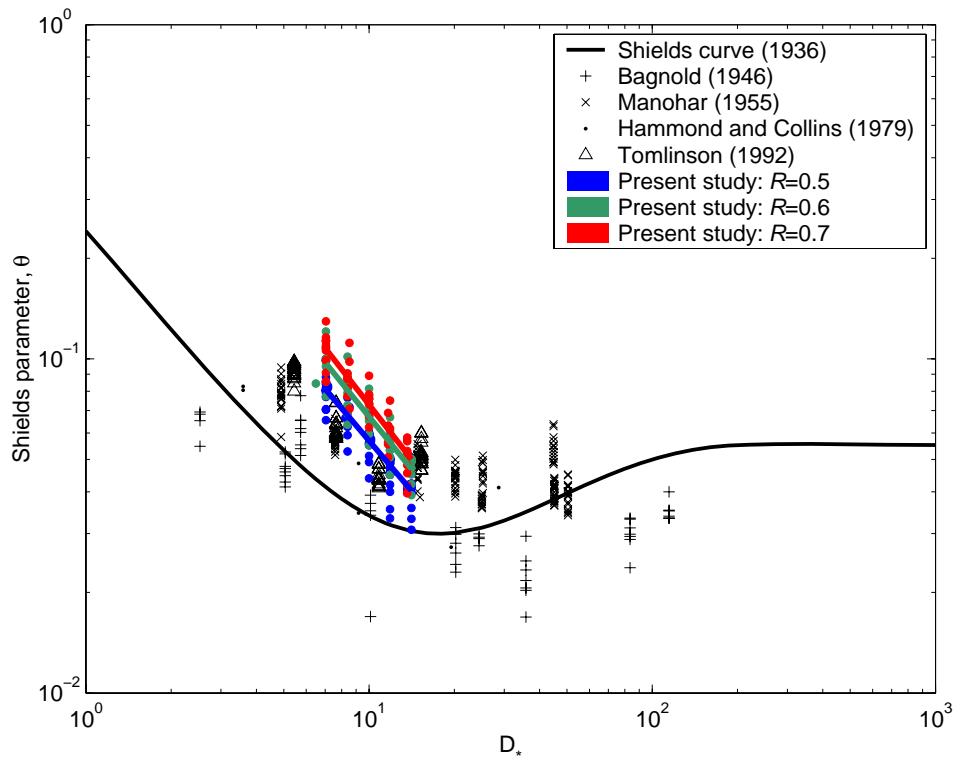


Figure 7.33. The Shields curve for threshold of motion (Eq. 2.46) and threshold data for sinusoidal and asymmetric oscillatory flows.

The effect of flow asymmetry has been determined on the basis of the relationship between  $R$  and  $\tau_{c \text{ crit}}$  (Section 7.4). The data collected during the present study are plotted, in relation to the Shields curve and sinusoidal data from previous investigators, in Figure 7.33. In addition to the effect of  $T$ , previously described, the effect of asymmetry is to increase further the value of  $\theta_{\text{crit}}$  and  $\text{Re}_*$  (if used). This increase is consistent over the range of flow/sediment conditions investigated. For the same reasons discussed above, the apparent additional scatter is relatively greater when  $\theta_{\text{crit}}$  is plotted against  $\text{Re}_*$ , rather than  $D_*$ . In the Figure, the scatter associated with  $\delta\tau_{c \text{ crit}}/\delta R$  actually decreases, in absolute terms, into the transitional

region; however, it appears to remain nearly constant because the decrease is balanced (visually) by the logarithmic vertical scale.

In order to represent accurately the observations and results presented herein, the Shields curve should be plotted (preferably) using  $D_*$  on the abscissa. Whereas a single curve has typically been previously used, the new results would be represented more closely by a series of similar curves, shifted from a baseline representing large  $T$  (possibly equivalent to the unidirectional case), to larger  $\theta$  with decreasing  $T$  and increasing  $R$ . The magnitude of the shift should theoretically vary laterally across the plot with  $D_*$ , with a smaller range under laminar flows. This range would increase gradually over the transitional regime, possibly becoming stable at some larger range within the turbulent portion of the diagram.

Alternatively, a single Shields type curve may be maintained, by changing the numerator (representing erosive forces) in the construction of  $\theta$ . For laminar sinusoidal flows, the parameter  $\tau_{0 \text{ crit}}$ , in  $\theta$ , should be replaced with the time-mean shear stress parameter,

$$\left| \bar{\tau} \right|_{\omega(\tau_{\text{max}}) \pm 1.25\omega} \quad \text{Eq. 7.7}$$

utilising a mean characteristic time-averaging interval  $\Delta t=2.5s$ . This parameter will reduce the scatter relating to wave period effects within groups of data, by a factor of 2-4. Residual scatter of data groups (collected by different individuals) about the curve will still be present due to the use of a mean value of  $\Delta t$ ; this is primarily representative of differences in the methodologies used. In the turbulent regime, the shear stress should be replaced altogether, with a parameter reflecting  $U_{\infty \text{ crit}}$ . In order to maintain  $\theta$  as a dimensionless quantity,  $\tau_{0 \text{ crit}}$  may be replaced by,

$$U_{\infty}^2 \rho c \quad \text{Eq. 7.8}$$

where  $c$  is a scaling constant in order to maintain visual continuity of the curve between the transitional and turbulent portions of the diagram. Thus this parameter has the same units as  $\tau$  but is not scaled with  $T$  in the same way. In the transitional regime, the characteristic shear stress parameter lies between the laminar and turbulent solution; therefore, it should be a function of the relative presence of turbulence, at threshold (a function of the standard parameters, i.e.  $T$ ,  $R$ ,  $D$  and  $\rho_s$ ).

---

The inclusion of flow asymmetry is more complex, as the solution is a function of both  $T$  and  $R$ ; as such, it is suggested that an altogether separate diagram be constructed. This diagram would have separate curves, that increase in magnitude of  $\theta$  with decreasing  $T$ . Plotting sinusoidal or asymmetric data in the laminar/near laminar transitional regime, the parameter  $\tau_{c \text{ crit}}$  in  $\theta$  should be replaced with the phase-mean shear stress parameter,

$$\left| \bar{\tau} \right|_{\omega t_{(\tau \text{ max})} \pm 65^\circ} \quad \text{Eq. 7.9}$$

which utilises a mean characteristic phase-averaging interval,  $\Delta\omega t=130^\circ$ . Based upon a similar approach as that used for the sinusoidal data, this new parameter will be also closely representative of the laminar regime. In the turbulent regime, Eq. 7.9 may be applied theoretically but, due to a lack of data, it is not clear how this parameter should change under the influence of progressively greater turbulence within the transitional and turbulent regimes.

Alternatively, as applied previously to the critical velocity approach (Section 7.7.1), the critical stroke length may be hind-cast and applied directly to the asymmetric case.

In order to incorporate the above suggestions, the curve representing the threshold of motion will have to be redrawn as a ‘line of best fit’ to the data, on the basis of the new parameters (Eq. 7.7, Eq. 7.8, Eq. 7.9 and  $R$ ). Because of fundamental differences in the parameters representing laminar and turbulent flows it may be more appropriate to consider the single Shields curve approach as a numerical, rather than simply a graphical, approach to the prediction of sediment threshold.

### 7.7.3. The Moveability Number approach

The Moveability Number has been described in Section 2.15. The Moveability Number has been calculated for all of the sinusoidal and asymmetric data; it is plotted against  $D$ , in Figure 7.34. The implication of the ‘moveability curve’ is that, at small  $D$ , the fluid shear necessary to cause the threshold of motion is smaller, when compared to the fall velocity of the same particle within the same fluid. As such, the gradient of the curve represents flow conditions at threshold, changing from ‘dominantly laminar’ to ‘dominantly turbulent’ as the grain size increases. The location and shape of the curve (i.e. the distribution of data around the curve) is affected then by the effects of sediment density, wave period and flow asymmetry.

---

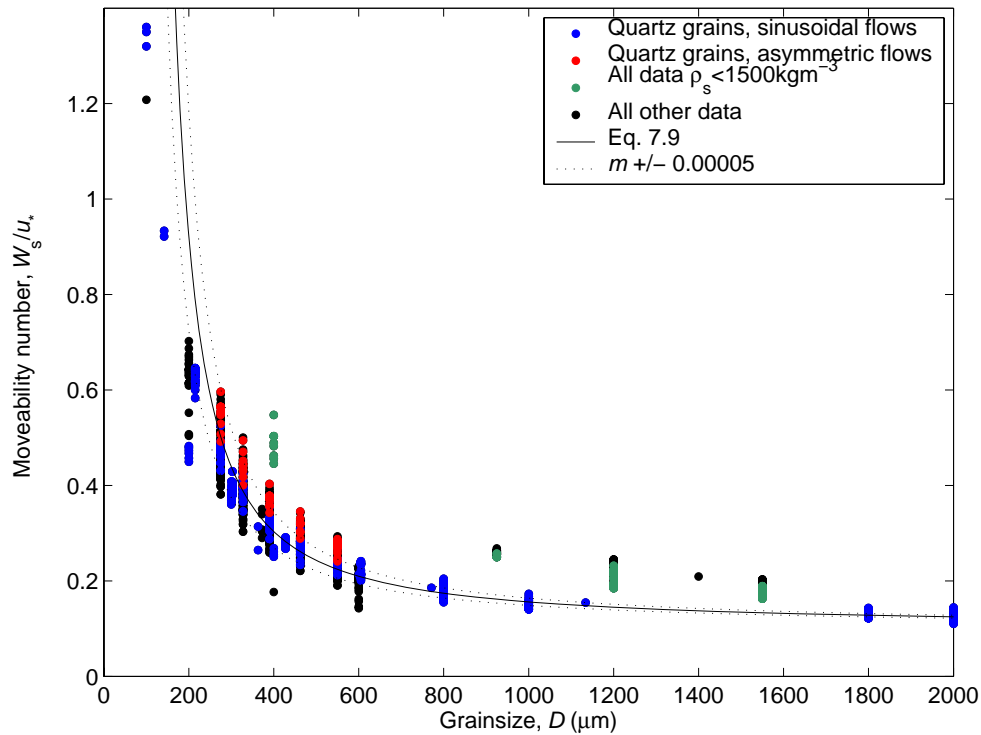


Figure 7.34. The Moveability Number parameter for all sinusoidal and asymmetric threshold of motion observations used in the present study.

When plotted against grain diameter, the Moveability Number (MN) parameter followed the relationship

$$MN = n \times e^{(m/D)} \quad \text{Eq. 7.10}$$

where  $n$  and  $m$  are fitting coefficients, dependant upon  $T$ ,  $\rho_s$ , and  $R$ . A general empirical relationship was fitted to all the sinusoidal data using [ $n=0.1$   $m=4.44 \times 10^{-4}$ ]. This relationship produced an error of the order  $\pm 50\%$  when reverse calculating the corresponding value of  $\tau_{c \text{ crit}}$  for all data. The majority of the error could be attributed to variation in the critical shear stress associated with  $T$  and  $\rho_s$ . The lesser effect of asymmetry was also present. The ‘moveability curve’ was generally shifted away from the origin, with decreasing  $T$  or with increasing  $\rho_s$  and/or  $R$ . By providing a single value of  $\tau_{c \text{ crit}}$ , the moveability curve represents the data no better (or worse) than any other methods, which do not include differences attributable to  $T$  or  $R$ .

Values of predicted  $\tau_{c \text{ crit}}$  were sensitive to any small offset, between the curve and the data used in the fitting of the curve. Given the complex interaction of the fluid and sediment parameters in regulating turbulence and susceptibility to erosion, it does not seem reasonable to assume that all the grain sizes may be represented by a simple exponential function covering laminar, transitional and turbulent flows. However, given the reasonable estimation of  $\tau_{c \text{ crit}}$  using the general solution (see above), the effect of turbulence appears to be largely implicitly accounted for by the use of the settling velocity. For accuracy, future users of such empirical relationships will have to use standardised methods to calculate  $W_s$ , as prescribed by the original investigator; failure to do so would result potentially in a significant offset in predicted values of  $\tau_{c \text{ crit}}$ . Such general relationships represent the mean of the available data and users will therefore also have to be aware of the potential offset in predicted  $\tau_{c \text{ crit}}$  as a result of  $\rho_s$ ,  $T$  and  $R$ ; additional variance might be observed as a result of other stochastic parameters such as grain pivoting angle (a result of grain shape and bed packing).

#### 7.7.4. Stochastic approaches

Stochastic approaches, used previously to estimate the threshold of motion under unidirectional flows, are described in Section 2.16. On the scale of individual grains, the stochastic approach still relies upon the concept of a critical shear stress being achieved, i.e. individual grains have an associated  $\tau_{c \text{ crit}}$  value which varies in an approximately normal distribution with the individual grain size/grain density/pivoting angle (with neighbouring grains) and the grain will be eroded if  $\tau > \tau_{c \text{ crit}}$ . Therefore, the values  $\tau_{c \text{ crit}}$  for the whole bed have a normal distribution and the resulting motion of the bed is in response to fluid shear stress; this is variable in a similar approximately normal distribution. This concept is relatively simple for unidirectional flows, as the distribution of both erosive and resistive parameters are relatively constant, over time. However, this does not transfer easily to oscillatory flows where stochastic relationships, describing the flow, will necessarily vary with phase (time) over the wave cycle. Instantaneous values might also be influenced to some extent by the timescale and magnitude of prior flow development, i.e. making this sensitive to wave period and flow asymmetry.

Under laminar flows, fluid shear forces follow the analytical laminar solution and their amplitude is greatest at the phase of  $\tau_c$  (e.g.  $45^\circ$  prior to the phase of  $U_\infty$  under sinusoidal flows). The stochastic distribution of fluid shear forces, about the predicted value at any instant, is theoretically zero or at least arguably very small, throughout the wave cycle. Under fully turbulent flows, the mean value follows the turbulent solution (e.g. where the phase of  $\tau_0$  is reduced to  $10^\circ$  prior to the phase of  $U_\infty$  under sinusoidal flows). In this case,

---

the stochastic distribution of velocity fluctuation about the mean value is time variable, becoming generally broader closer to the phase of  $U_c$ . Transitional flows experience alternating periods of laminar and turbulent flow; as such, they are represented intermittently by both laminar and turbulent solutions. The phase of onset of the turbulence and the duration and the intensity of each (laminar or turbulent) stage is a function of  $U_c$ ,  $T$ ,  $D$ ,  $R$ , i.e. the position of the flow condition (relative to the transitional range).

Through the utilisation of stochastic relationships, to describe both the erosive and resistive forces under oscillatory flow, this approach eliminates the concept of a single threshold condition. Indeed, under unidirectional flows, the stochastic approach predicts a gradually increasing probability of motion, with increasing mean shear stress (i.e. gradually increasing  $\theta$  at given  $D_*$ ) (Grass, 1970; Lopez and Garcia, 2001). However, the sudden onset of motion observed visually in the present study, under oscillatory flows (Section 4.3.3) disagrees with this concept. Here, very little grain motion was observed for flow amplitudes less than that required for threshold; however, when threshold was achieved, the number of grains in motion and, therefore, the probability of individual grain motion, increased suddenly. It is thought that BMF may be one important factor in this observation. If observations of a sudden step (representing threshold) in the probability of grain motion were made in other laboratory experiments and/or using stochastic numerical models, then the concept of a (more well) defined threshold condition may be applied to oscillatory flows.

Simplistic models developed as part of the present study (Sections 7.3.5.a and 7.4.3.a) suggest that the stochastic approach may permit, or indeed explain, the observed relationships between the threshold of motion and wave period and/or flow asymmetry. In order to more accurately describe the instantaneous and time-varying stochastic distribution of turbulence over the wave cycle, further investigation is required.

## Chapter 8. Conclusions

### 8.1. Velocity profiling

The laminar boundary layer produced by the oscillating trolley used in the present study follows closely the velocity distribution predicted by the laminar second-order Stokes model. Hence, this flow model may be used, in conjunction with observations of the transition to turbulence or the threshold of sediment motion (under laminar flows), to investigate (numerically), patterns in these data associated with wave period and/or flow asymmetry. Also, the ability of the equipment to simulate adequately such flows (excluding secondary effects such as horizontal pressure gradients and boundary layer streaming) is validated.

### 8.2. Transition to turbulence

Transition to turbulence data representing a wide range of wave periods ( $T$ ), grain diameters ( $D$ ) and degrees of flow asymmetry ( $R$ ) were analysed as part of the present study. These data (both that collected previously and as part of the present study) were collected using oscillating trolley equipment, using similar methodology in each case for the definition and observation of transition. Comparison between these data and similar observations made using a wave channel suggest that transition may occur at smaller flow Reynolds numbers under the latter experimental conditions. Therefore, it is suggested that a more detailed comparison of such data is necessary, before the results of the present study may be applied directly and with confidence, to predicting transition under free surface gravity waves in the laboratory or in the field.

The transition to turbulence, over flat beds of uniform granular roughness under sinusoidal oscillatory flow, is represented well by the flow Reynolds number ( $Re$ ); its critical value increases linearly with the wave period (intercept = 0), up to a maximum ( $Re = 1.66 \times 10^5$ ). Because  $Re \propto T$ , the critical value of  $Re$  is a scalar multiple of the parameter  $a/D$ , where  $a$  is the orbital amplitude and the coefficient is proportional to  $D$ . For smooth beds transition occurred at the limiting value of  $Re$  for  $T > 3.5s$ . However, at smaller wave periods,  $Re_{crit}$  decreased in proportion to  $T$  and the intercept of the 'best fit' linear relationship between  $T$  and  $Re$  was greater than zero.

Transition under asymmetric flows was represented well by the boundary Reynolds number ( $RE$ ). The effect of flow asymmetry is to progressively stabilise the boundary layer, relative to the critical Reynolds number for the sinusoidal case. The increase in the critical Reynolds

---

number is a non-linear function of  $R$ ; this relative stabilising effect is greatest over smooth beds and is reduced with increasing  $D$ . Asymmetry is included in the proposed predictive relationships as an adjustment to the corresponding value calculated for the equivalent sinusoidal flow case (of the same  $T$  and  $D$ ). For the range of conditions investigated and  $R > 0.5$ , transition occurs initially under the crest half cycle in most cases; however, under some circumstances (typically large  $D$  and  $R$ ), transition may occur initially in the trough half cycle, whilst the crest half cycle remains laminar.

The balance between stabilising and destabilising forces within the boundary layer has been used to explain the observed dependence on wave period and flow asymmetry. Stabilisation of the boundary layer is achieved by: (a) increasing rates of fluid acceleration; and (b) by reducing the time frame for the development of turbulence. Over smooth beds, destabilisation is considered to be caused primarily by velocity shear in the lower-middle region of the boundary layer; over rough beds, the shedding of eddies from individual roughness elements is thought to be the dominant cause. Smooth bed processes dominate over beds  $D < 400\text{-}500\mu\text{m}$  and rough bed processes dominate for  $D > 2000\mu\text{m}$ ; intermediate grain sizes experience a balance between the two conditions. The proportional relationship between  $Re$  and  $T$  is likely to be caused by the linear relationship between  $T$  and the magnitude of the mid-boundary layer velocity shear, boundary layer thickness, flow acceleration, etc. The stabilising effect of flow asymmetry is considered to result from the increased rates of fluid acceleration and the reduced time scale for turbulence development; this more than offsets the increase in velocity amplitude, over the crest half-cycle. The balance of stability is typically affected in the opposite manner, under the trough.

### **8.3. Threshold of motion**

Threshold of motion data, representing a wide range of  $T$ ,  $D$  and  $R$ , were analysed as part of the present study. These data were all collected using oscillating trolley equipment and using similar methodology for the definition and observation of threshold. Additional forces introduced potentially by the equipment, not related to real phenomena in nature or the methods used and described herein, were considered. Such effects were discounted subsequently but included: inertial forces imparted to grains, by acceleration of the trolley; and/or systematic bias introduced by the methodology or criteria used to observe the threshold condition. However, comparison between these data and (a limited number of) similar observations made using a wave channel suggest that threshold may occur at a smaller flow Reynolds number under the latter experimental conditions. Therefore, it is suggested that further comparison of such different sources of data are necessary, before the

---

results of the present study may be applied directly and with confidence, to predicting threshold under free surface gravity waves in the laboratory, or in the field.

Under sinusoidal and asymmetric, laminar and transitional flows, the onset of sediment motion occurs some finite time ( $\omega t \approx 20^\circ - 45^\circ$ ) following the peak in shear stress. The subsequent duration of sediment motion ( $\sim 0.5 - 1$  s) is centered about the peak in the outer layer velocity. The cause of this delay is attributed to an unidentified mechanism, by which kinetic energy is somehow stored within the bed. This mechanism permits significant grain motion only following exposure of the bed to a sufficiently large force for a sufficient period of time (equivalent, in principle, to a mean or cumulative shear force). Hence, the onset of grain motion at threshold occurs only following the peak in bed shear stress. Once sediment motion is initiated, it is then maintained by a combination of: fluid pressure from the flow above the bed; and grain impact forces between saltating grains and grains at rest. Hence, the duration of sediment motion at threshold (as defined in the present study) is significant and typically spans symmetrically, the peak in outer flow velocity.

A greater critical shear stress,  $\tau_{c \text{ crit}}$  (calculated using laminar theory) is necessary to cause threshold of motion under smaller wave periods and/or with increasing flow asymmetry. Wave period dependence follows closely a linear relationship. The gradient  $\delta \tau_{c \text{ crit}} / \delta T$  is generally slight for threshold occurring under laminar or near laminar flow conditions but is present consistently; it tends to steepen with increasing presence of turbulence through the transitional regime. In the presence of flow asymmetry, the critical value of the orbital amplitude is approximately constant, for given  $T$ ,  $D$  and  $\rho_s$ . Therefore, the resulting increase in  $\tau_{c \text{ crit}}$  attributable to asymmetry is simply a (non-linear) function of  $R$ ; the relative increase is greatest at small values of  $R$ .

The most likely causes of the observed wave period and flow asymmetry dependences are considered to be: (i) inaccurate representation of the instantaneous flow field, by use of a single (peak) value to represent the shear stress; and (ii) the incorrect assumption that initial sediment motion is an immediate response to an instantaneous flow condition (see below).

- Under laminar flows, (i) may be ignored as the shear stress is theoretically uniform over the bed and follows the laminar solution closely. In this case, the critical condition is more closely described by the mean shear stress; for sinusoidal and asymmetric flows, this is calculated over a bandwidth centered upon the peak in shear stress  $\Delta t \approx 2.5$  s and  $\Delta \omega t \approx 130^\circ$ , respectively. In conjunction with the observation
-

of the delayed onset of sediment motion, following the peak in shear stress, this suggests that sediment threshold (of any significant volume) occurs suddenly. Likewise, only in response to a sufficiently large erosive force, applied over a sufficient duration.

- Under transitional/turbulent flows, the above argument may be applied also, but (i) also applies and the dependencies are exaggerated further by the effect of turbulence. The stochastic approach provides the clearest explanation for this, whereby longer wave periods and/or flows of lesser asymmetry produce a wider stochastic distribution of instantaneous shear stress. Under such a distribution, threshold occurs directly in response to the larger instantaneous shear forces (greater than the mean value); however, the flow is represented traditionally by the mean value, which will appear to decrease, with increasing width of the shear stress distribution.

Relationships used previously to estimate the threshold of motion in terms of critical velocity or shear stress (i.e. the Shields curve) both make the same (now seemingly incorrect) assumption that a single value of shear stress is necessary. As such, both equally misrepresent the data in this respect.

The importance of a (more) correct estimation of the threshold of motion is typified by the commonly used ‘excess shear stress’ type general relationships for predicting sediment transport. The present study shows that at smaller wave periods and greater flow asymmetry, transport equations in their present construction underestimate the conditions required for the threshold of motion, hence overestimating the excess shear stress and the resulting sediment transport. Adopting a ‘Shields similarity’ approach to the selection of sediment to be used in mobile bed scale models will have roughly the same effect.

#### **8.4. Other findings**

The wave friction factor,  $f_w$ , for sinusoidal and asymmetric flows under laminar conditions can be derived directly from the second-order Stokes model. In conjunction with the new relationships for the transition to turbulence provided herein, the point of departure from the laminar solution for  $f_w$  can be determined. From this model,  $f_w$  in the transitional region exhibits dependence upon wave period and flow asymmetry; at the point of departure from the laminar solution,  $f_w$  is larger for smaller  $T$  and/or smaller  $R$ . This effect becomes greater at large  $a/D$ .

### 8.5. Recommendations for future research

The conclusions summarised above and the relationships presented in previous Chapters provide new data and fresh insight into several fields of research. A number of study areas (discussed below) have been identified that will help to consolidate and extend this information. A wide range of detailed studies, utilising complex numerical simulations, are available presently in the literature and seem to be becoming a preferred tool for such investigations. However, the present study has shown that it is important to now re-assess and re-establish the expected, qualitative (if not quantitative), patterns associated with wave period and flow asymmetry. Once this is accomplished, a clearer identification and better understanding of the processes important in regulating either turbulence or the erosion of sediment, should aid the efficient future development of such numerical models.

To follow up the investigations relating to the transition to turbulence, it is recommended that the existing data set should be re-measured. This will help to fill in the gaps present in the data and may produce more consistent patterns during subsequent analysis. It is recommended that experiments be undertaken also, similar to those by Jensen *et al.* (1989) and Lodahl *et al.* (1998), i.e. phase mapping of the wave friction factor over the transitional range. This is preferable to a more traditional approach, as the transitional condition is not described by a set of otherwise subjective criteria. Significantly more information is obtained regarding the progressive nature of the development of turbulence and clearer comparison may be drawn between independently collected data sets. These experiments should be undertaken, using both smooth and rough beds, over a wide range of  $T$  and  $R$ . Rough beds should be chosen, in order to resolve the apparent transition between the dominantly ‘smooth’ and ‘rough’ bed conditions (Section 6.5). In addition, such data may be used to investigate and to quantify the stochastic distribution of turbulence (instantaneous shear stress) over a wide range of flow parameters. Similarly, relationships are required in order to express the development of such distributions throughout the wave cycle.

A significant break from traditional methods is required, in order to incorporate the concept of a variable, critical, peak shear stress amplitude for given sediment, under oscillatory flows. However, those developing methods of stochastic representation of threshold may more readily accept this concept. Further work is needed, in order to demonstrate consistency and to build confidence in the proposed relationships, across a wide range of experimental parameters (i.e.  $D$ ,  $\rho_s$ ,  $T$ ,  $R$ ). Similarly, a comparative study would be useful, (but not essential) between the different physical contexts typically being considered, i.e. in oscillating trolleys or water tunnels, in wave flumes and/or in the field. It is suggested that

---

this should include a review of all data previously collected, concerning the threshold of motion under oscillatory flows. With awareness for other potential causes of disagreement (e.g. subjectivity of visual criteria, choice of methodology), patterns in the critical flow parameters relating to wave period may be analysed further; additional data might allow investigation of such patterns throughout the transitional range and possibly into the fully rough turbulent regime.

Another potential direct application for this data is to ‘excess shear stress’ type sediment transport relationships. It is recommended that a study be undertaken to investigate wave period dependence in such observations, using the original Shields curve; following this, the threshold relationships presented herein may be used instead, to test for improvement of the estimate accuracy.

In relation to the broader fields of transition to turbulence or the threshold of motion for sediment, under oscillatory flows, it is recommended that future investigations be undertaken over a broad range of  $D$ ,  $T$  and  $R$ . Likewise, that analysis of such data should be undertaken on the basis of variation with respect to these variables. If a wide range of any parameter is not used, then the values used should be clearly reported and this potential limitation incorporated into the subsequent data analysis.

The new approach to the wave friction factor presented in Section 7.3.5.a has great implications for the (numerical) estimation of shear stress in the transitional, or indeed the laminar regime. It is recommended that existing (transitional) observations of  $f_w$  be re-analysed in the light of these suggestions to determine the validity and the nature (e.g. linear, logarithmic) of the suggested relationships. The laminar regime may be dealt with analytically, however, it is recommended that an investigation be undertaken to establish firmly, any effect of wave period or flow asymmetry on the relationship between  $f_w$  and  $(a/D)$  in the rough turbulent regime.

It is recommended that the oscillating trolley is a practical and versatile choice of equipment for such studies. The equipment is relatively cost effective, the sampling areas are easily accessible and a wide range of flow conditions may be simulated with relative ease. Studies relating to the transition to turbulence should use appropriately high-resolution flow measurement equipment, i.e. an LDV system, that permits coincidental recording of the phase of plate motion (or outer flow velocity).

## References

- Abbot, J.E. and Francis, J.R.D. (1977). Saltating and suspended trajectories of solid grains in a water stream. *Philosophical Transactions of the Royal Society of London, Series A*, **284**, p225-254.
- Amos, C.L., Li, M.Z. and Sutherland, T.F. (1998). The contribution of ballistic momentum flux to the erosion of cohesive beds by flowing water. *Journal of Coastal Research*, **14** (2), p564-569.
- Bagnold, R.A. (1936). *The Physics of Blown Sand and Desert Dunes*. Chapman and Hall, London. 265p.
- Bagnold, R. A. (1946). Motion of waves in shallow water. Interaction between waves and sand bottoms. *Proceedings of the Royal Society. Series A.*, **187**, p1 - 15.
- Bagnold, R.A. (1966). An approach to the sediment transport problem from general physics. U.S. *Geological Survey Professional Paper*, **4421**, 37p.
- Belibassakis, K. A. and Athanassoulis, G. A. (2002). Extension of second-order Stokes theory to variable bathymetry. *Journal of Fluid Mechanics*, **464**, p35-80.
- Blennerhassett, P. J. and Bassom, A. P. (2002). The linear stability of flat Stokes layers. *Journal of Fluid Mechanics*, **464**, p393-410.
- Buffington, J. M. (1999). The legend of A.F. Shields. *Journal of Hydraulic Engineering, ASCE.*, **125**, p376 - 387.
- Childs, S. J. (2001). Incipient motion criteria for a rigid sediment grain on a rigid surface. *Journal of Engineering Mechanics*, **127**, p524 - 529.
- Christensen, B. A. (1981). On the risk of erosion of cohesionless sea floors. *OCEANS '81, IEEE. New York, N.Y.*, p706-714.
- Collins, M. B. and Rigler, J. K. (1982). The use of settling velocity in defining the initiation of motion of heavy mineral grains, under unidirectional flow. *Sedimentology*, **29**, p419-426.
- Cosgrove, J. A., Buick, J. M., Tonge, S. J., Munro, C. G., Greated, C. A. and Campbell, D. M. (2003). Application of the lattice Boltzmann method to transition in oscillatory channel flow. *Journal of Physics A - Mathematical and General*, **36**, p2609-2620.
- Dancey, C. L., Panayiotis, D., Papanicolaou, A. and Bala, M. (2002). Probability of individual grain movement and threshold condition. *Journal of Hydraulic Engineering*, **128**, p1069-1075.
-

- 
- Dean, R. G. (1970). Relative validities of water wave theories. *Journal of the Waterways and Harbours Division, ASCE.*, **96**, p105 - 119.
- Dean, R. G. and Dalrymple, R. A. (1990). *Water wave mechanics for engineers and scientists*. World Scientific. 353p.
- Dean, R. G. and Dalrymple, R. A. (2002). *Coastal Processes*. Cambridge University Press.
- Du Toit, C. G. and Sleath, J. F. A. (1981). Velocity measurements close to rippled beds in oscillatory flow. *Journal of Fluid Mechanics*, **112**, p71 - 96.
- Einstein, H.A. (1950). *The Bed-Load Function for Sediment Transport in Open Channel Flows*. US Department of Agriculture. Soil Conservation Service. Technical Bulletin 1026.
- Francisco, G. and Santos, C. R. (2001). Transition to turbulence in the Reynolds' experiment. *Physica A*, **297**, p73-78.
- Fredsøe, J. and Deigaard, R. (1992). *Mechanics of Coastal Sediment Transport*. World Scientific.
- Garcia, M. H., Laursen, T. S., Michel, C. and Buffington, J. M. (2000). Discussion of "The legend of A.F. Shields". *Journal of Hydraulic Engineering*, **126**, p718-723.
- George, C. B. and Sleath, J. F. A. (1978). Oscillatory laminar flow above a rough bed. *Proc. 16th Coastal Engineering Conf.*, **1**, p898-910.
- Godreche, C. and Manneville, P. (1998). *Hydrodynamics and Non-Linear Instability*. Cambridge University Press.
- Grant, W. D., Boyer, L. F. and Sanford, L. P. (1982). The effects of bioturbation on the initiation of motion of intertidal sands. *Journal of Marine Research*, **40**, p659 - 677.
- Grass, A. J. (1970). Initial instability of fine bed sand. *Journal of the Hydraulics Division, ASCE.*, **96**, p619 - 632.
- Hammond, T. M. and Collins, M. B. (1979). On the threshold of transport of sand-sized sediment under the combined influence of unidirectional and oscillatory flow. *Sedimentology*, **26**, p795 - 812.
- Hammond, T. M. and Collins, M. B. (1979). Notes on the design of an oscillating trolley wave-simulator for installation in unidirectional flow flumes. *Journal of Sedimentary Petrology*, **49**, p643 - 646.
- Hino, M., Kashiwayanagi, M., Nakayama, A. and Hara, T. (1983). Experiments on the turbulence statistics and the structure of a reciprocating oscillatory flow. *Journal of Fluid Mechanics*, **131**, p363-400.
- Hino, M., Sawamoto, M. and Takasu, S. (1976). Experiments on transition to turbulence in an oscillatory pipe flow. *Journal of Fluid Mechanics*, **75**, p193-207.
- Hinze, J. O. (1975). *Turbulence (2nd ed.)*. McGraw-Hill. 790p.
-

- 
- Hughes, S. A. (1993). *Physical models and laboratory techniques in coastal engineering*. World Scientific. 550p.
- Jensen, B. L., Sumer, B. M. and Fredsøe, J. (1989). Turbulent oscillatory boundary layer at high Reynolds numbers. *Journal of Fluid Mechanics*, **206**, p265 - 297.
- Jonsson, I. G. (1966). Wave boundary layers and friction factors. *Proc. 10th Coastal Engineering Conf., ASCE.*, p127 - 148.
- Jonsson, I. G. (1980). A new approach to oscillatory rough turbulent boundary layers. *Ocean Engineering*, **7**, p109 - 152.
- Juárez, L. H. and Ramos, E. (2003). Direct numerical simulation of transition to turbulence in an oscillatory channel flow. *Comptes Rendus Mecanique*, **331**, p55-60.
- Justesen, P. (1988). Prediction of turbulent oscillatory flow over rough beds. *Coastal Engineering*, **12**, p257-284.
- Kaczmarek, L. M. and Ostrowski, R. (1996). Asymmetric and irregular wave effects on bedload: Theory versus laboratory and field experiments. *Proc. 25th Coastal Engineering Conf.*, p3467 - 3480.
- Kajiura, K. (1968). A model of the bottom boundary layer in water waves. *Bulletin of the Earthquake Research Institute.*, **46**, p75-123.
- Kalkanis, G. (1964). Transportation of bed material due to wave action., US Army Coastal Engineering Research Centre, Technical Memo 2., 38p.
- Kamphuis, J. W. (1975). Friction factor under oscillatory waves. *Journal of the Waterways, Harbours and Coastal Engineering Division, ASCE.*, **101**, p135-144.
- Kapdasli, M. S. and Dyer, K. R. (1986). Threshold conditions for sand movement on a rippled bed. *Geo-Marine Letters*, **6**, p161 - 164.
- Kemp, P. H. (1975). Wave asymmetry in the nearshore zone and breaker area. In Hails, J. and Carr, A. (Eds), *Nearshore Sediment Dynamics and Sedimentation*, John Wiley & Sons, 316p.
- Kleinhans, M. G. and van Rijn, L. C. (2002). Stochastic prediction of sediment transport in sand-gravel bed rivers. *Journal of Hydraulic Engineering*, **128**, p412-425.
- Komar, P. D. (1987). Selective gravel entrainment and the empirical evaluation of flow competence. *Sedimentology*, **34**, p1165 - 1176x.
- Komar, P. D. and Clemens, K. E. (1986). The relationship between a grain's settling velocity and threshold of motion under unidirectional currents. *Journal of Sedimentary Petrology*, **56**, p258-266.
- Komar, P. D. and Li, M. Z. (1986). Pivoting analyses of the selective entrainment by sediments by shape and size with application to gravel threshold. *Sedimentology*, **33**, p425 - 436.
-

- 
- Komar, P. D. and Miller, M. C. (1973). The threshold of sediment movement under oscillatory water waves. *Journal of Sedimentary Petrology*, **43**, p1101 - 1110.
- Komar, P. D. and Miller, M. C. (1974a). Sediment threshold under oscillatory waves. *Proc. 14th Coastal Engineering Conf., ASCE.*, p756 - 775.
- Kramer, H. (1935). Sand mixtures and sand movement in fluvial models. *Transactions, ASCE*, **100**, p798-838.
- Kuo, C. T. and Chen, W. J. (1990). Bottom shear stress and friction factor due to the asymmetric wave action. *Proc. 22nd Coastal Engineering Conf.*, p637 - 646.
- Lamb, H. (1932). *Hydrodynamics*. Cambridge University Press.
- Lambkin, D. O., Collins, M. B. and Paphitis, D. (In press). Wave period and flow asymmetry effects on the transition to turbulence in relation to sediment dynamics. *Journal of Geophysical Research*.
- Lavelle, W. J. and Mofjeld, H. O. (1987). Do critical stresses for incipient motion and erosion really exist? *Journal of Hydraulic Engineering, ASCE.*, **113**, p370 - 385.
- Lavelle, W. J. and Mofjeld, H. O. (1987). Bibliography on sediment threshold velocity. *Journal of Hydraulic Engineering, ASCE.*, **113**, p389 - 392.
- Le Mehaute, B. (1976). *An Introduction to Hydrodynamics and Water Waves*. Springer-Verlag. 315p.
- Le Roux, J. P. (2001). A simple method to predict the threshold of particle transport under oscillatory waves. *Sedimentary Geology*, **143**, p59-70.
- Le Roux, J. P. (2003). Wave friction factor as related to the Shields parameter for steady currents. *Sedimentary Geology*, **155**, p37-43.
- Le Roux, J. P. (2004). Reply to discussion - Le Roux, J.P., 2001. A simple method to predict the threshold of particle transport under oscillatory waves. *Sedimentary Geology* 143 (2001): 59–70. *Sedimentary Geology*, **163**, p327-330.
- Leeder, M.R. (1979) Bedload dynamics: grain impacts, momentum transfer and derivation of a grain Froude number. *Earth Processes*, **4**, p291-295.
- Lee Young, J. S. and Sleath, J. F. A. (1988). Initial motion in combined wave and current flows. *Proc. 21st Coastal Engineering Conf., ASCE*, p1141 - 1151.
- Lhermitte, M. P. (1958). Contribution à l'étude de la couche limite des houles progressives: Application aux mouvements de matériaux sous l'action des houles., C.O.E.C. Imprimerie Nationale. No. 136, 171p.
- Li, H. (1954). *Stability of Oscillatory Laminar Flow Along a Wall*, Technical Memo 47, University of California, Berkley, California., 35p.
- Li, M. Z. and Komar, P. D. (1986). Laboratory measurements of pivoting angles for applications to selective entrainment of gravel in a current. *Sedimentology*, **33**, p413 - 423.
-

- 
- Li, M. Z. and Komar, P. D. (1992). Selective entrainment and transport of mixed size and density sands: Flume experiments simulating the formation of black-sand placers. *Journal of Sedimentary Petrology*, **62**, p584 - 590.
- Li, Z. and Davies, A. G. (2001). Turbulence closure modelling of sediment transport beneath large waves. *Continental Shelf Research*, **21**, p243-262.
- Lodahl, C., Sumer, B. M. and Fredsøe, J. (1998). Turbulent combined oscillatory flow and current in a pipe. *Journal of Fluid Mechanics*, **373**, p313-348.
- Lopez, F. and Garcia, M. H. (2001). Risk of sediment erosion and suspension in turbulent flows. *Journal of Hydraulic Engineering*, **127**, p231-235.
- Madsen, O. S. and Grant, W. D. (1976). *Sediment Transport in the Coastal Environment*, Technical report 209 - Ralph M. Parsons Lab for Water Resources and Hydrodynamics, MIT., 105p.
- Manohar, M. (1955). *Mechanics of Bottom Sediment Movement Due to Wave Action.*, Technical Memo No. 75., Beach Erosion Board., 121p.
- Mantz, P. A. (1977). Incipient transport of fine grains and flakes by fluids-extended Shields diagram. *Journal of the Hydraulics Division, ASCE.*, **103**, p601-615.
- Mantz, P. A. (1980). Low sediment transport rates over flat beds. *Journal of the Hydraulics Division, ASCE.*, **106**, p1173 - 1190.
- Matas, J.-P., Morris, J. F. and Guazzelli, E. (2003). Influence of particles on the transition to turbulence in pipe flow. *Philosophical Transactions of the Royal Society London, Series A.*, **361**, p911-919.
- Middleton, G. V. (1992). Sediment transport processes in Nierenberg (Ed), *Encyclopedia of Earth System Science*, Academic Press, p81 - 92.
- Miller, M. C., McCave, I. N. and Komar, P. D. (1977). Threshold of sediment motion under unidirectional currents. *Sedimentology*, **24**, p507 - 527.
- Mingmin, H. and Qiwei, H. (1982). Stochastic model of incipient motion. *Journal of the Hydraulics Division, ASCE.*, **108**, p211 - 224.
- Mouazé, D. (2001). *Etude expérimentale de la couche limite générée par la houle autour d'un cylindre*. Department of fluid mechanics, Université de Caen, 193p.
- Myrhaug, D. (1989). A rational approach to wave friction coefficients for rough, smooth and transitional turbulent flow. *Coastal Engineering*, **13**, p11-21.
- Neill, C. R. and Yalin, M. S. (1969). Quantitative definition of beginning of bed movement. *Journal of the Hydraulics Division, ASCE.*, **95**, p585 - 588.
- Nielsen, P. and Callaghan, D. P. (2003). Shear stress and sediment transport calculations for sheet flow under waves. *Coastal Engineering*, **47**, p347-354.
- Nowell, A. R. M., Jumars, P. A. and Eckman, J. E. (1981). Effects of biological activity on the entrainment of marine sediments. *Marine Geology*, **42**, p133 - 153.
-

- Oldenziel, D. M. and Brink, W. E. (1974). Influence of suction and blowing on entrainment of sand particles. *Journal of the Hydraulics Division, ASCE.*, **100**, p935 - 949.
- Pangiotopoulos, I., Voulgaris, G. and Collins, M. B. (1997). The influence of clay on the threshold of movement of fine sandy beds. *Coastal Engineering*, **32**, p19-43.
- Papanicolaou, A., Diplas, P., Evaggelopoulos, N. and Fotopoulos, S. (2002). Stochastic incipient motion criterion for spheres under various bed packing conditions. *Journal of Hydraulic Engineering*, **128**, p369-380.
- Paphitis, D. and Collins, M. B. (2001a). The 5m Long Recirculating Flume at the School of Ocean and Earth Sciences (SOES), University of Southampton. Part I: Descriptive Manual., Internal Document No. 67. 29p.
- Paphitis, D. and Collins, M. B. (2001b). The 5m Long Recirculating Flume at the School of Ocean and Earth Sciences (SOES), University of Southampton. Part II: Unidirectional Flow Characteristics., Internal Document No. 68. 76p.
- Paphitis, D. (2001). Sediment movement under unidirectional flows: an assessment of empirical threshold curves. *Coastal Engineering*, **43**, p227 - 245.
- Paphitis, D., Collins, M. B., Nash, L. A. and Wallbridge, S. (2002). Settling velocities and entrainment thresholds of biogenic sands (shell fragments) under unidirectional flow. *Sedimentology*, **49**, p211 - 225.
- Paphitis, D., Velegrakis, A. F., Collins, M. B. and Muirhead, A. (2001). Laboratory investigations into the threshold of movement of natural sand-sized sediments, under unidirectional, oscillatory and combined flows. *Sedimentology*, **48**, p645 - 659.
- Ramakrishna Rao, A. R. and Sitaram, N. (1999). Stability and mobility of sand-bed channels affected by seepage. *Journal of Irrigation and Drainage Engineering*, **125**, p370 - 379.
- Reynolds, O. (1883). An experimental investigation of the circumstances which determine whether the motion of water shall be direct or sinuous, and of the law of resistance in parallel channels. *Philosophical Transactions of the Royal Society London*, **174**, p935 - 982.
- Ribberink, J. S. and Al-Salem, A. A. (1994). Sediment transport in oscillatory boundary layers in cases of rippled beds and sheet flow. *Journal of Geophysical Research*, **99**, p12,707 - 12,727.
- Ribberink, J. S., Katopodi, I., Ramadan, K. A. H., Koelewijn, R. and Longo, S. (1994). Sediment transport under (non)-linear waves and currents. *Proc. 24th Coastal Engineering Conf.*, pp. 2527 - 2541.
- Ribberink, J. S. and Al-Salem, A. A. (1995). Sheet flow and suspension of sand in oscillatory boundary layers. *Coastal Engineering*, **25**, p205 - 225.
-

- Rigler, J. K. and Collins, M. B. (1984). Initial grain motion under oscillatory flow: A comparison of some threshold criteria. *Geo-Marine Letters*, **3**, p43 - 48.
- Rosenthal, G. N. and Sleath, J. F. A. (1986). Measurements of lift in oscillatory flow. *Journal of Fluid Mechanics*, **164**, p449 - 467.
- Rubey, W. W. (1933). Settling velocities of gravel, sand and silt particles. *American Journal of Science*, **25**, p325-338.
- Sato, S. and Horikawa, K. (1986). Laboratory studies on sand transport over ripples due to asymmetric oscillatory flows. *Proc. 20th Coastal Engineering Conf., ASCE.*, pp. 1481 - 1495.
- Schlichting, H. (1968). *Boundary Layer Theory*. McGraw-Hill.
- Sekiguchi, T. and Sunamura, T. (2004). Effects of bed perturbation and velocity asymmetry on ripple initiation: wave-flume experiments. *Coastal Engineering*, **50**, p231-239.
- Shields, A. (1936). *Anwendung der Ahnlichkeitsmechanik und der Turbulenzforschung auf die Geschiebebewegung. Heft 26*. Preussische Versuchsanstalt für Wasserbau und Schiffbau., 43p.
- Sleath, J. F. A. (1974a). Stability of laminar flow at seabed. *Journal of the Waterways and Harbours and Coastal Engineering Division, ASCE.*, **100**, p105 - 122.
- Sleath, J. F. A. (1974b). Velocities above rough bed in oscillatory flow. *Journal of the Waterways and Harbours Division, ASCE.*, **100**, p287 - 304.
- Sleath, J. F. A. (1975). Transition in oscillatory flow over rippled beds. *Proc. Institute of Coastal Engineering. Pt. 2*, **59**, p309-322.
- Sleath, J. F. A. (1978). Measurements of bed load in oscillatory flow. *Journal of the Waterways and Harbours Division, ASCE.*, **104**, p291 - 307.
- Sleath, J. F. A. (1982). The effect of jet formation on the velocity distribution in oscillatory flow over flat beds of sand or gravel. *Coastal Engineering*, **6**, p151 - 177.
- Sleath, J. F. A. (1984). *Sea Bed Mechanics*. Wiley. 335p.
- Sleath, J. F. A. (1987). Turbulent oscillatory flow over rough beds. *Journal of Fluid Mechanics*, **182**, p369-409.
- Sleath, J. F. A. (1991). Velocities and shear stresses in wave-current flows. *Journal of Geophysical Research*, **96**, p15,237 - 15,244.
- Soulsby, R. L. (1997). *Dynamics of Marine Sands*. Thomas Telford Publications. 249p.
- Soulsby, R. L. and Whitehouse, R. J. S. (1997). Threshold of sediment motion in coastal environments. *13th Australasian Coastal and Ocean Engineering Conference and the 6th Australasian Port and Harbour Conference. Christchurch, N.Z.* p149-154.
- Sternberg, R. W. (1971). Measurements of incipient motion of sediment particles in the marine environment. *Marine Geology*, **10**, p113 - 119.
-

- 
- Stokes, G. G. (1851). On the effect of internal friction of fluids on the motion of pendulums. *Transactions of the Cambridge Philosophical Society.*, **9**, p20 - 21.
- Tanaka, H. (1988). Bed load transport due to non-linear wave motion. *Proc. 21st Coastal Engineering Conf. ASCE.*, p1803 - 1817.
- Tanaka, H. and Sana, A. (1994). Numerical study on transition to turbulence in a wave boundary layer. *Euromech 310*, p14 - 25.
- Tanaka, H., Sana, A., Kawamura, I. and Yamaji, H. (2000). Stability of asymmetric wave boundary layers. *Proceedings of the 4th International Conference on Hydrodynamics. Yokohama.*, p563 - 568.
- Tanaka, H., Sana, A., Yamaji, H. and Samad, M. A. (1998b). Experimental and numerical investigation on asymmetric oscillatory boundary layers. *Journal of Hydroscience and Hydraulic Engineering.*, **16**, p117 - 126.
- Tanaka, H., Sumer, B. M. and Lodahl, C. (1998d). Theoretical and experimental investigation on laminar boundary layers under cnoidal wave motion. *Coastal Engineering Journal, JSCE.*, **40**, p81 - 98.
- Tanaka, H., Yamaji, H. and Sana, A. (1998a). A generation method of asymmetric oscillatory motion simulating cnoidal waves. *Coastal Engineering Journal, JSCE.*, **40**, p291 - 306.
- Tanaka, H., Yamaji, H. and Sana, A. (1998c). Experimental study on non-linear wave boundary layers. *Proc. 26th Coastal Engineering Conf. ASCE.*, pp. 471 - 483.
- Taylor, B. D. and Vanoni, V. A. (1972). Temperature effects in low-transport, flat-bed flows. *Journal of the Hydraulics Division, ASCE.*, **98**, p1427-1445.
- Tomlinson, B. N. (1993). *Erosion Studies of Mixed Sand Beds Under the Combined Action of Waves and Currents*. PhD Thesis, School of Ocean and Earth Science, University of Southampton, 260p.
- Tucker, M. J. (1991). *Waves in Ocean Engineering: Measurement, Analysis, Interpretation*. Ellis Horwood. 431p.
- van Rijn, L. C. (1993). *Principles of Sediment Transport in Rivers, Estuaries and Coastal Seas*. Aqua Publications.
- Vanoni, V. A., Benedict, P. C., Bondurant, D. C., McKee, J. E., Piest, R. and Smallshaw, J. (1967). Sediment transport mechanics: Initiation of motion. Closure. *Journal of the Hydraulics Division, ASCE.*, **93**, p297 - 302.
- Vanoni, V. A., Benedict, P. C., Bondurant, D. C., McKee, J. E., Piest, R. and Smallshaw, J. (1967). Sediment transport mechanics: Initiation of motion. Progress Report. *Journal of the Hydraulics Division, ASCE.*, **92**, p291 - 314.
- Vincent, C. E., Young, R. A. and Swift, D. J. P. (1981). Bed-load transport under waves and currents. *Marine Geology*, **39**, p71-80.
-

- 
- Vincent, G. E. (1957). Contribution to the study of sediment transport on a horizontal bed due to wave action. *Proc. 6th Coastal Engineering Conf.*, p327 - 355.
- Vittori, G. (2003). Sediment suspension due to waves. *Journal of Geophysical Research*, **108**, p4.1-4.17.
- Vittori, G. and Verzicco, R. (1998). Direct simulation of transition in an oscillatory boundary layer. *Journal of Fluid Mechanics*, **371**, p207-232.
- Voulgaris, G., Wallbridge, S., Tomlinson, B. N. and Collins, M. B. (1995). Laboratory investigations into wave period effects on sand erodibility, under the combined action of waves and currents. *Coastal Engineering*, **26**, p117 - 134.
- Voulgaris, G., Wallbridge, S., Tomlinson, B. N. and Collins, M. B. (1997). Laboratory investigations into wave period effects on sand erodibility, under the combined action of waves and currents: Reply to the comments of Z.-J. You. *Coastal Engineering*, **30**, p161 - 166.
- Wallbridge, S., Voulgaris, G., Tomlinson, B. N. and Collins, M. B. (1999). Initial motion and pivoting characteristics of sand particles in uniform and heterogeneous beds: experiments and modelling. *Sedimentology*, **46**, p17-32.
- Watters, G. Z. and Rao, M. V. P. (1971). Hydrodynamic effects of seepage on bed particles. *Journal of the Hydraulics Division, ASCE.*, **97**, p421 - 439.
- Waywell, M. N. and Sajjadi, S. G. (1997). Transition from laminar to turbulence in oscillatory boundary layer flows over a smooth flat plate. *Mathematical Engineering in Industry*, **6**, p79-97.
- White, S. J. (1970). Plane bed thresholds of fine grained sediments. *Nature*, **228**, p152 - 153.
- Willets, B. B. and Drossos, M. E. (1975). Local erosion caused by rapid forced infiltration. *Journal of the Hydraulics Division, ASCE.*, **101**, p1477 - 1488.
- Yalin, M. S. (1972). *Mechanics of Sediment Transport*. Pergamon Press. 290p.
- Yang, C. T. (1996). *Sediment Transport: Theory and Practice*. McGraw-Hill. 396p.
- You, Z. J. (1997). Laboratory investigations into wave period effects on sand bed erodibility under the combined action of waves and currents by G. Voulgaris et al: Comments. *Coastal Engineering*, **30**, p157 - 160.
- You, Z. J. (1998). Initial motion of sediment in oscillatory flow. *Journal of Waterway, Port, Coastal and Ocean Engineering.*, **124**, p68-72.
- You, Z. J. (2000). A simple model of sediment initiation under waves. *Coastal Engineering*, **41**, p399 - 414.
- You, Z. J. and Yin, B. S. (2004). A discussion of the paper ‘‘A simple method to predict the threshold of particle transport under oscillatory waves’’ by J.P. Le Roux. *Sedimentary Geology*, **163**, p323-325.
-

- Zhang, S. and Williams, A. N. (1996). Time domain simulation of the generation and propagation of second-order Stokes waves in a two-dimensional wave flume. Part I: Monochromatic wavemaker motions. *Journal of Fluids and Structures*, **10**, p319-335.
- Zyserman, J., Justesen, P., Fredsøe, J. and Deigaard, R. (1987). *Resulting bed shear stress due to asymmetric waves*. Institute of Hydrodynamics and Hydraulic Engineering, Technical University, Denmark., p31 - 35.

## Appendix A. Laminar boundary layer theory

### A.1. Linear theory

The velocity distribution in the boundary layer, under laminar oscillatory flow conditions, is given by the well-known laminar boundary layer solution, first presented by Stokes (1851). The original model was an analytical solution of the Navier-Stokes equations for a boundary oscillating: with a simple harmonic motion; under laminar flow conditions; in still water, sufficiently deep to allow unhindered boundary layer development. The assumption of ‘no-slip’ at the bed-water interface, implies the boundary conditions:

$$z = 0: \quad u_{(0,t)} = U_0 \cos \omega t + \varphi \quad \text{Eq. A.1}$$

$$z = \infty: \quad u_{(\infty,t)} = 0 \quad \text{Eq. A.2}$$

The laminar boundary layer solution, with axes fixed in the still water, is as follows,

$$u_{(z,t)} = U_0 (e^{-\beta z} \cos(\omega t + \varphi - \beta z)) \quad \text{Eq. A.3}$$

Where  $u$  is the velocity,  $z$  denotes the coordinate normal to the surface of the plate,  $t$  is the time,  $U_0$  is the velocity amplitude of the moving plate,  $\varphi$  is the phase lag,  $\omega (=2\pi/T)$  is the radian frequency and  $\beta$  is the Stokes parameter,

$$\beta = \frac{1}{\delta} = \sqrt{\frac{\omega}{2\nu}} \quad \text{Eq. A.4}$$

Where  $\delta$  is the Stokes length, which represents a measure of the boundary layer thickness; and,  $\nu$  is the kinematic viscosity.

Additional measures may be taken directly from these formulae. Fluid layers above the plate oscillate with a damped harmonic motion, of amplitude  $U_0 e^{-\beta z}$  and with a phase lag  $\beta z$  in relation to the motion of the plate. The height at which  $|U_{(z)}|_{\max} = 0.99U_c$  (i.e. the extent of the boundary layer),  $\delta_{0.99}$ , is  $4.6052/\beta$ .

It has been shown since, that if the axes of reference are transferred to the moving boundary (i.e. the oscillating plate), then the resulting flow solution is the same as the reciprocal case of fluid oscillating over a static bed (as may be found under a free surface gravity wave at the sea bed, using small amplitude wave theory), (Lamb, 1932; Schlichting, 1968; Sleath, 1984). For axes fixed in the oscillating plate,

$$u_{(z,t)} = U_0 (\cos(\omega t + \varphi) - e^{-\beta z} \cos(\omega t + \varphi - \beta z)) \quad \text{Eq. A.5}$$

From laminar flow theory, there is no component of velocity perpendicular to the axis of oscillation, either parallel to the plane of the bed or normal to the plane of the bed. Hence for axes fixed in either the still water or the moving plate,

$$v_{(z,t)} = 0, \quad w_{(z,t)} = 0 \quad \text{Eq. A.6}$$

However, it is unlikely that observation of actual flows will demonstrate zero flow in these components; small-amplitude, uniform variations in velocity will likely be observed, due to fluid motions and/or instability not associated with turbulence, and also due to instrument noise.

## A.2. Second-Order Theory

Under laminar flow conditions, the second-order solution is expressed as the summation of the two individual harmonics:

for axes fixed in still water,

$$u_{(z,t)} = U_1 (e^{-\beta_1 z} \cos(\omega t + \varphi_1 - \beta_1 z)) + U_2 (e^{-\beta_2 z} \cos(2\omega t + \varphi_2 - \beta_2 z)) \quad \text{Eq. A.7}$$

and for axes fixed in the moving plate,

$$u_{(z,t)} = U_1 \cos(\omega t + \varphi_1) + U_2 \cos(2\omega t + \varphi_2) - \dots \quad \text{Eq. A.8}$$

$$[U_1 (e^{-\beta_1 z} \cos(\omega t + \varphi_1 - \beta_1 z)) + U_2 (e^{-\beta_2 z} \cos(2\omega t + \varphi_2 - \beta_2 z))]$$

Where:  $\varphi_1$  and  $\varphi_2$  are the phase lags, and  $\beta_1$  and  $\beta_2$  are the Stokes parameters, for the principle and second harmonics, respectively,

$$\beta_1 = \sqrt{\frac{\omega}{2\nu}} \quad \beta_2 = \sqrt{\frac{2\omega}{2\nu}} \quad \text{Eq. A.9}$$

Equation A.6 still applies, and  $\delta_{0.99}$  may be calculated as  $4.6052/\beta_j$ . However, other quantities of interest such as velocity amplitude and phase, at intermediate heights, cannot easily be calculated directly; alternatively, values are easily found by solving the implicit equation for sufficient time steps over one wave period.

### A.3. The extended theory of Du Toit and Sleath (1981)

It is often the case that the fluid body overlying the oscillating trolley will develop small amplitude ‘parasitic’ oscillations; these free surface oscillations result from fluid displacement and friction, as the plate is moved. The additional oscillation in the region just outside of the boundary layer may be expressed as a harmonic variation in velocity at the same period as the primary harmonic of plate motion, with amplitude  $U_\infty$  and phase  $\varphi_\infty$ . For axes fixed in ‘still water’ the additional boundary condition is therefore

$$z = \infty : u_{(\infty,t)} = U_\infty \cos(\omega t + \varphi_\infty) \quad \text{Eq. A.10}$$

The boundary layer flow with axes fixed in the moving plate resulting from the outer layer oscillation is,

$$u_{(z,t)} = U_\infty (\cos(\omega t + \varphi_\infty) - e^{-\beta z} \cos(\omega t + \varphi_\infty - \beta z)) \quad \text{Eq. A.11}$$

Provided that the assumption of laminar flow is maintained, an extended flow model is created simply by the summation of Equations A.11 and A.8; this extended solution was first presented for sinusoidal flows in Du Toit and Sleath (1981).

The form of the velocity cycle may deviate from a sinusoidal variation, at certain resonant frequencies or under the influence of longer period, asymmetric plate motions. Using similar notation to that used in Eq. A.8, the second-order approximation for the outer layer is,

$$u_{(z,t)} = U_{\infty 1}(\cos(\omega t + \varphi_{\infty 1}) - e^{-\beta_1 z} \cos(\omega t + \varphi_{\infty 1} - \beta_1 z)) + \dots \quad \text{Eq. A.12}$$

$$U_{\infty 2}(\cos(2\omega t + \varphi_{\infty 2}) - e^{-\beta_2 z} \cos(2\omega t + \varphi_{\infty 2} - \beta_2 z))$$

and the extended flow model is created by the summation of Equations A.12 and A.8. Parasitic oscillations in the present experiment were reduced by a combination of solid and porous baffles, designed to dampen free fluid motion; the velocity amplitude of these oscillations was typically 5-10% of  $U_I$  ( $\sim 1.5 \text{cms}^{-1}$ ), and did not exceed 11.8%.

## **Appendix B. Velocity profiling results**

Appendix B – Velocity profiling results

Bed	Resolution*	$T$ (s)	$S$ (m)	$R$	$U_1$ (ms <sup>-1</sup> )	$U_2$ (ms <sup>-1</sup> )	$U_c$ (ms <sup>-1</sup> )	$\delta_{0.99}$ (mm)	$U_\infty^\#$ (ms <sup>-1</sup> )	Deviation (cms <sup>-1</sup> )	Fluctuation (cms <sup>-1</sup> )	Temp (°C)	Vis Turb <sup>+</sup>
Smooth	High	6	0.25	0.5	0.131	0	0.131	6.4	0.0074	4	1.5-2	20	L
Smooth	High	6	0.50	0.5	0.262	0	0.262	6.4	0.0165	5	2	20	L
Smooth	High	9	0.50	0.5	0.175	0	0.175	7.8	0.008	2	1-1.5	20	L
Smooth	High	9	0.75	0.5	0.262	0	0.262	7.8	0.0166	2	2	20	L
Smooth	High	12	0.50	0.5	0.131	0	0.131	9.0	0.0197	0.5-1	0.5-1	20	L
Smooth	High	12	0.90	0.5	0.236	0	0.236	9.0	0.0399	1-2	1.5-2	20	L
Smooth	High	6	0.50	0.6	0.258	0.052	0.310	6.4	0.0236	1-1.5	2	20	L/L
Smooth	High	9	0.50	0.6	0.172	0.034	0.206	7.8	0.024	0.5-1	1	20	L/L
Smooth	High	12	0.50	0.6	0.129	0.026	0.155	9.0	0.0234	1-1.5	0.5-1	20	L/L
Smooth	High	9	0.50	0.7	0.164	0.066	0.230	7.8	0.031	4	0.5-1	20	L/L
550 $\mu$ m	Medium	6	0.50	0.5	0.262	0	0.272	6.4	0.0051	4	1	20	-
550 $\mu$ m	Medium	9	0.50	0.5	0.175	0	0.175	7.8	0.0066	1-2	2	20	-
550 $\mu$ m	Medium	9	0.75	0.5	0.262	0	0.262	7.8	0.0114	1-2	1	20	-
550 $\mu$ m	Medium	12	0.50	0.5	0.131	0	0.131	9.0	0.013	2	1-2	20	-
550 $\mu$ m	Medium	12	0.90	0.5	0.236	0	0.236	9.0	0.0176	1-2	2-3	20	-

Table B.1. Summary of phase referenced velocity profiling cases and results.

\* Resolution of the data profile, see Table B.3.

# The velocity amplitude measured in the outer layer ( $z > \delta_{0.99}$ ).

+ The degree of visible turbulence in the boundary layer (visual estimate only): laminar (L); transitional (Tr). For asymmetric cases, descriptions are given for the crest/trough, respectively.

Appendix B – Velocity profiling results

Bed	Resolution*	$T$ (s)	$S$ (m)	$R$	$U_1$ (ms <sup>-1</sup> )	$U_2$ (ms <sup>-1</sup> )	$U_c$ (ms <sup>-1</sup> )	$\delta_{0.99}$ (mm)	$U_\infty^\#$ (ms <sup>-1</sup> )	Deviation (cms <sup>-1</sup> )	Fluctuation (cms <sup>-1</sup> )	Temp (°C)	Vis Turb <sup>+</sup>
275µm	Low	6	0.25	0.5	0.131	0	0.131	6.4	0.0029	0.5	0.5	21	L
275µm	Low	6	0.50	0.5	0.262	0	0.262	6.4	0.0041	1	0.5	20	L
275µm	Low	9	0.50	0.5	0.175	0	0.175	7.8	0.0117	0.5	1	20	L
275µm	Low	9	0.75	0.5	0.262	0	0.262	7.8	0.0103	1	0.5	20	Tr
275µm	Low	12	0.50	0.5	0.131	0	0.131	9.0	0.0145	2	1	20	L
275µm	Low	12	0.90	0.5	0.236	0	0.236	9.0	0.0178	3	1	21	L
275µm	Low	9	0.50	0.55	0.174	0.017	0.191	7.8	0.01	2	1	20	L/L
275µm	Low	12	0.50	0.55	0.131	0.013	0.144	9.0	0.0119	1-1.5	0.5-1	20	L/L
275µm	Low	6	0.50	0.6	0.258	0.052	0.310	6.4	0.0058	3	0.5-1	20	L/Tr
275µm	Low	9	0.50	0.6	0.172	0.034	0.206	7.8	0.0116	1-2	0.5-1	20	L/L
275µm	Low	12	0.50	0.6	0.129	0.026	0.155	9.0	0.0139	2-3	0.5-1	20	L/L
550µm	Low	6	0.25	0.5	0.131	0	0.131	6.4	0.0022	3	0.5-1	20	L-Tr
550µm	Low	6	0.50	0.5	0.262	0	0.262	6.4	0.0043	4	1	20	Tr
550µm	Low	9	0.50	0.5	0.175	0	0.175	7.8	0.0089	1-2	2	20	L
550µm	Low	9	0.75	0.5	0.262	0	0.262	7.8	0.0132	1-2	1	21	Tr
550µm	Low	12	0.50	0.5	0.131	0	0.131	9.0	0.0158	2	1-2	20	L
550µm	Low	12	0.90	0.5	0.236	0	0.236	9.0	0.014	1-2	2-3	21	Tr
550µm	Low	9	0.50	0.55	0.174	0.017	0.191	7.8	0.0087	1-2	2	20	L/L
550µm	Low	12	0.50	0.55	0.131	0.013	0.144	9.0	0.0127	1-2	1-1.5	20	L/L
550µm	Low	6	0.50	0.6	0.258	0.052	0.310	6.4	0.0029	1-3	1-1.5	20	Tr/Tr
550µm	Low	9	0.50	0.6	0.172	0.034	0.206	7.8	0.0071	1-2	0.5-1	20	L/L
550µm	Low	12	0.50	0.6	0.129	0.026	0.155	9.0	0.0142	2	0.5-1	21	L/L

Table B.2. Summary of non-phase referenced velocity profiling cases and results.

\* Resolution of the data profile, see Table B.3; # The velocity amplitude measured in the outer layer ( $z > \delta_{0.99}$ ); + The degree of visible turbulence in the boundary layer (visual estimate only): laminar (L); transitional (Tr). For asymmetric cases, descriptions are given for the crest/trough, respectively.

	<b>High</b>	<b>Medium</b>	<b>Low</b>
	0	16.1	0
	0.1	17.1	0.2
	0.2	18.1	0.4
	0.3	19.1	0.6
	0.4	20.1	0.8
	0.5	21.1	1
	0.6	41.1	1.2
	0.7	61.1	1.6
	0.8	81.1	1.8
	0.9	101.1	2
	1	121.1	2.25
	1.1	141.1	2.5
	1.2	161.1	2.75
	1.3	181.1	3
	1.4	201.1	3.25
	1.5	221.1	3.5
	1.6	241.1	3.75
	1.8	261.1	4
	2		4.5
	2.2		5
	2.4		5.5
	2.6		6
	2.85		6.5
	3.1		7
	3.35		8
	3.6		9
	4.1		10
	4.6		11
	5.1		12
	5.6		14
	6.1		16
	6.6		20
	7.1		60
	7.6		80
	8.1		100
	8.6		250
	9.1		
	9.6		
	10.1		
	11.1		
	12.1		
	13.1		
	14.1		
	15.1		
	<i>continued...</i>		

Table B.3. Profile resolutions used during the velocity profiling experiments. Values indicate heights above the bed, z (mm) at which time series were collected.

## Appendix C. Transition to turbulence results

$T$ (s)	$R$	$S_{c \text{ crit}}$ (m)	$S_{t \text{ crit}}$ (m)	$U_c$ (ms <sup>-1</sup> )	$U_t$ (ms <sup>-1</sup> )	Temp (°C)	Methodology*	$\delta u / \delta z$ <sup>+</sup>
3	0.6	0.54	0.54	0.667	0.445	20	VTS	316.5
6	0.5	0.78	0.78	0.408	0.408	20	VTS	146.9
6	0.55	0.75	0.76	0.430	0.357	18	VTS	148.9
6	0.6	0.74	0.78	0.457	0.321	19	VTS	153.3
6	0.7	0.74	0.8	0.508	0.235	19	VTS	163.2
9	0.5	0.94	0.94	0.328	0.328	20	VTS	96.4
9	0.6	0.86	-	0.354	-	18	VTS	97.0
3	0.6	0.5	0.51	0.618	0.420	20	TI	293.1
6	0.5	0.74	0.74	0.388	0.388	20	TI	139.4
6	0.55	0.72	0.72	0.413	0.338	18	TI	143.0
6	0.6	0.74	0.74	0.457	0.305	19	TI	153.3
6	0.65	0.69	-	0.452	-	18	TI	147.9
6	0.7	0.71	-	0.487	-	19	TI	156.6
9	0.6	0.85	-	0.350	-	18	TI	95.8
9	0.7	0.85	-	0.389	-	19	TI	101.9

Table C.1. Transition to turbulence results for experiments using a smooth bed.

$T$ (s)	$R$	$S_{c \text{ crit}}$ (m)	$S_{t \text{ crit}}$ (m)	$U_c$ (ms <sup>-1</sup> )	$U_t$ (ms <sup>-1</sup> )	Temp (°C)	Methodology*	$\delta u / \delta z$ <sup>+</sup>
3	0.5	0.30	0.30	0.314	0.314	17	VO	159.6
3	0.55	0.26	0.31	0.299	0.292	19	VO	146.2
6	0.5	0.48	0.48	0.249	0.249	17	VO	89.5
6	0.55	0.47	0.53	0.270	0.249	19	VO	93.4
9	0.5	0.61	0.61	0.213	0.213	17	VO	62.5
3	0.5	0.37	0.37	0.388	0.388	19	VTS	196.9
3	0.55	0.36	-	0.414	-	19	VTS	202.2
3	0.6	0.39	-	0.482	-	19	VTS	228.7
3	0.7	0.36	-	0.495	-	19	VTS	224.2
6	0.5	0.62	0.62	0.325	0.325	19	VTS	116.8
6	0.55	0.60	0.72	0.344	0.338	19	VTS	119.1
6	0.6	0.58	0.72	0.358	0.296	19	VTS	120.2
6	0.7	0.60	-	0.412	-	17	VTS	132.3
9	0.6	0.77	-	0.317	-	17	VTS	86.8
9	0.7	0.75	-	0.343	-	17	VTS	89.9
3	0.5	0.33	0.33	0.346	0.346	19	TI	175.6
3	0.55	0.36	-	0.414	-	19	TI	202.2
6	0.5	0.69	0.69	0.361	0.361	19	TI	130.0
6	0.55	0.66	0.66	0.379	0.310	19	TI	131.1
6	0.6	0.60	0.62	0.371	0.255	19	TI	124.3
6	0.7	0.64	-	0.440	-	17	TI	141.1
9	0.7	0.75	-	0.343	-	17	TI	89.9

Table C.2. Transition to turbulence results for experiments using a fixed granular bed roughness,  $D=275\mu\text{m}$ .

\* Methodology used: visual observation method (VO); velocity time series method (VTS); turbulence intensity method (TI).

<sup>+</sup> Velocity gradient parameter – the maximum value of  $\delta u / \delta z$  in the boundary layer at  $\omega t = 130^\circ$ .

$T$ (s)	$R$	$S_{c \text{ crit}}$ (m)	$S_{t \text{ crit}}$ (m)	$U_c$ (ms <sup>-1</sup> )	$U_t$ (ms <sup>-1</sup> )	Temp (°C)	Methodology*	$\delta u / \delta z$ <sup>+</sup>
3	0.5	0.18	0.18	0.189	0.189	17	VO	95.8
3	0.55	0.18	0.25	0.207	0.235	17	VO	101.4
3	0.6	0.19	0.28	0.235	0.231	18	VO	111.7
6	0.5	0.35	0.35	0.183	0.183	17	VO	65.9
6	0.55	0.42	0.47	0.241	0.221	17	VO	83.5
6	0.6	0.34	0.43	0.210	0.177	18	VO	70.5
9	0.5	0.5	0.5	0.175	0.175	17	VO	51.3
9	0.55	0.5	0.55	0.191	0.172	18	VO	54.1
9	0.6	0.4	0.56	0.165	0.154	19	VO	45.1
3	0.5	0.17	0.17	0.178	0.178	17	VTS	90.5
3	0.55	0.18	-	0.207	-	17	VTS	101.4
3	0.6	0.18	-	0.223	-	18	VTS	105.8
3	0.7	0.25	-	0.344	-	18	VTS	155.8
6	0.5	0.38	0.38	0.199	0.199	18	VTS	71.6
6	0.55	0.42	0.42	0.241	0.197	15	VTS	83.5
6	0.6	0.38	0.38	0.235	0.157	16	VTS	78.7
6	0.7	0.47	-	0.323	-	18	VTS	103.7
9	0.5	0.55	0.55	0.192	0.192	17	VTS	56.4
9	0.55	0.5	-	0.191	-	19	VTS	54.1
9	0.6	0.46	-	0.189	-	16	VTS	51.9
9	0.7	0.74	-	0.339	-	18	VTS	88.7
12	0.5	0.68	0.68	0.178	0.178	18	VTS	45.3
12	0.55	0.65	-	0.187	-	18	VTS	45.7
3	0.7	0.23	-	0.317	-	18	TI	143.4
6	0.55	0.36	0.39	0.207	0.183	15	TI	71.5
6	0.6	0.35	0.36	0.216	0.148	16	TI	72.6
9	0.5	0.54	0.54	0.189	0.189	17	TI	55.4
9	0.55	0.56	-	0.214	-	19	TI	60.5
9	0.7	0.63	-	0.288	-	18	TI	75.6
12	0.5	0.66	0.66	0.173	0.173	17	TI	44.0
12	0.55	0.65	-	0.187	-	17	TI	45.7

Table C.3. Transition to turbulence results for experiments using a fixed granular bed roughness,  $D=550\mu\text{m}$ .

\* Methodology used: visual observation method (VO); velocity time series method (VTS); turbulence intensity method (TI).

<sup>+</sup> Velocity gradient parameter – the maximum value of  $\delta u / \delta z$  in the boundary layer at  $\omega t = 130^\circ$ .

## **Appendix D. Threshold of motion results**

Appendix D – Threshold of motion results

$T$ (s)	$R$	$S$ (m)	Temp (°C)	$S_{\infty}$ (m)	$U_c$ (ms <sup>-1</sup> )	$\tau_{crit}$ (Nm <sup>-2</sup> )
3	0.5	0.32	22	1	0.335	0.485
4	0.5	0.42	22	1	0.330	0.413
5	0.5	0.58	22	1	0.364	0.409
6	0.5	0.68	22	1	0.356	0.364
7	0.5	0.80	22	1	0.359	0.340
8	0.5	0.91	22	3	0.357	0.317
9	0.5	1.00	22	5	0.349	0.292
4	0.55	0.42	22	1	0.362	0.459
5	0.55	0.58	22	1	0.400	0.454
6	0.55	0.65	22	1	0.373	0.387
7	0.55	0.73	22	1	0.359	0.345
8	0.55	0.89	22	3	0.383	0.344
9	0.55	1.00	22	5	0.382	0.324
4	0.6	0.43	21	1	0.399	0.517
5	0.6	0.57	21	1	0.422	0.490
6	0.6	0.65	21	1	0.401	0.425
7	0.6	0.76	21	1	0.402	0.394
8	0.6	0.88	21	3	0.407	0.374
9	0.6	1.00	21	5	0.411	0.356
4	0.65	0.42	22	1	0.413	0.548
5	0.65	0.53	22	1	0.417	0.494
6	0.65	0.66	22	1	0.432	0.468
7	0.65	0.81	22	1	0.454	0.456
8	0.65	0.92	22	3	0.452	0.424
4	0.7	0.40	22	1	0.412	0.558
5	0.7	0.52	22	1	0.429	0.519
6	0.7	0.64	22	1	0.440	0.486
7	0.7	0.74	22	1	0.436	0.446
8	0.7	0.88	22	3	0.453	0.434
9	0.7	0.93	22	5	0.426	0.384

Continued...

Continued...

$T$ (s)	$R$	$S$ (m)	Temp (°C)	$S_{\infty}$ (m)	$U_c$ (ms <sup>-1</sup> )	$\tau_{crit}$ (Nm <sup>-2</sup> )
6	0.5	0.68	22	1	0.356	0.364
6	0.5	0.66	22	1	0.346	0.354
6	0.5	0.67	22	1	0.351	0.359
6	0.5	0.65	22	1	0.340	0.348
6	0.5	0.70	21	1	0.367	0.375
6	0.5	0.70	21	1	0.367	0.375
6	0.5	0.70	22	1	0.367	0.375
6	0.5	0.70	22	1	0.367	0.375
6	0.5	0.68	22	1	0.356	0.364
6	0.5	0.68	22	1	0.356	0.364
6	0.5	0.67	22	1	0.351	0.359
6	0.5	0.70	22	1	0.367	0.375
6	0.55	0.65	22	1	0.373	0.387
6	0.55	0.67	22	1	0.384	0.398
6	0.55	0.68	22	1	0.390	0.404
6	0.55	0.69	22	1	0.396	0.410
6	0.6	0.65	21	1	0.401	0.425
6	0.6	0.63	21	1	0.389	0.412
6	0.6	0.65	21	1	0.401	0.425
6	0.6	0.68	21	1	0.420	0.445
6	0.65	0.66	22	1	0.432	0.468
6	0.65	0.66	22	1	0.432	0.468
6	0.65	0.65	22	1	0.426	0.461
6	0.65	0.64	22	1	0.419	0.454
6	0.7	0.64	22	1	0.440	0.486
6	0.7	0.62	22	1	0.426	0.471
6	0.7	0.63	22	1	0.433	0.478
6	0.7	0.65	22	1	0.447	0.494

Table D.1. Threshold of motion results for aragonite sediment [ $\rho_s=2700\text{kgm}^{-3}$ ,  $D=275\mu\text{m}$ ].

Appendix D – Threshold of motion results

<i>T</i> (s)	<i>R</i>	<i>S</i> (m)	Temp (°C)	<i>S</i> <sub>∞</sub> (m)	<i>U</i> <sub><i>c</i></sub> (ms <sup>-1</sup> )	$\tau_{crit}$ (Nm <sup>-2</sup> )
3	0.5	0.31	22	1	0.325	0.470
4	0.5	0.42	22	1	0.330	0.413
5	0.5	0.51	22	1	0.320	0.359
6	0.5	0.63	22	1	0.330	0.338
7	0.5	0.75	22	1	0.337	0.319
8	0.5	0.86	22	3	0.338	0.299
9	0.5	0.93	22	5	0.325	0.271
3	0.55	0.35	22	1	0.402	0.590
4	0.55	0.45	22	1	0.388	0.492
5	0.55	0.57	22	1	0.393	0.446
6	0.55	0.66	22	1	0.379	0.393
7	0.55	0.76	22	1	0.374	0.359
8	0.55	0.91	22	3	0.392	0.351
9	0.55	0.96	22	5	0.367	0.311
3	0.6	0.30	21	1	0.371	0.556
4	0.6	0.43	21	1	0.399	0.517
5	0.6	0.55	21	1	0.408	0.473
6	0.6	0.65	21	1	0.401	0.425
7	0.6	0.75	21	1	0.397	0.389
8	0.6	0.92	21	3	0.426	0.391
9	0.6	1.00	21	5	0.411	0.356
3	0.65	0.30	22	1	0.394	0.603
4	0.65	0.42	22	1	0.413	0.548
5	0.65	0.53	22	1	0.417	0.494
6	0.65	0.65	22	1	0.426	0.461
7	0.65	0.77	22	1	0.432	0.433
8	0.65	0.89	22	3	0.437	0.410
9	0.65	0.97	22	5	0.423	0.374
3	0.7	0.29	22	1	0.399	0.624
4	0.7	0.39	22	1	0.402	0.545
5	0.7	0.49	22	1	0.404	0.489
6	0.7	0.60	21	1	0.412	0.456
7	0.7	0.70	21	1	0.412	0.422
8	0.7	0.88	21	3	0.453	0.434
9	0.7	0.96	21	5	0.439	0.396

Continued...

Continued...

<i>T</i> (s)	<i>R</i>	<i>S</i> (m)	Temp (°C)	<i>S</i> <sub>∞</sub> (m)	<i>U</i> <sub><i>c</i></sub> (ms <sup>-1</sup> )	$\tau_{crit}$ (Nm <sup>-2</sup> )
6	0.5	0.63	22	1	0.330	0.338
6	0.5	0.63	22	1	0.330	0.338
6	0.5	0.64	22	1	0.335	0.343
6	0.5	0.64	22	1	0.335	0.343
6	0.5	0.68	21	1	0.356	0.364
6	0.5	0.67	21	1	0.351	0.359
6	0.5	0.70	21	1	0.367	0.375
6	0.5	0.68	22	1	0.356	0.364
6	0.5	0.68	22	1	0.356	0.364
6	0.5	0.68	22	1	0.356	0.364
6	0.5	0.71	22	1	0.372	0.380
6	0.5	0.71	22	1	0.372	0.380
6	0.55	0.66	22	1	0.379	0.393
6	0.55	0.68	22	1	0.390	0.404
6	0.55	0.69	22	1	0.396	0.410
6	0.55	0.67	22	1	0.384	0.398
6	0.6	0.65	21	1	0.401	0.425
6	0.6	0.66	21	1	0.408	0.432
6	0.6	0.65	21	1	0.401	0.425
6	0.6	0.67	21	1	0.414	0.438
6	0.65	0.65	22	1	0.426	0.461
6	0.65	0.64	22	1	0.419	0.454
6	0.65	0.65	22	1	0.426	0.461
6	0.65	0.65	22	1	0.426	0.461
6	0.7	0.60	21	1	0.412	0.456
6	0.7	0.61	21	1	0.419	0.463
6	0.7	0.60	21	1	0.412	0.456
6	0.7	0.62	22	1	0.426	0.471

Table D.2. Threshold of motion results for aragonite sediment [ $\rho_s=2700\text{kgm}^{-3}$ ,  $D=327.5\mu\text{m}$ ].

Appendix D – Threshold of motion results

<i>T</i> (s)	<i>R</i>	<i>S</i> (m)	Temp (°C)	<i>S</i> <sub>∞</sub> (m)	<i>U</i> <sub><i>c</i></sub> (ms <sup>-1</sup> )	$\tau_{crit}$ (Nm <sup>-2</sup> )
3	0.5	0.33	22	1	0.346	0.500
4	0.5	0.44	22	1	0.346	0.433
5	0.5	0.55	22	1	0.346	0.387
6	0.5	0.64	22	1	0.335	0.343
7	0.5	0.76	22	1	0.341	0.323
8	0.5	0.85	22	3	0.334	0.296
9	0.5	0.96	22	5	0.335	0.280
3	0.55	0.30	22	1	0.345	0.506
4	0.55	0.42	22	1	0.362	0.459
5	0.55	0.54	22	1	0.372	0.422
6	0.55	0.65	22	1	0.373	0.387
7	0.55	0.79	22	1	0.389	0.373
8	0.55	0.89	22	3	0.383	0.344
9	0.55	0.97	22	5	0.371	0.314
3	0.6	0.30	22	1	0.371	0.556
4	0.6	0.41	22	1	0.380	0.493
5	0.6	0.53	22	1	0.393	0.456
6	0.6	0.62	22	1	0.383	0.406
7	0.6	0.73	22	1	0.386	0.379
8	0.6	0.87	22	3	0.403	0.369
9	0.6	0.97	22	5	0.399	0.345
3	0.65	0.26	22	1	0.341	0.523
4	0.65	0.39	22	1	0.383	0.509
5	0.65	0.51	22	1	0.401	0.476
6	0.65	0.62	22	1	0.406	0.440
7	0.65	0.74	22	1	0.415	0.416
8	0.65	0.82	22	3	0.403	0.378
9	0.65	0.97	22	5	0.423	0.374
3	0.7	0.24	22	1	0.331	0.517
4	0.7	0.36	22	1	0.371	0.503
5	0.7	0.46	22	1	0.379	0.460
6	0.7	0.60	22	1	0.412	0.456
7	0.7	0.71	22	1	0.418	0.428
8	0.7	0.82	22	3	0.422	0.404
9	0.7	0.95	22	5	0.435	0.393

Continued...

Continued...

<i>T</i> (s)	<i>R</i>	<i>S</i> (m)	Temp (°C)	<i>S</i> <sub>∞</sub> (m)	<i>U</i> <sub><i>c</i></sub> (ms <sup>-1</sup> )	$\tau_{crit}$ (Nm <sup>-2</sup> )
6	0.5	0.64	22	1	0.335	0.343
6	0.5	0.63	22	1	0.330	0.338
6	0.5	0.64	22	1	0.335	0.343
6	0.5	0.65	22	1	0.340	0.348
6	0.5	0.65	22	1	0.340	0.348
6	0.5	0.68	22	1	0.356	0.364
6	0.5	0.70	22	1	0.367	0.375
6	0.5	0.69	22	1	0.361	0.370
6	0.5	0.68	22	1	0.356	0.364
6	0.5	0.69	22	1	0.361	0.370
6	0.5	0.71	22	1	0.372	0.380
6	0.5	0.70	22	1	0.367	0.375
6	0.55	0.65	22	1	0.373	0.387
6	0.55	0.64	22	1	0.367	0.381
6	0.55	0.68	22	1	0.390	0.404
6	0.55	0.66	22	1	0.379	0.393
6	0.6	0.62	22	1	0.383	0.406
6	0.6	0.63	22	1	0.389	0.412
6	0.6	0.64	22	1	0.395	0.419
6	0.6	0.66	22	1	0.408	0.432
6	0.65	0.62	22	1	0.406	0.440
6	0.65	0.63	22	1	0.412	0.447
6	0.65	0.62	22	1	0.406	0.440
6	0.65	0.63	22	1	0.412	0.447
6	0.7	0.60	22	1	0.412	0.456
6	0.7	0.57	22	1	0.392	0.433
6	0.7	0.58	22	1	0.398	0.440
6	0.7	0.60	22	1	0.412	0.456

Table D.3. Threshold of motion results for aragonite sediment

[ $\rho_s=2700\text{kgm}^{-3}$ ,  $D=390\mu\text{m}$ ].

Appendix D – Threshold of motion results

$T$ (s)	$R$	$S$ (m)	Temp (°C)	$S_{\infty}$ (m)	$U_c$ (ms <sup>-1</sup> )	$\tau_{crit}$ (Nm <sup>-2</sup> )
3	0.5	0.31	22	1	0.325	0.470
4	0.5	0.41	22	1	0.322	0.404
5	0.5	0.51	22	1	0.320	0.359
6	0.5	0.62	22	1	0.325	0.332
7	0.5	0.76	22	1	0.341	0.323
8	0.5	0.86	22	3	0.338	0.299
9	0.5	0.94	22	5	0.328	0.274
3	0.55	0.29	21	1	0.333	0.489
4	0.55	0.41	21	1	0.353	0.448
5	0.55	0.52	21	1	0.358	0.407
6	0.55	0.66	21	1	0.379	0.393
7	0.55	0.77	21	1	0.379	0.363
8	0.55	0.87	21	3	0.374	0.336
9	0.55	0.98	21	5	0.375	0.317
3	0.6	0.29	22	1	0.359	0.537
4	0.6	0.39	22	1	0.362	0.469
5	0.6	0.51	22	1	0.378	0.439
6	0.6	0.62	22	1	0.383	0.406
7	0.6	0.77	22	1	0.407	0.399
8	0.6	0.88	22	3	0.407	0.374
9	0.6	0.92	22	5	0.378	0.327
3	0.65	0.27	22	1	0.354	0.543
4	0.65	0.39	22	1	0.383	0.509
5	0.65	0.50	22	1	0.393	0.466
6	0.65	0.61	22	1	0.399	0.433
7	0.65	0.74	21	1	0.415	0.416
8	0.65	0.83	21	3	0.407	0.382
9	0.65	0.95	21	5	0.415	0.367
3	0.7	0.25	22	1	0.344	0.538
4	0.7	0.33	22	1	0.341	0.461
5	0.7	0.45	22	1	0.371	0.450
6	0.7	0.56	22	1	0.385	0.425
7	0.7	0.69	22	1	0.406	0.416
8	0.7	0.77	22	3	0.396	0.380
9	0.7	0.86	22	5	0.394	0.355
10	0.7	0.92	22	12	0.379	0.324

Continued...

$T$ (s)	$R$	$S$ (m)	Temp (°C)	$S_{\infty}$ (m)	$U_c$ (ms <sup>-1</sup> )	$\tau_{crit}$ (Nm <sup>-2</sup> )
6	0.5	0.62	22	1	0.325	0.332
6	0.5	0.64	22	1	0.335	0.343
6	0.5	0.65	22	1	0.340	0.348
6	0.5	0.65	22	1	0.340	0.348
6	0.5	0.64	22	1	0.335	0.343
6	0.5	0.65	22	1	0.340	0.348
6	0.5	0.68	22	1	0.356	0.364
6	0.5	0.68	22	1	0.356	0.364
6	0.5	0.68	21	1	0.356	0.364
6	0.5	0.65	21	1	0.340	0.348
6	0.5	0.69	21	1	0.361	0.370
6	0.5	0.68	22	1	0.356	0.364
6	0.55	0.66	21	1	0.379	0.393
6	0.55	0.65	21	1	0.373	0.387
6	0.55	0.68	21	1	0.390	0.404
6	0.55	0.65	21	1	0.373	0.387
6	0.6	0.62	22	1	0.383	0.406
6	0.6	0.61	22	1	0.377	0.399
6	0.6	0.62	22	1	0.383	0.406
6	0.6	0.61	22	1	0.377	0.399
6	0.65	0.61	22	1	0.399	0.433
6	0.65	0.60	21	1	0.393	0.426
6	0.65	0.63	21	1	0.412	0.447
6	0.65	0.61	22	1	0.399	0.433
6	0.7	0.56	22	1	0.385	0.425
6	0.7	0.59	22	1	0.405	0.448
6	0.7	0.56	22	1	0.385	0.425
6	0.7	0.57	22	1	0.392	0.433

Table D.4. Threshold of motion results for aragonite sediment

$[\rho_s=2700\text{kgm}^{-3}, D=462.5\mu\text{m}]$ .

Appendix D – Threshold of motion results

$T$ (s)	$R$	$S$ (m)	Temp (°C)	$S_{\infty}$ (m)	$U_c$ (ms <sup>-1</sup> )	$\tau_{crit}$ (Nm <sup>-2</sup> )
3	0.5	0.30	22	1	0.314	0.455
4	0.5	0.41	22	1	0.322	0.404
5	0.5	0.51	22	1	0.320	0.359
6	0.5	0.63	22	1	0.330	0.338
7	0.5	0.75	22	1	0.337	0.319
8	0.5	0.85	22	3	0.334	0.296
9	0.5	0.92	22	5	0.321	0.268
3	0.55	0.29	21	1	0.333	0.489
4	0.55	0.40	21	1	0.345	0.438
5	0.55	0.49	21	1	0.338	0.383
6	0.55	0.63	21	1	0.362	0.375
7	0.55	0.75	21	1	0.369	0.354
8	0.55	0.85	21	3	0.366	0.328
9	0.55	0.93	21	5	0.356	0.301
3	0.6	0.30	21	1	0.371	0.556
4	0.6	0.37	21	1	0.343	0.445
5	0.6	0.50	21	1	0.371	0.430
6	0.6	0.63	21	1	0.389	0.412
7	0.6	0.75	21	1	0.397	0.389
8	0.6	0.87	21	3	0.403	0.369
9	0.6	0.97	21	5	0.399	0.345
3	0.65	0.28	22	1	0.367	0.563
4	0.65	0.37	22	1	0.364	0.483
5	0.65	0.48	22	1	0.377	0.448
6	0.65	0.59	22	1	0.386	0.418
7	0.65	0.70	22	1	0.393	0.394
8	0.65	0.83	22	3	0.407	0.382
9	0.65	0.92	22	5	0.401	0.355
3	0.7	0.25	21	1	0.344	0.538
4	0.7	0.36	21	1	0.371	0.503
5	0.7	0.47	21	1	0.388	0.470
6	0.7	0.58	21	1	0.398	0.440
7	0.7	0.68	21	1	0.400	0.410
8	0.7	0.81	21	3	0.417	0.399
9	0.7	0.90	21	5	0.412	0.372

Continued...

Continued...

$T$ (s)	$R$	$S$ (m)	Temp (°C)	$S_{\infty}$ (m)	$U_c$ (ms <sup>-1</sup> )	$\tau_{crit}$ (Nm <sup>-2</sup> )
6	0.5	0.63	22	1	0.330	0.338
6	0.5	0.64	22	1	0.335	0.343
6	0.5	0.62	22	1	0.325	0.332
6	0.5	0.65	22	1	0.340	0.348
6	0.5	0.65	21	1	0.340	0.348
6	0.5	0.66	21	1	0.346	0.354
6	0.5	0.66	21	1	0.346	0.354
6	0.5	0.66	21	1	0.346	0.354
6	0.5	0.66	21	1	0.346	0.354
6	0.5	0.64	21	1	0.335	0.343
6	0.5	0.68	22	1	0.356	0.364
6	0.5	0.66	22	1	0.346	0.354
6	0.55	<b>0.63</b>	21	1	0.362	0.375
6	0.55	0.64	21	1	0.367	0.381
6	0.55	0.65	21	1	0.373	0.387
6	0.55	0.64	21	1	0.367	0.381
6	0.6	0.63	21	1	0.389	0.412
6	0.6	0.61	21	1	0.377	0.399
6	0.6	0.66	21	1	0.408	0.432
6	0.6	0.64	21	1	0.395	0.419
6	0.65	0.59	22	1	0.386	0.418
6	0.65	0.59	22	1	0.386	0.418
6	0.65	0.61	22	1	0.399	0.433
6	0.65	0.59	22	1	0.386	0.418
6	0.7	0.58	21	1	0.398	0.440
6	0.7	0.58	21	1	0.398	0.440
6	0.7	0.60	21	1	0.412	0.456
6	0.7	0.55	21	1	0.378	0.418

Table D.5. Threshold of motion results for aragonite sediment

$[\rho_s=2700\text{kgm}^{-3}, D=550\mu\text{m}]$ .

Appendix D – Threshold of motion results

$T$ (s)	$R$	$S$ (m)	Temp (°C)	$S_{\infty}$ (m)	$U_c$ (ms <sup>-1</sup> )	$\tau_{crit}$ (Nm <sup>-2</sup> )
6	0.5	0.34	23	1	0.178	0.182
6	0.5	0.34	23	1	0.178	0.182
6	0.5	0.34	23	1	0.178	0.182
6	0.5	0.36	23	1	0.189	0.193
6	0.55	0.32	23	1	0.184	0.191
6	0.55	0.32	23	1	0.184	0.191
6	0.55	0.34	23	1	0.195	0.203
6	0.55	0.33	23	1	0.190	0.197
6	0.6	0.31	23	1	0.192	0.203
6	0.6	0.31	23	1	0.192	0.203
6	0.6	0.32	23	1	0.198	0.209
6	0.6	0.30	23	1	0.185	0.196
6	0.65	0.27	23	1	0.177	0.192
6	0.65	0.27	23	1	0.177	0.192
6	0.65	0.28	23	1	0.184	0.199
6	0.65	0.28	23	1	0.184	0.199
6	0.7	0.26	23	1	0.179	0.198
6	0.7	0.26	23	1	0.179	0.198
6	0.7	0.25	23	1	0.172	0.190
6	0.7	0.25	23	1	0.172	0.190

Table D.6. Threshold of motion results for Bakelite sediment

$[\rho_s=1400\text{kgm}^{-3}, D=925\mu\text{m}]$ .

$T$ (s)	$R$	$S$ (m)	Temp (°C)	$S_{\infty}$ (m)	$U_c$ (ms <sup>-1</sup> )	$\tau_{crit}$ (Nm <sup>-2</sup> )
4	0.5	0.23	22	1	0.181	0.226
5	0.5	0.29	22	1	0.182	0.204
6	0.5	0.37	22	1	0.194	0.198
7	0.5	0.45	22	1	0.202	0.191
8	0.5	0.51	22	1	0.200	0.178
9	0.5	0.53	22	3	0.185	0.155
10	0.5	0.65	22	5	0.204	0.162
11	0.5	0.69	22	9	0.197	0.149
12	0.5	0.76	22	10	0.199	0.144
4	0.55	0.22	23	1	0.190	0.241
5	0.55	0.31	23	1	0.214	0.243
6	0.55	0.36	23	1	0.207	0.214
7	0.55	0.46	23	1	0.226	0.217
8	0.55	0.53	23	1	0.228	0.205
9	0.55	0.60	23	3	0.230	0.194
10	0.55	0.66	23	5	0.227	0.182
11	0.55	0.70	23	9	0.219	0.168
12	0.55	0.77	23	10	0.221	0.162
4	0.6	0.21	23	1	0.195	0.253
5	0.6	0.27	23	1	0.201	0.233
6	0.6	0.32	23	1	0.198	0.209
7	0.6	0.41	23	1	0.217	0.213
8	0.6	0.51	23	1	0.236	0.217
9	0.6	0.55	23	3	0.226	0.196
10	0.6	0.66	23	5	0.245	0.201
11	0.6	0.73	23	9	0.246	0.192
12	0.6	0.81	23	10	0.250	0.187

Table D.7. Threshold of motion results for Bakelite sediment

$[\rho_s=1400\text{kgm}^{-3}, D=1200\mu\text{m}]$ . *Continued...*

Appendix D – Threshold of motion results

Continued...

$T$ (s)	$R$	$S$ (m)	Temp (°C)	$S_{\infty}$ (m)	$U_c$ (ms <sup>-1</sup> )	$\tau_{crit}$ (Nm <sup>-2</sup> )
4	0.65	0.17	23	1	0.168	0.222
5	0.65	0.26	23	1	0.205	0.243
6	0.65	0.32	23	1	0.210	0.227
7	0.65	0.41	23	1	0.230	0.231
8	0.65	0.49	23	1	0.241	0.226
9	0.65	0.57	23	3	0.249	0.220
10	0.65	0.65	23	5	0.255	0.214
11	0.65	0.72	23	9	0.257	0.206
12	0.65	0.76	23	10	0.249	0.191
4	0.7	0.18	23	1	0.186	0.252
5	0.7	0.24	23	1	0.198	0.240
6	0.7	0.30	23	1	0.206	0.228
7	0.7	0.36	23	1	0.212	0.217
8	0.7	0.43	23	1	0.222	0.212
9	0.7	0.51	23	3	0.234	0.211
10	0.7	0.55	23	5	0.227	0.194
11	0.7	0.63	23	9	0.236	0.193
12	0.7	0.67	23	10	0.230	0.180
6	0.5	0.37	22	1	0.194	0.198
6	0.5	0.36	22	1	0.189	0.193
6	0.5	0.36	22	1	0.189	0.193
6	0.5	0.37	22	1	0.194	0.198
6	0.5	0.38	23	1	0.199	0.204
6	0.5	0.39	23	1	0.204	0.209
6	0.5	0.36	23	1	0.189	0.193
6	0.5	0.36	23	1	0.189	0.193
6	0.5	0.38	23	1	0.199	0.204
6	0.5	0.39	23	1	0.204	0.209
6	0.5	0.37	23	1	0.194	0.198
6	0.5	0.37	23	1	0.194	0.198
6	0.55	0.36	23	1	0.207	0.214
6	0.55	0.37	23	1	0.212	0.220
6	0.55	0.37	23	1	0.212	0.220
6	0.55	0.38	23	1	0.218	0.226

Continued...

$T$ (s)	$R$	$S$ (m)	Temp (°C)	$S_{\infty}$ (m)	$U_c$ (ms <sup>-1</sup> )	$\tau_{crit}$ (Nm <sup>-2</sup> )
6	0.6	0.32	23	1	0.198	0.209
6	0.6	0.34	23	1	0.210	0.223
6	0.6	0.32	23	1	0.198	0.209
6	0.6	0.34	23	1	0.210	0.223
6	0.65	0.32	23	1	0.210	0.227
6	0.65	0.31	23	1	0.203	0.220
6	0.65	0.33	23	1	0.216	0.234
6	0.65	0.35	23	1	0.229	0.249
6	0.7	0.30	23	1	0.206	0.228
6	0.7	0.29	23	1	0.199	0.221
6	0.7	0.30	23	1	0.206	0.228
6	0.7	0.29	23	1	0.199	0.221

Table D.7. Threshold of motion results for Bakelite sediment  
 $[\rho_s=1400\text{kgm}^{-3}, D=1200\mu\text{m}]$ .

$T$ (s)	$R$	$S$ (m)	Temp (°C)	$S_{\infty}$ (m)	$U_c$ (ms <sup>-1</sup> )	$\tau_{crit}$ (Nm <sup>-2</sup> )
4	0.5	0.21	23	1	0.165	0.207
5	0.5	0.28	23	1	0.176	0.197
6	0.5	0.36	23	1	0.189	0.193
7	0.5	0.44	23	1	0.198	0.187
8	0.5	0.53	23	1	0.208	0.184
9	0.5	0.61	23	3	0.213	0.178
10	0.5	0.70	23	5	0.220	0.174
11	0.5	0.77	23	9	0.220	0.166
12	0.5	0.82	23	10	0.215	0.155

Table D.8. Threshold of motion results for Bakelite sediment  
 $[\rho_s=1400\text{kgm}^{-3}, D=1550]$ . *Continued...*

Appendix D – Threshold of motion results

Continued...

$T$ (s)	$R$	$S$ (m)	Temp (°C)	$S_{\infty}$ (m)	$U_c$ (ms <sup>-1</sup> )	$\tau_{crit}$ (Nm <sup>-2</sup> )
4	0.55	0.22	23	1	0.190	0.241
5	0.55	0.28	23	1	0.193	0.219
6	0.55	0.36	23	1	0.207	0.214
7	0.55	0.46	23	1	0.226	0.217
8	0.55	0.56	23	1	0.241	0.216
9	0.55	0.65	23	3	0.249	0.210
10	0.55	0.72	23	5	0.248	0.199
11	0.55	0.76	23	9	0.238	0.182
12	0.55	0.81	23	10	0.232	0.170
4	0.6	0.18	23	1	0.167	0.217
5	0.6	0.28	23	1	0.208	0.241
6	0.6	0.35	23	1	0.216	0.229
7	0.6	0.43	23	1	0.228	0.223
8	0.6	0.54	23	1	0.250	0.230
9	0.6	0.63	23	3	0.259	0.224
10	0.6	0.68	23	5	0.252	0.207
11	0.6	0.75	23	9	0.253	0.198
12	0.6	0.80	23	10	0.247	0.185
4	0.65	0.17	23	1	0.168	0.222
5	0.65	0.24	23	1	0.189	0.224
6	0.65	0.29	23	1	0.190	0.206
7	0.65	0.35	23	1	0.197	0.197
8	0.65	0.46	23	1	0.226	0.212
9	0.65	0.54	23	3	0.236	0.208
10	0.65	0.64	23	5	0.251	0.211
11	0.65	0.71	23	9	0.254	0.203
12	0.65	0.78	23	10	0.255	0.196
4	0.7	0.16	23	1	0.166	0.224
5	0.7	0.22	23	1	0.182	0.220
6	0.7	0.30	23	1	0.206	0.228
7	0.7	0.40	23	1	0.236	0.241
8	0.7	0.47	23	1	0.242	0.232
9	0.7	0.57	23	3	0.261	0.236
10	0.7	0.60	23	5	0.247	0.212

Continued...

$T$ (s)	$R$	$S$ (m)	Temp (°C)	$S_{\infty}$ (m)	$U_c$ (ms <sup>-1</sup> )	$\tau_{crit}$ (Nm <sup>-2</sup> )
11	0.7	0.72	23	9	0.270	0.220
12	0.7	0.81	23	10	0.278	0.217
6	0.5	0.36	23	1	0.189	0.193
6	0.5	0.38	23	1	0.199	0.204
6	0.5	0.36	23	1	0.189	0.193
6	0.5	0.36	23	1	0.189	0.193
6	0.5	0.38	23	1	0.199	0.204
6	0.5	0.39	23	1	0.204	0.209
6	0.5	0.39	23	1	0.204	0.209
6	0.5	0.38	23	1	0.199	0.204
6	0.5	0.38	23	1	0.199	0.204
6	0.5	0.39	23	1	0.204	0.209
6	0.5	0.39	23	1	0.204	0.209
6	0.5	0.38	23	1	0.199	0.204
6	0.5	0.38	23	1	0.199	0.204
6	0.5	0.37	23	1	0.194	0.198
6	0.55	0.36	23	1	0.207	0.214
6	0.55	0.38	23	1	0.218	0.226
6	0.55	0.37	23	1	0.212	0.220
6	0.55	0.37	23	1	0.212	0.220
6	0.6	0.35	23	1	0.216	0.229
6	0.6	0.34	23	1	0.210	0.223
6	0.6	0.34	23	1	0.210	0.223
6	0.6	0.34	23	1	0.210	0.223
6	0.65	0.29	23	1	0.190	0.206
6	0.65	0.30	23	1	0.197	0.213
6	0.65	0.29	23	1	0.190	0.206
6	0.65	0.30	23	1	0.197	0.213
6	0.7	0.30	23	1	0.206	0.228
6	0.7	0.29	23	1	0.199	0.221
6	0.7	0.28	23	1	0.193	0.213
6	0.7	0.31	23	1	0.213	0.236

Table D.8. Threshold of motion results for Bakelite sediment

$[\rho_s=1400\text{kgm}^{-3}, D=1550\mu\text{m}]$ .

Appendix D – Threshold of motion results

$T$ (s)	$R$	$S$ (m)	Temp (°C)	$S_{\infty}$ (m)	$U_c$ (ms <sup>-1</sup> )	$\tau_{crit}$ (Nm <sup>-2</sup> )
4	0.5	0.44	21	1	0.346	0.433
5	0.5	0.54	21	1	0.339	0.380
6	0.5	0.65	21	1	0.340	0.348
7	0.5	0.74	21	1	0.332	0.315
8	0.5	0.90	21	3	0.353	0.313
9	0.5	1.00	21	5	0.349	0.292
4	0.55	0.46	21	1	0.396	0.503
5	0.55	0.53	21	1	0.365	0.414
6	0.55	0.68	21	1	0.390	0.404
7	0.55	0.75	21	1	0.369	0.354
8	0.55	0.86	21	3	0.370	0.332
9	0.55	0.93	21	5	0.356	0.301
4	0.6	0.44	21	1	0.408	0.529
5	0.6	0.55	21	1	0.408	0.473
6	0.6	0.66	21	1	0.408	0.432
7	0.6	0.80	21	1	0.423	0.415
8	0.6	0.88	21	3	0.407	0.374
9	0.6	0.95	21	5	0.391	0.338
4	0.65	0.42	22	1	0.413	0.548
5	0.65	0.55	22	1	0.432	0.513
6	0.65	0.65	22	1	0.426	0.461
7	0.65	0.74	22	1	0.415	0.416
8	0.65	0.86	22	3	0.422	0.396
9	0.65	0.97	22	5	0.423	0.374
4	0.7	0.40	21	1	0.412	0.558
5	0.7	0.50	21	1	0.412	0.499
6	0.7	0.66	21	1	0.453	0.501
7	0.7	0.73	21	1	0.430	0.440
8	0.7	0.82	21	3	0.422	0.404
9	0.7	0.92	21	5	0.421	0.380

Continued...

Continued...

$T$ (s)	$R$	$S$ (m)	Temp (°C)	$S_{\infty}$ (m)	$U_c$ (ms <sup>-1</sup> )	$\tau_{crit}$ (Nm <sup>-2</sup> )
6	0.5	0.65	21	1	0.340	0.348
6	0.5	0.62	21	1	0.325	0.332
6	0.5	0.62	21	1	0.325	0.332
6	0.5	0.66	21	1	0.346	0.354
6	0.5	0.68	21	1	0.356	0.364
6	0.5	0.68	21	1	0.356	0.364
6	0.5	0.68	21	1	0.356	0.364
6	0.5	0.69	21	1	0.361	0.370
6	0.5	0.65	21	1	0.340	0.348
6	0.5	0.64	21	1	0.335	0.343
6	0.5	0.66	22	1	0.346	0.354
6	0.5	0.67	22	1	0.351	0.359
6	0.55	0.68	21	1	0.390	0.404
6	0.55	0.68	21	1	0.390	0.404
6	0.55	0.66	21	1	0.379	0.393
6	0.55	0.64	21	1	0.367	0.381
6	0.6	0.66	21	1	0.408	0.432
6	0.6	0.67	21	1	0.414	0.438
6	0.6	0.66	21	1	0.408	0.432
6	0.6	0.66	21	1	0.408	0.432
6	0.65	0.65	22	1	0.426	0.461
6	0.65	0.66	22	1	0.432	0.468
6	0.65	0.66	22	1	0.432	0.468
6	0.65	0.64	22	1	0.419	0.454
6	0.7	0.66	21	1	0.453	0.501
6	0.7	0.63	21	1	0.433	0.478
6	0.7	0.64	21	1	0.440	0.486
6	0.7	0.62	21	1	0.426	0.471

Table D.9. Threshold of motion results for quartz sediment [ $\rho_s=2650\text{kgm}^{-3}$ ,  $D=275\mu\text{m}$ ].

Appendix D – Threshold of motion results

$T$ (s)	$R$	$S$ (m)	Temp (°C)	$S_{\infty}$ (m)	$U_c$ (ms <sup>-1</sup> )	$\tau_{crit}$ (Nm <sup>-2</sup> )
4	0.5	0.43	21	1	0.338	0.423
5	0.5	0.56	21	1	0.352	0.394
6	0.5	0.68	21	1	0.356	0.364
7	0.5	0.78	21	1	0.350	0.332
8	0.5	0.90	21	3	0.353	0.313
9	0.5	0.96	21	6	0.335	0.280
4	0.55	0.46	20	1	0.396	0.503
5	0.55	0.55	20	1	0.379	0.430
6	0.55	0.65	20	1	0.373	0.387
7	0.55	0.76	20	1	0.374	0.359
8	0.55	0.89	20	3	0.383	0.344
9	0.55	1.00	20	6	0.382	0.324
4	0.6	0.44	21	1	0.408	0.529
5	0.6	0.54	21	1	0.400	0.464
6	0.6	0.66	21	1	0.408	0.432
7	0.6	0.73	21	1	0.386	0.379
8	0.6	0.84	21	3	0.389	0.357
9	0.6	0.93	21	5	0.383	0.331
4	0.65	0.45	21	1	0.442	0.587
5	0.65	0.52	21	1	0.409	0.485
6	0.65	0.64	21	1	0.419	0.454
7	0.65	0.76	21	1	0.427	0.428
8	0.65	0.88	21	3	0.432	0.405
9	0.65	0.99	21	5	0.432	0.382
4	0.7	0.41	22	1	0.423	0.573
5	0.7	0.52	22	1	0.429	0.519
6	0.7	0.61	21	1	0.419	0.463
7	0.7	0.72	21	1	0.424	0.434
8	0.7	0.83	21	3	0.428	0.409
9	0.7	0.91	22	5	0.416	0.376

Continued...

Continued...

$T$ (s)	$R$	$S$ (m)	Temp (°C)	$S_{\infty}$ (m)	$U_c$ (ms <sup>-1</sup> )	$\tau_{crit}$ (Nm <sup>-2</sup> )
6	0.5	0.65	21	1	0.340	0.348
6	0.5	0.62	21	1	0.325	0.332
6	0.5	0.62	21	1	0.325	0.332
6	0.5	0.66	21	1	0.346	0.354
6	0.5	0.68	21	1	0.356	0.364
6	0.5	0.68	21	1	0.356	0.364
6	0.5	0.68	21	1	0.356	0.364
6	0.5	0.69	21	1	0.361	0.370
6	0.5	0.65	21	1	0.340	0.348
6	0.5	0.64	21	1	0.335	0.343
6	0.5	0.66	22	1	0.346	0.354
6	0.5	0.67	22	1	0.351	0.359
6	0.55	0.68	21	1	0.390	0.404
6	0.55	0.68	21	1	0.390	0.404
6	0.55	0.66	21	1	0.379	0.393
6	0.55	0.64	21	1	0.367	0.381
6	0.6	0.66	21	1	0.408	0.432
6	0.6	0.67	21	1	0.414	0.438
6	0.6	0.66	21	1	0.408	0.432
6	0.6	0.66	21	1	0.408	0.432
6	0.65	0.65	22	1	0.426	0.461
6	0.65	0.66	22	1	0.432	0.468
6	0.65	0.66	22	1	0.432	0.468
6	0.65	0.64	22	1	0.419	0.454
6	0.7	0.66	21	1	0.453	0.501
6	0.7	0.63	21	1	0.433	0.478
6	0.7	0.64	21	1	0.440	0.486
6	0.7	0.62	21	1	0.426	0.471

Table D.10. Threshold of motion results for quartz sediment [ $\rho_s=2650\text{kgm}^{-3}$ ,  $D=327.5\mu\text{m}$ ].

Appendix D – Threshold of motion results

$T$ (s)	$R$	$S$ (m)	Temp (°C)	$S_{\infty}$ (m)	$U_c$ (ms <sup>-1</sup> )	$\tau_{crit}$ (Nm <sup>-2</sup> )
4	0.5	0.43	21	1	0.338	0.423
5	0.5	0.52	21	1	0.327	0.366
6	0.5	0.64	21	1	0.335	0.343
7	0.5	0.76	21	1	0.341	0.323
8	0.5	0.89	21	2	0.350	0.310
9	0.5	0.95	21	5	0.332	0.277
4	0.55	0.45	22	1	0.388	0.492
5	0.55	0.55	22	1	0.379	0.430
6	0.55	0.66	21	1	0.379	0.393
7	0.55	0.76	21	1	0.374	0.359
8	0.55	0.84	21	2	0.361	0.324
9	0.55	0.92	22	5	0.352	0.298
4	0.6	0.42	21	1	0.389	0.505
5	0.6	0.56	21	1	0.415	0.482
6	0.6	0.65	21	1	0.401	0.425
7	0.6	0.78	21	1	0.413	0.405
8	0.6	0.87	21	2	0.403	0.369
9	0.6	0.96	21	6	0.395	0.342
4	0.65	0.40	22	1	0.393	0.522
5	0.65	0.51	22	1	0.401	0.476
6	0.65	0.63	22	1	0.412	0.447
7	0.65	0.78	22	1	0.438	0.439
8	0.65	0.84	22	3	0.412	0.387
9	0.65	0.96	22	5	0.419	0.370
4	0.7	0.39	21	1	0.402	0.545
5	0.7	0.48	21	1	0.396	0.480
6	0.7	0.63	21	1	0.433	0.478
7	0.7	0.71	21	1	0.418	0.428
8	0.7	0.86	21	3	0.443	0.424
9	0.7	0.95	21	5	0.435	0.393

Continued...

Continued...

$T$ (s)	$R$	$S$ (m)	Temp (°C)	$S_{\infty}$ (m)	$U_c$ (ms <sup>-1</sup> )	$\tau_{crit}$ (Nm <sup>-2</sup> )
6	0.5	0.64	21	1	0.335	0.343
6	0.5	0.69	21	1	0.361	0.370
6	0.5	0.68	21	1	0.356	0.364
6	0.5	0.63	21	1	0.330	0.338
6	0.5	0.68	21	1	0.356	0.364
6	0.5	0.68	21	1	0.356	0.364
6	0.5	0.66	21	1	0.346	0.354
6	0.5	0.67	21	1	0.351	0.359
6	0.5	0.66	21	1	0.346	0.354
6	0.5	0.65	22	1	0.340	0.348
6	0.5	0.66	22	1	0.346	0.354
6	0.5	0.66	22	1	0.346	0.354
6	0.55	0.66	21	1	0.379	0.393
6	0.55	0.66	21	1	0.379	0.393
6	0.55	0.68	22	1	0.390	0.404
6	0.55	0.63	22	1	0.362	0.375
6	0.6	0.65	21	1	0.401	0.425
6	0.6	0.67	21	1	0.414	0.438
6	0.6	0.63	21	1	0.389	0.412
6	0.6	0.66	21	1	0.408	0.432
6	0.65	0.63	22	1	0.412	0.447
6	0.65	0.66	22	1	0.432	0.468
6	0.65	0.64	22	1	0.419	0.454
6	0.65	0.63	22	1	0.412	0.447
6	0.7	0.63	21	1	0.433	0.478
6	0.7	0.61	21	1	0.419	0.463
6	0.7	0.61	21	1	0.419	0.463
6	0.7	0.59	21	1	0.405	0.448

Table D.11. Threshold of motion results for quartz sediment [ $\rho_s=2650\text{kgm}^{-3}$ ,  $D=390\mu\text{m}$ ].

Appendix D – Threshold of motion results

$T$ (s)	$R$	$S$ (m)	Temp (°C)	$S_{\infty}$ (m)	$U_c$ (ms <sup>-1</sup> )	$\tau_{crit}$ (Nm <sup>-2</sup> )
4	0.5	0.44	21	1	0.346	0.433
5	0.5	0.52	21	1	0.327	0.366
6	0.5	0.61	21	1	0.319	0.327
7	0.5	0.74	21	1	0.332	0.315
8	0.5	0.86	21	2	0.338	0.299
9	0.5	0.91	21	5	0.318	0.265
10	0.5	1.00	21	8	0.314	0.249
4	0.55	0.42	21	1	0.362	0.459
5	0.55	0.56	21	1	0.386	0.438
6	0.55	0.65	21	1	0.373	0.387
7	0.55	0.74	21	1	0.364	0.349
8	0.55	0.86	21	2	0.370	0.332
9	0.55	0.97	21	7	0.371	0.314
4	0.6	0.41	21	1	0.380	0.493
5	0.6	0.52	21	1	0.385	0.447
6	0.6	0.60	21	1	0.371	0.393
7	0.6	0.72	21	1	0.381	0.374
8	0.6	0.88	21	3	0.407	0.374
9	0.6	0.93	21	5	0.383	0.331
4	0.65	0.41	21	1	0.403	0.535
5	0.65	0.52	21	1	0.409	0.485
6	0.65	0.68	21	1	0.445	0.482
7	0.65	0.77	21	1	0.432	0.433
8	0.65	0.87	21	2	0.427	0.401
9	0.65	0.95	21	5	0.415	0.367
4	0.7	0.39	21	1	0.402	0.545
5	0.7	0.50	20	1	0.412	0.499
6	0.7	0.62	20	1	0.426	0.471
7	0.7	0.70	20	1	0.412	0.422
8	0.7	0.84	20	2	0.432	0.414
9	0.7	0.92	20	6	0.421	0.380

Continued...

Continued...

$T$ (s)	$R$	$S$ (m)	Temp (°C)	$S_{\infty}$ (m)	$U_c$ (ms <sup>-1</sup> )	$\tau_{crit}$ (Nm <sup>-2</sup> )
6	0.5	0.61	21	1	0.319	0.327
6	0.5	0.62	21	1	0.325	0.332
6	0.5	0.64	21	1	0.335	0.343
6	0.5	0.67	21	1	0.351	0.359
6	0.5	0.67	21	1	0.351	0.359
6	0.5	0.68	21	1	0.356	0.364
6	0.5	0.67	21	1	0.351	0.359
6	0.5	0.66	21	1	0.346	0.354
6	0.5	0.68	21	1	0.356	0.364
6	0.5	0.69	21	1	0.361	0.370
6	0.5	0.68	21	1	0.356	0.364
6	0.5	0.66	21	1	0.346	0.354
6	0.55	0.65	21	1	0.373	0.387
6	0.55	0.63	21	1	0.362	0.375
6	0.55	0.66	21	1	0.379	0.393
6	0.55	0.66	21	1	0.379	0.393
6	0.6	0.60	21	1	0.371	0.393
6	0.6	0.64	21	1	0.395	0.419
6	0.6	0.63	21	1	0.389	0.412
6	0.6	0.65	21	1	0.401	0.425
6	0.65	0.68	21	1	0.445	0.482
6	0.65	0.67	21	1	0.439	0.475
6	0.65	0.64	21	1	0.419	0.454
6	0.65	0.65	21	1	0.426	0.461
6	0.7	0.62	20	1	0.426	0.471
6	0.7	0.62	20	1	0.426	0.471
6	0.7	0.62	20	1	0.426	0.471
6	0.7	0.61	21	1	0.419	0.463

Table D.12. Threshold of motion results for quartz sediment [ $\rho_s=2650\text{kgm}^{-3}$ ,  $D=462.5\mu\text{m}$ ].

Appendix D – Threshold of motion results

$T$ (s)	$R$	$S$ (m)	Temp (°C)	$S_{\infty}$ (m)	$U_c$ (ms <sup>-1</sup> )	$\tau_{crit}$ (Nm <sup>-2</sup> )
4	0.5	0.45	20	1	0.353	0.443
5	0.5	0.52	21	2	0.327	0.366
6	0.5	0.64	21	1	0.335	0.343
7	0.5	0.75	21	1	0.337	0.319
8	0.5	0.85	21	3	0.334	0.296
9	0.5	0.94	21	6	0.328	0.274
4	0.55	0.42	20	1	0.362	0.459
5	0.55	0.56	20	1	0.386	0.438
6	0.55	0.67	20	1	0.384	0.398
7	0.55	0.79	20	1	0.389	0.373
8	0.55	0.88	20	2	0.379	0.340
9	0.55	0.96	20	4	0.367	0.311
5	0.6	0.51	21	1	0.378	0.439
6	0.6	0.66	21	1	0.408	0.432
7	0.6	0.76	21	1	0.402	0.394
8	0.6	0.87	21	3	0.403	0.369
9	0.6	0.96	21	5	0.395	0.342
4	0.65	0.40	20	1	0.393	0.522
5	0.65	0.50	20	1	0.393	0.466
6	0.65	0.60	20	1	0.393	0.426
7	0.65	0.69	20	1	0.387	0.388
8	0.65	0.79	20	2	0.388	0.364
9	0.65	0.89	20	5	0.388	0.343
10	0.65	0.96	20	7	0.377	0.316
4	0.7	0.36	19	1	0.371	0.503
5	0.7	0.49	19	1	0.404	0.489
6	0.7	0.59	19	1	0.405	0.448
7	0.7	0.71	19	1	0.418	0.428
8	0.7	0.82	19	2	0.422	0.404
9	0.7	0.90	19	4	0.412	0.372
10	0.7	1.00	19	8	0.412	0.353

Continued...

Continued...

$T$ (s)	$R$	$S$ (m)	Temp (°C)	$S_{\infty}$ (m)	$U_c$ (ms <sup>-1</sup> )	$\tau_{crit}$ (Nm <sup>-2</sup> )
6	0.5	0.66	20	1	0.346	0.354
6	0.5	0.67	21	1	0.351	0.359
6	0.5	0.66	21	1	0.346	0.354
6	0.5	0.68	21	1	0.356	0.364
6	0.5	0.64	19	1	0.335	0.343
6	0.5	0.66	19	1	0.346	0.354
6	0.5	0.68	20	1	0.356	0.364
6	0.5	0.68	20	1	0.356	0.364
6	0.5	0.68	20	1	0.356	0.364
6	0.5	0.66	20	1	0.346	0.354
6	0.5	0.64	21	1	0.335	0.343
6	0.55	0.67	20	1	0.384	0.398
6	0.55	0.68	20	1	0.390	0.404
6	0.55	0.68	20	1	0.390	0.404
6	0.55	0.69	20	1	0.396	0.410
6	0.6	0.66	21	1	0.408	0.432
6	0.6	0.63	21	1	0.389	0.412
6	0.6	0.66	21	1	0.408	0.432
6	0.6	0.67	21	1	0.414	0.438
6	0.65	0.60	20	1	0.393	0.426
6	0.65	0.60	20	1	0.393	0.426
6	0.65	0.63	20	1	0.412	0.447
6	0.65	0.63	20	1	0.412	0.447
6	0.7	0.59	19	1	0.405	0.448
6	0.7	0.62	19	1	0.426	0.471
6	0.7	0.62	19	1	0.426	0.471
6	0.7	0.60	19	1	0.412	0.456

Table D.13. Threshold of motion results for quartz sediment

$[\rho_s=2650\text{kgm}^{-3}, D=550\mu\text{m}]$ .

## **Appendix E. Lambkin, Collins and Paphitis (In Press)**

### **Wave period and flow asymmetry effects on the transition to turbulence in relation to sediment dynamics.**

Lambkin, D.O.<sup>1</sup>, Collins, M.B.<sup>2</sup> and Paphitis, D.<sup>3</sup>

<sup>1,2,3</sup> *School of Ocean and Earth Science, Southampton Oceanography Centre, University of Southampton, European Way, Southampton, SO14 3ZH, U.K.*

*e-mail: <sup>1</sup> D.O.Lambkin@soc.soton.ac.uk, <sup>2</sup> mbc@soc.soton.ac.uk, <sup>3</sup> Doros@soc.soton.ac.uk*

#### **ABSTRACT**

The presence or absence of turbulence in near-bed flows is known to affect patterns of sediment transport. Therefore, the accurate prediction of turbulence is important when considering the initiation of motion of medium to coarse sands as such grains may be eroded by conditions similar to those causing turbulence. An experimental study is described to investigate boundary layer stability under non-linear (asymmetric) oscillatory flows. In addition, the results are combined with data collected elsewhere to better explain the dependence of initial transition to turbulence on bed roughness and oscillatory period.

An oscillating trolley system simulating such oscillatory flows at prototype scale, is described. The transition to turbulence under asymmetric (non-linear) oscillatory flow is investigated utilising visual techniques and the high-resolution measurement of near-bed

velocity. These data are used in conjunction with the extensive data sets of Li (1954) and Manohar (1955) for linear oscillatory flows, collected using similar equipment and methods. Relationships are presented to describe such transition over smooth and fixed (granular) roughness beds under linear and non-linear flows.

The transition to turbulence is shown to have a strong positive linear correlation with both oscillatory period and grain roughness, up to a maximum Reynolds number for linear flows. An additional positive non-linear relationship with asymmetry is observed; this was proportionately greater with increasing bed roughness (from smooth beds to a uniform bed roughness of 550 $\mu\text{m}$ ). These relationships suggest that transition is regulated by a balance between stabilising and destabilising forces or conditions, namely: rates of fluid acceleration; the time frame for development of turbulence; and sources of the initial flow perturbation. It is argued that (wave) period dependence observed in threshold of motion data may be explained by a combination of: (a) period dependency in the transition to turbulence; or (b) by translation of the proposed regulatory mechanisms for the transition to turbulence.

**Keywords:** Asymmetric oscillatory flows, transition to turbulence, threshold of motion, oscillating trolleys, laminar oscillatory flow.

## 1. INTRODUCTION

Understanding the hydrodynamic behaviour of oscillatory flows at the seabed is of great importance to oceanographers, sedimentologists and coastal engineers within the context of fluid- and sediment-dynamics processes. Such information may be used to model a wide range of processes, including: sediment mobility; seabed or coastal geomorphological changes; and flow interaction with structures and the seabed.

On the basis of the investigations of Komar and Miller (1973, 1974) a critical grain size of 500 $\mu\text{m}$  for quartz sand was suggested as the break point between sediment erosion under laminar or turbulent flow. This point relates directly with the Shields diagram minima and was assumed to correlate to the significant shedding of eddies from individual roughness elements causing turbulence. In general, sediments are more readily eroded by the presence of turbulence but the full transition to turbulence is a gradual process over a range of flow conditions (see below). For quartz sands this range of flows correspond to the threshold of motion for grains of  $\sim 100\text{-}2000\mu\text{m}$  in diameter. Therefore, the prediction of the transition to turbulence together with an understanding of the intermediate stages of turbulence development are of fundamental importance for the accurate prediction of the initiation of motion of these sediments.

The hydrodynamic stability of the boundary layer and in particular, the transition to turbulence under sinusoidal oscillatory flows, has been investigated previously in both laboratory and numerical studies. These data, together with the numerical techniques used previously are reviewed elsewhere (e.g. Hino *et al.*, 1976; Jensen *et al.*, 1989; Sleath, 1984, 1990; Tanaka and Sana, 1994; Lodahl *et al.* 1998; and Tanaka *et al.*, 2000). The term ‘transition’ in relation to turbulence is considered generally as the beginning of ‘transitional’ flow or initial deviation from laminar flow solutions. Previous laboratory investigations into boundary layer stability (transition to turbulence and turbulence structure) have typically employed oscillating water tunnels or other types of pipe flow equipment. Such equipment has been used to simulate sinusoidal (e.g. Du Toit and Sleath, 1981; Hino *et al.*, 1983; Sleath 1987; and Jensen *et al.* 1989) and asymmetric oscillatory flows (e.g. Tanaka *et al.*, 1998; Tanaka *et al.*, 2000). In these investigations, air and water have been used successfully as the fluid medium. Likewise, other researchers have made observations of the transition to turbulence under sinusoidal flow conditions in wave flumes (Vincent, 1957; and Lhermitte, 1958) and over oscillating trolleys (Li, 1954; and Manohar, 1955). In such studies it was noted that oscillating trolleys do not reproduce the horizontal pressure gradients associated with free surface gravity waves or oscillating water tunnels. The vector of this pressure

---

gradient is periodic and is thought to interact with and enhance the stabilising/destabilising effects of vertical gradients of horizontal velocity and fluid acceleration to some extent.

The transition to turbulence over smooth beds has traditionally been defined as occurring at a particular Reynolds number. However, as first described by Hino *et al.* (1976), the full transition from laminar to fully turbulent flow over smooth beds occurs over a range of Reynolds numbers. More recently, similar observations from the results of pipe flow and oscillating tunnel experiments have been discussed quantitatively by Jensen *et al.* (1989) and Lodahl *et al.* (1998). These results have shown that the early stages of turbulence are evident as small amplitude fluctuations in velocity about the laminar signal. This is followed by the sudden development of turbulent spikes in the velocity or shear stress signals that are limited initially to periods of flow deceleration. Described as ‘conditional turbulence’ by Hino *et al.*, this early transition is characterised by re-laminarisation of the signal during flow acceleration. Lodahl *et al.* suggest that the adverse pressure gradient during the deceleration phase combined with small near-wall velocities provides a favourable environment for the initiation of turbulence. It is suggested also that turbulence during these phases may be caused by shear instability of the velocity profile in the region of flow inflection. As the Reynolds number is increased, turbulence spreads progressively throughout the oscillatory cycle. Limited data have been presented for transition over a smooth bed under asymmetric (cnoidal) oscillatory flows (Tanaka *et al.*, 2000) where the critical Reynolds number was expressed as a non-linear function of the degree of asymmetry.

Over an hydrodynamically rough bed, limits have been proposed to describe initial transition (Manohar, 1955) and the limit for fully developed turbulence (Kajiura, 1968). These limits expressed the critical Reynolds number as  $[c^*(a/D)]$  where  $c$  is a scalar coefficient (104 and 1000, respectively),  $a$  is the orbital amplitude and  $D$  is the grain size. The relationship of Manohar was an empirical fit to a large dataset collected using an oscillating trolley including similar data collected using the same equipment by Li (1954) and represented the earliest transition to turbulence observed in the data as plotted. However, for the majority of the data, the transition was significantly under-estimated by the relationship. Similar relationships have been proposed by Jonsson (1966) and Kamphuis (1975). The former obliquely bisects the relationship of Manohar whilst the latter follows closely that of Kajiura. A summary of these data in the original format may be found in Sleath (1984).

The use of oscillating trolleys for the simulation of wave-induced flows at the seabed is well established in the field of fluid dynamics. The principle of the apparatus is that when a plate

---

is oscillated within a still fluid medium, the dynamic response of the fluid in terms of boundary layer development and flow stability relative to axes fixed in the moving plate will be the same as for the reciprocal case. Simple oscillations of the plate are characterised by: an oscillatory period ( $T$ ); and a stroke length ( $S$ ) (equivalent to the orbital excursion of fluid at the bed). Mobile sediment resting upon such an apparatus will experience an additional inertial force due to acceleration; however, it has been argued that this does not affect results if the magnitude of the inertial force remains small in comparison to the fluid shear force. Inertial force considerations are not necessary in fluid experiments over fixed beds, such as those reported in the present study.

Several experimental studies have utilised an oscillating trolley to investigate: the threshold of motion for sand (Bagnold, 1946; Manohar, 1955; Hammond and Collins, 1979; Rigler and Collins, 1984; Voulgaris *et al.*, 1995; Paphitis *et al.* 2001); the velocity distribution above the bed (Kalkanis, 1964; Du Toit and Sleath, 1981); lift/drag forces at the bed (Bagnold, 1946; Rosenthal and Sleath, 1986); the transition to turbulence (Li, 1954; and Manohar, 1955); and turbulence structure (Sleath, 1987). In these investigations, various experimental trolley designs, methodologies and fluids have been used to great effect. These have allowed process studies to be undertaken over a variety of time and length scales not possible in traditional wave tanks. Due to equipment design, studies have often represented oscillatory flows as sinusoidal variations in fluid displacement or velocity (*sinusoidal flow*). Consequently, flows exhibiting non-linear shallow-water effects causing wave and flow asymmetry (*asymmetric flow*) have not yet been considered in studies utilising oscillating trolleys. Oscillating tunnels have also been used in a small number of studies for the investigation of sediment transport, velocity structure, boundary layer stability and turbulence under asymmetric flows (e.g. Ribberink and Al-Salem, 1995; Tanaka *et al.*, 1998; Tanaka *et al.*, 2000). Such studies have indicated the potential importance of flow asymmetry in sediment dynamics.

Relationships reported previously, describing the transition to turbulence over rough beds, do not represent the data well at large grain sizes and (for both smooth and rough beds) do not account for variation associated with wave period or flow asymmetry. This investigation presents new data describing the transition to turbulence under sinusoidal and asymmetric oscillatory flows, over flat featureless beds of immobile uniform sediment ranging from fine to coarse sands. These data were collected using an oscillating trolley system in a fluid medium (water), using a variety of visual and numerical interpretative methods. New empirical relationships for sinusoidal and asymmetric flows are constructed from these data

---

in conjunction with the large (sinusoidal) data sets of Li (1954) and Manohar (1955). These latter data sets provide observations made using similar equipment and methodology over relatively large ranges of grain size and wave period. By using laboratory observations, no numerical assumptions are necessary regarding the mechanisms by which turbulence is initiated, under such a variety of conditions. Accepting the scatter caused potentially by experimental noise and differences in methodology, the absolute and relative effect of the flow and bed parameters are studied. The relationships between several aspects of the boundary layer, considered to be important in regulating the transition to turbulence, are then discussed.

## 2. METHODOLOGY

### 2.1 Experimental Design and Instrumentation

The oscillating trolley apparatus as utilised in the present study is shown in Figure 1. This equipment has been used successfully elsewhere in a variety of sediment dynamics investigations (Hammond and Collins, 1979; Rigler and Collins, 1984; Voulgaris *et al.*, 1995; and Paphitis *et al.*, 2001) and the details of operation are described therein also. Several technological advancements and modifications were implemented for the present study, including: (i) replacement of the original flywheel drive with an hydraulic ram, controlled through computer software; (ii) placement of (vertical) solid and (diagonal) porous baffles above the oscillating plate (as illustrated in Figure 1) to reduce the amplitude of ‘parasitic’ standing waves caused by the motion of the oscillating plate (see also Du Toit and Sleath, 1981); and (iii) an increase of the effective water depth within the flume, through the utilisation of smaller (5cm in height) bottom rails (reduced from 10cm) for the trolley, which reduced further the motion in the overlying fluid.

The utilisation of this new hydraulic system which was controlled through a computer software interface enhanced the experimental flexibility in relation to the possible conditions that could be simulated. For the first time, this unique combination of hardware and software allowed the simulation of asymmetric flows using oscillating trolley equipment. In the present study, such flows are represented by second-order Stokes theory. This particular wave model is suitable for the characterisation of waves entering relatively ‘shallow water’ conditions, i.e. closely following the point where the seabed rises above the depth of zero orbital motion. This typically represents the inner continental shelf (<60m water depth) for wave periods  $T \approx 5-9$ s or the coastal zone (5-20m water depth) for  $T \approx 2-5$ s. Flows at the seabed resulting from typical combinations of wavelength and water depth in this region are characterised primarily by  $T$  and  $S$  (the orbital diameter at the bed); likewise by a degree of

---

asymmetry and resulting peak velocity amplitude. These flows are at a scale appropriate to the capabilities of the hydraulics in the available laboratory set-up. From second-order Stokes theory the orbital velocity over time ( $t$ ) can be expressed as,

$$u_t = U_1 \cos \omega t + U_2 \cos 2\omega t \quad (1)$$

where  $U_1$  and  $U_2$  are the velocity amplitude of the primary and second harmonics, respectively; and  $\omega (=2\pi/T)$  is the radian frequency. These parameters and the resulting degree of asymmetry ( $R$ ) are shown schematically in Figure 2. Within the context of the present study, asymmetry represents a stronger peaking of velocity under the wave crest and a corresponding reduction of velocity and elongation of the trough half-cycle. The value  $R$  describes simply the peak positive velocity as a proportion of the velocity range (as measured between the crest and mid-trough). Using second-order Stokes theory (e.g. Kemp, 1975), a representative storm wave ( $T=5s$ , wave height=1m) will produce significant asymmetry ( $R=0.55$ ) at a water depth of approximately 7m; this increases rapidly and smoothly to  $R=0.65$ , at approximately 5m. Likewise, a representative swell wave ( $T=10s$ , wave height=3m) is affected similarly at approximately 25m and 18m water depth, respectively.

Different artificial beds were prepared for the various experimental conditions investigated during the present study. For the hydrodynamically smooth bed experiments a flat sheet of polished glass was fixed rigidly to the upper surface of the oscillating trolley. Two artificially roughened beds were prepared for the rough bed experiments, these consisted of a fixed (single) layer of uniform sand (275 $\mu$ m and 550 $\mu$ m mean grain diameter, respectively) glued onto similar sheets of polished glass. All of the beds provided a continuous flat surface 1.2m in length; this was in excess of the maximum stroke length simulated (1m).

Flow velocity (horizontal ( $u$ ) and vertical ( $w$ ) components) measurements were obtained at predetermined elevations (computer controlled) above the level of the experimental bed using a TSI two-component Laser Doppler Velocimeter (LDV) system in backscatter mode. The LDV system was provided by Biral, on loan through the Engineering and Physical Sciences Research Council (EPSRC) equipment pool. The bed reference level ( $z=0$ ) was determined experimentally for each bed by simulating a known oscillation with associated velocity amplitude. The sampling volume was then lowered until the measured peak velocity was equal to the plate velocity amplitude; therefore,  $z=0$  corresponded to the level of the ‘no-slip’ condition at the bed. This reference level was reset at regular intervals. The measuring

---

volumes (0.0905mm in diameter and 1.3mm in length) were formed by the intersection of two circular beams (for each velocity component) at a half-crossing angle of 3.95° which were coincident at the central point of the flume (in relation to its width). The LDV was configured to sample at a fixed rate of 200Hz for 120s during the transition to turbulence experiments.

## 2.2 Boundary Layer Velocity Structure

The velocity distribution in the boundary layer under laminar flow conditions is given by the well-known laminar boundary layer solution first presented by Stokes (1851). The original model was an analytical solution of the Navier-Stokes equations for flows that are under laminar conditions, with reference axes fixed in still water and adjacent to a boundary moving with a harmonic motion. Subsequently, it has been shown that if the axes of reference are transferred to the moving bed, the resulting flow in the boundary layer is the same as the reciprocal case of fluid oscillating over a static bed (as under a free surface gravity wave) (Lamb, 1932; Schlichting, 1968; and Sleath, 1984). The second-order solution is expressed as the summation of the individual harmonics. For axes fixed in the moving plate this expression becomes:

$$u_{(z,t)} = U_1 \cos(\omega t + \varphi) + U_2 \cos(2\omega t + \varphi) - [U_1 (e^{-\beta_1 z} \cos(\omega t + \varphi - \beta_1 z)) + U_2 (e^{-\beta_2 z} \cos(2\omega t + \varphi - \beta_2 z))] \quad (2)$$

where  $z$  is the height above the bed,  $\varphi$  is the phase lag ( $\varphi=0$  for all of the experiments in the present study) and  $\beta_1$  and  $\beta_2$  are the Stokes parameters, defined as:

$$\beta_1 = \frac{1}{\delta} = \sqrt{\frac{\omega}{2\nu}} \quad , \quad \beta_2 = \sqrt{\frac{2\omega}{2\nu}} \quad (3)$$

where  $\delta$  is the Stokes length (a measure of the laminar boundary layer thickness) and  $\nu$  is the kinematic viscosity. The laminar boundary layers under sinusoidal and asymmetric ( $R=0.7$ ) flows are compared directly in Figure 3 where differences in velocity and acceleration between the two cases may be clearly seen. Figure 3 also illustrates the phase lead of the lower boundary layer which results in vertical gradients of horizontal velocity and a zone of flow inflection.

Often it is the case that the fluid body overlying the oscillating trolley will develop small amplitude ‘parasitic’ oscillations resulting from fluid displacement and friction as the plate is moved. Parasitic oscillations were reduced in the present investigation by the introduction of solid and porous baffles (see Fig. 1) designed to dampen the free fluid motion. The remaining amplitude of these oscillations was typically 5-10% of  $U_I$  (i.e.  $\sim 1.5\text{cms}^{-1}$ ) and did not exceed 11.8%. For the purposes of the present study, the oscillation in the outer layer was adequately expressed by a sinusoidal variation in velocity at the same period as the primary harmonic of the plate motion, with amplitude  $U_\infty$  and phase  $\varphi_\infty$ . The resulting boundary layer flow with axes fixed in the theoretical ‘still water’ is

$$u_{(z,t)} = U_\infty [\cos(\omega t + \varphi_\infty) - e^{-\beta z} \cos(\omega t + \varphi_\infty - \beta z)] \quad (4)$$

An extended laminar flow model is created by the summation of Equations 4 and 2 (where  $U_\infty$  and  $\varphi_\infty$  are determined experimentally). This extended flow model was first used for sinusoidal flows by Du Toit and Sleath (1981) and reduced observed errors to less than 3% of  $U_I$  in all cases.

### 2.3 Transition to turbulence

The general experimental procedure for determining transition to turbulence was to simulate flows with various combinations of the oscillatory parameters ( $T$ ,  $S$  and  $R$ ) and of the different fixed roughness beds described in Section 2.1. The hydrodynamic conditions were observed subsequently and interpreted using three methods, namely: ‘visual observation’; ‘velocity time-series’; and, ‘turbulent intensity’ methods (see below). The oscillatory period and degree of asymmetry of the flow was set (over one of the artificially prepared beds) and this then remained constant throughout the experimental run. An initial value of  $S$  was determined on the basis of relationships proposed previously (Sleath, 1984) such that initial conditions would be within the laminar flow regime but close to the point of transition. The initial flow conditions were confirmed as being laminar, either by visual observation (for the visual observation method) or by inspection of the initial velocity time-series (for the velocity time-series and turbulent intensity methods).

During each experimental run,  $S$  was then increased by increments of between 1 and 2cm corresponding to an increase of  $\sim 1\text{cms}^{-1}$  in velocity amplitude, until the transition to turbulence occurred. At least 3 further increments and observations were made beyond the first signs of transition occurring. At each value of  $S$ , the flow was allowed to adjust over

---

three full oscillatory cycles prior to observations being made or to the initiation of the LDV data collection. For the ‘velocity time-series’ and ‘turbulent intensity’ methods flow velocity measurements were made at a height of 3mm above the bed for one minute following each increment of  $S$  and allowing time for flow adjustment. A minimum of 6 time-series were collected during each experiment.

The data collected in the present study was also reanalysed to investigate differences in the point of transition under the crest and trough portion of the wave cycle. This was achieved by applying the same three methods to only the data from the crest or trough, identified by positive or negative bed-parallel velocities, respectively.

### *2.3.1 Visual observation method.*

Visual observations of the transition to turbulence were performed by placing a small crystal of potassium permanganate on the oscillating plate. Under laminar flow conditions a ‘stable’ longitudinal streak of dye was formed close to the bed, i.e. initial dye dispersion from the streak was through molecular diffusion processes only. As the flow ( $S$  and/or  $U_c$ ) amplitude was increased, instability waves were observed to develop at the top of the dye streak. Following this, tongues of dye were ejected from within the boundary layer at the point of flow deceleration and reversal which became more regular and widespread with slight increases of the flow. At this point the dye streak became dispersed rapidly by eddy diffusion processes; the observation of this dispersion was designated as the transition to turbulence. The progression of such instability events have been described previously by several investigators (Li, 1954; Vincent, 1957; and George and Sleath, 1978).

### *2.3.2 Velocity time-series method.*

The measured time-series corresponding to laminar flow appeared as a smooth harmonic signal for the horizontal ( $u$ ) (Figure 4a) component of velocity. The vertical ( $w$ ) component appeared as a small-amplitude signal that was uniform over the wave cycle within a narrow envelope ( $\pm 0.005\text{ms}^{-1}$ ) (Figure 4b). In laminar flow theory the cross-stream ( $v$ ) and vertical ( $w$ ) components of the velocity field are (ideally) zero. However, as shown above it is uncommon that observations of actual flows will demonstrate zero flow in each of these components. As the flow increases, the signal suddenly begins to deviate from the laminar solution with both components of velocity showing evidence of high-frequency fluctuations ( $\pm 0.05\text{ms}^{-1}$ ) (Figures 4c and 4d). This is attributed here to the periodic ejection of eddies from within the boundary layer. Such a condition was designated as the ‘point of transition’

and is consistent with the principle of the ‘visual observation’ method. The transition occurred typically over a narrow range of velocity amplitudes (1-2cms<sup>-1</sup>).

### 2.3.3 Turbulent intensity method.

Using the measured velocity data (Section 2.3.2), the vertical component of the turbulent intensity ( $E$ ) was calculate for each time-series, where

$$E = \overline{\rho w'^2} \quad (5)$$

where  $\rho$  is the density of the fluid and  $w'$  is the fluctuating component of  $w$ .  $E$  was plotted then against  $S$  for each combination of bed type, oscillating period and asymmetry. The case of the  $D=275\mu\text{m}$ ,  $T=6\text{s}$  and  $R=0.55$  is presented as an example of this approach in Figure 5. The computed value of  $E$  derived from the experimental runs was observed to remain nearly constant until the point of transition; at this, it increased suddenly. A baseline was drawn as the mean of the values representing stable or laminar flow whilst a second straight line was fitted to the data points associated with elevated  $E$  values. The ‘critical’ stroke length ( $S_{crit}$ ) corresponding to the transition to turbulence was defined then as the point where the fitted line intersected the baseline and was expressed to the nearest centimetre. This method is consistent with the observation of ‘significant eddy formation’ used in the other two methods (see above).

## 3. RESULTS

In total, 37 conditions were simulated and interpreted using the velocity time-series and turbulent intensity methods. In addition, the visual observation method was incorporated into 14 of these conditions. All of the results have undergone careful screening to exclude certain conditions that: (i) exceeded the theoretical limitations of the oscillating trolley equipment in terms of maximum velocity amplitude; and/or (ii) did not extend sufficiently into the transitional regime to provide a clear transitional point. Of 88 possible observations, 68 were considered to be acceptable; of these, 15 were collected over a smooth bed.

Although three distinct methods were used to define and observe transition, the observed critical flow parameter values compared well between methods. This indicated that the various methods represent a consistent and comparable set of hydrodynamic conditions. As such, all the screened data were used in the overall analyses to reduce bias introduced by any single method.

**3.1 Smooth Beds.**

Smooth beds are a limiting case that may be representative of featureless mudflats or possibly planar beds of very fine sands. The smooth bed observations of Li (1954) were used to investigate patterns in the transition to turbulence, caused by difference in wave period under sinusoidal flows. A positive linear relationship with  $T$  was observed, following the relationship:

$$\begin{aligned}
 RE_{crit} &= 41T + 430 \quad \text{or} \quad Re_{crit} = 2.1 \times 10^4 T + 9.25 \times 10^4 && \text{for } T \leq 3.5s, R = 0.5 \\
 \text{and} \\
 RE_{crit} &= 576 \quad \text{or} \quad Re_{crit} = 1.66 \times 10^5 && \text{for } T > 3.5s, R = 0.5
 \end{aligned}
 \tag{7}$$

where

$$RE_{c,t} = \frac{U_{c,t} \sqrt{2\nu/\omega}}{\nu} \quad \text{and} \quad Re_{c,t} = \frac{U_{c,t} a}{\nu}
 \tag{6}$$

where the length scale used for the boundary Reynolds number  $RE$  is  $\delta$  and (for all parameters) the subscripts ‘crit’, ‘c’ and ‘t’ identify critical values and flows observed under the crest and the trough, respectively. For  $R=0.5$ , the two Reynolds numbers are related by  $RE = \sqrt{2} Re$ . The relationship for the transition to turbulence under asymmetric flows proposed on the basis of the results of the present study is shown in Figure 6. On the basis that no roughness element should be present on the bed, only the velocity time-series and turbulent intensity methods were used during the present experimental program for such beds. In Figure 6, open and filled circles represent all of the observed time-series data that have been classified as ‘laminar’ or ‘transitional/turbulent’ under the crest only, according to the criteria described in Section 2.3. In addition, individual points indicating the transition to turbulence as defined by the methods described in Section 2.3 have been identified separately for observations under the crest and under the trough. Using a least squares method, a polynomial curve of the form  $[a+b(R-0.5)^c]$  (where  $a$ ,  $b$  and  $c$  are coefficients) was fitted empirically to the crest data representing the boundary between laminar and transitional/turbulent conditions. An envelope representing the 99% confidence interval is also shown.

For second-order Stokes formulations,  $U$  and other values proportional to variations in  $U$  (e.g. Reynolds numbers) may be calculated interchangeably under the crest and the trough

---

using  $x_t=(x_c/R)\times(1-R)$ . Using this method, a corresponding curve for flows under the trough was drawn from the relationship fitted to the crest data. This curve was found to describe the trough data well in most cases but on average  $RE_{t_{crit}}$  was slightly underestimated. This suggested that in some cases transition occurs initially under the crest and then under the trough at greater overall flow amplitudes (i.e a larger orbital amplitude ( $a=S/2$ )) for the same  $T$  and  $R$ .

Scatter in the observations obtained from the present study can be attributed to: (i) slight differences between the observational methods; (ii) slight disturbances associated potentially with the mechanical action of the oscillating plate; and (iii) natural variability in the complex hydrodynamic processes involved. The data appear also to indicate a possible sensitivity to the period of oscillation. However, following data screening insufficient data points were available to draw firm conclusions on this particular observation.

For comparison to the results observed under second-order Stokes type flows, the curve for cnoidal waves proposed by Tanaka *et al.* (2000) is shown in Figure 6; this relationship was based primarily on the results of a  $\kappa$ - $\varepsilon$  boundary layer model. The two curves for transition under the crest are somewhat similar in shape as both demonstrate an increase in the critical value of RE with progressively higher asymmetry. However, in absolute terms they exhibit several dissimilarities. The laboratory and numerical studies of Hino *et al.* (1976) and Tanaka *et al.* (2000) respectively, have identified that transition at very low asymmetry ( $R=0.5$ ) occurs at  $RE=550$  ( $Re=1.51\times 10^5$ ). For the present study, an alternative value of  $RE=566$  was used as a fixed origin in the fitted curve corresponding to the generally accepted value of  $Re=1.6\times 10^5$  for transition over smooth beds (Sleath, 1984). From Eq. 7 the latter value may not be accurate for conditions where  $T<3.5s$  but is suitable for larger  $T$ . The value ( $RE=550$ ) used by Tanaka *et al.* is smaller and (from Eq. 7) is typically representative of small  $T$  ( $\sim 2.8s$ ) in the data sets presented herein. The difference in the two models at  $R=0.5$  corresponds to only a small difference in predicted velocity amplitude or stroke length (around 3%). As it is not clear whether the form of the asymmetric relationship should vary with  $T$  as well as  $R$ , it is possible that the curve of Tanaka *et al.* is more representative of small values of  $T$ .

The relationship proposed by Tanaka *et al.* (2000) and the relationship derived on the basis of the present study exhibit stronger disagreement at  $R>0.65$  (20% difference in predicted  $U_c$  and  $S$  at  $R=0.7$ ). In comparison, by applying second-order Stokes and cnoidal flows to laminar boundary layer theory, the rate of fluid acceleration/deceleration and gradients of

---

velocity under second-order Stokes flows are typically lower than under the equivalent cnoidal flow. The principle cause of this deviation was the formation of a secondary hump (a reduction in absolute flow velocity) in the central part of the trough half-cycle by the second-order Stokes model; conversely, the cnoidal model maintained a smooth trough without inflection. As such, the boundary layers predicted by the two models are very similar prior to the initial development of the secondary hump at  $R=0.62$  but do not become significant until approximately  $R=0.65$ . The increase in  $Re_{crit}$  in the cnoidal example suggests that the inclusion of additional harmonics may have an enhanced stabilising effect, delaying the onset of turbulence in the case of smooth beds. The appropriate inclusion of higher harmonics and the relative validities of water wave theories for specific combinations of wavelength, wave height, water depth, etc., are discussed elsewhere (e.g. Dean, 1970; Le Mehaute, 1976; Sleath, 1984).

### 3.2 Rough Beds.

The observations of Li (1954) and Manohar (1955) relating to sinusoidal flows were used in combination with the asymmetric crest and trough data of the present study to provide 308 observations of the transition to turbulence. These represent 10 grain sizes within the range  $D=0.025$ - $1.38$ cm and oscillatory periods in the range  $T=0.9$ - $15$ s for all grain diameters, but in some cases as high as  $T=34$ s. In the experiments of Li and Manohar, transition was determined by observing the dispersion of dye over a fixed granular bed using an oscillating trolley apparatus, i.e. a variation upon the visual observation method (see above).

A detailed analysis of all the data was undertaken to investigate the dependence of the fitting coefficient  $c$  from the original relationship of Manohar ( $Re_{crit}=c(a/D)$ ) on the experimental parameters. This analysis revealed a strong positive linear correlation with  $D$  for  $D \geq 410 \mu m$  and a significant negative linear correlation with  $T$  for  $D \leq 275 \mu m$ . For  $R=0.5$  the observed value of  $Re_{crit}$  can be described by

$$Re_{crit} = \left( (1.32 \times 10^5 D) + 46 \right) \times (a/D) \quad \text{for } 421 \mu m \leq D \leq 13807 \mu m \quad (8)$$

and

$$Re_{crit} = \left( (-2.4T) + 107 \right) \times (a/D) \quad \text{for } 235 \mu m \leq D \leq 275 \mu m$$

In comparison to the suggested relationship of Manohar (1955) where  $c=104$ , over relatively rough beds, Eq. 8 corresponded to a coefficient  $c=110-310$  for grains  $D=500-2000\mu\text{m}$  and over relatively smooth beds,  $c=100-71$  for  $T=3-15\text{s}$ , respectively. Rearranging Equation 8, this relationship may be expressed instead in terms of a critical grain Reynolds number

$$\frac{UD}{\nu} = (1.32 \times 10^5 D) + 46 \quad \text{for } 421\mu\text{m} \leq D \leq 13807\mu\text{m} \quad (9)$$

*and*

$$\frac{UD}{\nu} = (-2.42T) + 107 \quad \text{for } 235\mu\text{m} \leq D \leq 275\mu\text{m}$$

This representation avoids the explicit use of  $a$  in both the predictive and resultant equations. This is advantageous as the quantity  $a$  is not always easily extracted from field or laboratory observations, especially in the presence of flow asymmetry. The effect of flow asymmetry has been described as a scalar increase in  $\text{Re}_{\text{crit}}$  from the equivalent  $R=0.5$  case calculated using Equations 7, 8 or 9. The relationship is of the form

$$\text{Re}_{c \text{ crit}} = \text{Re}_{c \text{ crit}} \times (1 + j(R - 0.5)^k) \quad (10)$$

*and*

$$\text{Re}_{t \text{ crit}} = (\text{Re}_{c \text{ crit}} / R) \times (1 - R)$$

where  $j$  and  $k$  are fitting coefficients and were determined to be [ $j=12.7, k=1.470$ ] for  $D=550\mu\text{m}$  and [ $j=12.7, k=1.960$ ] for  $D=275\mu\text{m}$ . For comparison, the coefficients for the smooth bed were [ $j=6.2, k=2.133$ ]. On the basis of detailed analysis of the  $D=550\mu\text{m}$  data it was observed that the coefficient  $k$  decreased steadily with increasing  $T$ , hence the value presented is the mean value. This observation implies increasing stability with  $R$  in this case at larger  $T$ .

Of the three beds investigated, the relationship derived for the  $D=275\mu\text{m}$  bed coincided most closely with the case where  $S_{\text{crit}}$  remains roughly constant and all other related parameters ( $U_c$  and  $\text{Re}$ ) increase simply as a function of  $R$ ; this idealised relationship is closely approximated by [ $j=1.23, k=0.840$ ]. In comparison,  $S_{\text{crit}}$  decreased with  $R$  in the smooth bed case and increased with  $R$  in the  $D=550\mu\text{m}$  case. Over smooth beds, transition takes place first during the crest half cycle and only then under the trough following further increase in

---

the flow amplitude. On some occasions over the  $D=550\mu\text{m}$  bed transition was observed to occur under the trough at a lower value of  $Re$  than predicted by the second part of Equation 10, i.e. at smaller  $a_{crit}$  for a given  $T$  and  $R$ . The significance of this observation is that transition is occurring initially in the trough whilst flow under the crest remains laminar. Insufficient observations of this occurrence were made to quantify the conditions where this would occur.

The resulting values of  $Re_{crit}$  calculated using Equations 7, 8 and 10 are compared in Figure 7 to the observed values for sinusoidal and asymmetric flows over smooth and rough beds. The mean error in the predicted values of  $Re_{crit}$  for the data of Li and Manohar was  $\pm 5.3 \times 10^3$  ( $\pm 11\%$  of the observed value) whilst values in the mostly asymmetric data of the present study were typically over estimated by  $1.77 \times 10^4$  ( $+14\%$ ). The latter value represents an equivalent degree of scatter to the former but includes a consistent slight over-prediction of values. Therefore the definition of transition used in the present study corresponded to conditions at a lower Reynolds number than that used in the studies of Li and Manohar. The results of the present study provide an improved representation of the data when compared with the original relationship proposed by Manohar; the latter typically underestimated  $Re_{crit}$  by a mean value of  $2.2 \times 10^4$  ( $44.2\%$ ) but by as much as  $6.0 \times 10^4$  ( $92.8\%$ ) for large  $D$ .

The data were also reassessed to express  $Re_{crit}$  as a single combined function of  $T$  and  $D$ , using similar empirical fitting techniques to those used above. Transition for flows where  $R=0.5$  is described by

$$Re_{crit} = T \left( 2400 \times e^{5.73 \times 10^{-4} / D} \right) \quad \text{for } 240 \mu\text{m} < D < 13807 \mu\text{m} \quad (11)$$

with an upper limit of  $1.66 \times 10^5$ . The effect of asymmetry was described then by using Equation 10. Equation 11 reflects a positive linear relationship between  $Re_{crit}$  and  $T$  where the gradient decreases with  $D$  but the intercept remains constant (zero). This gradient increases sharply with decreasing  $D < 421 \mu\text{m}$  but becomes almost constant for  $D > 2000 \mu\text{m}$  with a smooth transition between the two conditions. The observed trends in the transition to turbulence over smooth and rough beds for sinusoidal flows, as described by Equations 7 and 11, are summarised in Figure 8. Effectively, Equation 11 combines the two groupings used in Equation 8. However, although the trend analysis highlighted clear relationships, the

---

absolute error in predicted values from Eq. 11 was increased by a factor of 2 over those from Eq. 8.

#### 4. DISCUSSION AND CONCLUSIONS

Differences in the smooth and rough bed relationships for sinusoidal flows suggest that rates of fluid acceleration, sources of initial flow perturbation, velocity distribution and time-scales are all processes that are in balance and are important in regulating the development of turbulence. Over relatively smooth beds the initial source of flow perturbation is fluid shear in the vertical velocity profile. When destabilising shear becomes large with respect to other stabilising forces, turbulence is initiated. It follows that under laminar flows, the vertical gradient in horizontal velocity and therefore, the transition to turbulence are proportional to  $T$ . Conversely, in the case of very rough beds initial flow perturbation is caused primarily by eddies shed from individual roughness elements. The strength of this eddy development and as such, the transition to turbulence are proportional to  $D$ . From the limits used in Equation 9 (see also Figure 8) and the form of the relationship described by Equation 11, smooth bed processes dominate for  $D < 400\text{-}500\mu\text{m}$  whilst rough bed processes dominate for  $D > 2000\mu\text{m}$  (under sinusoidal flows). Intermediate grain sizes experience a balance between both processes. A similar pattern (without reference to wave period effects) has been observed for transition over rippled beds of increasing ripple steepness (Sleath, 1984). As analogous processes these observations are likely to be related by similar mechanisms at different length scales.

The above arguments may be applied also to the less straightforward case of asymmetric flows. Under the crest there is an increase in the vertical gradients of horizontal velocity and flow rates around roughness elements (the principle destabilising processes over smooth and rough beds, respectively (see above)) with smaller  $T$  and/or larger  $R$ . These destabilising processes are balanced by the associated increases in flow acceleration (a known stabilising process), likewise by corresponding decreases in the time available for the development of turbulence in the deceleration phase. The opposite pattern can be identified when considering the transition to turbulence under the trough. Here, vertical gradients of horizontal velocity and the flow rate around individual grains are reduced but are associated also with lower rates of fluid acceleration and a longer time frame for turbulence development. The data show that the balance of forces is primarily grain size dependent and is also likely to be period dependant. As  $R$  increases, it seems that stabilising processes increase at a lower rate than destabilising processes for smooth beds whilst the opposite is true for rough beds. This balance is apparently maintained over beds of  $D \approx 275\mu\text{m}$ . It is anticipated that a larger data

---

set with a greater range and resolution of flow parameters will demonstrate non-linear relationships similar in form to that for smooth beds as shown in Figure 6, that are a function of both  $T$  and  $D$ .

In another investigation highlighting previously unrecognised wave period dependency effects, Voulgaris *et al.* (1995) show that to achieve the threshold of motion for quartz sands, a larger shear force is needed to erode sediment under a shorter wave period. This pattern is observed also in the threshold of motion data presented by other researchers, e.g. Bagnold (1946), Manohar (1955) or Hammond and Collins (1979). Wave asymmetry has been shown to cause patterns of sediment movement different to those observed under sinusoidal flows (Ribberink and Al Salem, 1995). Further, previous relationships developed using sinusoidal data tend to underestimate rates of transport when applied directly to the asymmetric case (Davies and Li, 1997). The results of the present study could provide potentially some explanation for such differences through more accurate representation of the onset or duration of turbulence as an additional erosive force.

#### **Acknowledgements**

One of the authors (DOL) was funded by the Engineering and Physical Sciences Research Council (EPSRC), as part of a postgraduate study program (Award 0031101X). The LDV equipment used was provided also by the EPSRC equipment pool. Mrs Kate Davies is thanked for her assistance in the final preparation of the Figures.

Bagnold, R.A., Motion of waves in shallow water. Interaction between waves and sand bottoms, *Proceedings of the Royal Society. Series A.*, 187, 1-15, 1946.

Davies, A.G., and M.Z. Li, Modelling sediment transport beneath regular symmetrical and asymmetrical waves above a plane bed., *Continental Shelf Research*, 17 (5), 555 - 582, 1997.

Dean, R.G., Relative validities of water wave theories, *Journal of the Waterways and Harbours Division, ASCE.*, 96 (1), 105-119, 1970.

Du Toit, C.G., and J.F.A. Sleath, Velocity measurements close to rippled beds in oscillatory flow, *Journal of Fluid Mechanics*, 112, 71-96, 1981.

George, C.B., and J.F.A. Sleath, Oscillatory laminar flow above a rough bed, *Proc. 16th Coastal Engineering Conference*, 1, 898-910, 1978.

- Hammond, T.M., and M.B. Collins, On the threshold of transport of sand-sized sediment under the combined influence of unidirectional and oscillatory flow, *Sedimentology*, 26, 795-812, 1979.
- Hino, M., M. Sawamoto, and S. Takasu, Experiments on transition to turbulence in an oscillatory pipe flow, *Journal of Fluid Mechanics*, 75, 193-207, 1976.
- Jensen, B.L., B.M. Sumer, and J. Fredsøe, Turbulent oscillatory boundary layer at high Reynolds numbers, *Journal of Fluid Mechanics*, 206, 265-297, 1989.
- Kalkanis, G., *Transportation of bed material due to wave action*, pp. 38, US Army Coastal Engineering Research Centre, Technical Memo 2, 1964.
- Kajiura, K., A model of the bottom boundary layer in water waves, *Bulletin of the Earthquake Research Institute*, 46, 75-123, 1968.
- Kemp, P.H., Wave asymmetry in the nearshore zone and breaker area, in *Nearshore Sediment Dynamics and Sedimentation*, edited by J. Hails, and A. Carr, pp. 316, John Wiley & Sons, London, 1975.
- Komar, P.D., and M.C. Miller, Sediment threshold under oscillatory waves, in *Proc. 14th Coastal Engineering Conf., ASCE.*, 756 - 775, 1974.
- Lamb, H., *Hydrodynamics*, 738 pp., Cambridge University Press, 1932.
- Le Mehaute, B., *An introduction to hydrodynamics and water waves*, 315 pp., Springer-Verlag, New York, 1976.
- Lhermitte, M.P., *Contribution à l'étude de la couche limite des houles progressives: Application aux mouvements de matériaux sous l'action des houles*, pp. 171, C.O.E.C. Imprimerie Nationale. No. 136, Paris, 1958.
- Li, H., *Stability of oscillatory laminar flow along a wall*, pp. 35, Technical Memo 47, University of California, Berkley, California, California, US, 1954.
- Lodahl, C., B. M. Sumer, and J. Fredsøe, Turbulent combined oscillatory flow and current in a pipe. *Journal of Fluid Mechanics*, 373, 313-348, 1989.
- Manohar, M., *Mechanics of bottom sediment movement due to wave action*, pp. 121, Technical Memo No. 75, Beach Erosion Board., 1955.
- Paphitis, D., A.F. Velegrakis, M.B. Collins, and A. Muirhead, Laboratory investigations into the threshold of movement of natural sand-sized sediments, under unidirectional, oscillatory and combined flows, *Sedimentology*, 48 (3), 645-659, 2001.
- Ribberink, J.S., and A.A. Al-Salem, Sheet flow and suspension of sand in oscillatory boundary layers, *Coastal Engineering*, 25, 205-225, 1995.
- Rigler, J.K., and M.B. Collins, Initial grain motion under oscillatory flow: A comparison of some threshold criteria, *Geo-Marine Letters*, 3, 43-48, 1984.
-

- Rosenthal, G.N., and J.F.A. Sleath, Measurements of lift in oscillatory flow, *Journal of Fluid Mechanics*, 164, 449-467, 1986.
- Schlichting, H., *Boundary Layer Theory*, 748 pp., McGraw-Hill, New York, 1968.
- Sleath, J.F.A., *Sea Bed Mechanics*, 335 pp., Wiley, Chichester, 1984.
- Sleath, J.F.A., Seabed boundary layers, in *Ocean Engineering Science: Part B*, edited by B. Le Mehaute, and D.M. Hanes, pp. 693-728, Wiley-Interscience, New York, 1990.
- Sleath, J.F.A., Stability of laminar flow at seabed, *Journal of the Waterways and Harbours and Coastal Engineering Division, ASCE.*, 100 (WW2), 105-122, 1974.
- Sleath, J.F.A., Turbulent oscillatory flow over rough beds, *Journal of Fluid Mechanics*, 182, 369-409, 1987.
- Stokes, G.G., On the effect of internal friction of fluids on the motion of pendulums, *Transactions of the Cambridge Philosophical Society*, 9, 20-21, 1851.
- Tanaka, H., A. Sana, I. Kawamura, and H. Yamaji, Stability of asymmetric wave boundary layers, in *Proceedings of the 4th International Conference on Hydrodynamics*, pp. 563-568, Yokohama., 2000.
- Tanaka, H., and A. Sana, Numerical study on transition to turbulence in a wave boundary layer, in *Euromech 310*, edited by M. Belorgey, R.D. Rajaona, and J.F.A. Sleath, pp. 14-25, World Scientific, Singapore, 1994.
- Tanaka, H., H. Yamaji, and A. Sana, A generation method of asymmetric oscillatory motion simulating cnoidal waves, *Coastal Engineering Journal, JSCE.*, 40 (3), 291-306, 1998.
- Vincent, G.E., Contribution to the study of sediment transport on a horizontal bed due to wave action, in *Proc. 6th Coastal Engineering Conf.*, pp. 327-355, 1957.
- Voulgaris, G., S. Wallbridge, B.N. Tomlinson, and M.B. Collins, Laboratory investigations into wave period effects on sand erodibility, under the combined action of waves and currents, *Coastal Engineering*, 26, 117-134, 1995.

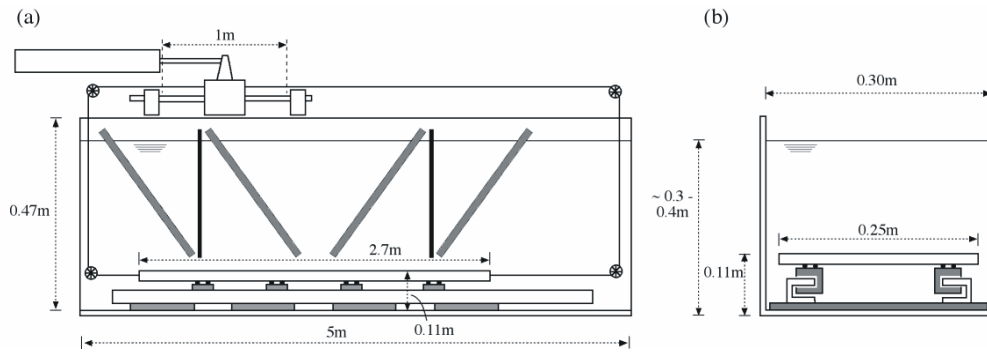


Figure 1. Schematic diagram of the oscillating trolley equipment, as used in the present study: (a) elevation; and, (b) cross-sectional views. See the text for details.

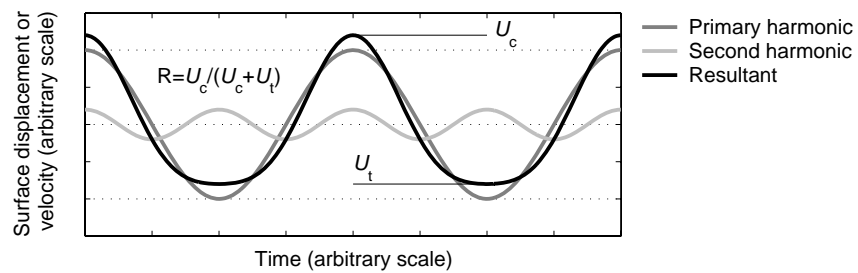


Figure 2. Harmonic components and the form of the velocity cycle outside of the boundary layer, as predicted under a second-order Stokes wave ( $R=0.6$ ).

**Key:**  $U_c$  and  $U_t$  are the absolute near-bed velocities under the crest and trough of the wave ( $\omega t=0^\circ$  and  $180^\circ$ ), respectively.

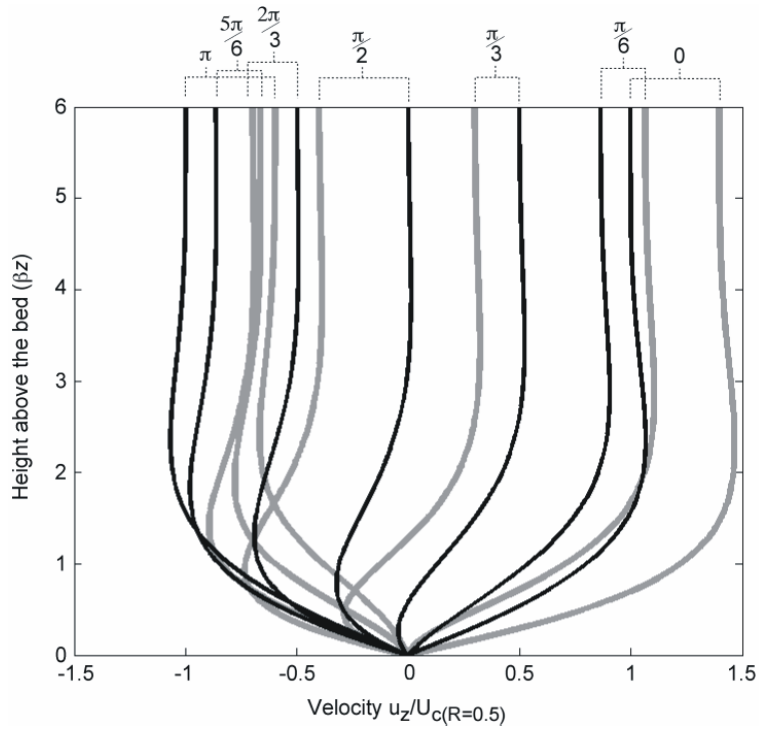


Figure 3. Velocity distribution within the laminar boundary layer ( $\omega t=0-\pi$ , normalised to  $R=0.5$ ), for linear and second-order Stokes flows, illustrating differences in fluid acceleration and vertical gradients of horizontal velocity.

**Key:** Black lines –  $[R=0.5]$ ; Grey lines –  $[R=0.7]$ .

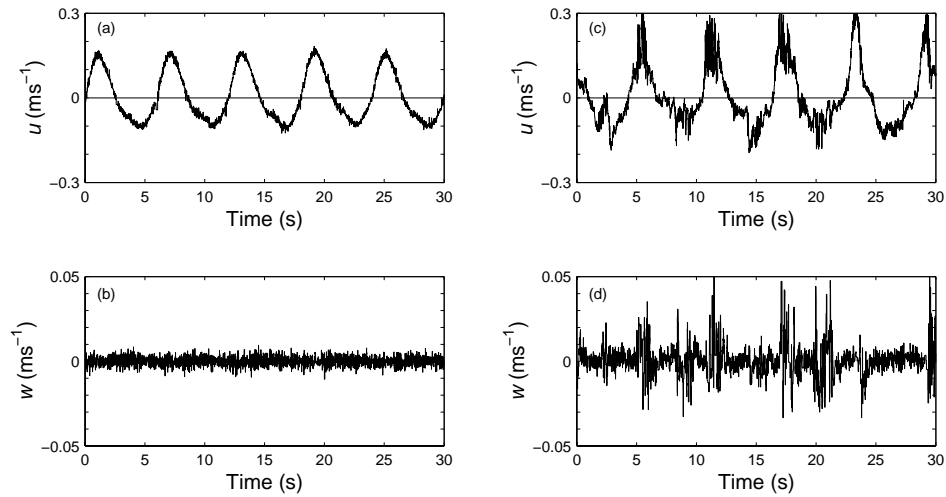


Figure 4. Recorded time-series of velocity at  $z=3\text{mm}$ , corresponding to laminar (a) & (b), stroke length = 66cm, and  $RE = 573$ ), and transitional/turbulent (c) & (d), stroke length = 82cm, and  $RE = 712$ ) flows, over a smooth bed ( $T = 6\text{s}$ ,  $R=0.6$ ).

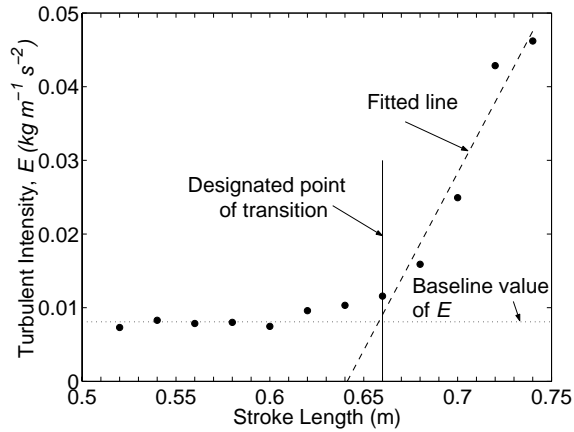


Figure 5. Turbulent intensity,  $E$ , at  $z=3\text{mm}$ , with increasing stroke length, demonstrating the transition to turbulence. Data for case [ $D=275\mu\text{m}$ ,  $T=6\text{s}$ ,  $R=0.55$ ].

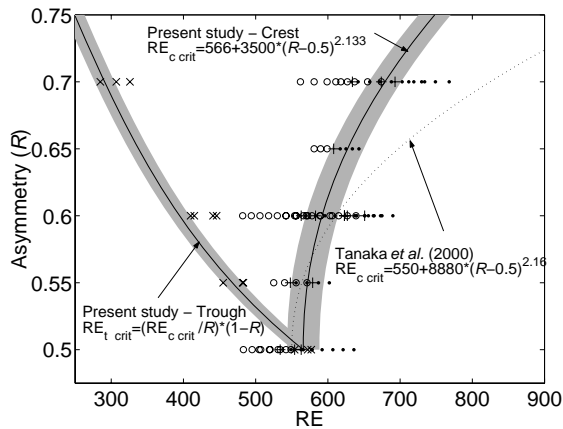


Figure 6. Stability of the oscillatory boundary layer over a flat, smooth bed.

**Key:** Laminar (O) and transitional/turbulent (●) conditions and flows at the initial transition under the crest (+) and trough (×) half cycles, as observed in the present study; solid line and envelope – least squares fit to crest data (and corresponding curve for the trough) and 99% confidence interval; dotted line – relationship for cnoidal flows, as proposed by Tanaka *et al.* (2000).

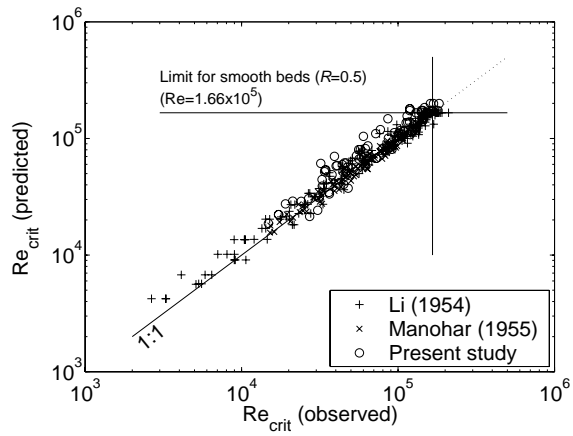


Figure 7. Comparison of the observed values of  $Re_{c,t,crit}$  over flat, rough (granular) and smooth beds together with values predicted using Equations 8 and 10. The linear data of Li (1954) and Manohar (1955) are shown, together with the linear and non-linear data of the present study ( $Re_{c,crit}$  and  $Re_{t,crit}$ ).

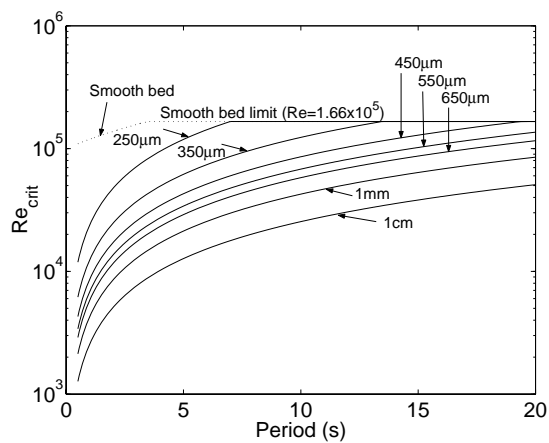


Figure 8. Transition to turbulence under linear oscillatory flow over rough (granular) and smooth, flat beds.